Behaviour of reinforced concrete members incorporating recycled rubber materials

A thesis submitted to

Imperial College London

for the degree of

Doctor of Philosophy

by Bowen Xu

BSc, MSc

Department of Civil and Environmental Engineering

Imperial College London

London SW7 2AZ, UK

October 2018

To my family

Declaration of originality

I hereby declare that the work presented in this thesis is my own work. No part of this thesis has been submitted for any degree or other purposes. Any other source included in this work, which is not my own, has been properly referenced.

Bowen Xu

October 2018

Copyright declaration

The copyright of this thesis rests with the author and is made available under a Creative Commons Attribution Non-Commercial No Derivatives licence. Researchers are free to copy, distribute or transmit the thesis on the condition that they attribute it, that they do not use it for commercial purposes and that they do not alter, transform or build upon it. For any reuse or redistribution, researchers must make clear to others the licence terms of this work

Bowen Xu

October 2018

Abstract

This thesis deals with the behaviour of concrete materials and reinforced concrete members incorporating recycled rubber particles, as partial replacement for mineral aggregates. The research involves several experimental investigations on materials and members, coupled with detailed numerical simulations and parametric assessments.

Tests on cylindrical material specimens focuses on examining the uniaxial behaviour of rubberised concrete. The experimental investigation, combined with detailed assessment of data from previous tests, show that the rubber particles influence the mechanical properties as a function of the quantity and type of replaced aggregates. A series of expressions and analytical models defining the mechanical properties of rubberised concrete are proposed. Further tests on confined rubberised concrete cylinders show that external confinement provides significant enhancement to the strength and deformation capacity of the material.

The experimental behaviour of rubberised concrete members under shear loading is also investigated in this research. The design of an asymmetric four-point shear test set-up is discussed and a detailed account of test results on eighteen prismatic rubberised concrete members, with or without confinement, is presented. Close observation of specimens exhibiting shear-governed failure shows that rubber particles have a significant influence on the member shear resistance and force transfer mechanisms along the cracked interface.

In addition to the material and shear tests, the experimental performance of large-scale beam-column members is examined in the thesis. Tests on fourteen large scale reinforced rubberised concrete members, subjected to lateral cyclic displacements and co-existing axial loading, are reported. The test results enable a direct assessment of key response characteristics of beam-column specimens. It is shown that members with rubber particles can offer a better balance between capacity and ductility compared to conventional reinforced concrete members. In addition, external confinement, such as using fibre reinforced polymer (FRP) sheets, can be adopted to recover the loss of strength and provide highly stable hysteretic response.

Numerical simulations of all the test series are performed using nonlinear finite element analysis and validated against the corresponding experimental results. The numerical models are then used to conduct parametric studies in order to examine the effect of key material and geometric factors on the behaviour of rubberised concrete members. Based on the findings from the experimental and numerical investigations, a series of expressions to assess the key performance characteristics of rubberised concrete members are proposed in a form that is suitable for practical design application.

Acknowledgements

I would like to express my sincere gratitude to my principle supervisor Prof. Ahmed Elghazouli for his constant support and encouragement. His constructive and clear suggestions are invaluable throughout my study experience. My sincere appreciation also goes to my co-supervisors Dr. Ana Ruiz-Teran and Dr. Peter Stafford for valuable comments.

I am also grateful to Dr. Dan Bompa, my colleague, collaborator and friend, who willingly provided me great support and technical guidance during my studies. His suggestions and encouragement have also been precious gains.

The financial support of Chinese Scholarship Council (CSC) and Dixon Scholarship provided by the Department of Civil and Environmental Engineering are gratefully acknowledged. The financial support of the research project was provided by the European Union Seventh Framework Programme within the project 'Anagennisi: Innovative Use of all Tyre Components in Concrete'. The discussions with collaborators within the project, particularly from the University of Sheffield, are also gratefully acknowledged.

I would like to thank the staffs of Structural Laboratories at Imperial College London, including Mr. Stefan Algar, Mr. Les Clark, Mr. Gordon Herbert, Mr. Bob Hewitt, Mr. Trevor Stickland and Mr. Ron Millward. Their assistance during my experimental work is much appreciated. I am particularly grateful to Mr. Trevor Stickland and Mr. Ron Millward. Their contribution is invaluable for the research.

I would like to thank all my colleagues and friends of the Structures section for being part of life during the years. They also made my PhD experience much more meaningful.

My special thanks to my girlfriend Miss Linghui Zhou, who provided me great love and support through the years, especially during my hardest time. Our wonderful moments together during this experience are and will always be my precious assets.

Finally, I would like to express my most sincere love and gratitude to my parents and grandfather. They continuously provided huge support and encouragement throughout my research. I am indebted to them and I could never finish my PhD without their help.

Table of contents

Abstract **5**

Acknowledgements **6**

List of Figures **12**

List of Tables **22**

1 Introduction **24**

1.1 General 24

1.2 Rubberised concrete 25

1.3 Aim and organisation of the present work 26

2 Literature review **29**

2.1 Behaviour of rubberised concrete materials 29

2.1.1 Influence of rubber particles 29

2.1.2 Merits of rubberised concrete material 34

2.1.3 Mechanical properties 40

2.2 Behaviour of FRP confined concrete 45

2.2.1 Types of FRP confinement 45

2.2.2 Properties of FRP confined concrete 47

2.3 Assessment of shear in rubberised concrete 50

2.3.1 Ultimate shear behaviour in concrete 51

2.3.2 Shear mechanisms in rubberised concrete 54

2.4 Behaviour of rubberised concrete members 56

2.4.1 Unconfined members 57

2.4.2 Confined members 62

2.5 Concluding remarks 70

3 Material tests **72**

Nomenclature 72

3.1 General 72
3.2 Experimental programme 73
3.2.1 Mix design and specimen details 73
3.2.2 Testing arrangements 80
3.3 Mechanical properties of rubberised concrete 82
3.3.1 Pilot tests 82
3.3.2 Stress-strain response 84
3.3.3 Influence of rubber content 86
3.4 Prediction of mechanical properties 89
3.4.1 Compressive strength 91
3.4.2 Modulus of elasticity 94
3.4.3 Splitting strength 95
3.5 Uniaxial Unconfined constitutive relationships 96
3.5.1 Proposed model 96
3.5.2 Validation against test results 99
3.6 Effect of AFRP confinement 102
3.6.1 Stress-strain behaviour of confined tests 102
3.6.2 Influence of AFRP jacket on the mechanical properties 105
3.7 Concluding remarks 108
4 Asymmetric shear tests 111
Nomenclature 111
4.1 General 111
4.2 Experimental programme 112
4.2.1 Mix design and specimen details 113
4.2.2 Testing arrangement 114
4.3 Test results 124
4.3.1 Tensile-governed and mixed-mode responses 128
4.3.2 Shear-governed response 130

4.3.3 Restrained dilation tests (AFRP confined tests) 133
4.4 Comparative assessments 136
4.5 Concluding remarks 139
5 Experimental methodology for member tests 141
Nomenclature 141
5.1 General 141
5.2 Specimen details 142
5.3 Testing arrangements 147
5.3.1 Self-reaction test rig for Ø250 members 148
5.3.2 Large-scale test rig for Ø350 members 151
5.4 Instrumentation 153
5.4.1 Strain gauges 154
5.4.2 Linear variable displacement transducers (LVDT) and inclinometers 156
5.4.3 Digital image correlation (DIC) system 158
5.5 Concluding remarks 158
6 Results of beam-column member tests 160
Nomenclature 160
6.1 Material properties 161
6.1.1 Concrete characteristics 161
6.1.2 Steel reinforcement 164
6.2 Test results and observations 165
6.2.1 Rubberised concrete members 167
6.2.2 Confined rubberised concrete members 177
6.2.3 Moment-rotation response 184
6.2.4 Ductility considerations 188
6.3 Comparative assessment 188
6.3.1 Strength interaction 188
6.3.2 Ductility considerations 193

6.3.3 Plasticity length of reinforcement 196
6.3.4 Energy dissipation 198
6.4 Concluding Remarks 200
7 Numerical simulations 202
Nomenclature 202
7.1 General 202
7.2 Concrete modelling 203
7.2.1 Yield and failure criteria 203
7.2.2 Post-elastic behaviour 205
7.3 Asymmetric shear tests 207
7.3.1 Modelling procedures 207
7.3.2 Constitutive properties 209
7.3.3 Comparative results 210
7.4 Beam-column member tests 212
7.4.1 Modelling procedures 212
7.4.2 Constitutive parameters 214
7.4.3 RC and RRuC member tests 217
7.4.4 Externally confined (CRRuC) member tests 221
7.5 Concluding remarks 226
8 Parametric assessments and design considerations 228
Nomenclature 228
8.1 General 228
8.2 Behaviour of asymmetric shear members 229
8.3 Beam-column modelling 232
8.3.1 Idealised member model 232
8.3.2 Main parameters 234
8.3.3 Failure criteria 235
8.4 Performance of beam-column members 235

8.4.1 Member stiffness 236
8.4.2 Strength interaction 237
8.4.3 Member ductility 241
8.4.4 Spread of plasticity 245
8.5 Concluding remarks 251
9 Closure 252
9.1 Summary and conclusions 252
9.2 Suggestions for future research 256
References 258

List of Figures

Figure 1.1 Tyre waste destruction involving: (a) burning (Tyre Pyrolysis Plant 2016) and (b) burying (Old Tyres Around the World 2017) 24

Figure 2.1 a) Crack formation procedure under compression (Hsu et al. 1963; Vonk 1992), b) force transfer between aggregates 30

Figure 2.2 Crack propagation mechanism in rubberised concrete under: a) compression, b) splitting tension, as proposed by Eldin and Senouci (1993) 31

Figure 2.3 Micrographs showing: a) indentations on cement pasteafter rubber particles pull out, b) extensive microcracking at rubber particle vicinity, and c) tension cracks propagating in rubber particles: TRP=tire rubber particle, CP=cement paste (Taha et al. 2008) 32

Figure 2.4 Influence of rubber grading and quantity on compressive strength (Fattuhi and Clark 1996) 33

Figure 2.5 Typical compressive stress-strain behaviour of concrete related with crack progressing states (Vonk 1992) 34

Figure 2.6 Separation of tensile stress-strain behaviour into an elastic behaviour and a localised crack opening behaviour 35

Figure 2.7 Influence of rubber particles on the softening behaviour of rubberised concrete under compression (adapted from Batayneh et al. 2007) 36

Figure 2.8 Four-point bending test results: a) load-deflection relationship, b) normalised load (Turatsinze and Garros 2008) 36

Figure 2.9 Rubber particles restraining crack opening (Aiello and Luezzi 2010) 36

Figure 2.10 Illustration of the flexural toughness 38

Figure 2.11 Four-point flexural test results by Toutanji (1995) 38

Figure 2.12 Energy dissipated by concrete with different rubber content: a) at maximum load, b) versus time progressing (adapted from Atahan and Yucel 2012) 39

Figure 2.13 Correlation between Popovics model and: a) compression, b) tensile test results proposed by Eldin and Senouci (1993) 41

Figure 2.14 Stress reduction factor versus rubber content (Ghaly and Cahill 2005) 42

Figure 2.15 Regression model proposed by Guneyisi et al. (2004) describing the reduction factors for: a) compressive strength, b) tensile strength, with different rubber content 43

Figure 2.16 Correlation between experimental results and analytical model (Taha et al. 2008)..... 44

Figure 2.17 Material characteristics of GFRP, CFRP, AFRP and steel fibres 46

Figure 2.18 Confinement action of concrete core and FRP jacket 47

Figure 2.19 Characteristic stress-strain behaviour of FRP confined concrete from Saafi et al. (1999): a) CFRP confinement, b) GFRP confinement, Xiao and Wu (2000) c) CFRP confinement, d) GFRP confinement, Dai et al. (2011) e) AFRP confinement and f) corresponding typical failure type..... 48

Figure 2.20 Classification of stress-strain curves of FRP confined concrete: a) increasing type (sufficient confinement), b) decreasing type ($f_{cu} > f_{c0}$), c) decreasing type ($f_{cu} < f_{c0}$) (insufficient confinement) (adapted from Lam and Teng 2003) 49

Figure 2.21Characteristic stress-strain behaviour of FRP confined concrete from Youssf et al. 2014: a) CFRP confined normal concrete, b) CFRP confined rubberised concrete, c) Raffoul et al. 2017- AFRP confined rubberised concrete, d) corresponding typical failure type..... 50

Figure 2.22 Mode I and Mode II fractures of concrete..... 51

Figure 2.23 Influence of the length of shear band on the fracture behaviour of concrete (Non-scaled sketches adapted from Arrea and Ingraffea (1982), Bazant and Preiffer (1986))..... 52

Figure 2.24 Test methods for assessment of shear resistance: a) Iosipescu and Negotia (1969), b) Bazant and Preiffer (1986), c) JSCE-SF6 (1990), Tuan et al. (2016), d) Luong (1990, 1992), e) Reinhard et al. (1997), f) Mattock and Hawkins (1972), g) Watkin (1972). 54

Figure 2.25 a) Aggregate interlock mechanism, b) stress transfer and equilibrium states 55

Figure 2.26 a) Test setup, mid-span deformation of RC and RRuC columns under axial compression with reference normal concrete strength of: b) f_{c0}=24 MPa, c) f_{c0}=28 MPa (from Son et al. 2011).. 58

Figure 2.27 a) Energy dissipation, b) curvature ductility, as a function of rubber content (adapted from Son et al. 2011)..... 58

Figure 2.28 Four-point bending test setup on RRuC beam members (Ismail and Hassan 2016)..... 59

Figure 2.29 Four-point flexural test results on RRuC beams: a) load-deflection behaviour, b) ductility, c) toughness with different rubber contents (adapted from Ismail and Hassan 2016) 60

Figure 2.30 Beam-column member under combined axial and lateral load (Youssf et al. 2015) 61

Figure 2.31 Hysteretic behaviour: a) RC member, b) RRuC member, c) backbone curves 61

Figure 2.32 Energy dissipation of RC and RRuC beam-column members (Youssf et al. 2015) 62

Figure 2.33 Test scheme of CFST and RuCFST beam-column test (Duarte et al. 2016)..... 63

Figure 2.34 Envelope curves of RuCFST columns with: a) square, b) rectangular, c) circular cross-section under the same level of axial loads (adapted from Duarte et al. 2016) 64

Figure 2.35 Energy and ductility: a) definition, b) CFST members, c) RuCFST members with 5% rubber content, d) RuCFST members with 15% rubber content (adapted from Duarte et al. 2016) . 65

Figure 2.36 Neutral axis position: a) CFST (normal concrete), b) RuCFST (rubberised concrete) (adapted from Duarte et al. 2016) 66

Figure 2.37 Global damage patterns of all test specimens (Youssf et al. 2016) 67

Figure 2.38 Hysteretic behaviour of specimens: a) RC, b) CRC-2L, c) RRuC, d) CRRuC-2L, e) CRRuC-4L, f) envelope curves of all specimens (adapted from Youssf et al. 2016)..... 68

Figure 2.39 Energy dissipation of all test specimens: a) up to 5% drift, b) up to 10% drift (Youssf et al. 2016) 69

Figure 3.1 a) Rubberised concrete samples, b) Rubberised concrete constituents, c) Rubberised conrete mix..... 74

Figure 3.2 Sieve analysis for mineral aggregates and recycled rubber..... 75

Figure 3.3 Mixing machine and ingredients 77

Figure 3.4 a) AFRP roller, b) bonding adhesive and hardener, c) AFRP sheet components..... 78

Figure 3.5 AFRP preparation procedure a) cutting the sheet, b) mixing adhesive and hardener, c) soaking the sheet in adhesive 79

Figure 3.6 Test arrangement for cylinders a) general review, b) layout 80

Figure 3.7 View of testing for: a) compression test on cubes, b) splitting test on cylinders 81

Figure 3.8 a) Longitudinal cross section through a rubberised concrete cylinder, b) Stress-strain response of pilot tests with 60% replacement, c) Failure of pilot cylindrical samples..... 83

Figure 3.9 Stress-strain relationships for a) normal concrete R00, b) rubberised concrete with 20% replacement R20, c) rubberised concrete with 40% replacement R40, d) rubberised concrete with 60% replacement R60 85

Figure 3.10 Influence of rubber content ρ_{vr} on the mechanical properties of concrete: a) elastic modulus E_{cr}, b) compressive strength f_{cr}, c) peak axial strain ε_{cr1}, d) peak lateral strain ε_{cr1}, e) splitting strength $f_{ctr,sp}$, f) crushing energy G_c 88

Figure 3.11 Comparative view of tested samples 89

Figure 3.12 Compressive strength degradation as a function of volumetric rubber ratio ρ_{vr} 92

Figure 3.13 a) Relationship between modulus of elasticity E_{cr} and compressive strength f_{cr} for rubberised concrete, b) degradation of stiffness as a function of volumetric rubber ratio ρ_{vr} 95

Figure 3.14 a) Relationship between splitting strength $f_{ctr,sp}$ and compressive strength f_{cr} for rubberised concrete, b) degradation of $f_{ctr,sp}$ as a function of volumetric rubber ratio ρ_{vr} 96

Figure 3.15 Uniaxial constitutive model for rubberised concrete 97

Figure 3.16 Relationship between stress ratio and lateral-to-axial strain ratio 98

Figure 3.17 a) Relationship between maximum crack width and rubber content, b) assumed stress-strain diagram in tension 99

Figure 3.18 Comparison between test and predicted stress-strain responses (black and red curves represent experimental and predicted response, respectively) 101

Figure 3.19 Comparison between stress-strain responses predicted by EC2 and the proposed model 102

Figure 3.20 Typical failure modes of confined rubberised concrete specimens: a) R00F3, b) R40F2, c) R60F2, d) R60F3 103

Figure 3.21 Compression test stress-strain behaviour for AFRP confined and unconfined concrete specimens: a) R00F3, b) R40F2, c) R60F2, d) R60F3 105

Figure 3.22 Influence of confinement ratio f_l/f_{cr} on the mechanical properties of confined rubberised concrete: a) compressive strength f_{crc}, b) ultimate axial strain $\varepsilon_{crc1,u}$, c) ultimate lateral strain $\varepsilon_{crc2,u}$, d) stiffness of second linear branch E_{crc2} 107

Figure 4.1 a) Rubberised concrete sample, b) Confined rubberised concrete sample 114

Figure 4.2 Configuration of direct shear test 114

Figure 4.3(a) Prototype and (b) failure pattern of cutting shear test (no shear stress produced) 115

Figure 4.4 Different shear test configurations (Boulifa et al. 2012): (a) push-off test; (b) mixed mode device (Richard 1981); (c) mixed device (Bank-Sills and Arcan 1983). 116

Figure 4.5 Double shear test layout by Luong (1992): a) elevation view, b) shear area 117

Figure 4.6 Failure pattern of double shear test by Garcia et al. (2016) 117

Figure 4.7 JSCE-SF6 shear test: a) layout, b) anticipated and unusable failure types..... 118

Figure 4.8 a) Iosipescu shear test setup, b) corresponding shear and bending diagrams..... 119

Figure 4.9 Fracture modes: (a) and (b) Mode 1 (tensile) failure and (c) Mode 2 (shear) failure (Bažant and Pfeiffer, 1986)..... 120

Figure 4.10 Failure mechanism for 4-point shear test with: (a) freely rotating supports and (b) fixed supports (Schlangen 1993)..... 121

Figure 4.11 Testing arrangement: a) General view, b) Layout; Instrumentation c) devices, d) digital image correlation system (DIC)..... 123

Figure 4.12 Pilot tests: a) R00N-0, b) R00N-1, c) R60-0, d) R60-1..... 124

Figure 4.13 Load–displacement response for: a) Tensile-governed failures (TGF), b) Mixed-mode failure (MMF), c) Shear-governed failures (SGF)..... 126

Figure 4.14 Crack patters prior to failure as obtained from the DIC system: a) Tensile governed failures (TGF), b) Mixed mode failures (MMF), c) Shear governed failures (SGF)..... 127

Figure 4.15 Crack with and slip for R20-2 and R45-3 with tensile-governed failures (TGF)..... 128

Figure 4.16 Crack with and slip for: a) R00H-1, R00N-2, b) R60-2 with mixed-mode failures (MMF)..... 129

Figure 4.17 Crack kinematics for shear-governed members (SGF): a) R00N-1, b) R20-1, c) R45-2, d) R60-1; The legends represent the ratio between the load at which the measurement is assessed and the maximum load P/Pu, with (P)=pre-peak, (I)=inter-peak and (A)= post peak represent the stage on the P-δ curve 131

Figure 4.18 SGF members: a) Average crack width, b) Crack slip 132

Figure 4.19 a) Load-displacement response for AFRP confined tests, b) shear-governed failure types 133

Figure 4.20 Crack kinematics for confined R60F members: a) R60F-1, b) R60-2 134

Figure 4.21 a) Average crack width, b) Crack slip for shear governed confined members 135

Figure 4.22 a) τ_u vs ρ_{vr} from tests, b) τ_u vs f_c from tests..... 136

Figure 4.23 member toughness T_s 137

Figure 5.1 a) Foundation steel cage, b) column steel cage and moulds of Ø250 specimens 143

Figure 5.2 a) Foundation steel cage, b) column steel cage and moulds of Ø350 specimens 143

Figure 5.3 AFRP sheets wrapping 143

Figure 5.4 a) Typical Ø250 reinforced conventional concrete specimen (RC), b) Ø250 reinforced rubberised concrete specimen (RRuC), c) Ø250 AFRP confined reinforced rubberised concrete member (CRRuC) 144

Figure 5.5 Ø250 specimens geometry and reinforcement layout 145

Figure 5.6 Ø350 specimens geometry and reinforcement layout 146

Figure 5.7 a) Typical Ø350 reinforced rubberised concrete specimen (RRuC), b) typical Ø350 AFRP confined reinforced rubberised concrete member (CRRuC) 147

Figure 5.8 Typical lateral displacement sequence 148

Figure 5.9 General view of the self-reacting test rig 149

Figure 5.10 Schematic of self-reacting test rig 150

Figure 5.11 Detailed dimensions of load transfer box 150

Figure 5.12 Dimensions of out-of-plane rail support 151

Figure 5.13 General view of the large-scale test rig: a) skew view, b) side view 152

Figure 5.14 Schematic of large-scale test rig 153

Figure 5.15 Detailed strain gauge locations for: a) Ø250 specimens, b) Ø350 specimens 154

Figure 5.16 Strain gauges on: a) longitudinal reinforcement, b) stirrups with waterproof material 155

Figure 5.17 strain gauges on external confinement 156

Figure 5.18 General view: a) vertical LVDTs layout, b) horizontal LVDTs layout 156

Figure 5.19 Locations of LVDTs and inclinometers: a) Ø250 specimens, b) Ø350 specimens 157

Figure 5.20 DIC system setup 158

Figure 6.1 Constitutive σ-ε response: a) R45 Ø100 cylinders, b) R60 Ø100 cylinders, c) strength degradation curve (Section 3.4), d) strength degradation curve and properties of rubberised concrete materials 162

Figure 6.2 Steel rebar testing 164

Figure 6.3 Typical stress-strain characteristics of reinforcement 165

Figure 6.4 D250-R00-F0-N2: a) hysteric load-deformation response, b) vertical load applied, c) reinforcement fracture 167

Figure 6.5 D250-R00-F0-N1: a) hysteric load-deformation response, b) vertical load applied, c) reinforcement fracture 168

Figure 6.6 D250-R60-F0-N1: a) hysteric load-deformation response, b) vertical load applied, c) reinforcement fracture 169

Figure 6.7 D350-R45-F0-N0: a) hysteric load-deformation response, b) reinforcement fracture ... 170

Figure 6.8 D350-R45-F0-N1: a) hysteric load-deformation response, b) vertical load applied, c) reinforcement fracture 171

Figure 6.9 D350-R60-F0-N0: a) hysteric load-deformation response, b) reinforcement fracture ... 171

Figure 6.10 D350-R60-F0-N1: a) hysteric load-deformation response, b) vertical load applied, c) reinforcement fracture 172

Figure 6.11 D350-R60-F0-N2: a) hysteric load-deformation response, b) vertical load applied, c) sliding failure 173

Figure 6.12 D350-R60-F0-N2S a) hysteric load-deformation response, b) vertical load applied, c) reinforcement fracture 174

Figure 6.13 RRuC member kinematics from camera and DIC: a) D350-R45-F0-N0 with no axial load, b) D350-R45-F0-N2 with high axial load 175

Figure 6.14 Bottom transverse stirrup strains: a) D350-R45-F0-N0, b) D350-R45-F0-N1, c) D350-R60-F0-N0, d) D350-R60-F0-N1, e) D350-R60-F0-N2, f) D350-R60-F0-N2S 176

Figure 6.15 D250-R60-F3-N1: a) hysteric load-deformation response, b) vertical load applied, c) undamaged AFRP at failure 177

Figure 6.16 D350-R45-F2-N0: a) load-deformation response, b) AFRP stretches and interface gap 178

Figure 6.17 D350-R45-F2-N2: a) load-deformation response, b) vertical load applied, c) AFRP stretches and interface gap 179

Figure 6.18 D350-R60-F3-N0: a) load-deformation response, b) failure of AFRP and concrete core 180

Figure 6.19 D350-R60-F3-N2: a) load-deformation response, b) vertical load applied, c) failure of AFRP and concrete core 180

Figure 6.20 CRRuC member kinematics as obtained from the DIC: a) D350-F60-F3-N0, b) D350-R60-F3-N2 181

Figure 6.21 Maximum strain reading on AFRP jackets of all the Ø350 CRRuC members 182

Figure 6.22 Views of Specimen D350-R45-F2-N0 after testing: a) stretched regions and interface gap, b) damage state after removal of external confinement 183

Figure 6.23 Calculation of bending moment considering P-delta effect 184

Figure 6.24 Envelope moment-rotation (M-ψ) curves: a) Ø250 members, b) Ø350 R45 RRuC members, c) Ø350 R60 RRuC members, d) Ø350 CRRuC members 185

Figure 6.25 Typical stress-strain response of rubberised concrete materials 189

Figure 6.26 a) Influence of ρ_{vr} on ε_2; stress-strain σ-ε curves for assessment of M-N interaction diagram for: b) D350-R60-F3 columns, c) D350-R45-F2 columns; d) regression analysis for assessment of proportionality factors in Equation (6.2) 191

Figure 6.27 Bending-axial interaction curves for Ø350 RRuC members a) D350-R45-F0, b) D350-R60-F0; Ø350 CRRuC members c) D350-R45-F2, d) D350-R60-F3; Ø250 members e) RC - D350-R00-F0-N1, f) RRuC – D350-R60-F0-N1, g) CRRuC – D350-R60-F3-N1 193

Figure 6.28 Inelastic response assessment: a) member configuration, b) definitions of slope and deflection angle, c) plastic hinge zone, d) moment diagram at ultimate, e) rotational ductility 194

Figure 6.29 Ductility considerations: a) ultimate rotation ψ_u, b) rotation ductility $\mu_{\psi+1}$ 195

Figure 6.30 Reinforcement strains and plasticity distribution 197

Figure 6.31 Estimated plasticity region 197

Figure 6.32 Energy dissipation: a) Ø250 members, b) Ø350 R60 members without axial load, c) Ø350 R45 members without axial load, d) Ø350 R45 members with axial load, e) Ø350 R60 members with axial load 199

Figure 7.1 Typical yield surface on the deviatoric plane 204

Figure 7.2 Yield criteria of concrete damage plasticity model in the meridian plane 205

Figure 7.3 Uniaxial loading response of concrete in damage plasticity model 206

Figure 7.4 Tri-dimensional numerical modelling configuration of asymmetric shear tests 208

Figure 7.5 Sensitivity studies on R00N-1 configuration: a) Mesh size, b) Dilation angle 209

Figure 7.6 Comparison of numerical and test results: a) R00N-1, b) R20-1, c) R45-2, d) R60-1 ... 211

Figure 7.7 Predicted load reduction compared to the corresponding test results 211

Figure 7.8 Three-dimensional numerical representation for: a) Ø350 specimen, b) Ø350 reinforcement cage, c) Ø250 specimen and d) Ø250 reinforcement cage 213

Figure 7.9 Numerical modelling of FRP jackets 214

Figure 7.10 Mesh sensitivity analysis of the Reference Specimen D350-R60-F0-N2 215

Figure 7.11 Influence of dilation angle on the behaviour of Specimen D350-R60-F0-N2 216

Figure 7.12 Load-displacement response of RRuC beam-column members 219

Figure 7.13 Longitudinal strain at the specimen-footing interface of RRuC beam-column members 220

Figure 7.14 Numerical model of rubberised concrete cylinders and FRP jacket 221

Figure 7.15 Numerical simulation of material cylinders: a) unconfined and b) FRP confined 222

Figure 7.16 Typical ultimate behaviour of the CRRuC member models 223

Figure 7.17 Load-displacament response of CRRuC beam-column members 224

Figure 7.18 Longitudinal strain at the specimen-footing interface of CRRuC beam-column members 226

Figure 8.1 Influence of rubber content on the shear governed load capacity of concrete with reference compressive strength of: a) 20MPa, b) 40MPa, c) 60MPa, d) 70 MPa 231

Figure 8.2 Relationships between: a) τ_u and ρ_{vr} from SGF numerical simulations; b) Prediction of the shear resistance τ_u (Equation 8.1) 231

Figure 8.3 Comparison between original and simplified numerical models: (a) modelling geometry, (b) load-displacement response 233

Figure 8.4 Stiffness reduction ratio between RRuC and RC members with reinforcement ratio of ρ_1= *1.0*%, (b) ρ_2= 1.7% and (c) ρ_3= 4.0% 236

Figure 8.5 Bending-axial interaction diagrams for: a) R00, b) R20, c) R40 and d) R60 models 238

Figure 8.6 Comparison of axial capacity enhancement ratio from analysis compared to existing and proposed models with reinforcement ratio of: (a) ρ_1= *1.0*%, (b) ρ_2= 1.7% and (c) ρ_3= 4.0% 239

Figure 8.7 Comparison between the ultimate compressive strain from EC2 (Equation 8.8) and the proposed value (Equation 8.9) 241

Figure 8.8 Ultimate state of member failed in CF criterion specified in this research 242

Figure 8.9 Development of $\varepsilon_{cr,c}$ with respect to lateral displacement for the test members 243

Figure 8.10 Relationship between (a) ductility and axial load μ_ψ -υ, (b) modified ductility and axial load μ_ψ'-υ' 244

Figure 8.11 Spread of plasticity at various drift ratios for the selected models.....248

Figure 8.12 Prediction of: (a) $L_{sp,gradient}$ of Equation (8.11), (b) $L_{sp,local}$ of Equation (8.12), (c) L_{sp} of Equation (8.13).....250

List of Tables

Table 3-1 Proportions of concrete mixes 76

Table 3-2 Physical and mechanical properties of AFRP 79

Table 3-3 Results of the pilot tests 84

Table 3-4 Summary of test results 87

Table 3-5 Predictions of Equation 3.2 90

Table 3-6 AFRP confined test results 106

Table 4-1 Concrete mixes 113

Table 4-2 Specimen details and results 125

Table 4-3 Residual shear strength and equivalent shear strength 137

Table 5-1 Specimen details 142

Table 6-1 Concrete mix 161

Table 6-2 Concrete properties for each specimen 163

Table 6-3 Summary of reinforcement properties 165

Table 6-4 Summary of test results 166

Table 6-5 Stiffness and ductility characteristics 187

Table 7-1 Input parameters used in the analysis for shear-governed specimens 210

Table 7-2 Test results and numerical simulation of the shear governed failure cases 211

Table 7-3 Input parameters of concrete material used in the analysis of beam-column member tests 216

Table 7-4 Summary of monotonic analysis results for the RRuC specimens 217

Table 7-5 Summary of reinforcement analysis for RRuC specimens 218

Table 7-6 Summary of comparative results for the CRRuC specimens 223

Table 7-7 Summary of reinforcement analysis for the CRRuC specimens 225

Table 8-1 Details and results for asymmetric shear members 230

Table 8-2 Details of the control model 234

Table 8-3 Bilinear representation of stiffness reduction ratios of RRuC members 237

Table 8-4 Axial compression capacities from numerical analysis and Equation (8.2) 239

Table 8-5 Axial capacity enhancement ratio based on Equation (8.3) and the numerical analysis . 240

Table 8-6 Comparison of ultimate displacement from the tests and analysis 243

Table 8-7 Summary of spread length of plasticity of selected models 248

Chapter 1

1 Introduction

1.1 General

With the rapid development of industrial economies in recent decades, poisonous waste materials are increasingly being created and accumulated in both quantity and complexity. Several billion tons of solid waste materials are produced annually and the number is still increasing. Among these, solid waste such as rubber can be regarded as a non-decaying material that disturbs the environment. The lightweight, low cost and long life are factors that contribute to this growth. As a result, the accumulation of rubber products, such as used tyres, has become a major concern as it can lead to significant environmental and health hazards. In the USA alone, over 300 million scrap tyres are generated per year, representing well over 1% by weight of all municipal solid waste (Douglah and Everett 1998; Epps 1994), which is approximately one tyre for every person**.** Only 5% of these rubber products can be retreated for reuse, leaving the rest to be disposed of through other means including in landfills (Zheng et al. 2008). No organized collection system has been set up to provide a proper method to handle these wastes. Hence, the most widely used methods to destroy rubber waste involve burying or burning which can cause even greater environmental issues (see Figure 1.1). Moreover, due to the water impermeability and non-degradability, buried and discarded waste rubber piles can be perfect breeding grounds for insects and bacteria that may lead to infectious diseases (Zheng et al. 2008).


(a)

(b)

Figure 1.1 Tyre waste destruction involving: (a) burning (Tyre Pyrolysis Plant 2016) and (b) burying (Old Tyres Around the World 2017)

In recent decades, disposing of rubber scraps in landfills has become increasingly difficult due to the rapid depletion of available sites. As a result, this prevailing method will be drastically restricted in Europe due to the introduction of European Union directives which include critical standards on this practice considering the concepts of both materials and energy recovery (Benazzouk et al. 2007). For example, France, which generates more than 10 million waste tyres annually, has announced a new law since July 2002 that forbids any landfill disposal of rubber waste in order to reduce misuse of lands. Besides, the stockpiles of rubber wastes in landfills possess a potential threat of fire hazards. A tyre pile fire can burn for months, sending highly toxic chemicals and ashes into the air, while the waste liquid after melting also contaminates water resources. The waste tyre stream represents significant environmental, health, economic and aesthetic problems.

Existing solutions involving the re-use of tyre constituents, namely rubber and steel fibres, include their use in asphalt mixtures for road constructions, reuse in plastic and rubber products (Siddique and Naik 2004) and incineration for the production of steam or energy. Amongst existing alternatives, recycling waste tyres to produce novel concrete materials is an attractive option that could potentially combine environmental and performance advantages. As a result, in recent years, several investigations have been conducted to assess the feasibility of using recycled rubber materials in concrete (Topcu 1995; Azmi et al. 2008).

1.2 Rubberised concrete

Concrete incorporating recycled rubber material, namely “rubberised concrete”, is created by replacing a certain ratio of the mineral aggregates with rubber particles which are recycled from used vehicle tyres. The steel components and free textile are removed from the recycled tyre by magnet and vacuum during decomposition, followed by mechanical shredding to create different sizes of rubber particles. Rubber aggregates can be classified as chips, granulated crumb or powders according to their type and size.

Rubber is a highly durable material with significant strength and ability to maintain its volume under stress. This makes it an ideal candidate as a replacement of conventional brittle aggregate of concrete mix, aiming at a highly deformable structural element. The strength and stiffness of concrete, as expected, is reduced due to the existence of rubber particles and aggregate (Eldin and Senouci 1993). On the other hand, recent research suggested that rubberised concrete provided with additional lateral confinement (e.g. fibre reinforced polymer sheets) can lead to a strong material with considerable deformation capacity (Raffoul et al. 2017). In general, the expected result of concrete incorporating recycled rubber materials is a highly deformable material with sufficient strength. However, due to the lack of adequate research, there is a need for further investigations in

order to assess and quantify the inelastic characteristics of structural elements incorporating recycled rubber particles.

1.3 Aim and organisation of the present work

The purpose of this work is to investigate the mechanical properties of unconfined and externally confined rubberised concrete members with various level of rubber content, including constitutive relationships for constituent materials, shear behaviour, flexural response and performance under cyclic loading conditions. This research contributes towards this aim through extensive experimental results on the material and member levels, alongside detailed numerical simulations as well parametric and design assessments.

Previous experimental and analytical studies assessing the mechanical properties of rubberised concrete materials are reviewed in Chapter 2. The interaction between the rubber particles and the concrete mixture is firstly discussed, followed by the influence of rubber particles on the mechanical properties of concrete mixes as well as the behaviour of rubberised concrete structural members. In addition, the properties of externally confined rubberised concrete are also introduced. The limitations of the available investigations on rubberised concrete behaviour are then highlighted based on the literature survey, which shapes the research and methodologies described in the following chapters.

Chapter 3 focuses on examining the uniaxial behaviour of rubberised concrete materials. A detailed account of a set of material tests on rubberised concrete cylindrical samples, in which fine and coarse mineral aggregates are replaced in equal volumes by rubber particles with various sizes, is presented. The experimental results carried out in this investigation, combined with detailed examination of data available from previous tests on rubberised concrete materials, show that the rubber particles influence the mechanical properties as a function of the quantity and type of the mineral aggregates replaced. The test results and observations enable the definition of a series of expressions to estimate the mechanical properties of rubberised concrete materials. An analytical model is also proposed for the detailed assessment of the complete stress-strain response as a function of the volumetric rubber ratio. The effect of external confinement on the stress-strain behaviour of rubberised concrete is also investigated.

In Chapter 4, the experimental behaviour of rubberised concrete members subjected to asymmetric four-point shear loading is discussed in detail. The results enable direct assessment of strength and complete deformation characteristics including the post-peak response for ultimate behaviour governed both by shear and mixed-mode tensile-shear. The main observations from detailed

measurements of the crack kinematics through a digital image correlation monitoring system, with focus on members developing shear-governed response, are reported. Moreover, comparative assessments in terms of shear resistance, toughness and force transfer across the cracked interfaces are performed and discussed.

The experimental methodology for large-scaled beam-column tests of unconfined and externally confined reinforced rubberised concrete members is introduced in Chapter 5. This includes the description of material properties, details of member manufacture, testing arrangements, instrumentation of specimens and loading sequence.

Following the introduction of the experiment methodology in Chapter 5, Chapter 6 presents the experimental investigation into the cyclic behaviour of reinforced rubberised concrete members. The main results and observations are provided and discussed. The test results enable a direct comparative assessment of the key response characteristics of the specimens, with focus on stiffness properties and strength interaction, as well as ductility and energy dissipation. It is shown that rubberised reinforced concrete members can offer a good balance between bending capacity and ductility in comparison with conventional reinforced concrete members, particularly for low levels of axial loads. In the presence of relatively high axial loading and when a significant proportion of rubber content is used, external confinement such as through Fibre Reinforced Polymer (FRP) sheets is adopted to recover the required capacity and to provide highly stable hysteretic response.

Complementary numerical simulations of the experimental behaviour of unconfined and externally confined rubberised concrete specimens using the advanced nonlinear finite element analysis program Abaqus are discussed in detail in Chapter 7. Calibration of the uniaxial compressive behaviour of rubberised concrete is firstly carried out in conjunction with the cylinder tests described in Chapter 3. This procedure provides reliable material models which are then applied in further validation against the prismatic shear tests as well as the large-scale beam-column member tests described in Chapters 4 and 6, respectively.

Using the validated numerical procedures, Chapter 8 describes the details of parametric assessments on shear-type elements as well as beam-column members using Abaqus. The parametric investigation on asymmetric shear members accounts for a range of material constitutive parameters focusing on the rubber content and concrete compressive strength. Representative expressions for the shear resistance as a function of the rubber content and concrete compressive strength are proposed. On the other hand, the parametric studies on reinforced rubberised beam-column members assess the key response characteristics related to stiffness, strength and ductility. The findings are used to provide simplified procedures that can be employed in practical application in

order to provide information necessary for the assessment and design of rubberised concrete members.

Finally, the last chapter draws general conclusions from the present studies, alongside recommendations for further research on the subject.

Chapter 2

2 Literature review

This chapter provides a review of previous studies carried out on concrete materials and members incorporating recycled rubber materials, together with relevant related studies on conventional concrete. Together with a discussion of the findings from previous investigation, this chapter also highlights areas in which further research is needed.

2.1 Behaviour of rubberised concrete materials

Material tests on both fresh and hardened concrete indicated that the replacement of mineral aggregates with rubber particles modifies significantly the mechanical properties of the new composite material (Hernandez-Olivares et al. 2002; Moustafa and Elgawady 2015; Sgobba et al. 2015; Youssf et al. 2016; Rezaifar et al. 2016). Concrete is brittle material whose property is a function of the strength of the cement paste, whereas rubber is a hyper-elastic incompressible material with high Poisson ratio and a high tensile strength. The combination of the two results in a novel material benefitting from the strength of the concrete matrix, which governs the elastic constitutive behaviour, and the energy absorption properties of rubber.

The workability of fresh concrete, defined as the ease with which it can be mixed or transported has been shown to be affected by the presence of rubber particles. Several investigations (Eldin and Senouci 1993; Khaloo 2008; Turatsinze and Garros 2008) proposed the same conclusion that the slump of rubberised concrete mix decreases significantly with the increase of rubber content. It is commonly agreed that the rough surface of rubber particles increases the friction between the mixture and particles while the particles also form an interlocking structure due to their low self-weight which resists the normal flow of the mix under its own weight. Bing and Ning (2014) also pointed out that the nonpolar nature of rubber particles results in higher water absorption, and hence decreases the slump. To this end, the main focus of existing studies has been on the hardened properties of rubberised concrete as a potential load resisting material.

2.1.1 Influence of rubber particles

The fracture mechanics of concrete material have long been discussed since the early 1900s. It was widely accepted that tensile cracking is the most important cause of crack formation in concrete. Due to the heterogeneity of concrete, the uniform stress field in concrete is disturbed in the way that tensile strains are always found even under uniaxial compressive loading (Vonk 1992). For this

reason, the fracture of concrete can be related to: 1) bond cracks, 2) mortar cracks and 3) combined cracks.

In compressive stress-strain curve of concrete, for instance, the crack-growth process can be characterised as shown in Figure 2.1a (Hsu et al. 1963; Vonk 1992). A significant number of cracks already exist prior to loading due to creep and shrinkage. The failure of concrete starts with the formation of new bond cracks and the existing cracks start to grow around the aggregates when the load is over 30% of peak strength. Further increase of load causes the internal cracks within the mortar which form bridges between adjacent bond cracks. When the load reaches over 90% of the peak strength, more cracks coalesce and hence the structure becomes unstable. Aggregates play a significant role in the load transfer mechanics in concrete. As shown in Figure 2.1b, compressive forces can be transferred between stiff aggregates while tensile forces occur in the perpendicular direction which weakens the concrete.

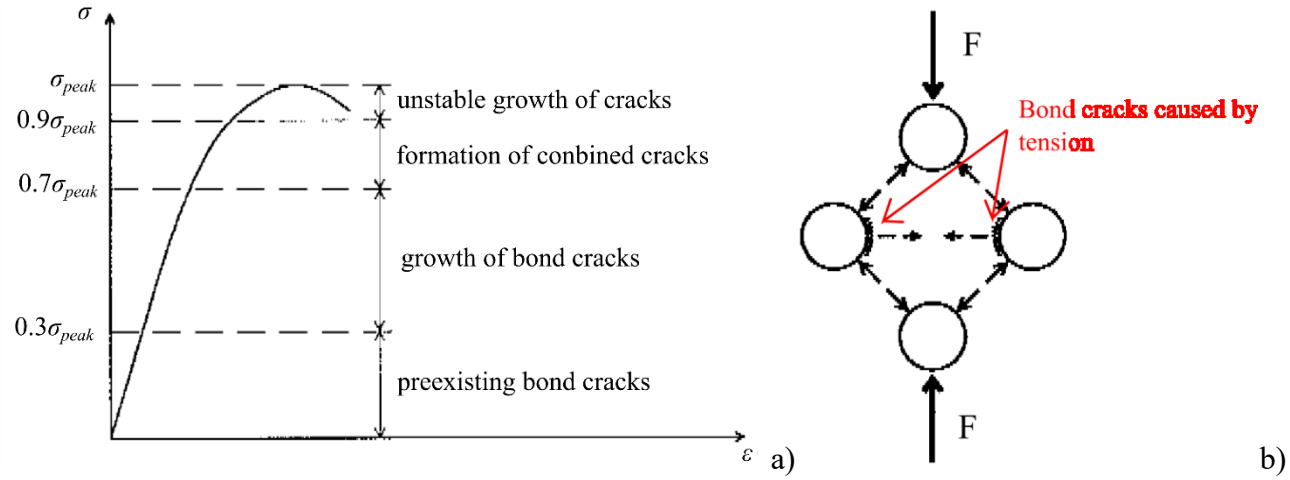


Figure 2.1 a) Crack formation procedure under compression (Hsu et al. 1963; Vonk 1992), b) force transfer between aggregates

In rubberised concrete, similar bonding failure and load transfer mechanisms were considered in early studies. Apart from the reduction in the unit weight of concrete due to the relatively low self-weight of rubber (Bing and Ning 2014), the replacement of mineral aggregates with rubber also results in a decrease in compressive strength, splitting tensile strength and elastic modulus (Naito et al. 2014). The strength loss due to the replacement of mineral aggregates with rubber crumb were shown in some studies (Eldin and Senouci 1993; Toutanji 1996; Xue and Shinozuka 2013) and is to be related to the relatively poor bonding between the rubber and the cement. Early investigation presented by Eldin and Senouci (1993) suggested crack propagation mechanisms in rubberised

concrete as shown in Figure 2.2a. When the rubberised concrete sample is loaded under compression, the rubber particles have the ability to undergo large elastic deformations under perpendicular tension before failure as illustrated in Figure 2.1b. Consequently, tension cracks can only form on cement paste and propagate through the specimen by going around rubber particles. Following this mechanism, a crack must overcome the bond between the paste and rubber particles hence the failure of the rubberised concrete specimen occurs due to the de-bonding of the two matrices.

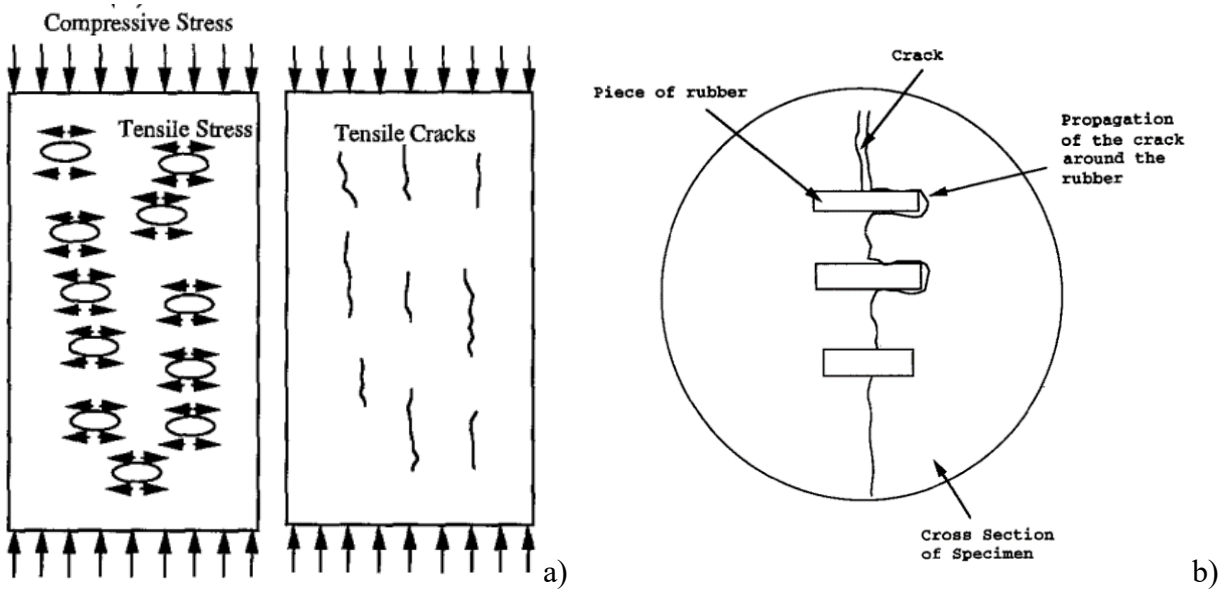
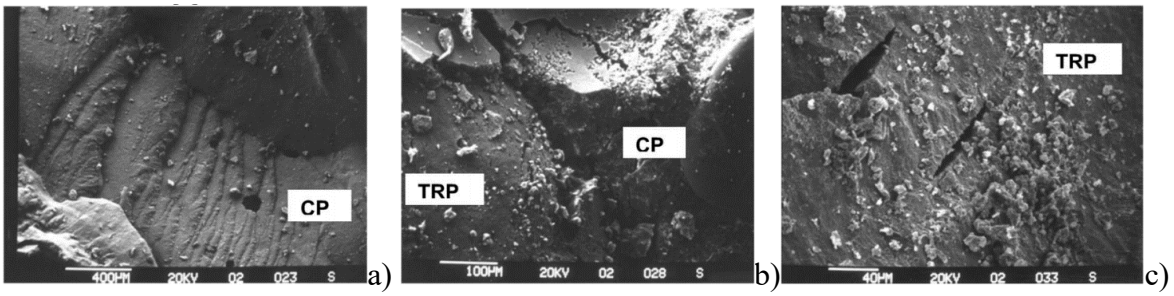


Figure 2.2 Crack propagation mechanism in rubberised concrete under: a) compression, b) splitting tension, as proposed by Eldin and Senouci (1993)

Microstructural investigations on rubberised concrete, however, support the view that the strength reduction is primarily related to the soft aggregate behaviour of the rubber particles more than due to the reduction in bond as shown in Figure 2.3 (Taha et al. 2008). Detailed investigation of the rubber-concrete interface showed observable indentations where rubber particles were pulled out. These indentations are clear evidence of the enhancement of the bond strength between rubber particles and cement paste as shown in Figure 2.3a. Figure 2.3b shows extensive microcracking in the vicinity of rubber particles, indicating that cracks occur within the cement paste area. Moreover, these observations also support the theory that the soft aggregate behaviour of rubber particles generates tensile strain resulting in cracks in the cement paste. On the other hand, Figure 2.3c also shows microcracks within the rubber particle matrix itself when the test specimen fails due to tension cracks. This observation indicates that rubber particles experience considerable tensile stress prior to specimen failure and illustrates the stress transfer mechanism between rubber and cement

paste. This microstructural observation that rubberised concrete fails due to flexural tension actions, as carried out by Taha et al. (2008), contradicts the former comments on the weak bond between rubber particles and cement paste. Consequently, the modification of rubberised concrete properties was shown to be related more to the mechanical properties of rubber particle itself.



a) b) c)

Figure 2.3 Micrographs showing: a) indentations on cement pasteafter rubber particles pull out, b) extensive microcracking at rubber particle vicinity, and c) tension cracks propagating in rubber particles: TRP=tire rubber particle, CP=cement paste (Taha et al. 2008)

Previous studies have shown that the modification of mechanical properties is mainly a function of the grain size and percentage of rubber replacement (Ganjian et al. 2009; Atahan and Yucel 2012), as well as rubber treatment (He et al. 2016), with the rubber type only having a marginal effect (Fattuhi and Clark 1996). Several studies have proposed analytical models to predict the influence of rubber content on mechanical properties of rubberised concrete based on their experimental work. Khatib and Bayomy (1999) suggested an exponential relationship between the strength reduction factor and rubber content of rubberised concrete based on their test results as follows:

$$SRF = a + (1-a)(1-R)^m \tag{2.1}$$

where *SRF* is strength reduction factor, *R* is rubber content, as a total volumetric replacement ratio of aggregates, and *a* and *m* are functional parameters determined by types of strength and rubber particles. Similar research by Li et al. (2009) proposed linear relationships between rubberised concrete and reference normal concrete in terms of their strength and elastic modulus strengths as given in Equation 2.2.

$$f_{cr(,cube)} = af_{c0(,cube)} - b \tag{2.2a}$$

$$E_{cr} = cE_{c0} - d \tag{2.2b}$$

where f_{cr}/E_{cr}, f_{c0}/E_{c0} represent the compressive strength and elastic modulus of rubberised and reference normal concrete, whereas a, b, c and d are functional parameters varying with different rubber content.

In addition to the rubber replacement ratio, several studies proposed that the type and size of rubber particles also have a clear influence on the material's properties. Fattuhi and Clark (1996) reported that concrete containing rubber with fine grading has lower compressive strength than that containing rubber with coarse grading. As shown in Figure 2.4, test results indicated that concrete containing fine grading rubber particles (size 1-16 mm) had an average of 15% higher compressive strength than concrete containing low-grade rubber (particle size 1-4 mm) for the same aggregate replacement ratio.

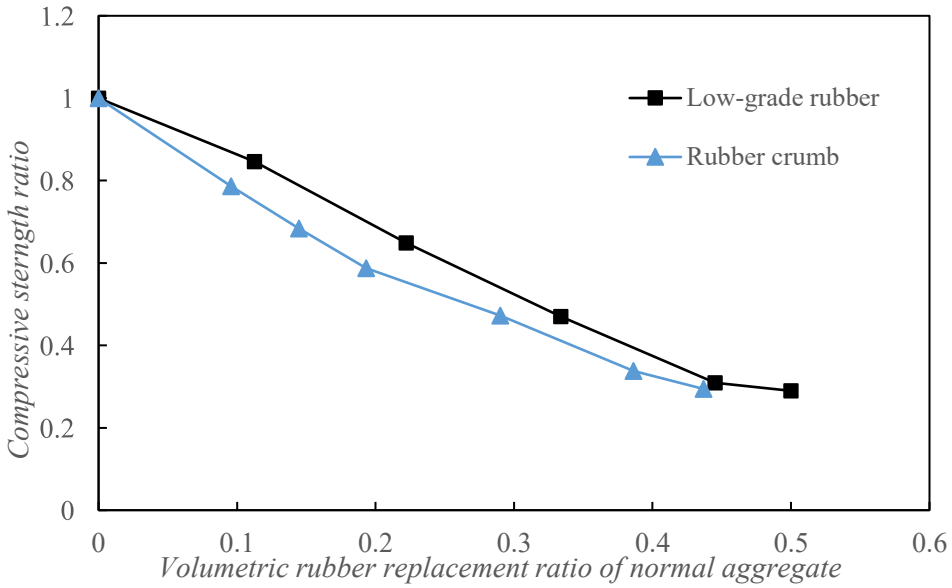


Figure 2.4 Influence of rubber grading and quantity on compressive strength (Fattuhi and Clark 1996)

For the same rubber particle content of coarse aggregate, the reduction rate of high-strength concrete was also found to be greater than that of low-strength concrete (Bing and Ning 2014). In addition, the reduction in mechanical properties was shown to be more significant when coarse aggregate rather than sand is replaced by rubber (Eldin and Senouci 1993). Among all the factors listed above, the particle size and volumetric percentage of rubber replacement are regarded as the essential aspects that modify the mechanical properties of rubberised concrete.

2.1.2 Merits of rubberised concrete material

Early studies have shown that the mechanical resistance of concrete is decreased gradually when under either compression or tension (Vonk 1992; Hordijk 1992). In the case of compression, the softening behaviour of concrete is controlled by the progressive failure of internal bond as noted before. As shown in Figure 2.5, microcracks start to form in the pre-peak region and the softening behaviour of concrete under compression is mainly due to the formation of major cracks within the mortar and diminishing number of internal bond. The material is hence gradually weakened with the increase of deformation. Instead of an overall distribution of cracks along the specimen, the softening behaviour of concrete under tension, on the other hand, is generally due to the localization of deformation. With the increase in tensile deformation or load, the number of cracks in concrete and their widths increase as well. This increase results in instability of tensile crack growth and coalescence of cracks. With the propagation of this cracking instability, only a small zone of concrete will have concentrated tension crack. As shown in Figure 2.6, the softening behaviour of concrete under tension is hence mainly controlled by the opening of the major crack while the uncracked part of the specimen only contributes to the elastic hardening behaviour of concrete. Rubberised concrete mixtures exhibit lower compressive and splitting tensile strength, and hence reduced elastic energy absorbed in comparison with normal concrete (Topcu 1995). However, they typically demonstrate a much more ductile post-peak behaviour that has the ability to absorb a relatively large amount of plastic energy under compressive and tensile loads (Eldin and Senouci 1993).

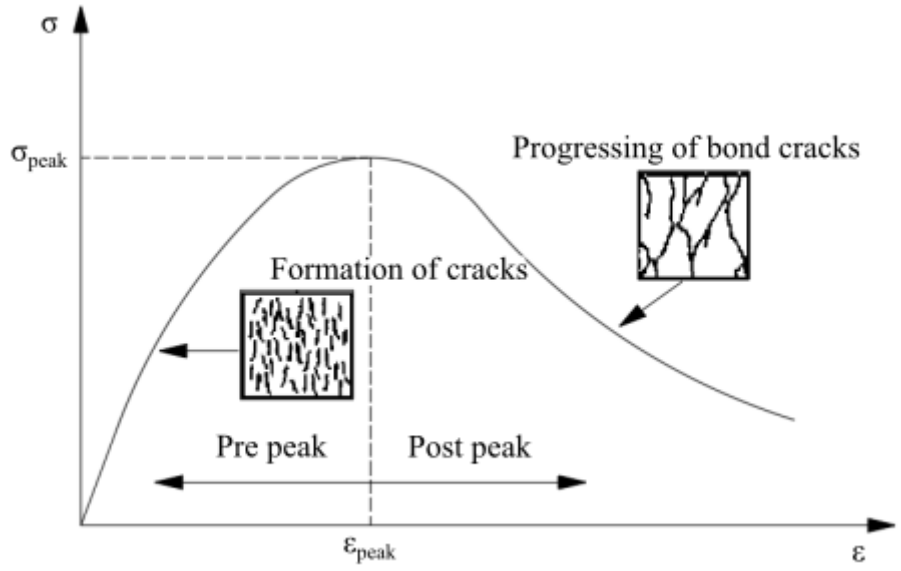


Figure 2.5 Typical compressive stress-strain behaviour of concrete related with crack progressing states (Vonk 1992)

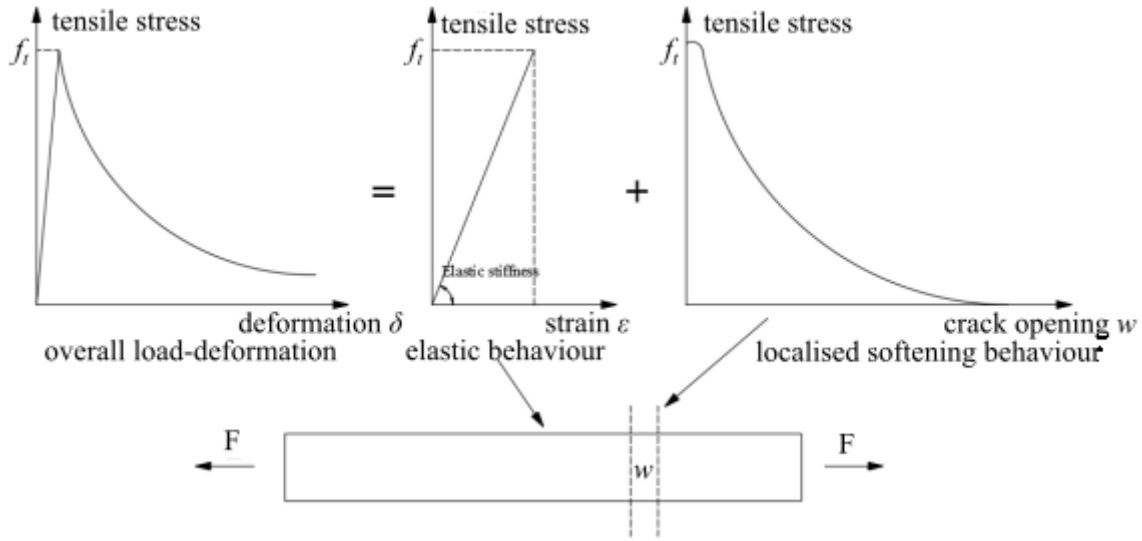


Figure 2.6 Separation of tensile stress-strain behaviour into an elastic behaviour and a localised crack opening behaviour

Tyre rubber particles also provide other energy consumption mechanisms in concrete such as particle pull-out and rubber internal cracking that do not exist in normal concrete as noted before (Taha et al. 2008). Compared to the softening behaviour of conventional concrete as discussed before, the rubber particles reduce the stress singularity at the first crack tips running into the rubber/cement–matrix interface, which slows crack kinetics and delays macro-crack localisation (Turatsinze and Garros 2008). Stress-strain behaviour of rubberised concrete indicates the influence of rubber particles in slowing the softening process of the material. As proposed by Batayneh et al. (2007) (Figure 2.7), with the increase of crumb rubber content, the stiffness of the softening branches (E_{soft}) of the stress-strain curves decrease, which also indicates that concrete with rubber particles has the potential to absorb more crushing energy with the increase of rubber content. Four-point flexural tests also indicated that the rubber chips significantly increase the deflection capacity of rubberised concrete beams by enhancing the deformation ability at the unstable crack location. Turatsinze and Garros (2008) pointed out that though normal concrete beams had higher elastic stiffness and higher load capacity. As shown in Figure 2.8a, rubberised concrete beams with 25% of the coarse aggregates replaced by rubber chips maintained a higher level of softening stiffness and finally failed at twice the maximum deflection compared to that of the reference normal concrete beam (Figure 2.8b). Aiello and Luezzi (2010) (Figure 2.9) also indicated that the presence of rubber chips restrained the localised crack from opening progressively and avoided the sudden separation of the beam into two parts hence enabled the specimen to undergo higher displacement after reaching the peak load.

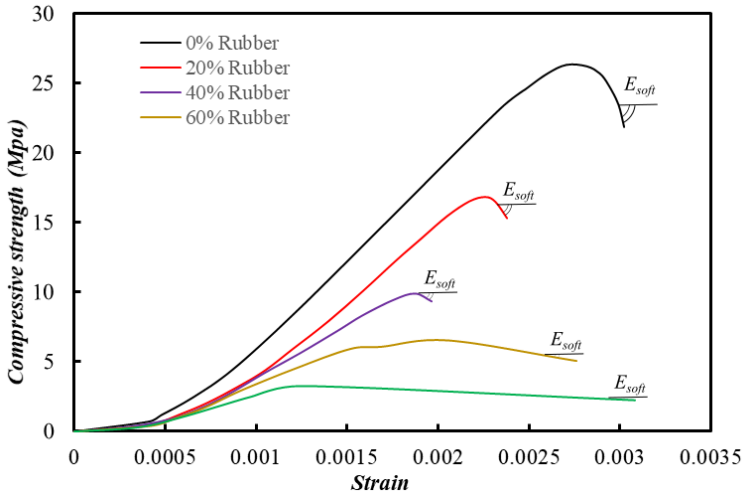


Figure 2.7 Influence of rubber particles on the softening behaviour of rubberised concrete under compression (adapted from Batayneh et al. 2007)

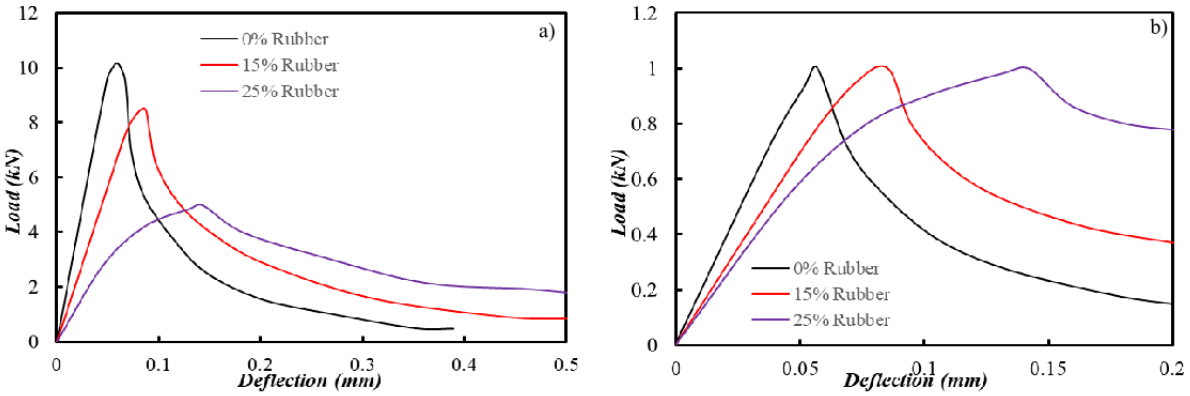


Figure 2.8 Four-point bending test results: a) load-deflection relationship, b) normalised load (Turatsinze and Garros 2008)

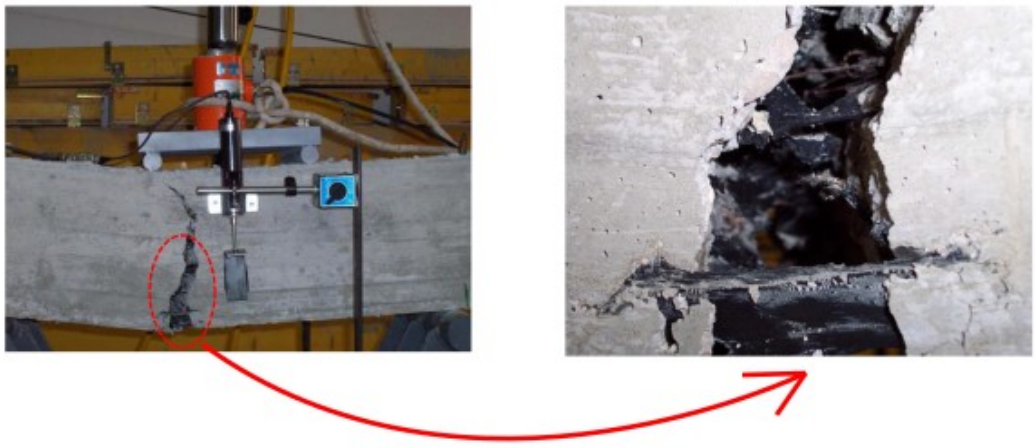


Figure 2.9 Rubber particles restraining crack opening (Aiello and Luezzi 2010)

It has also been reported that the replacement of coarse aggregate with rubber chips significantly increase the toughness of concrete compared to normal concrete and rubberised concrete with the presence of fine rubber particles. As a result, the flexural post-cracking behaviour of rubberised concrete is positively affected by the substitution of coarse aggregate with rubber particles, leading to favourable energy absorption and ductility properties. These capabilities were however reported to be reduced with significant levels of rubber particles (Bing and Ning 2014).

As shown in Figure 2.10, the toughness of a specimen is defined as the energy equivalent to the area under the load-deflection curve up to a specified deflection, defined as $T = A_1 + A_2$. The corresponding toughness index is obtained by dividing the area up to a specific deflection by the area up to the first crack, defined as $I = \frac{A_1 + A_2}{A_1}$. The general flexural energy absorption capability of rubberised concrete can be indicated by toughness, while the toughness index represents the ductility and the plastic energy dissipation ability of the material. Aiello and Leuzzi (2010) showed that toughness of rubberised concrete beam is increased by 73% when the coarse aggregate replacement ratio was increased from 50% to 75%. Meanwhile, Toutanji (1996) also performed the same standard four-point flexural test with a much clearer load-deflection result as shown in Figure 2.11. Although the normal concrete specimen failed with a higher strength and stiffness, it lacked the capability to experience further deformation while maintaining a certain level of residual strength. It was also proposed that the toughness index of rubberised concrete beams provided with tyre chips is increased by 21% compared to that of the reference concrete. Eldin and Senouci (1993), on the other hand, evaluated the toughness of rubberised concrete cylinders under uniaxial compressive loads. They showed that rubberised concrete samples with 100% of coarse aggregates replaced by rubber chips attained much higher toughness than for normal concrete. As a result, rubberised concrete with coarse aggregate replaced by rubber chips proved to be a more effective material in terms of energy dissipation.

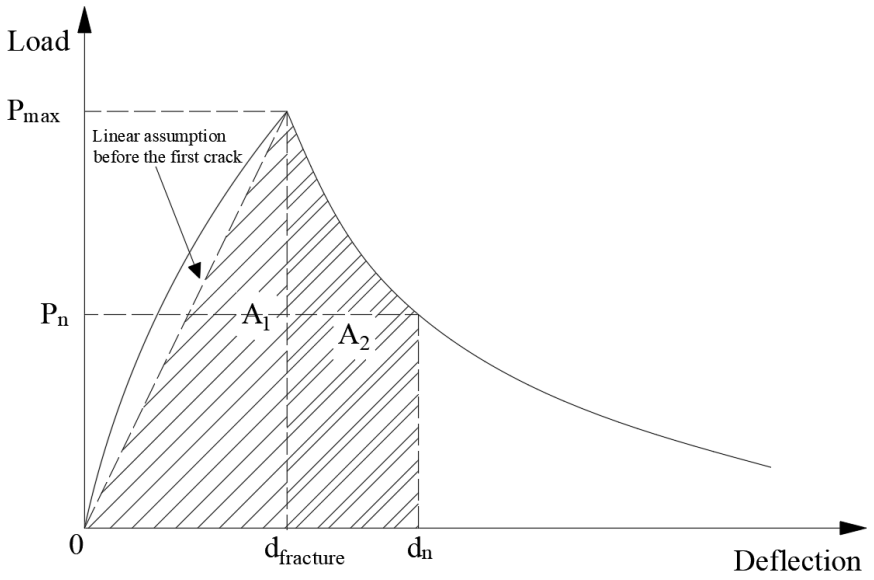


Figure 2.10 Illustration of the flexural toughness

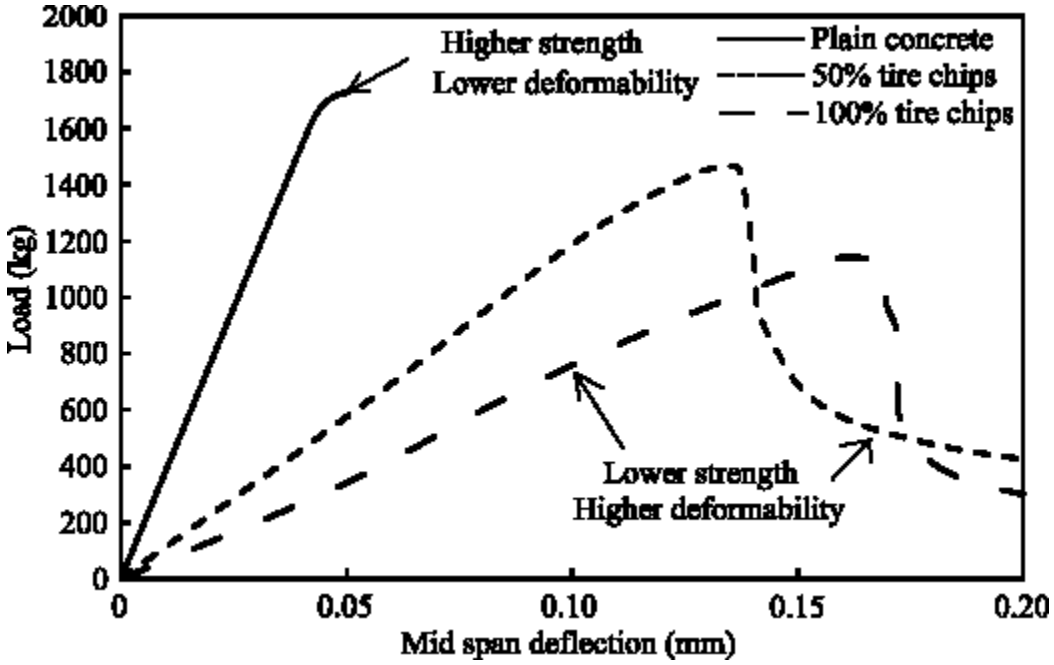


Figure 2.11 Four-point flexural test results by Toutanji (1995)

In addition to the above-mentioned studies, several other studies have investigated the impact resistance and energy dissipation capacity of rubberised concrete (Eldin and Senouci 1993; Atahan and Yucel 2012). For instance, Atahan and Yucel (2012) performed dynamic drop tests on normal and rubberised concrete cylinders. As shown in Figure 2.12, the energy absorbed by the specimens increased with the increase of the rubber content. Although there was a reduction of 71.6% in the strength of rubberised concrete with 100% of the aggregates replaced by rubber particles, the

energy dissipated at maximum load showed a significant increase of 161% compared to that of the control normal concrete specimen. As shown in Figure 2.12b, the normal concrete specimen absorbed higher energy before failure, yet it did not dissipate energy afterwards. On the other hand, rubber particles in rubberised concrete enabled the specimen to deform further after the maximum impact load which increased the impact time hence enabled the specimen to absorb much more impact energy with time. Consequently, the ductility of rubber particles also contributes to the impact energy absorption of rubberised concrete, and the inherent energy absorption capabilities of rubberised concrete makes it an evident candidate for impact-related applications (Naito et al. 2014, Fattuhi and Clark 1996).

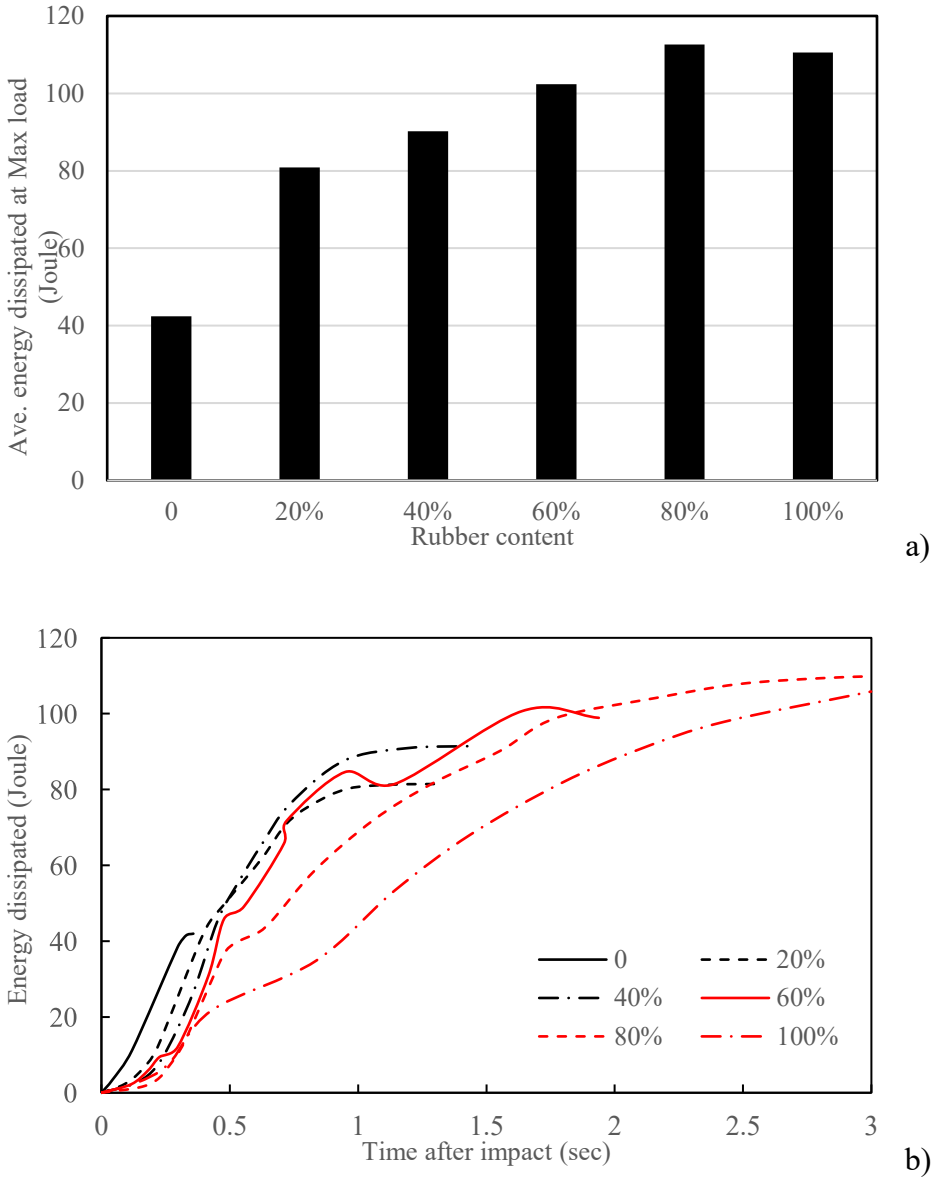


Figure 2.12 Energy dissipated by concrete with different rubber content: a) at maximum load, b) versus time progressing (adapted from Atahan and Yucel 2012)

2.1.3 Mechanical properties

As noted before, regardless of the reduction in strength, rubberised concrete has clear benefits in terms of energy dissipation. Clearly, in order to achieve satisfactory structural performance, a balance has to be sought between the enhanced energy dissipation and the reduction in mechanical properties with the increase in rubber content. This would, however, necessitate a reliable quantification of the influence of the constituent rubber on the key mechanical properties of concrete. Available studies have been related to specific sets of test data and typically addressed specific mechanical properties, particularly the elastic modulus and compressive strength. For example, Eldin and Senouci (1993) used an existing model proposed by Popovics (1987) that describes the reduction in concrete strength by accounting for the effects of macro-porosity in concrete samples where rubber aggregates were treated as large voids which did not have a significant role in resisting the applied load. This model described the reduction in compressive and tensile strength in the same way in which stress concentrations at the boundary of voids cause the reduction of strength. The model as proposed by Popovics (1987) is given in Equation 2.3.

$$f_{rel} = (1 - \frac{a}{a_{cr}})10\exp(-\delta\frac{a}{a_{cr}}) \tag{2.3}$$

where f_{rel} is the relative value of strength as a fraction of the strength of the reference normal (pore-free) concrete; a represents the volume of macro-porosity (rubber content) in the concrete mass, while a_{cr} represents the critical volume of macro-porosity when the strength of concrete becomes zero; and δ is the experimental parameter which depends on the stress field in the specimen. According to Popovics, a_{cr} can be chosen as 60% for concrete materials and δ was found to be $0.2\ln(\frac{\sigma_0}{0.007})$ by Eldin and Senouci (1993) based on the calibration with their own experimental results, where σ_0 is the compressive or tensile strength of the reference normal concrete. Therefore, the modified model proposed could be represented as:

$$f_{rel} = (1 - \frac{a}{a_{cr}})(\frac{\sigma_0}{0.007})\exp(0.2\frac{a}{a_{cr}}) \tag{2.4}$$

The validation of the model was based on a group of 9 test points as shown in Figure 2.13, which indicated good correlation with the test results. The influence of two types of rubber particles on the compressive strength of the mix, was also investigated, showing that mixes with sand replaced by crumb rubber had load reduction up to 20% smaller than that of mixes with coarse aggregate replacement. Equation (2.4), on the other hand, considers *a* as the uniform parameter describing the

volumetric replacement of aggregate with rubber particles regardless of the size effect, as mentioned above.

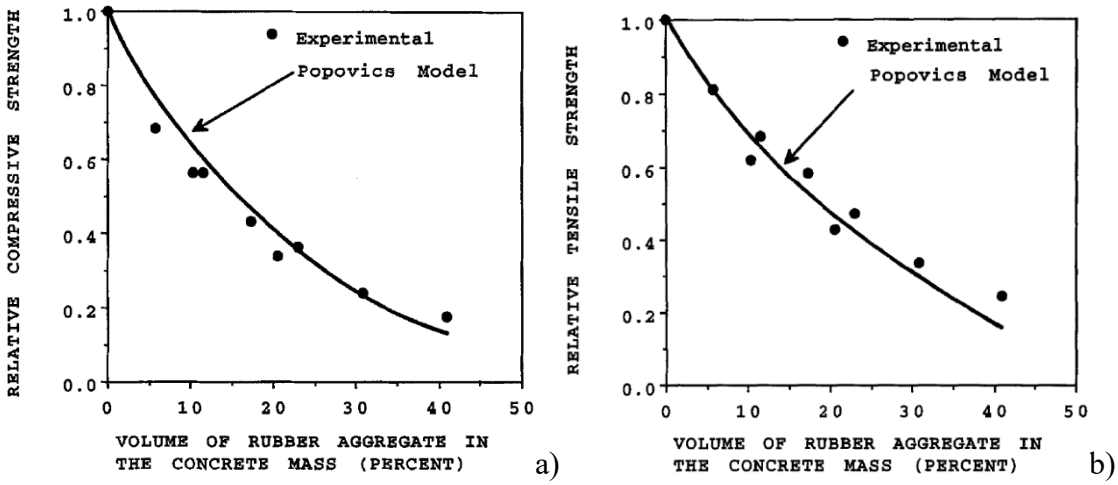


Figure 2.13 Correlation between Popovics model and: a) compression, b) tensile test results proposed by Eldin and Senouci (1993)

Besides rubber content, Ghaly and Cahill (2005) proposed a model to assess a dimensionless stress reduction factor limited to aggregate replacements up to 15%, as a function of compressive strength as well as the water-to-cement ratio. Experimental studies on rubberised concrete with rubber content up to 15%, and 3 different water-to-cement (w/c) ratios, were performed. These showed that the compressive strength of rubberised concrete (S_{cr}) decreased exponentially with the increase of rubber contents while the increase of w/c ratio accelerated the reduction of the rubberised concrete strength. The collective correlation between the dimensionless stress reduction factor (R_c) and rubber content (r) in percentage for all test results was given as the average prediction of all the best-fit curves for different w/c ratios as shown in Figure 2.14, expressed as:

$$R_c = (\frac{S_{cr}}{S_c})(\frac{w}{c})(r) = 0.0125(r)^{0.37} \quad (2.5)$$

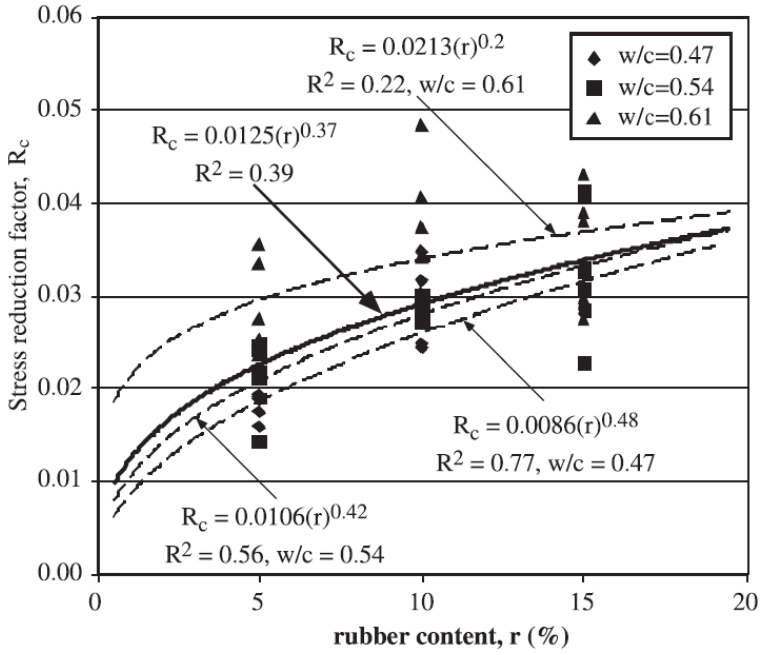


Figure 2.14 Stress reduction factor versus rubber content (Ghaly and Cahill 2005)

The above expression considers the w/c ratio as an influencing factor on the rubberised concrete strength in addition to the rubber content. The test data also focused on a relatively low rubber replacement ratio (up to 15%) while the expression may also only be valid when the w/c ratio of rubberised concrete mix lies between 0.47 and 0.61, which hinders its application as a universal model for the prediction of rubberised concrete strengths.

Guneyisi et al. (2004) extended the rubber content-dependent reduction model proposed by Khatib and Bayomy (1999), through Equations (2.1) and (2.2) noted before, which were validated against concrete mixes with replacement amounts of 50% of both fine and coarse aggregates. It was suggested based on the above experimental studies that the SRF could also be used to predict the reduction of elastic modulus with different function parameters (a, b and m).

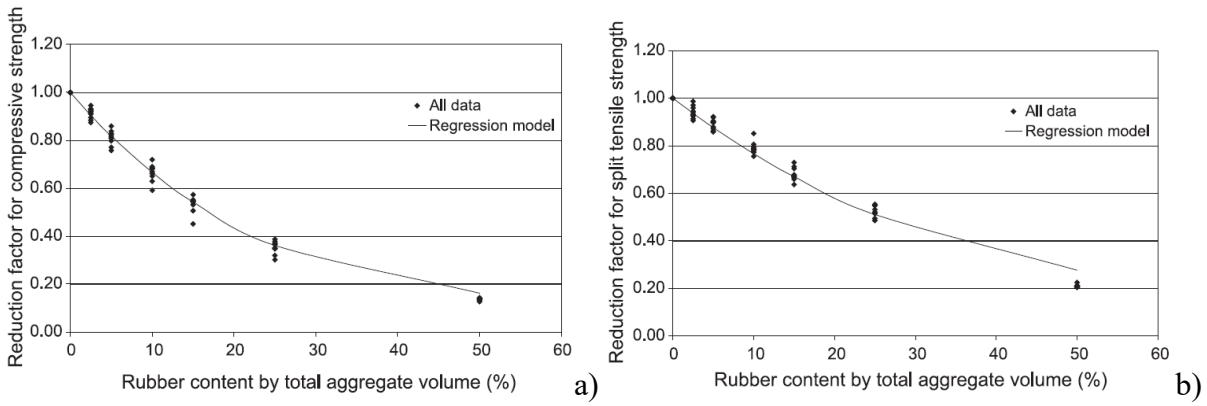


Figure 2.15 Regression model proposed by Guneyisi et al. (2004) describing the reduction factors for: a) compressive strength, b) tensile strength, with different rubber content

As noted from Figure 2.15, Equations (2.1) and (2.2) correlated well with the test results, and the w/c ratio seems to influence the strength of rubberised concrete in a uniform way. This indicates that the expression can be independent of the w/c ratio which is different from the suggestion of Ghaly and Cahill (2005) as noted before.

Taha et al. (2008) proposed similar characteristic equations that quantified the reduction in strength for rubberised concrete mixes based on a regression analysis as a function of rubber content up to 100% as replacement of fine and coarse aggregates. The model showed a polynomial relationship between the compressive strengths of rubberised (f_{RC}) and normal concrete (f_c), and rubber content (R). This be derived as indicated in Equations (2.6a) and (2.6b) for rubberised concrete with coarse rubber chips and crumb rubber particles, respectively.

$$f_{RC} = f_c - 0.1236R - 0.0006R^2 \tag{2.6a}$$

$$f_{RC} = f_c - 0.4496R + 0.004R^2 - 1.65\times10^{-5}R^3 \tag{2.6b}$$

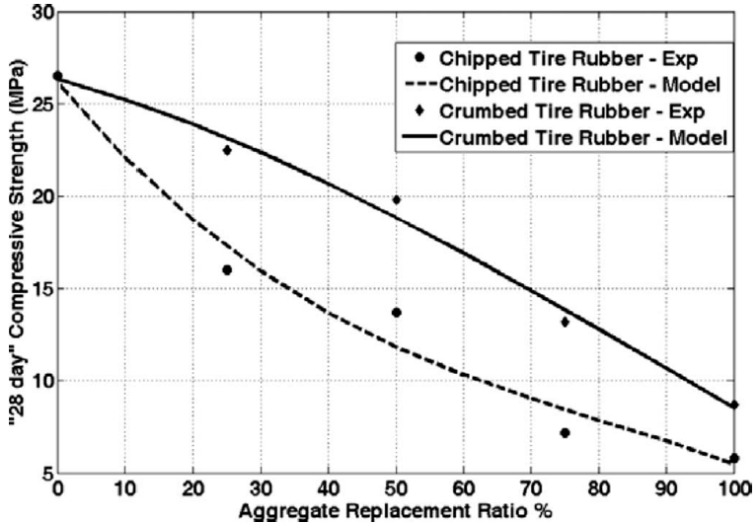


Figure 2.16 Correlation between experimental results and analytical model (Taha et al. 2008)

Unlike other models, Equation (2.6) considers the influence of rubber type (size) on the compressive strength of rubberised concrete. On the other hand, the validation of this expression was based on a limited number of data points as shown in Figure 2.16. In addition, the reverse of Equation (2.6b) seems to be inconsistent with other models.

As noted above, a number of previous studies have proposed expressions for estimating the individual material properties of rubberised concrete, primarily compressive strength, but all the expressions have clear limitations. Although a non-linear relationship between rubberised concrete strengths and corresponding rubber content can be established as shown in Equation (2.1) - (2.6), there is no general agreement on an overall representative expression. One of the main reasons is that all the analytical models listed above were proposed based on a limited number of tests performed with a specific range of rubber particle replacements, without having the insight of the overall data from other studies. In addition, all expressions consider rubber content as the single variable which influences the mechanical properties of rubberised concrete without considering other factors such as aggregate and rubber particle sizes.

As indicated in the above review, apart for the rubber replacement ratio, the type and size of rubber particles and corresponding aggregates are also factors that can influence the mechanical behaviour of rubberised concrete which existing expressions do not collectively consider. In addition, there is a lack of information on full constitutive relationships. Most existing analytical expressions for strength degradation are validated through a limited number of concrete mixes, with similar rubber aggregate sizes and type of mineral aggregates replaced, whereas information regarding the post-

peak behaviour is limited. One of the aims of this research is therefore to carry out a detailed assessment into the mechanical behaviour of rubberised concrete.

2.2 Behaviour of FRP confined concrete

Compared to conventional steel confinement, fibre reinforced polymer composites have the advantages of lighter weight, higher strength, ease of assembly and higher durability. The use of fibre reinforced polymer (FRP) as a confinement material for concrete has been extensively investigated during the past two decades and a many experimental and analytical studies have been performed to identify the compressive behaviour of FRP-confined concrete (Fardis and Khalili 1982; Samaan et al. 1998; Lam and Teng 2003; Xiao and Wu 2003; Binici 2005; Ozbakkaloglu et al. 2013). Since FRP provides a significant increase in the axial load capacity and ductility, combining the advantages of FRP confinement and rubberised concrete has gained attention in recent years (Li et al 2011; Youssf et al. 2014; Raffoul et al. 2017).

2.2.1 Types of FRP confinement

In FRP composites, fibres are embedded in resin matrixes. The mechanical properties of FRP composites are largely determined by the fibre reinforcement. The resin matrix mainly helps to form the fibres in a composite form and provides protection from the environment. There are mainly three types of fibres used in confining concrete specimens, namely carbon, glass and aramid. All types of FRP fibres behave as linear elastic under tension with a sudden failure when external tensile forces reach their capacities. Carbon FRP (CFRP) has the highest strength and stiffness in general. The typical strength of carbon fibres can reach 3.9-5.1 GPa which is about 20 times that of structural steel, with a stiffness ranging between 230 GPa and 390 GPa which is similar to that of steel. The typical tensile strength and stiffness of Glass FRP (GFRP) are 2.8 GPa and 104 GPa, respectively, which are lower than those of CFRP, yet GFRP can undergo more elongation before it breaks. Aramid FRP (AFRP) has similar mechanical properties compared to GFRP with a typical tensile strength of 2.1-2.9 GPa and stiffness of 88-133 GPa. The typical advantage of AFRP material is its heat resistance compared to the other two types. In addition, its microstructure makes the strength of chemical bond exploited more effectively. On the other hand, AFRP has nearly no resistance to compressive loads since it buckles relatively easily under compression. A general comparison of mechanical properties of FRP and steel fibres is shown in Figure 2.17.

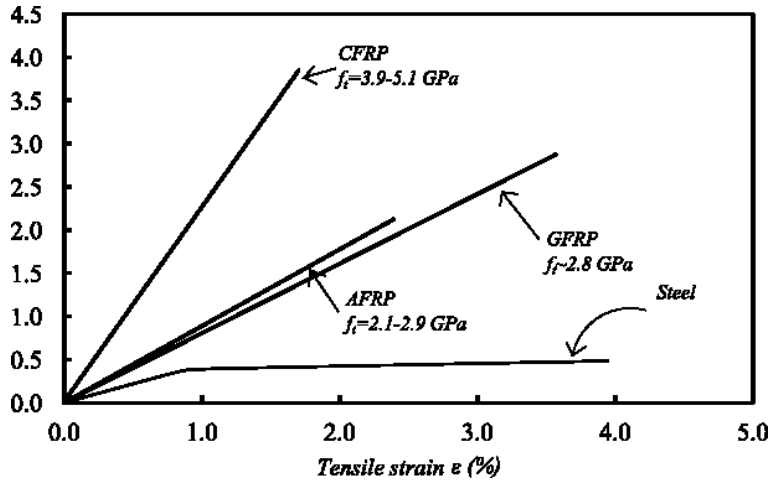


Figure 2.17 Material characteristics of GFRP, CFRP, AFRP and steel fibres

In most applications, the confinement provided by FRP jacket to concrete is passive in nature. When the concrete core is under compression, its lateral expansion is restrained by the FRP jacket which is loaded under tension in the hoop direction. Unlike steel-confined concrete, where the confining pressure changes as the steel yields, FRP jacket provides continuously increasing pressure with the increase of hoop strain. As shown in Figure 2.18, the lateral confinement pressure f_l can be defined as:

$$f_l = \frac{\sigma_f t_f}{R} = \frac{2\sigma_f t_f}{D} \tag{2.7a}$$

where σ_f is the tensile stress in FRP fibres, t is the thickness of confinement and R and D are the radius and diameter, respectively, of the concrete core. Since FRP is linear elastic before fracture, the above equation can be presented as:

$$\sigma_f = \varepsilon_f E_f \tag{2.7b}$$

$$f_l = \frac{2E_f t_f \varepsilon_f}{D} \tag{2.7c}$$

where E_f and ε_f are the elastic modulus and tensile strain of the FRP material.

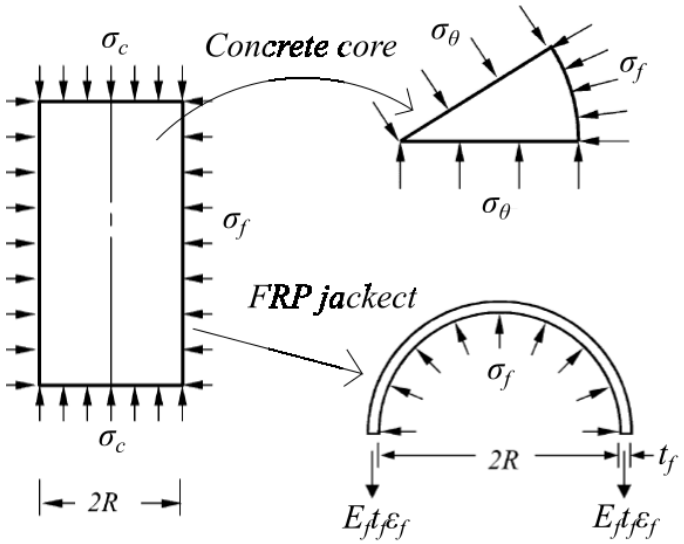


Figure 2.18 Confinement action of concrete core and FRP jacket

2.2.2 Properties of FRP confined concrete

The stress-strain behaviour of FRP confined concrete is represented by a monotonically ascending bi-linear curve, when a sufficient level of confinement is provided as shown in Figure 2.19 (Saafi et al. 1999; Xiao and Wu 2000; Dai et al. 2011). It can be noted from Figure 2.19a-e that regardless of the type of FRP used, the confined compressive strength (f_{cc}) and ultimate strain (ε_{cu}) of concrete are enhanced significantly compared to plain concrete (f_{c0}, ε_{c0}). The values increase when more layers of confinement are used. Saafi et al. (1999), Xiao and Wu (2003) also showed that CFRP confined concrete exhibits higher strength than concrete with the same level of GFRP jackets, due to the potential higher tensile failure strength of CFRP fibres, while the ultimate deformations showed no difference in both cases. All types of FRP confined concrete failed in the same mode. The concrete core was crushed at an early stage while further disintegration was restrained by the external confinement. With further increase of axial and lateral deformation, the confined concrete finally failed in an explosive mode when the FRP jackets ruptured as shown in Figure 2.19f.

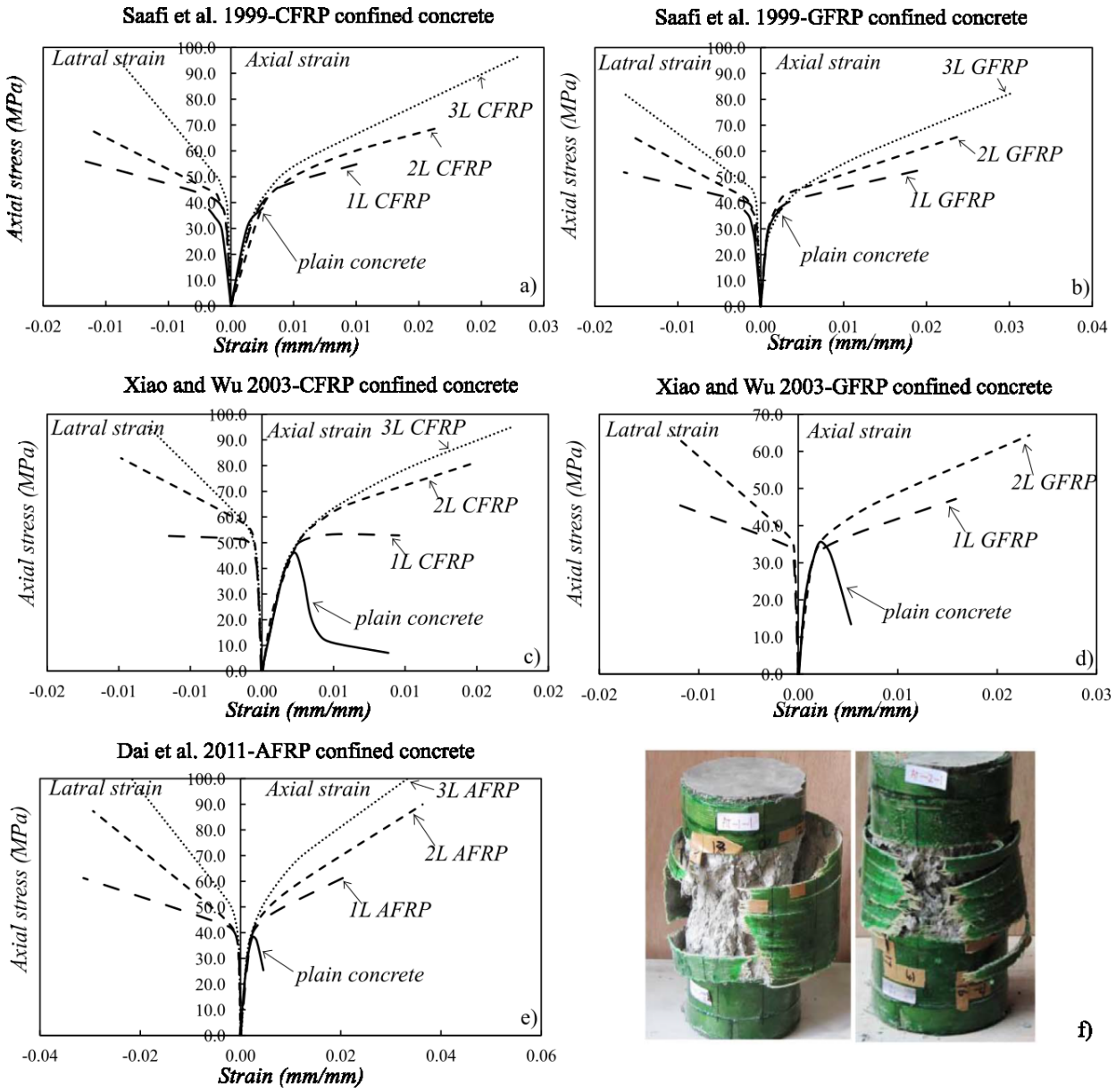


Figure 2.19 Characteristic stress-strain behaviour of FRP confined concrete from Saafi et al. (1999): a) CFRP confinement, b) GFRP confinement, Xiao and Wu (2000) c) CFRP confinement, d) GFRP confinement, Dai et al. (2011) e) AFRP confinement and f) corresponding typical failure type

It should be noted that this bilinear behaviour of confined concrete only occurs when sufficient level of confinement is provided. Insufficient confinement levels cannot provide enhancement of compressive strength, which leads to descending behaviour beyond the peak strength point in the stress-strain curve as shown in Figure 2.20 (Lam and Teng 2003). The test results also Xiao and Wu (2000) showed that normal concrete with only one layer of CFRP confinement had no enhancement of compressive strength as shown in Figure 2.19c. One of the specimens in this category also failed with a lower compressive strength than normal concrete (not shown in Figure 2.19). Consequently, adequate layers of FRP sheets need to be provided to enhance the strength and deformability of the confined specimen.

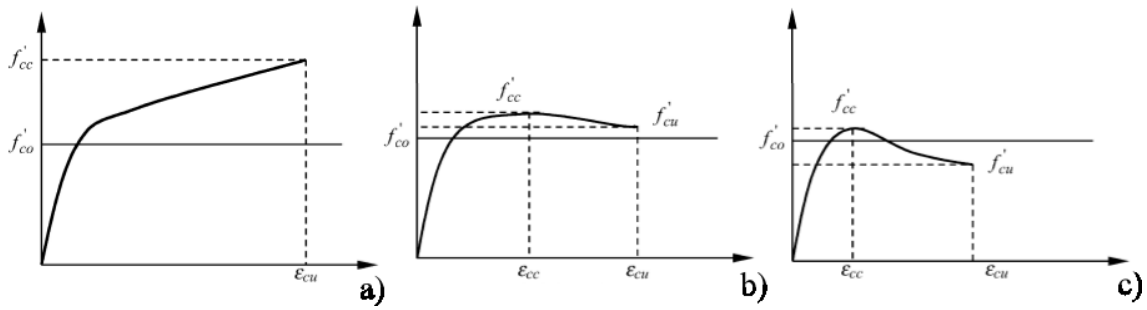


Figure 2.20 Classification of stress-strain curves of FRP confined concrete: a) increasing type (sufficient confinement), b) decreasing type ($f_{cu} > f_{c0}$), c) decreasing type ($f_{cu} < f_{c0}$) (insufficient confinement) (adapted from Lam and Teng 2003)

The bilinear stress-strain behaviour of confined concrete is characterised by two independent linear branches with different slopes (E_{c1}, E_{c2}) with a curved part in between. It can be seen from Figure 2.19 that in all cases the first linear branches of FRP confined concrete stress-strain behaviour are the same as those of the corresponding plain concrete regardless of the types and layers of confinement used. Under low level of axial loads, passive confinement such as FRP jacket is not activated hence the behaviour of confined concrete is controlled by the concrete core. Further increase of axial load and deformation leads to interaction between concrete and the confinement jacket. The lateral deformation of concrete core activates the external confinement hence the second linear branch of the stress-strain curve is controlled by the combination of the properties of concrete and the FRP jacket.

More recent research examined the response of rubberised concrete confined with FRP jackets. As shown in Figure 2.21a, b, Youssf et al. (2014) investigated the influence of CFRP confinement on rubberised concrete behaviour. The CFRP confinement enhanced the compressive strength and strain of rubberised concrete in the same way as those of normal concrete. On the other hand, due to the lower compressive strength of rubberised concrete, the strength enhancement ratio of rubberised concrete is generally higher than that of normal concrete provided with the same level of confinement (i.e. f_{cc}/f_c=1.70 for normal concrete with 2 layers of CFRP, and f_{cc}/f_c=2.27 for rubberised concrete with the same confinement). Raffoul et al. (2017) performed similar compression tests on rubberised concrete with 60% replacement of total aggregate confined by various layers of AFRP jackets. Since the rubberised concrete core had relatively low strength, the strength enhancement ratio reached a much higher value of f_{cc}/f_c=7.3 with only two layers of AFRP sheets (Figure 2.21c, d).

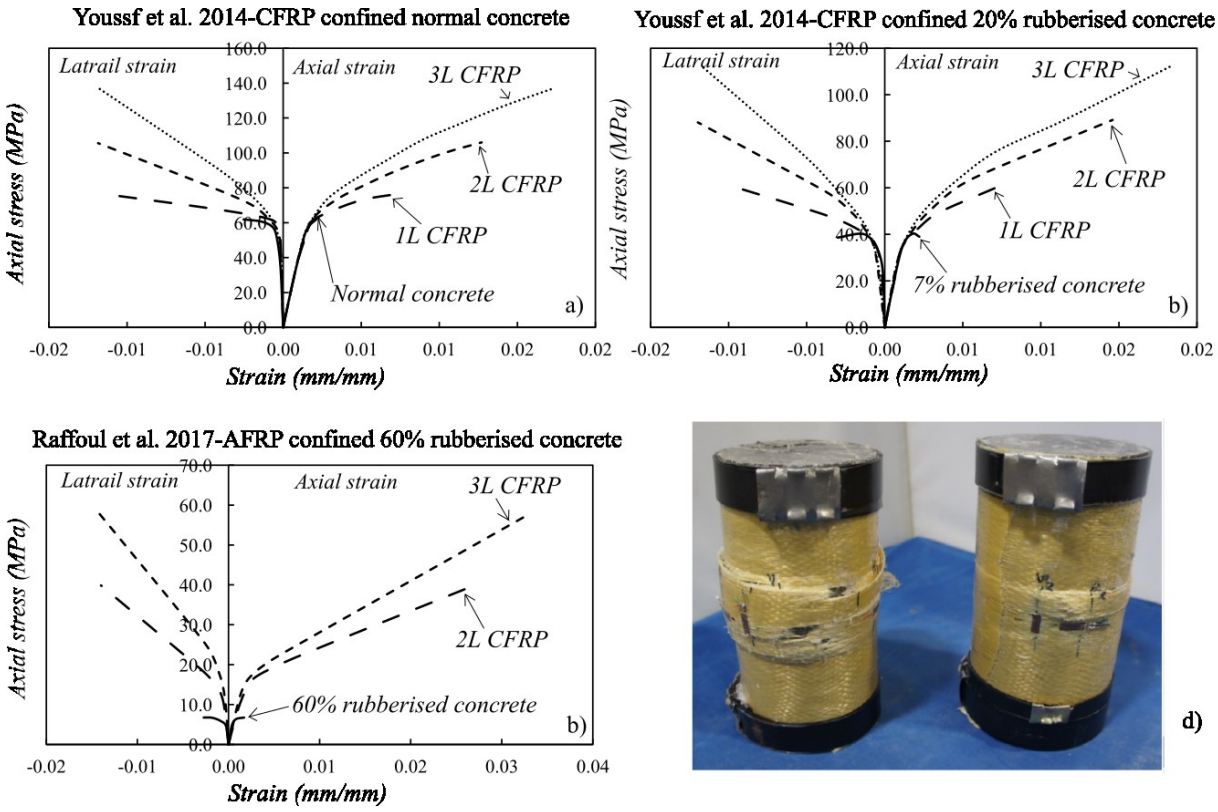


Figure 2.21Characteristic stress-strain behaviour of FRP confined concrete from Youssf et al. 2014: a) CFRP confined normal concrete, b) CFRP confined rubberised concrete, c) Raffoul et al. 2017-AFRP confined rubberised concrete, d) corresponding typical failure type

FRP confined rubberised concrete also exhibits bilinear stress-strain response under axial compression with several times enhancement of the compressive strength and deformability, while the final failure is explosive with rupture of the FRP jackets. Since rubberised concrete also has much lower compressive strength, the effectiveness of confinement (f_{cc}/f_c) can initially be much higher than that for normal concrete at the same level of confinement. As a result, FRP confinement can be an effective method for strengthening rubberised concrete while also maintaining its deformability. Several experimental assessments of rubberised concrete with different layers of AFRP confinements were performed during this research programme, as described in Chapter 3.

2.3 Assessment of shear in rubberised concrete

To define the shear strength of a material as a constitutive property, it is essential that the material fails due to pure shear actions when other actions normal to the failure surface are negligible. Everling (1964) proposed the definition of shear strength of a material $\tau=S/A$ as the breaking shear stress applied to the imposed plane of fracture without normal force, where S is the necessary shear force causing the failure of a surface and A represents the cross-sectional area of the corresponding failure plane.

2.3.1 Ultimate shear behaviour in concrete

In most cases, the failure of concrete can be characterised by the nucleation and propagation of cracks, which can be defined in two basic fracture modes as shown in Figure 2.22: 1) tensile fracture (referred to as Mode I), 2) shear fracture (referred to as Mode II), and the combination of both modes under various of loads (Schlangen 1993). Mode I fracture of concrete has been studied in detail and reliable analytical and numerical expressions have been proposed (Van Mier 1984; Hordijk 1992; Vonk 1992). On the other hand, pure shear crack paths occur in concrete elements only in rather restricted conditions. The tensile fracture mode (Mode I) would prevail at the fracture tip in most crack propagation situations. If Mode I is always applied, shear fracture would be impossible (Bazant 1985). This type of cracking has been observed even for the failure of concrete elements loaded in shear, the diagonal shear failure of beams and panels, as well as the torsional shear failure of beams for instance.

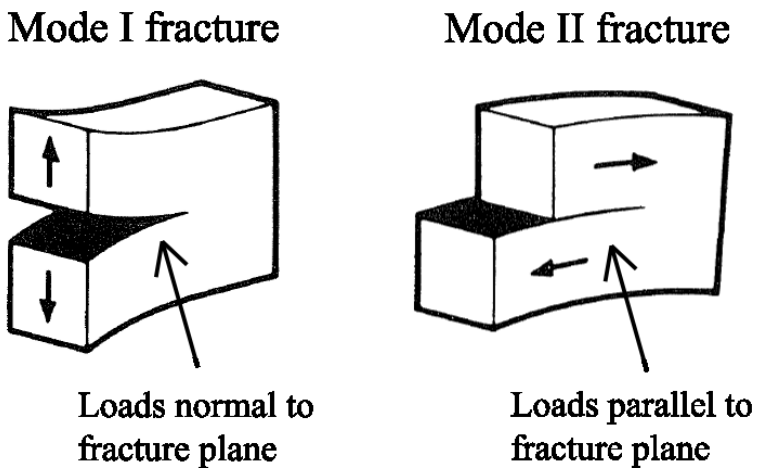


Figure 2.22 Mode I and Mode II fractures of concrete

Early investigations of Mode II fracture in concrete indicated that the fracture mode of concrete was always a mix of Mode I and Mode II. Arrea and Ingraffea (1982) first performed Mode II fracture tests on concrete beams with a starter notch, and showed that the crack did not propagate in the notch direction but ran sideway normal to the principle stress as indicated in Figure 2.23a. However, Bazant and Preiffer (1986) performed Mode II fracture tests under the same setup with a narrower shear band and showed that shear fracture existed in concrete only when the shear zone was narrow and concentrated as noted in Figure 2.23b. Based on theoretical fracture mechanics, the fracture propagation direction of concrete is governed by the maximum energy release rate. Mode I fracture propagates sideway from the notch tip, for the type of test with a narrow shear zone, and quickly

run into a low stress hence low strain energy zone (Bazant 1985; Bazant and Pfeiffer 1986). Consequently, further Mode I fracture can be controlled in a test with a narrow shear band. It should be noted that micro tensile fractures are still available under this type of shear test as a band of 45˚ crack to the load direction which is then connected by the major shear crack.

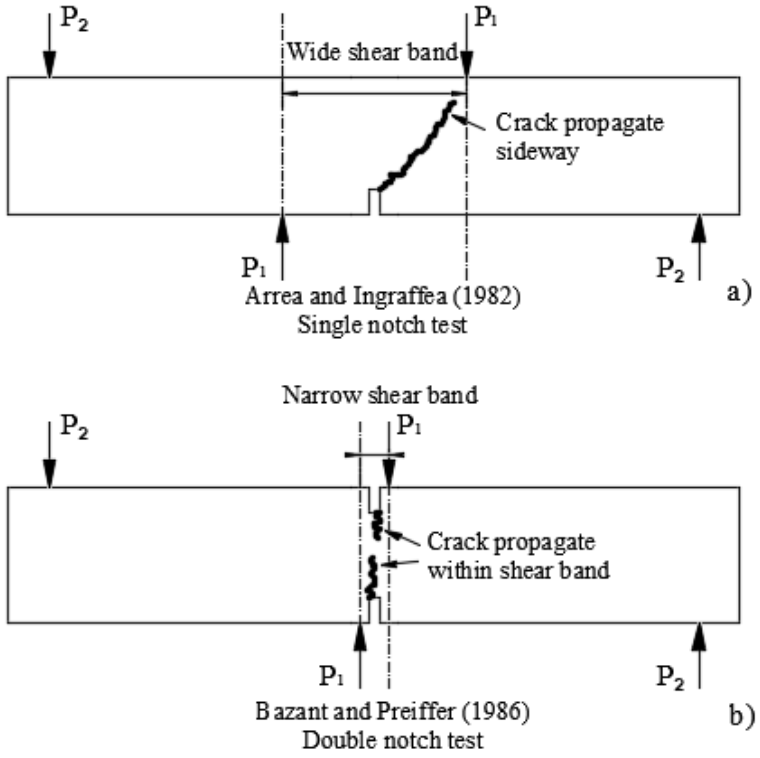


Figure 2.23 Influence of the length of shear band on the fracture behaviour of concrete (Non-scaled sketches adapted from Arrea and Ingraffea (1982), Bazant and Preiffer (1986))

Any tensile stress along the cross-section would also change the stress and strain distribution around the crack tip, which contributes to the crack propagation sideway from the desired direction (as Mode I) which fails to predict the actual shear behaviour of a material. Consequently, the challenge of performing tests for the quantification of concrete shear capacity lies in the methodology of creating a pure shear failure within a concentrated area on the target surface supporting no normal forces. There has however not been a commonly agreed configuration for shear testing, noting the following:

- The original setup in Figure 2.23 was first proposed by Iosipescu and Negoita (1969) for determining the shear behaviour of metallic beam specimens with V-shaped indentations at the top and bottom sides of the member as shown in Figure 2.24a.

- In the tests, the shape of notches did not have an influence on the behaviour. Hence, the four-point asymmetric test with one or two opposite notches as shown in Figure 2.24b was applied in the tests as noted above.
- The double shear-test shown in Figure 2.24c was introduced by the Japanese Standard JSCE-SF6 (1990) for the determination of the shear property of steel fibre reinforced concrete, and was shown to be effective in testing the shear behaviour of conventional concrete (Tuan et al. 2006). Similar to the previous setup, the concept involves creating concentrated shear action along the two desired failure planes without normal actions.
- A similar double plane shear failure set up was used for double-shear tests on cylindrical specimens, as shown in Figure 2.24d, as proposed by Luong (1990). Instead of applying concentrated cutting loads around the edges of the notches, this setup requires distributed loads to shear off the centre block of the cylindrical specimen.
- An alternative pure Mode II double-edge notched compression test is shown in Figure 2.24e as proposed by Reinhardt et al. (1997), aiming at creating pure shear fracture on high strength concrete specimens. This test setup was reported to generate a Mode II crack along the desired plane. However, due to the inhomogeneity of concrete, shortly after fracture, the crack propagated in an inclined manner which caused the final failure of concrete to occur in compression. Consequently, this type of setup may not be suitable for low strength concrete, such as rubberised concrete.
- Other methods such as push-off compression (Mattock and Hawkins 1972) (Figure 2.24f), axisymmetric punch-through (Watkins 1983) (Figure 2.24g) and off-centre notched beams (Jenq and Shah 1988) were all proposed to create pure shear fractures.

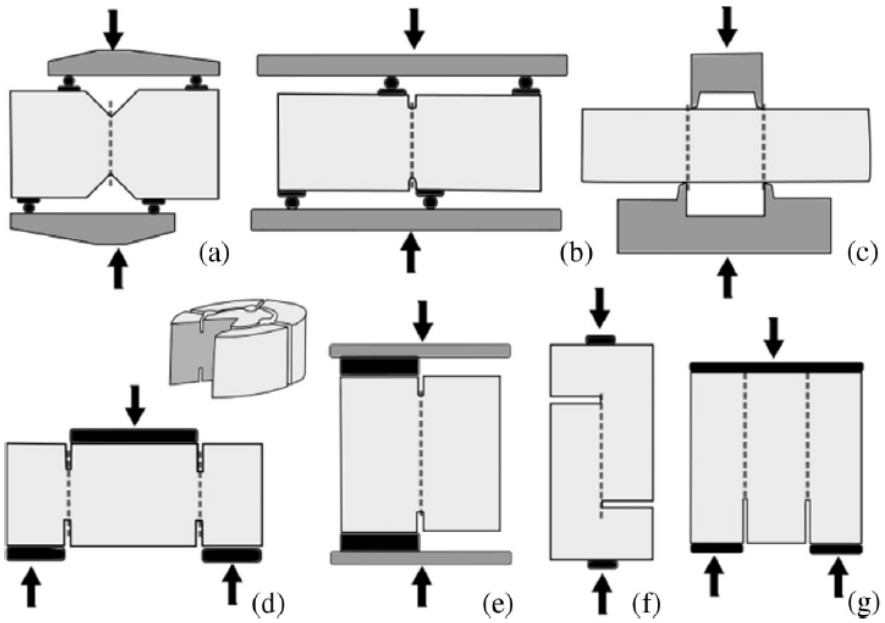


Figure 2.24 Test methods for assessment of shear resistance: a) Iosipescu and Negotia (1969), b) Bazant and Preiffer (1986), c) JSCE-SF6 (1990), Tuan et al. (2016), d) Luong (1990, 1992), e) Reinhard et al. (1997), f) Mattock and Hawkins (1972), g) Watkin (1972).

Despite efforts to obtain pure shear situations in tests (Mode II), it should be noted that in all cases listed, mixed-mode behaviour in which tensile crack growth (Mode I) takes over before Mode II failure occurs. Some testing arrangements may favour shear crack propagation against tensile crack propagation in comparison to others. However, as mentioned above, there is no common agreement on the most appropriate technique for obtaining pure shear behaviour. Hence, the choice of the testing arrangement and specimen geometry depends on practical issues related to ease of preparation and the stress conditions at the fracture plane.

2.3.2 Shear mechanisms in rubberised concrete

It is clear that the only shear transfer mechanism in plain concrete specimens is the aggregate interlocking action. As shown in Figure 2.25a, the aggregate interlocking contribution can be considered as the combination of normal and shear stresses acting along the crack surface. This is dependent on the aggregate types, their embedment depth in cement paste, the magnitude of crack slip and opening, as well as its roughness along the surface (Walraven and Reihardt 1981). As shown in Figure 2.25b, the stresses at the contact area can be resolved into a normal compressive stress σ_{pu} and a tangential shear stress τ_{pu} with the relationship:

$$\tau_{pu} = \mu \sigma_{pu} \tag{2.8}$$

where μ represents the coefficient of friction of the surface. According to the equilibrium condition shown in Figure 2.25b, the normal and shear forces acting on the crack face can be derived from the summary of each aggregate-cement paste interaction.

$$\Sigma N_{agg} = \sigma_{pu}(\Sigma A_s - \mu \Sigma A_w) \tag{2.9a}$$

$$\Sigma S_{agg} = \sigma_{pu}(\Sigma A_w + \mu \Sigma A_s) \tag{2.9b}$$

The values σ_{pu} and μ are constants along the crack based on the material, whilst the contact areas ΣA_s and ΣA_s represent the crack slip and opening magnitude, respectively, based on different phases (no contact, growing contact and maximum contact). The general formulation can be represented as:

$$\Sigma A = \int \rho_k \cdot \frac{4}{\pi} \cdot F(\frac{D}{D_{\max}}) \cdot G(\Delta, w, D) \cdot dD \tag{2.10}$$

The contact area is related to the total aggregate volume ρ_k, a function F of various aggregate size D to the maximum aggregate size D_{max}, and a function G of the crack slip Δ, crack opening w, and aggregate sizes (Walraven and Reihardt 1981).

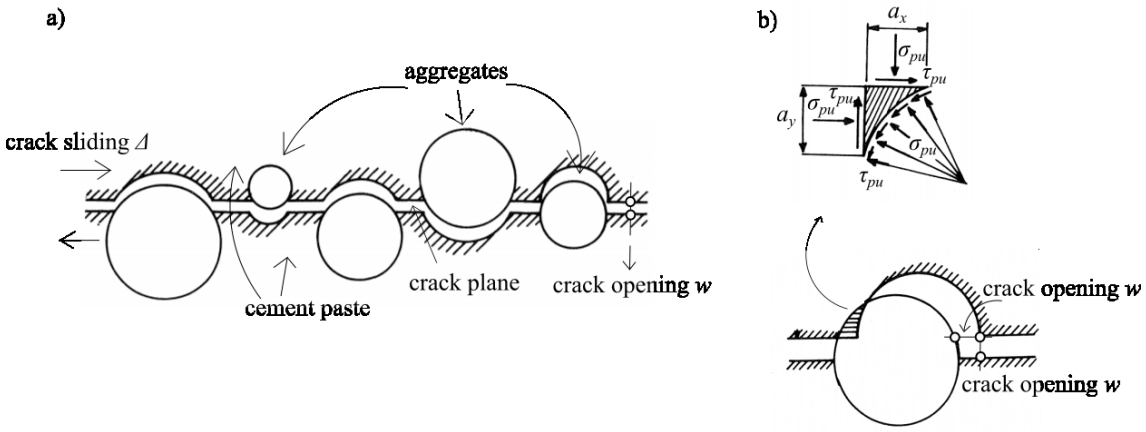


Figure 2.25 a) Aggregate interlock mechanism, b) stress transfer and equilibrium states

It is important to note that previous studies discussed in Section 2.2have focused on the axial and bending behaviour of rubberised concrete materials and members. Less attention has however been given to shear behaviour despite its importance as a possible governing factor in the failure mode under various loading situations. Although some studies have examined the impact behaviour of rubberised concrete at the material level (Naito et al. 2013, Ismail and Hassan 2016, Xue and Shinozuka 2013), investigations on rubberised concrete under direct shear are lacking. It should be noted that the above aggregate interlocking model is applicable in concrete mixes, where aggregates

have higher strength than the cement paste. In the case of rubberised concrete, although no studies seem to be available on the aggregate interaction between rubber particles and cement paste, it is reasonable to assume that the above model is still applicable in the normal aggregate range while the aggregate volume ρ_k needs to be modified with the rubber replacement ratio. In addition to the aggregate interlock mechanism, the soft rubber particles are able to provide clamping action, and the total shear transfer mechanism of rubberised concrete can be derived as the combination of aggregate interlock from gravel and clamping from rubber particles:

$$V_{tot} = V_{agg} + V_{clmp} \tag{2.11}$$

The clamping actions provided by rubber particles are contributed from the pull-out behaviour as introduced in Section 2.2.1 (Taha et al.2008). Unlike steel reinforcement, soft rubber particles are not able to provide additional bending and shear actions. Hence the clamping actions are fully based on the bond between rubber particles and cement paste. In order to identify the shear transfer mechanism in rubberised concrete, further studies are needed to quantify the interaction between rubber particles and cement paste. As a result, one of the key aims of this research is to investigate the shear (Mode II) fracture behaviour of rubberised concrete, as described in Chapter 4 of this thesis.

2.4 Behaviour of rubberised concrete members

As noted above, previous studies showed that the embedded rubber particles modify the fresh and hardened properties of the concrete as a function of the percentage of rubber replacement and grain size, with only a marginal effect arising from the type of rubber used. The relatively low specific gravity of rubber leads to a reduction in the unit weight in comparison with conventional concrete. The presence of rubber particles also leads to a reduction in compression strength, splitting tensile strength, elastic modulus and shear resistance of rubberised concrete materials, yet it can provide improved ductility and energy dissipation characteristics. However, most current applications of rubberised concrete have been primarily for use in non-structural elements such as crash barriers (Toutanji 1996; Taha et al. 2008; Atahan and Yucel 2012), floor surfaces (Cairns et al. 2004), cement aggregate bases under flexible pavements (Khatib and Bayomy 1999), and vibration control-applications such as sound barriers (Aliabdo et al. 2015; Ghizdavet et al. 2016; Medina et al. 2016). Although investigations on the behaviour of structural members incorporating rubberised concrete materials have been limited compared to studies at the material level, the potential benefits have been illustrated.

In addition to the load-displacement behaviour, the key issues related to reinforced rubberised concrete (RRuC) structural members are related to the energy dissipation and ductility capacities in comparison with those of conventional reinforced concrete (RC) members. This section also illustrates the potential benefits of combining the external confinement with RRuC members especially on the level of energy dissipation.

2.4.1 Unconfined members

Son et al. (2011) investigated the influence of rubber particles on the buckling behaviour of reinforced concrete columns. In this study, slender reinforced rubberised concrete columns were loaded under static axial loads. The results showed that although the axial load levels were decreased with the increase of rubber contents (from ρ_v=2.7%-5.4%), rubberised concrete specimens were capable of undergoing up to twice the lateral deformations before buckling compared to conventional concrete columns as shown in Figure 2.26.

The energy dissipation capacity and ductility of RRuC specimens were also more than twice those of corresponding conventional concrete. The curvature ductility μ_c, defined as the curvature ratio between the ultimate load state φ_u and the first yield of reinforcement moment φ_y ($\mu_c = \varphi_u / \varphi_y$) of RRuC column members under axial compression also proved to be significantly increased compared to that of conventional concrete specimens as shown in Figure 2.27. These initial test results indicated that although the RRuC member with relatively low rubber content (up to ρ_v=5.4%) had a lower load capacity, it exhibited improved energy dissipation and ductility than conventional RC members.

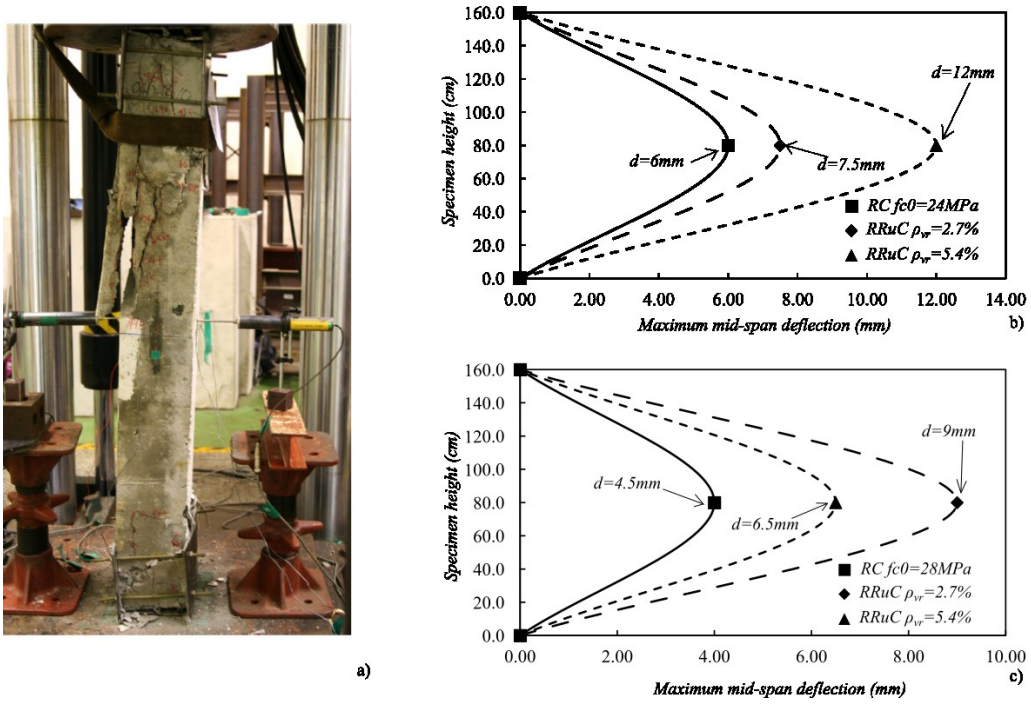


Figure 2.26 a) Test setup, mid-span deformation of RC and RRuC columns under axial compression with reference normal concrete strength of: b) f_{c0}=24 MPa, c) f_{c0}=28 MPa (from Son et al. 2011)

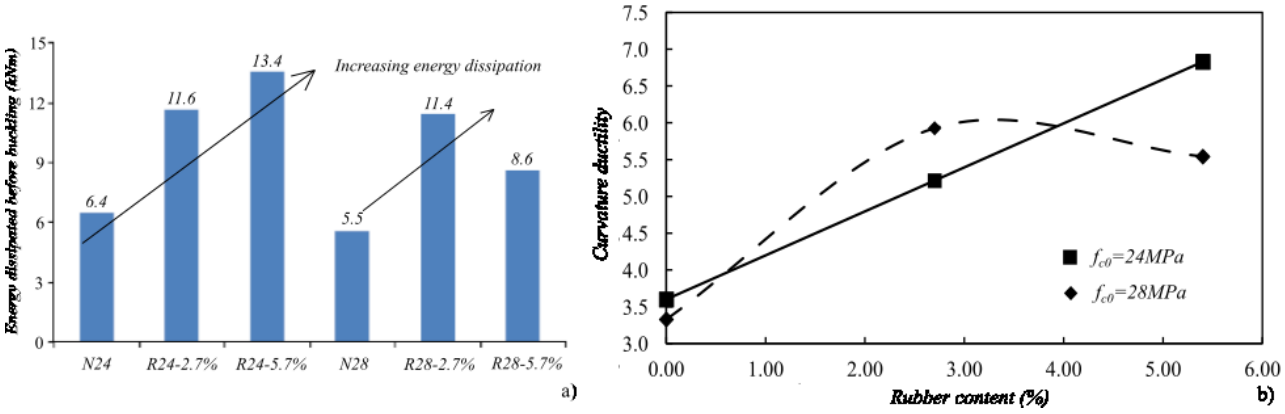


Figure 2.27 a) Energy dissipation, b) curvature ductility, as a function of rubber content (adapted from Son et al. 2011)

The behaviour of RRuC beam member under flexure was also investigated (Ismail and Hassan 2016). Four-point bending tests were performed on RRuC beam members with total volumetric rubber replacement ratios up to ρ_v=18% as shown in Figure 2.28. Similar load-mid-span deflection behaviour from the flexural tests was acquired showing that when the total rubber replacement ratio was below ρ_v=7.2%, the rubber particles did have a clear influence on the general stiffness and load capacities of RRuC beams, while the maximum deflection at failure (δ_u) of RRuC beams was

slightly increased with the increase of rubber content. Nevertheless, further increase of rubber content led to a noticeable reduction of both load and mid-span displacement capacities as shown in Figure 2.29a.

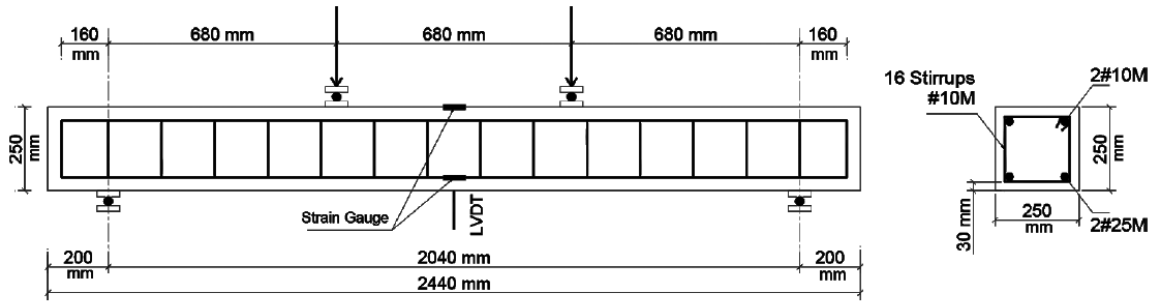


Figure 2.28 Four-point bending test setup on RRuC beam members (Ismail and Hassan 2016)

The influence of rubber content on the deflection ductility and energy dissipation at the maximum load points of RRuC beams were also reported. The deformation ductility μ_d of an RC beam may be defined as the mid-span deflection ratio at ultimate and yield $\mu_d = \varphi_u / \varphi_y$. As shown in Figure 2.29b,c, the ductility and energy dissipated for RRuC beams increased with the increase of rubber content when the total replacement was below 7.2%, while the values showed significant reduction with further increase of rubber content. It can be noted that rubber particles can enhance the ductility and toughness of RC flexural members to some extent, while an excessive amount of rubber content may lead to a significant loss of flexural capacity of the member, hence limits the energy dissipation (Ismail and Hassan 2016).

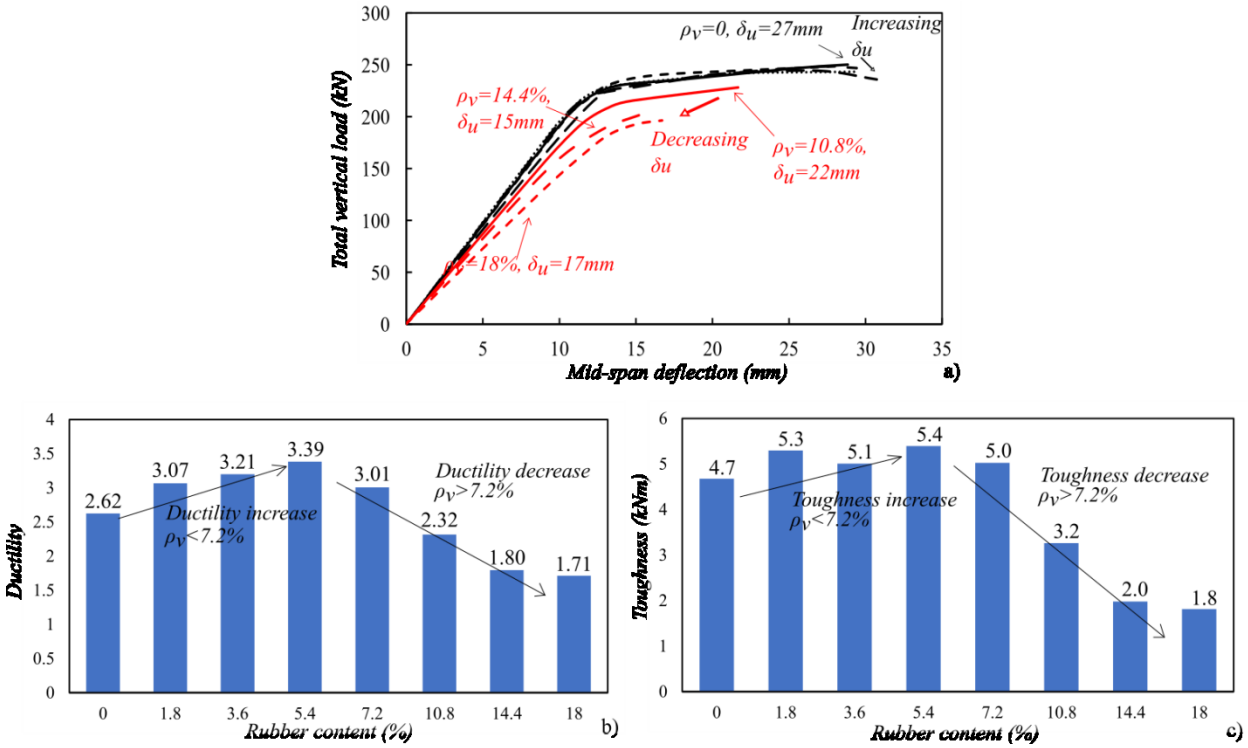


Figure 2.29 Four-point flexural test results on RRuC beams: a) load-deflection behaviour, b) ductility, c) toughness with different rubber contents (adapted from Ismail and Hassan 2016)

Further studies on the combined beam-column behaviour of RRuC members were performed by Youssf et al. (2015). Column specimens as shown in Figure 2.30 were tested under a constant value of axial load through a pre-tensioned steel bar, and lateral cyclic displacements. The entire RRuC column was cast in rubberised concrete with a total volumetric rubber replacement ratio of 9%. The general load-displacement curves and corresponding backbone curves of RC and RRuC columns are shown in Figure 2.31. It is shown that the introduction of rubber particles reduced the lateral load capacity (P_u) of the RRuC column by 1.4% as well as the ultimate drift (δ_u) (considering the loss of 20% of the maximum lateral load) by 8.5% compared to the RC member. The reduction in lateral load capacity and ultimate drift were mainly due to the lower strength of rubberised concrete. The axial forces for both the RC and RRuC columns were the same during this test leading to a higher axial load level for the RRuC member which also resulted in a reduction in deformation capacity. Similarly, Figure 2.31c shows that the RRuC member exhibited higher stiffness than the RC column while the higher axial load level produced higher stiffness. It is worth noting that in order to isolate the influence of rubber content on the performance of RRuC members, the applied axial load should be controlled to the same ratio of the compressive strength of rubberised concrete used.

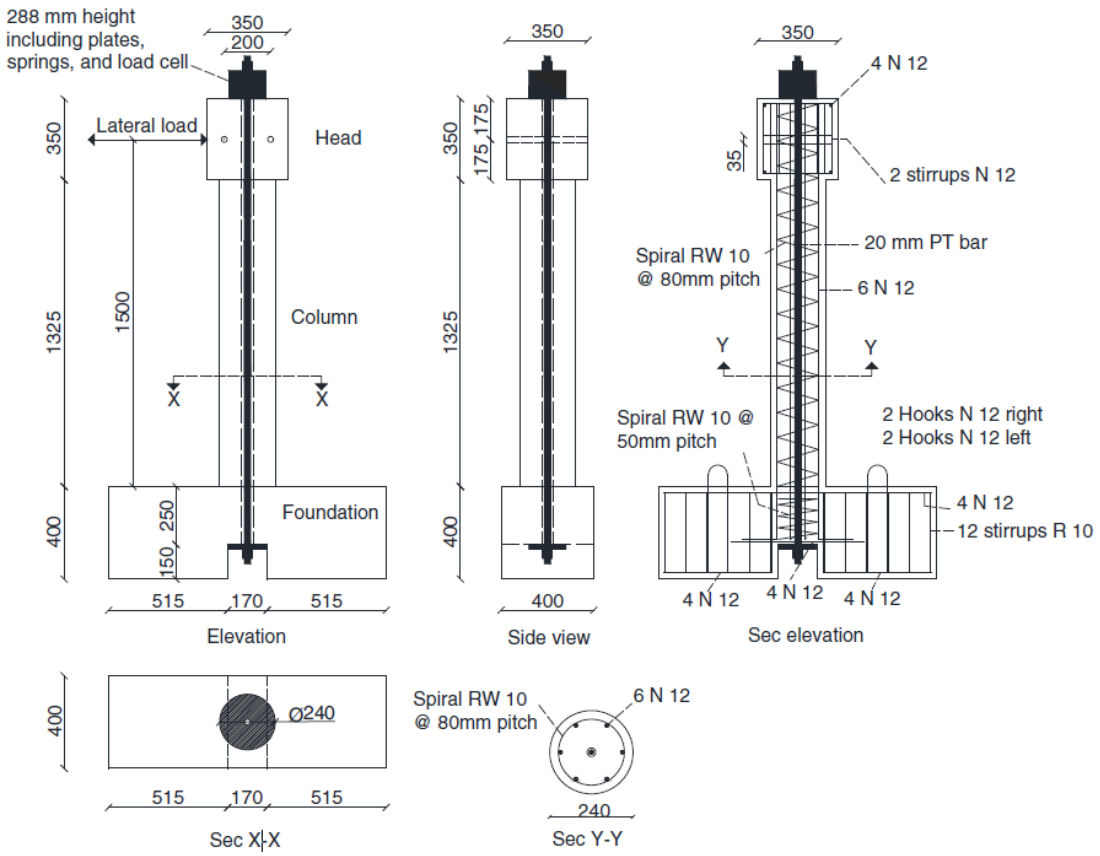


Figure 2.30 Beam-column member under combined axial and lateral load (Youssf et al. 2015)

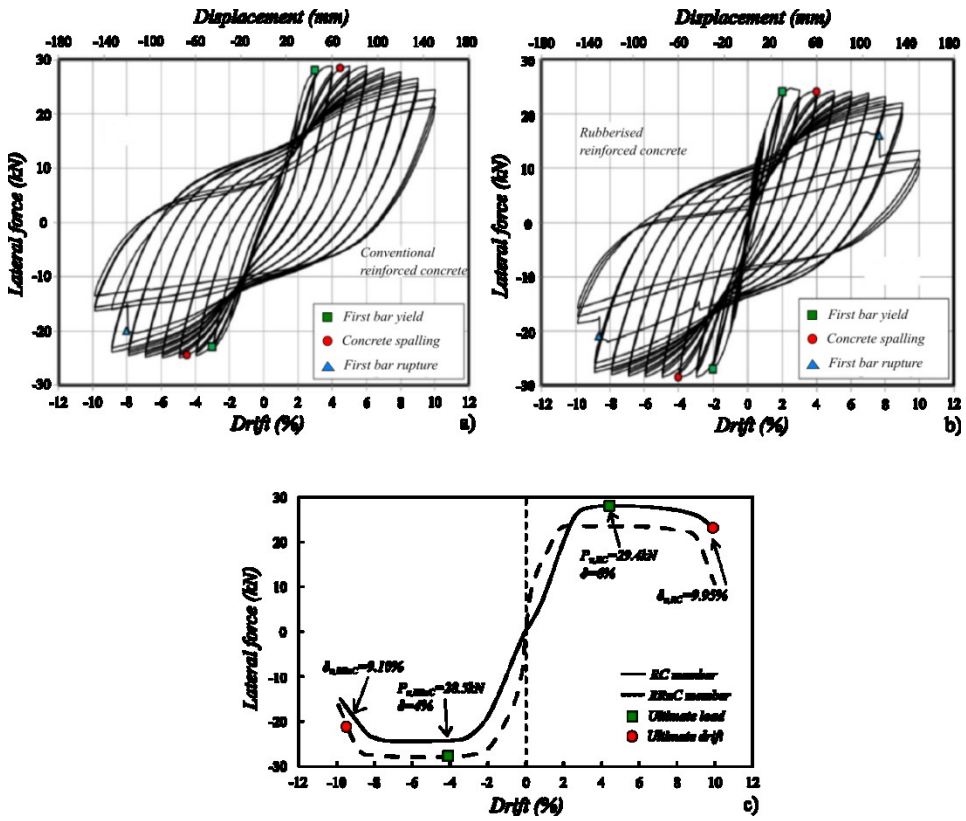


Figure 2.31 Hysteretic behaviour: a) RC member, b) RRuC member, c) backbone curves

The energy dissipation ability (E_d) of RRuC members, estimated based on the area enclosed in each hysterical hoop, was not found to be significantly different from the RC members (Youssf et al. 2015). As shown in Figure 2.32, due to the relatively low rubber content, the RRuC and RC column shared the same level of energy dissipation at each drift level until reported reinforcement rupture occurred (around 9% drift). Due to the continuous loss of post-yield stiffness and early concrete spalling, the RRuC beam-column member showed slightly lower energy dissipation capacity compared to the RC member. It was also reported the that although horizontal cracks and concrete spalling occurred at an earlier stage in RRuC member (at drift ratios of 3% and 4%, respectively) compared to the corresponding RC member (at drifts of 3.5% and 4.5%, respectively), the damaged area was more concentrated and the reinforcement ruptured at a later stage in the former case.

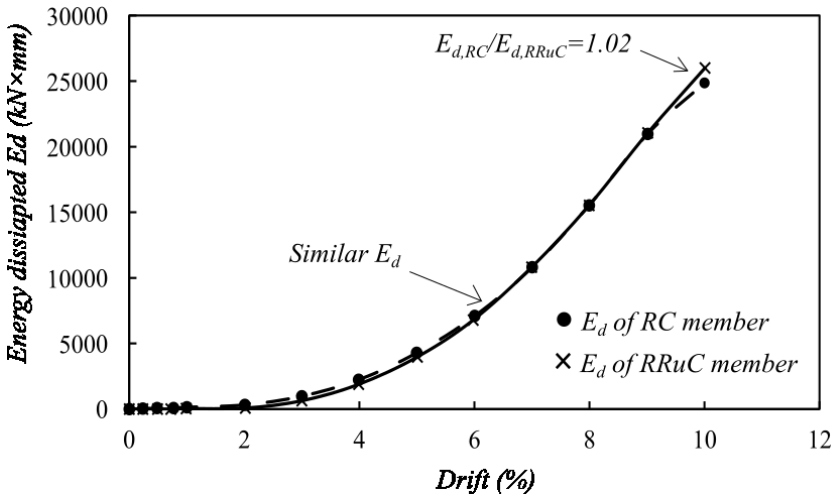


Figure 2.32 Energy dissipation of RC and RRuC beam-column members (Youssf et al. 2015)

Other tests on the seismic behaviour of RRuC members were also reported (Xue and Shinozuka 2013). Although available studies on RRuC member behaviour are still limited, it is evident that the load capacities of RRuC axial and flexural members are reduced by the presence of rubber particles. However, due to the relatively low rubber replacement ratio considered (less than 20%) and the limited number of tests performed, available test results did not quantify the actual influence of rubber content and axial load levels on the behaviour of RRuC members. As a result, further detailed studies are required for this purpose.

2.4.2 Confined members

As noted before, external confinement (such as FRP jackets) can improve both the strength and ductility of rubberised concrete significantly on the material level. Due to its low modulus of

elasticity and higher Poisson's ratio, rubberised concrete shows relatively higher lateral deformation at lower capacities. This activates the passive confinement such as steel or FRP jacket earlier than conventional concrete can achieve, which leads to a higher confinement effectiveness. Hence the utilisations of different types of confinement in RRuC structural members also need to be investigated.

Tests performed by Duarte et al. (2016) on beam-column behaviour of conventional concrete and rubberised concrete filled steel tubes (CFST and RuCFST) under combined axial load and lateral cyclic displacement, focused on the effects of cross-section geometries (square, rectangular and circular cross-sections) and rubber content, as shown in Figure 2.33. Although this experimental programme did not include comparative unconfined concrete specimens, the influence of rubber content and confinement properties on RuCFST members was observed.

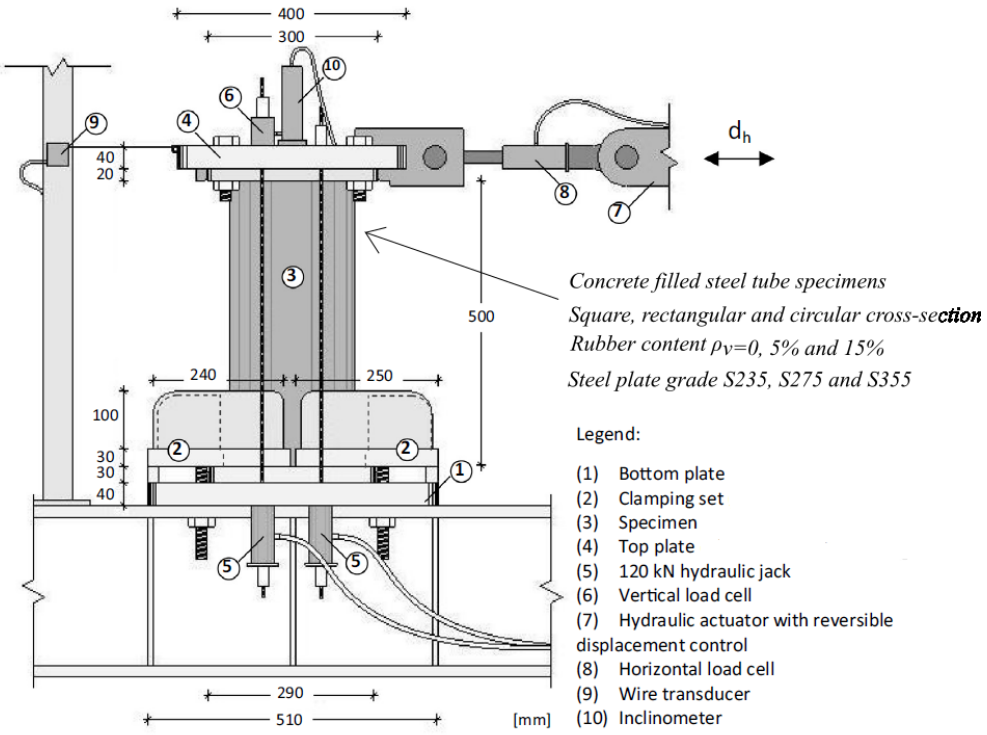


Figure 2.33 Test scheme of CFST and RuCFST beam-column test (Duarte et al. 2016)

The increase of rubber content caused an average reduction of 15% of lateral load capacity P_{max} when the total rubber content reached 15%, regardless of the cross-section shapes and yield strengths of the confining steel as shown in Figure 2.34. The ultimate failure states of all specimens, under low axial load (10% of compressive strength), corresponded to local buckling in the compression zones combined with cracking of steel in the tension zone. The failure modes of

specimens under double the axial load were fully controlled by the local buckling of the external steel confinement.

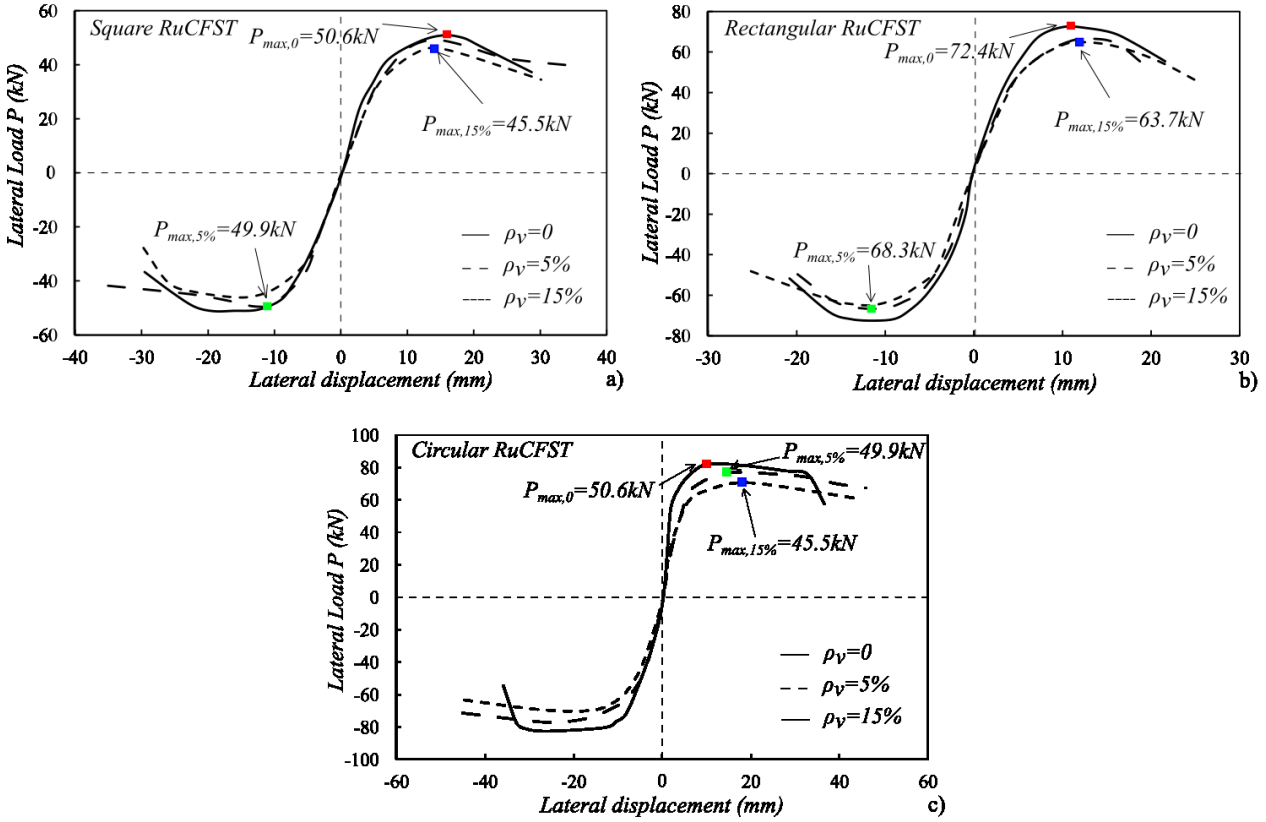


Figure 2.34 Envelope curves of RuCFST columns with: a) square, b) rectangular, c) circular cross-section under the same level of axial loads (adapted from Duarte et al. 2016)

The energy dissipation capacity of RuCFST column was defined as $\mu_E = E_{d,0.85F} / E_{dy}$, where $E_{d,0.85P}$ indicates the energy dissipated when the lateral load falls to 85% of the maximum value, and E_{dy} is the dissipated energy at first yield of the specimen as shown in Figure 2.35a. It was shown that the energy dissipations was influenced by both the cross-section type and rubber content. As shown in Figure 2.35b-d, RuCFST columns with circular cross-sections generally had higher energy dissipation compared to the other two types. The main reason is that circular steel sections can provide better confinement to the concrete core without the influence of corner effects, while local buckling is more likely to occur in the other two cases. It was also reported that the rubber content influences the energy dissipation of specimens in different ways. By increasing the total rubber content from 0% to 5%, the ductility increased in all cases between 12% and 52%, while further increase of rubber content from 5% to 15% caused the reduction in energy as illustrated in Figure 2.35b-d. These conclusions were similar to those noted above by Ismail and Hassan (2016).

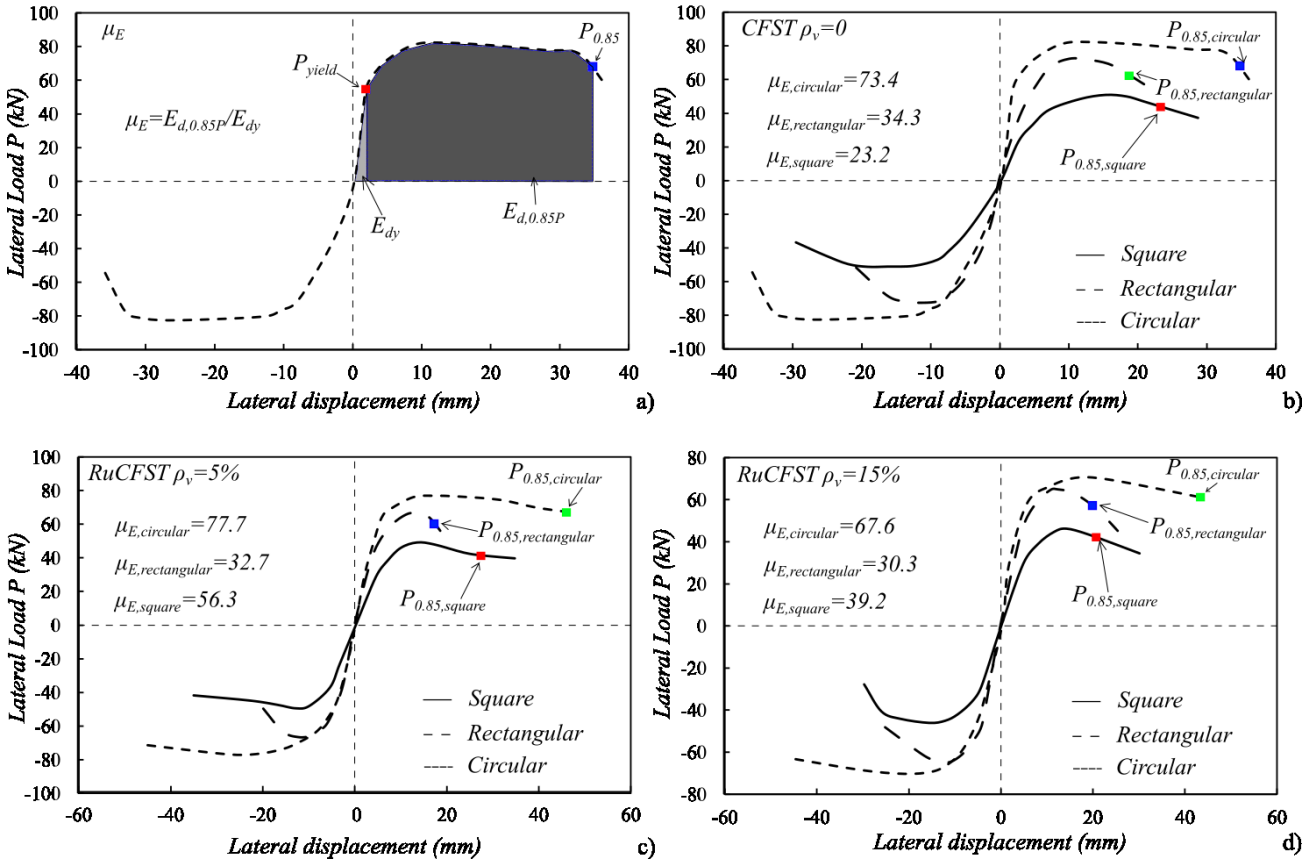


Figure 2.35 Energy and ductility: a) definition, b) CFST members, c) RuCFST members with 5% rubber content, d) RuCFST members with 15% rubber content (adapted from Duarte et al. 2016)

Unlike RuC beams under monotonic flexural loads, the cyclic behaviour of confined concrete is more complex since the external confinement plays a significant role in controlling the ductility of the specimen. The investigation carried out by Duarte et al. (2016) as shown in Figure 2.36, showed that the neutral axial of RuCFST columns was much closer to the centre of section than that of CFST columns when the applied bending moment reached the maximum capacity of the composite cross-section. Hence, with the increase of rubber content, a larger area of the steel tube is under compression, thus increases its susceptibility to local buckling and reduces the ductility effectiveness of the confinement to the concrete core.

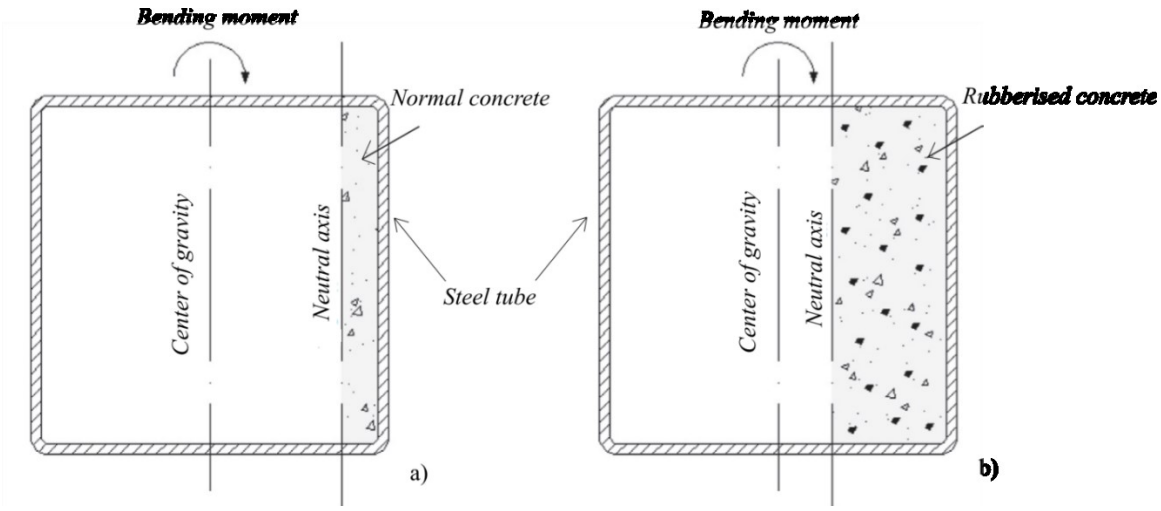


Figure 2.36 Neutral axis position: a) CFST (normal concrete), b) RuCFST (rubberised concrete) (adapted from Duarte et al. 2016)

A similar series of tests was performed by Silva et al. 2016 to investigate the flexural behaviour of circular RuCFST columns under combined axial and lateral loads. Similar conclusions were proposed, indicating that CFST and RuCFST columns exhibited high bending capacities and ductility and the failure modes of all specimens were controlled by the local buckling of the steel tubes. However, the rubber content was quite low (up to 9%), which does not provide adequate information on the influence of rubber content on the behaviour.

The above-discussed studies on the flexural behaviour of steel tube-confined concrete columns indicate the effectiveness of this type of confinement for enhancing both the flexural capacity and ductility of the members. Although rubberised concrete cores were used in both studies, the rubber content was relatively low. The steel tube confinement also showed significant detrimental behaviour associated with local buckling. Other studies on rubberised concrete columns confinement therefore recently examined other types of confinement material (i.e. FRP jackets).

Youssf et al. (2016) investigated the beam-column behaviour of confined reinforced rubberised concrete (CRRuC) members using FRP jackets. This study included reference groups of unconfined reinforced concrete (RC) and reinforced rubberised concrete (RRuC) specimens to illustrate the effects of FRP confinement explicitly. The test rig was the same as in previous research as shown in Figure 2.30. Additional confined reinforced concrete (CRC) specimens with 2 layers of CFRP jackets (CRC-2L) as well as CRRuC columns with 2 and 4 layers of CFRP jackets (CRRuC-2L, CRRuC-4L) were also tested. Since rubberised concrete was used in the entire shear span of the members as noted before, full wrapping with CFRP jackets was used as shown in Figure 2.37. After the failure of the confined specimens (reinforcement rupture), cracks occur along the FRP matrix

without damaging the fibres. On the other hand, Specimen CRRuC-2L failed with the rupture of FRP jackets due to the high lateral expansion of rubberised concrete. This behaviour indicates that sufficient confinement levels are needed for specimens with higher deformability.

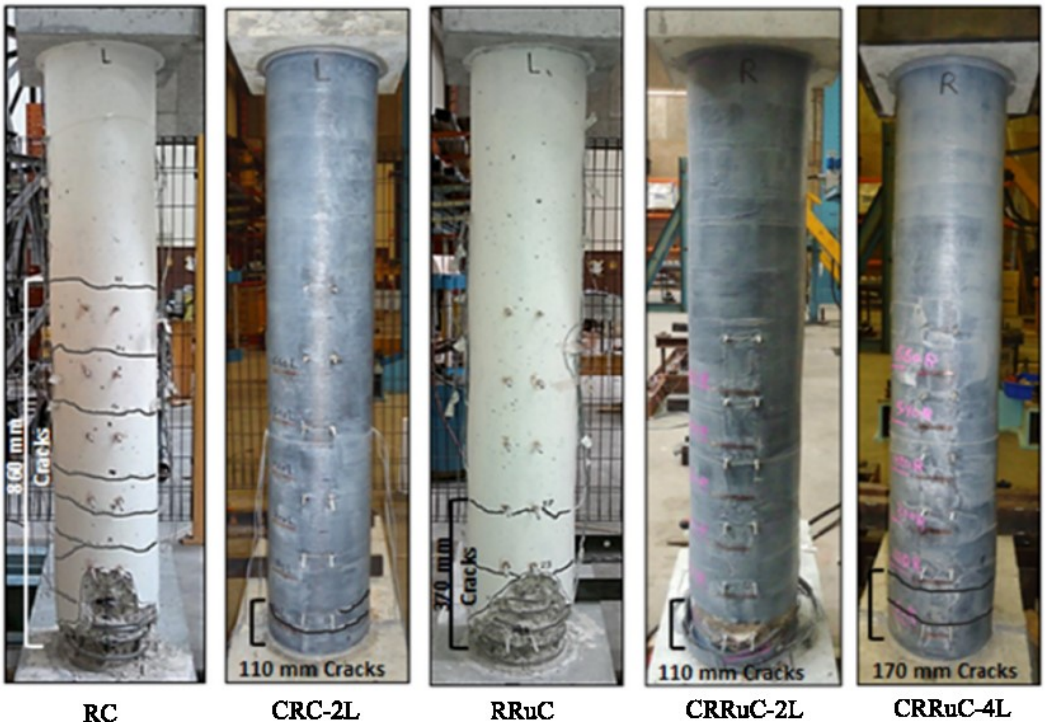


Figure 2.37 Global damage patterns of all test specimens (Youssf et al. 2016)

As shown in Figure 2.38, the hysteretic behaviour of all FRP confined specimens was more stable compared to the corresponding unconfined members. In addition, the FRP jacket prevented the spalling of the concrete cover, hence no strength degradation was found in these members until rupture of longitudinal reinforcement occurred. As a result, the corresponding ultimate drifts of FRP confined specimens were also increased compared to unconfined members as indicated in Figure 2.38a-f which led to higher ductility levels.

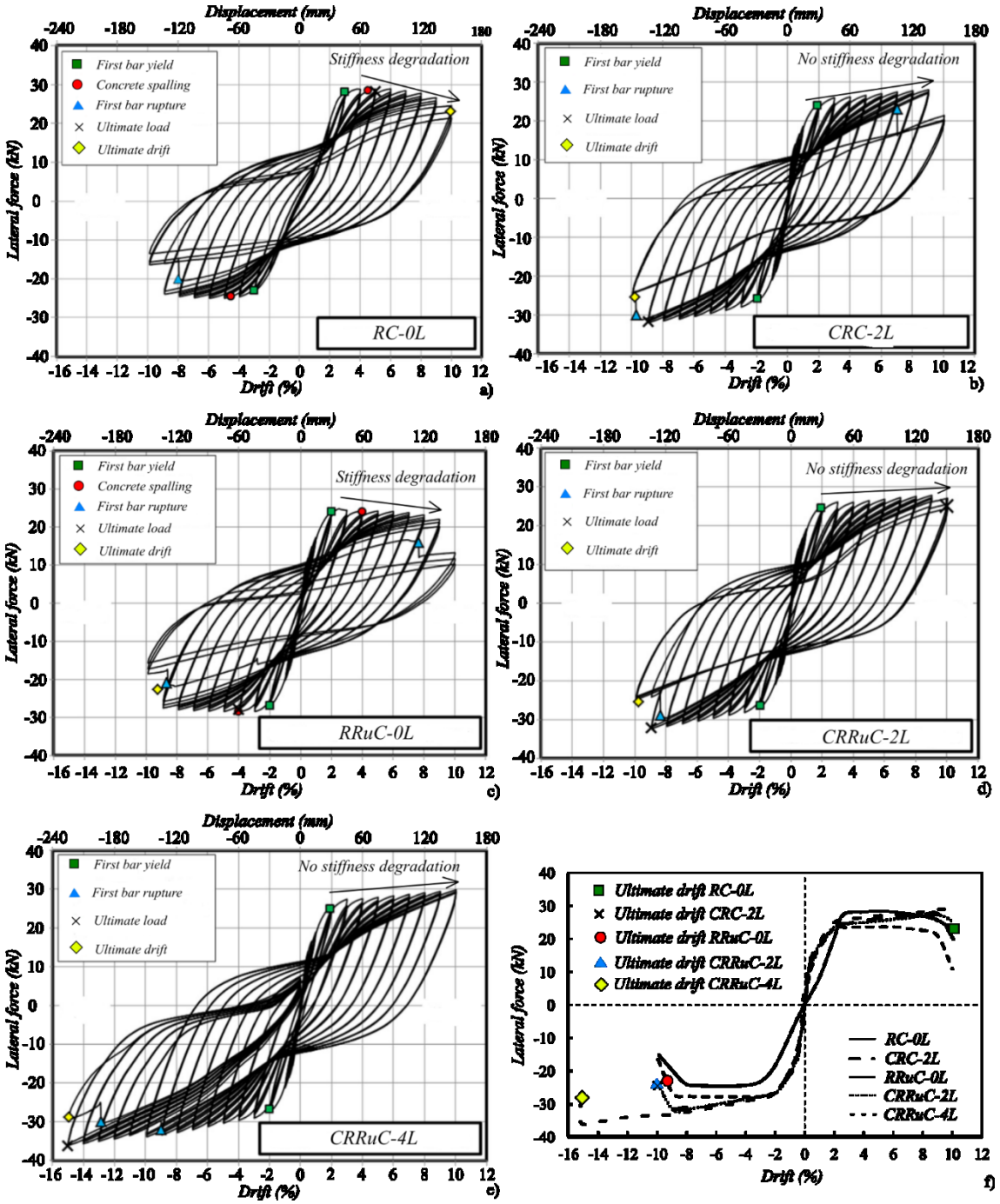


Figure 2.38 Hysteretic behaviour of specimens: a) RC, b) CRC-2L, c) RRuC, d) CRRuC-2L, e) CRRuC-4L, f) envelope curves of all specimens (adapted from Youssf et al. 2016)

Figure 2.39 shows a comparison of the energy dissipation of each specimen from the test. The FRP confinement was effective in enhancing the energy dissipation of the members at a high lateral displacement level (9% of drift) where the external confinement maintained the integrity of the concrete core. Unlike the envelope curves of CFST columns specimens as shown in Figure 2.35, FRP confined concrete columns did not show any stiffness degradation under cyclic loading as shown in Figure 2.38a-e. Cracks may form within the matrix of FRP jackets, yet it did not rupture

the FRP fibre hence did not affect the confinement action in the hoop direction. In contrast to CFST members whose failure modes are controlled by the local behaviour of the steel tube, the failure mode of FRP confined members is still the rupture of longitudinal reinforcement. It can be concluded that FRP jackets are more effective in providing lateral confinement on concrete members than conventional steel tubes.

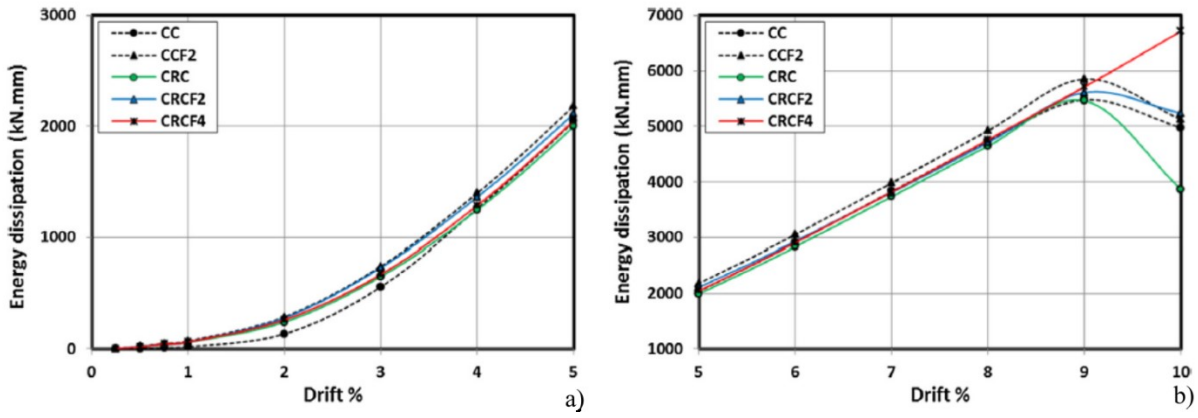


Figure 2.39 Energy dissipation of all test specimens: a) up to 5% drift, b) up to 10% drift (Youssf et al. 2016)

It is clear that the low strength of rubberised concrete leads to a reduction in strength. In contrast, the ductility and energy dissipation can be enhanced. As noted in the previous studies, as summarised in this chapter, this can be achieved by replacing relatively small amounts of aggregates with rubber particles. To overcome the reduction in strength when a high rubber content is used (Ismail and Hassan 2016; Youssf et al. 2015), external confinement, such as using steel tubes or FRP jackets can offer effective solutions.

As noted before, the maximum rubber content in all previous studies was below 20%, which represents only a small portion of aggregate replacement. As a result, several studies concluded that the rubber content did influence the member behaviour (Youssf et al. 2015), which may be misleading. Further research is therefore needed to examine the behaviour of members in which larger proportions of rubber content is incorporated. The influence of axial loading on the inelastic behaviour of rubberised concrete members needs further investigations. Moreover, the use of FRP jackets, which was shown to offer an effective solution for providing additional external confinement to rubberised concrete members, needs to be assessed and quantified in more detail. Accordingly, subsequent chapters of this thesis describe a detailed experimental investigation into the inelastic behaviour of large scale beam-column members, with and without external confinement, and incorporating significant levels of rubber content.

2.5 Concluding remarks

Recycling waste tyres to produce novel concrete materials is an attractive option that could potentially combine environmental and constructional advantages. As a result, in recent years, several investigations have been conducted to assess the feasibility of using recycled rubber materials in concrete.

An overview of previous research on the behaviour of rubberised concrete materials was given in this chapter. It was shown that nature of rubber particles hinders the workability of fresh rubberised concrete mixes which can be recovered by additional admixtures. The soft behaviour of rubber particles also leads to a reduction in concrete material strength. On the other hand, the uniaxial compressive and flexural behaviour of rubberised concrete specimens exhibit more flexible post-peak strength degradation. Compared to solid mineral aggregates, the soft rubber particles slow the crack propagation in the rubber/cement–matrix interface which also contributes to a higher deformability of rubberised concrete samples before final failure.

Whilst most studies have focused on assessing the compressive and flexural strength of rubberised concrete materials, there is a lack of information on the full constitutive response of rubberised concrete materials. Less attention has also been given to the shear behaviour, particularly with respect to the lack of studies on the pure shear (Mode II) type of failure. Even for conventional concrete members, there is no consensus on the testing arrangements that should be used to assess pure shear behaviour, with various proposed approaches having several drawbacks as discussed in detail in this chapter.

Several previous studies have also examined the behaviour of rubberised concrete members under axial, flexural or combined axial-flexural loads. However, these studies have been limited to rubber replacement ratio that are typically below 10%, with no studies reaching levels above 20%. As expected, incorporating rubber in concrete reduces the strength. However, it was also shown to result in significant enhancement in ductility and energy dissipation capabilities. In order to compensate for the loss of strength caused by the substitution of mineral aggregates with rubber particles, external confinement can be employed. Steel tubes can provide high levels of external lateral confinement, yet local buckling and practical issues may limit its effectiveness. Fibre reinforced polymeric (FRP) sheets, can provide an effective alternative favourable for external confinement due to its high strength, stiffness and low density.

Subsequent chapters of this thesis address several of the research needs identified through the literature review described above. The behaviour of rubberised concrete is examined in detail in

Chapter 3, with focus on quantifying for the first time the complete stress-strain response as well as providing analytical expressions for the main material properties. On the other hand, Chapter 4 described a novel experimental assessment into the shear behaviour of rubberised concrete members. A detailed experimental study into the inelastic behaviour of unconfined and externally confined RC members, with significant rubber content, and subjected to combined moment and axial actions, is also described in Chapter 5 and 6.

Chapter 3

3 Material tests

Nomenclature

Greek letters

σ – uniaxial compressive stress
$\varepsilon_{c01,1}$ - crushing strain for normal concrete
ε_{cr1} - axial strain
$\varepsilon_{cr1,1}$ - crushing strain for rubberised concrete
ε_{cr2} - lateral strain
$\varepsilon_{cr1,u}$ - ultimate strain of rubberised concrete at complete loss of strength
$\varepsilon_{cr1(\eta fcr)}$ - axial strain at $\eta \times f_{cr}$
$\varepsilon_{cr2(\eta fcr)}$ - lateral strain at $\eta \times f_{cr}$
$\varepsilon_{cr1,el}$ - strain at proportionality limit
ε_{fu} – ultimate strain of AFRP sheet
$\varepsilon_{crc1,u}$ – ultimate axial strain of confined rubberised concrete
$\varepsilon_{crc2,u}$ – ultimate lateral strain of confined rubberised concrete
η - stress factor
λ - factor for the type of aggregate replaced
ρ_{vr} - volumetric rubber ratio

Lowercase latin letters

$d_{g,repl}$ - replaced aggregate size
$d_{g,max}$ - maximum mineral aggregate size
$d_{r,avg}$ - average rubber particle size
$d_{r,max}$ - maximum rubber particle size
f_{c0} - normal concrete cylinder compressive strength
f_{cr} - rubberised concrete cylinder compressive strength
$f_{cr,cube}$ - rubberised concrete cube compressive strength
f_{ctr} - rubberised concrete tensile strength
$f_{ctr,sp}$ - rubberised concrete splitting strength
$f_{cr,ref}$ - mechanical strength of the reference sample
$f_{cr(d)}$ - converted mechanical strength of the sample
f_{crc} – confined rubberised concrete strength
f_l – lateral confining pressure
$g_{c,2}$ - post-crushing energy
t_f – external confinement thickness
$w_{max,r}$ - maximum crack displacement
w_{max0} - base crack displacement

Uppercase latin letters

G_c - crushing energy
E_{cr} - elastic modulus
E_{c1} – initial stiffness of confined concrete
E_{c2} – second stiffness of confined concrete
E_f – elastic modulus of AFRP sheet
$V_{cr,ref}$ - volume of the reference sample
$V_{cr(d)}$ - converted volume of the sample

3.1 General

As noted before in Chapter 2, a number of previous studies have proposed expressions for estimating the material properties of rubberised concrete, primarily focusing on the compressive strength, but there is a lack of information on the full constitutive relationships. Most existing analytical expressions to estimate the strength degradation are validated through a limited number of concrete mixes, with similar rubber aggregate sizes and type of mineral aggregate replaced, whereas information regarding the post-peak behaviour is scarce. To obtain a detailed insight into the behaviour, this chapter describes an experimental programme carried out on rubberised concrete in which fine and coarse mineral aggregates are replaced by rubber particles.

Cylindrical samples with up to 60% rubber replacement are tested under uniaxial compression to assess the complete stress-strain response including the post-peak behaviour. Additionally, compression tests on cubic samples, and splitting tests on cylindrical specimens, are carried out on compressive and tensile strengths, respectively (Bompa et al. 2017). In addition, 14 cylindrical rubberised concrete specimens confined with fibre reinforced polymer (FRP) sheets were also prepared to examine the influence of FRP confinement on rubberised concrete properties. Aramid FRP (AFRP) was chosen in this research as it combines good tensile strength and high ultimate elongation (Raffoul et al. 2017). Detailed descriptions of these material tests and a full account of the results obtained are given in this chapter.

3.2 Experimental programme

One hundred and ten (110) samples, including 60 cylindrical and 50 cubic material specimens, were prepared to assess the compressive and splitting strength, as well as the full constitutive compression behaviour of rubberised concrete with various replacement ratios of both fine and coarse mineral aggregates (Figure 3.1a). Following a series of trial mixes on 50 samples in which the cement type was varied whereas the remaining constituents of the mix remained unmodified, pilot tests on 4 cylindrical samples were carried out to determine the most effective testing configuration. Finally, four sets of samples (4×Ø100×200 cylinders and 4×100 mm cubes for compressive tests, and 4×Ø100×200 cylinders for splitting tests), with volumetric replacement ratios varying in the range of ρ_{vr} = 0–0.6 were tested to determine the complete stress-strain behaviour including the post-peak response, followed by 14×Ø100×200 cylinders with various rubber replacement ratios confined by AFRP jackets tested using the same approaches. The volumetric replacement ratio ρ_{vr} is herein defined as the ratio between the replaced volume of mineral aggregates in the rubberised concrete and the total volume of mineral aggregates in the reference normal concrete mix.

3.2.1 Mix design and specimen details

The rubber particles used in the rubberised concrete mixes were obtained from two sources. Rubber aggregates with dimensions up to 10 mm, produced from car tyre recycling (ADRIA). As depicted in Figure 3.1b, they were supplied in the following size ranges: 0–0.5 mm, 0.5–0.8 mm, 1.0–2.5 mm, 2–4 mm and 4–10 mm, and were used in the concrete mix in 5%, 5%, 15%, 20% and 10% ratio of the total added rubber content, respectively, with the remaining 45% being comprised of particles with sizes in the range 10–20 mm. The larger rubber particles were produced from truck or bus tyre recycling, with typically higher density than car tyre particles (CONICA). This portion was identified following a study of the workability of rubberized concrete within a wider European

research project (Anagennisi 2017; Pilakoutas et al. 2015; Raffoul et al. 2015; Raffoul et al. 2016). These proportions resulted from a detailed study on 40 mixes carried out by Raffoul et al. (2016) in which the best balance between workability and strength loss was sought. All rubber particles had 25% content of carbon black, polymers in the range of 40–55%, whereas the remaining constituents are softeners and fillers. The specific gravity of rubber was 1.1, whereas the water absorption was 7.1% for 4–10 mm particles and 1.05 for 10–20 mm particles. Sand and gravel aggregates shown in Figure 3.1b, from naturally occurring rock deposits consisting of combinations of various minerals (TARMAC), were used for the concrete mix shown in Figure 3.1c. The fine aggregates with sizes up to 5 mm had a specific gravity of 2.65 and a moisture content of 5%, whereas the coarse aggregate (5–10 mm) had a specific gravity of 2.65 and a moisture content of 3%. The particle size distribution of mineral aggregates and rubber particles was determined following EN 933-1:2012 as illustrated in Figure 3.2. In the trial mixes, CEM I 52.5N and CEM II 32.5N were used to assess their influence on the compressive concrete strength at 7 and 28 days. However, in the tests used for the assessment of the constitutive behaviour, the higher strength cement was used.



a)



b)


b)

Figure 3.1 a) Rubberised concrete samples, b) Rubberised concrete constituents, c) Rubberised conrete mix

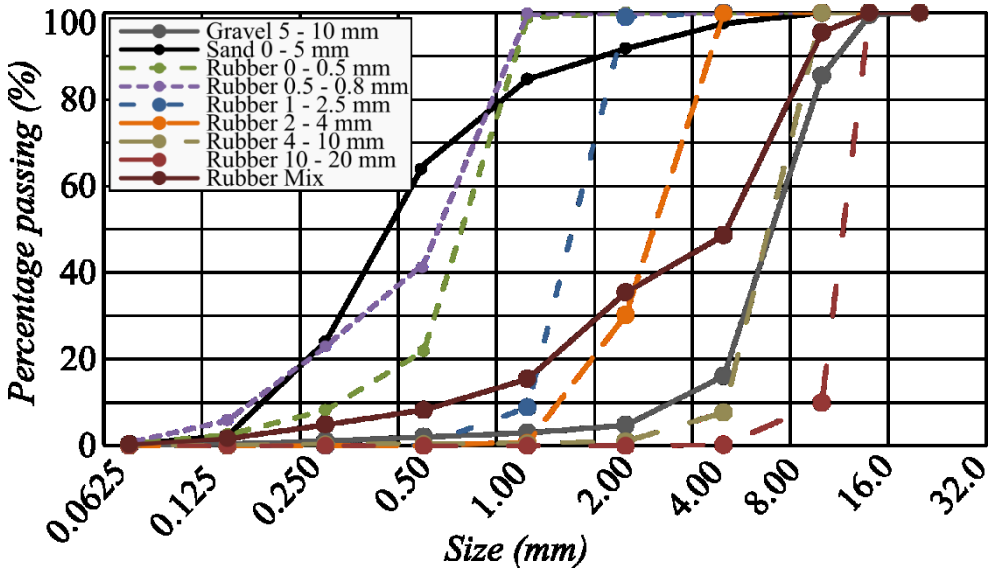


Figure 3.2 Sieve analysis for mineral aggregates and recycled rubber

A reference normal concrete mix with target compressive strength of 60 MPa, typically used in bridge piers as provided by an industrial partner of the project (Anagennisi 2017) based on practical experience, was prepared with the following mix ratios. This included also the amount of admixtures typically used in practice. The normal concrete (NC) reference mix had 425 kg/m^3 of cement, 820 kg/m^3 of sand, 1001 kg/m^3 of gravel, 149 L of tap water, with 2.5 L/m^3 of plasticiser (Sika Viscoflow 1000) and 5.1 L/m^3 of super-plasticiser (Sika Viscoflow 2000). In the rubberised concrete mixes, 20% of the cement was replaced in equal quantities with EN 450-1 fineness category S fly ash and Grade 940 silica fume (ELKEM). They were primarily added to improve workability, segregation and slump, and to optimise the particle packing of the mixture. Rubberised concrete mixes with 20%, 40% and 60% rubber replacement by volume of mineral aggregates were produced to assess the full constitutive characteristics of the rubberised concrete. The rubber quantities used in the mixes were 110 kg/m^3, 220 kg/m^3 and 330 kg/m^3, respectively.

Based on the mix optimisation study carried out by Raffoul et al. (2016), which was used as a basis for the mix ratios above, it was observed that the compressive strength is slightly more influenced by coarse rubber properties, while the fine rubber was slightly more detrimental to the concrete fresh properties. The mixes without silica fume and fly ash showed poorer workability and strength. Silica fume and fly ash improved the strength and flowability with 42% and 20%, respectively, for a mix with 40% replacement of fine aggregates. The same study (Raffoul et al. 2016) showed that the reduction of super plasticiser content by 40% reduced the flow (by up to 16%) and, more

importantly, led to a reduction in mix segregation. The mix proportions of normal and rubberised concrete are listed in Table 3-1.

Table 3-1 Proportions of concrete mixes

Material		Quantity (per m^3)			
		Reference	R20	R40	R60
Binders	Cement	425 kg	340 kg	340 kg	340 kg
	Silica fume	-	42.5 kg	42.5 kg	42.5 kg
	Fly ash	-	42.5 kg	42.5 kg	42.5 kg
Aggregates	Aggregate 0/5	820 kg	656 kg	492 kg	328 kg
	Aggregate 5/10	1001 kg	800.8 kg	600.6 kg	400.4 kg
Water and admixtures	Water	149 L	149 L	149 L	149 L
	Sika Viscoflow 1000 (plasticiser)	2.5 L	2.5 L	2.5 L	2.5 L
	Sika Viscoflow 2000 (superplasticiser)	5.1 L	5.1 L	5.1 L	5.1 L
Rubber particles	Size 0/0.5	-	5.5 kg	11.0 kg	16.5 kg
	Size 0.5/0.8	-	5.5 kg	11.0 kg	16.5 kg
	Size 1/2.5	-	16.5 kg	33.0 kg	49.6 kg
	Size 2/4	-	22.0 kg	44.0 kg	66.0 kg
	Size 4/10	-	11.0 kg	22.0 kg	33.0 kg
	Size 10/20	-	49.5 kg	99 kg	148.4 kg

A rotary mixing machine with a capacity of 40 L was mainly used for the mixes reported herein as shown in Figure 3.3. Initially, the mineral aggregates, rubber mix and binders were mixed separately in containers. All mineral aggregates and half of the water were mixed together in the mixer for 1 min. The rubber was then added to the mixer and mixed with the mineral aggregates and half of the water for another 1 min. In the following phase, the binders, and the remaining water including the admixtures were mixed all together for a minimum of 3 further minutes. A supplementary plasticiser was added where the observed workability was below acceptable levels. All materials were mixed for another 2 mins and placed afterwards in formworks, and subsequently compacted using a vibrating table until the air content in the fresh concrete was at a minimum. Although the mixing procedure may influence the performance, for the mixes reported here the mixing procedure was maintained throughout the experimental programme, hence no considerable differences were observed.

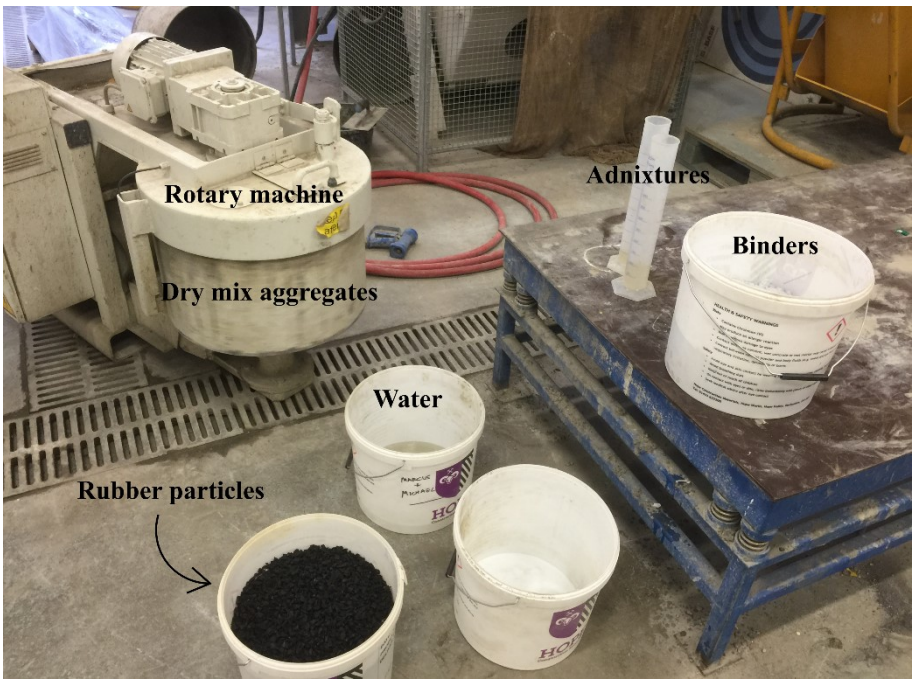


Figure 3.3 Mixing machine and ingredients

Codified provisions allow compressive material testing primarily on cylinder samples, and also on cube specimens with specific sizes (EN 206-1: 2000, ASTM C39/C39M). In this investigation, preliminary tests were carried out at 7 days, yet the fundamental observations from tests are made at 28 days from compression tests on 100 mm×200 mm cylinders, 100 mm cubes and splitting tests on cylinders with 100 and 102 mm diameter. The samples were cast directly in the size required in steel or plastic formworks and covered with plastic sheets until de-moulding. Two days after casting, the samples were placed in a water tank located in a curing room to ensure appropriate concrete hydration.

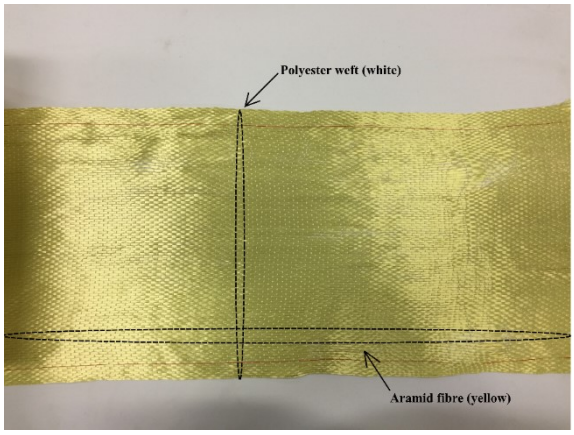
The ends of cylindrical samples were finished with a grinding machine on the day before the test. The cylindrical rubberised concrete samples were capped with high strength mortar and further polished with sand paper to ensure flatness of the surfaces and good contact conditions with the loading machine. The dimensions of all samples were measured to assess stress and strain characteristics as a function of the recorded force and displacement. The longitudinal dimensions of the cylindrical samples and their diameters were determined as the average of a minimum of three measurements at different locations. The average dimensions of cubic samples were assessed from two measurements for each orthogonal direction.

The rationale behind the mix design reported in this chapter and used throughout this research was to develop an environmentally friendly concrete, primarily provided with high deformability capacities even for significant strength losses which can be recovered by external confinement

when necessary as discussed before in Chapter 2. This was achieved with replacement ratios of up to 60% of both fine and coarse aggregates using the rubber particle sizes reported in this chapter and 2–3 layers of aramid fibre reinforced polymer (AFRP) jacket confinement for applications in bridge piers and/or base isolation systems. In this research, 14 cylinders with aggregate replacement ratios up to 60% were prepared with the external confinement of 2-3 layers of AFRP jacket for the assessment. The AFRP sheets, provided by the manufacturer (Weber.tec), as shown in Figure 3.4, consisted of unidirectional sheets with aramid fibres which were sewn up using polyester wefts in the perpendicular direction.


a)


b)



c)

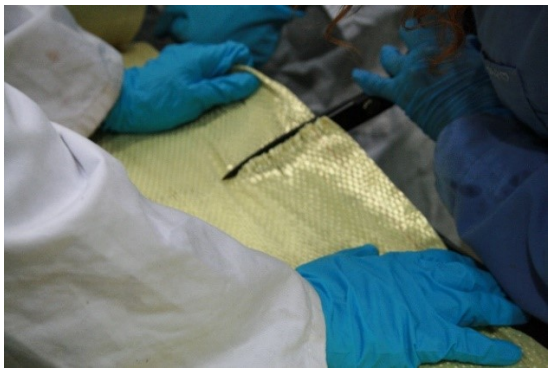
Figure 3.4 a) AFRP roller, b) bonding adhesive and hardener, c) AFRP sheet components

The AFRP sheet had a mean tensile strength of $f_{y,frp}$=2400 MPa, mean elastic modulus of E_{frp}=116 kN/mm^2, ultimate strain capacity of $\varepsilon_{u,frp}$=2.5% and thickness of t_{frp}=0.2 mm. Detailed technical data of the material is shown in Table 3-2. Before applying the AFRP confinement, the surface of the cylinder was brushed and cleaned to improve adherence. Figure 3.5 shows the preparation process of the confined specimens. The sheet was cut to length based on the number of layers needed with additional 50 mm overlapping area to create sufficient bonding. In order to avoid direct contact of the loading plate with AFRP jackets and prevent the load transfer through the

confinement directly, the height of the sheet was controlled as 180 mm, leaving 10 mm gaps at the top and bottom areas of the cylinder. The adhesive provided by the same manufacturer contained the bonding adhesive and hardener which were mixed in a clear barrel and uniformly applied over the entire sheet using a sponge roller and plastic squeegee to avoid damaging the fibre as shown in Figure 3.5b,c. The sheet was fully soaked with the adhesive before wrapping the cylinders while the adhesive still maintained its workability. The confinement jacket was wrapped around the cylinders with continuous compression to guarantee sufficient bonding between each sheet layers. The cylinders were then kept in room temperature for more than 72 hours before testing to ensure effective bonding.

Table 3-2 Physical and mechanical properties of AFRP

Physical properties		Mechanical properties	
Aramid weight	290 g/m^2	Thickness	0.2 mm
Polyester weft	30 g/m^2	Elastic modulus	116000 N/mm^2
Width	300 mm	Tensile strength	2400 N/mm^2
Fibre density	1.45 g/cm^3	Strain capacity	2-10%


a)

b)

c)

Figure 3.5 AFRP preparation procedure a) cutting the sheet, b) mixing adhesive and hardener, c) soaking the sheet in adhesive

3.2.2 Testing arrangements

The cylindrical specimens, used in the pilot tests and for assessing the full constitutive behaviour, were tested in a stiff four-post Instron Satec 3500 kN machine. These tests were carried out in displacement control with a compressive displacement rate of 0.1 mm/min (ASTM C39/C39M, RILEM TC 148-SSC). As illustrated in Figure 3.6a, the samples were placed on the bottom platform of the testing machine. Loading plates of high strength steel with a diameter of 100 mm were also added at both ends of the sample. The bottom plate, depicted in Figure 3.6b, was a stiff 50 mm thick steel element, whereas the top plate incorporated a 3D hinge with total thickness of 75 mm. Intermediate, 'sandwich', high strength steel plates were added between the testing machine and bearing pads to allow the recording of compressive displacements in the post-peak regime.

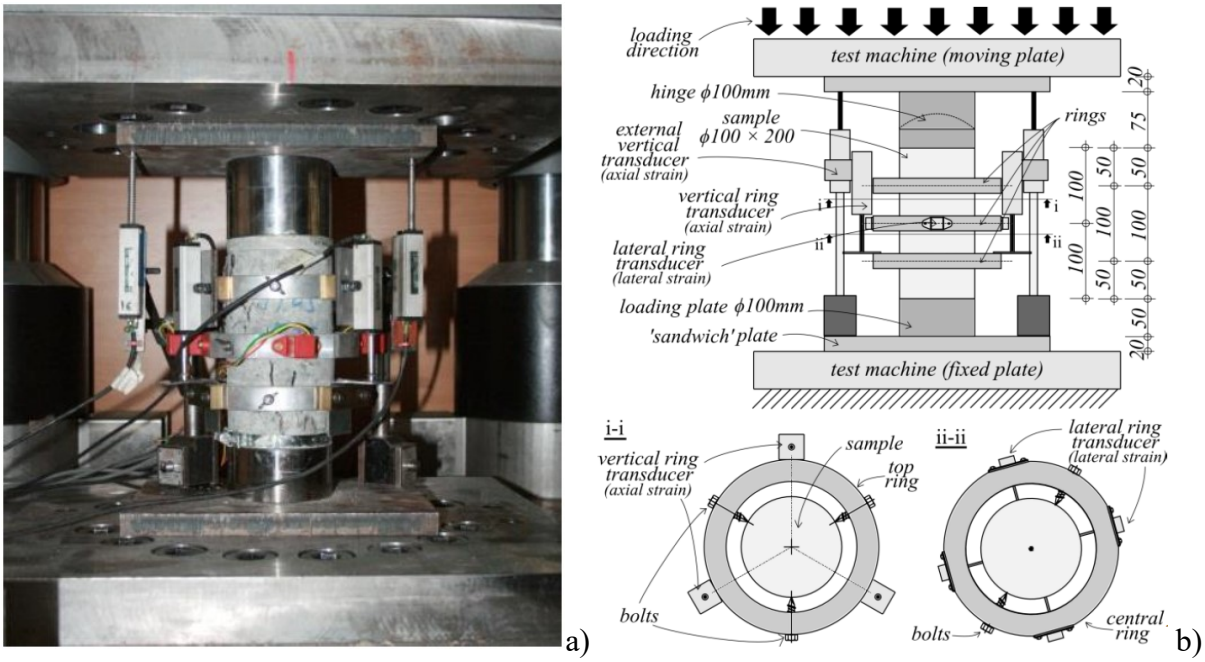


Figure 3.6 Test arrangement for cylinders a) general review, b) layout

For all cylindrical specimens tested in compression, the sample pre-peak axial behaviour was recorded using three displacement transducers attached to two steel rings positioned symmetrically around the central cross-section at a gauge length of 100 mm (Figure 3.6b). Each steel ring was connected directly to the sample through three steel bolts in order to avoid interaction with the specimen. Two other independent transducers were placed between the two sandwich plates to record the axial deformation in the post-peak regime. Test measurements were averaged and transformed into strains by using the measured gauge length for each sample. The two measurement systems were required in order to assess the complete constitutive characteristics since, in the pre-

peak range, the behaviour is governed by stable deformations, whereas in the post-peak regime the axial deformations are governed by macro-cracking which may lead to unstable measurements from the ring transducers (RILEM TC 148-SSC, van Mier et al. 1997). Lateral deformations were recorded by four transducers attached to the central steel ring located at the middle of the specimen, as illustrated in Figure 3.6b, and averaged to assess the constitutive behaviour.

On the other hand, compressive tests on cubes as shown in Figure 3.7a and splitting tests on cylinders as shown in Figure 3.7b, were carried out in force control using a 3000 kN Automax machine. The loading rate was 0.3 MPa/s (ASTM C39/C39M) and 0.01 MPa/s (ASTM C496/C496M) for the two types of tests, respectively. The force control testing machine had a top plate provided with a hinge to accommodate rotations from a potential non-symmetrical behaviour of the samples. The splitting tests were carried out in an existing testing rig positioned between the machine loading plates, specifically designed for this purpose.


a) b)

Figure 3.7 View of testing for: a) compression test on cubes, b) splitting test on cylinders

3.3 Mechanical properties of rubberised concrete

3.3.1 Pilot tests

The vibration of rubberised concrete may lead to agglomeration of rubber particles at the top of the sample. Under compressive testing, this may lead to end failure of the sample which is a characteristic of the specimen, rather than the material. An analysis of sample halves obtained from initial splitting tests (Figure 3.7b) using digital image processing techniques for examining aggregate distribution along their longitudinal cross-section show that the rubber had the tendency to lift during vibration of fresh concrete which leads to a zone of agglomeration of rubber particles at the top of the sample (Figure 3.8a). This created a weaker region, in which the strength of the material is governed by the rubber. For such cases, the end confinement is instrumental to translate the failure outside of this region. Although this effect was observed in some pilot material test samples, in large structural members (Elghazouli et al. 2017) tested recently, using rubberised concrete with 60% replacement of both fine and coarse aggregates and provided with longitudinal and transverse reinforcement, the exterior surface had a good appearance with no observed sign of segregation. In the structural members, use was made of poker vibrators after the concrete was poured in several layers to obtain the highest level of homogeneity possible. This technique may result in a better homogenization of the mix in comparison with the use of vibrating tables.

A series of pilot tests were carried out in which jubilee clips at the sample ends were used to overcome potential end failures. Additionally, a low friction bearing systems by means of polytetrafluorethylene (PTFE) sheets (RILEM TC 148-SSC), placed between the sample and loading plates, were used and compared with typical testing configurations without PTFE. Figure 3.8b depicts a comparison between four samples made of rubberised concrete with replacement ratio of ρ_{vr} = 0.6 as follows: (i) R60-00 without jubilee clips and with high friction loading system (i.e. direct contact between loading plates and sample); (ii) R60-J0 with jubilee clips and with high friction bearing system; (iii) R60-0P without jubilee clips and with low friction bearing system; and (iv) R60-JP with jubilee clips and with low friction bearing system.

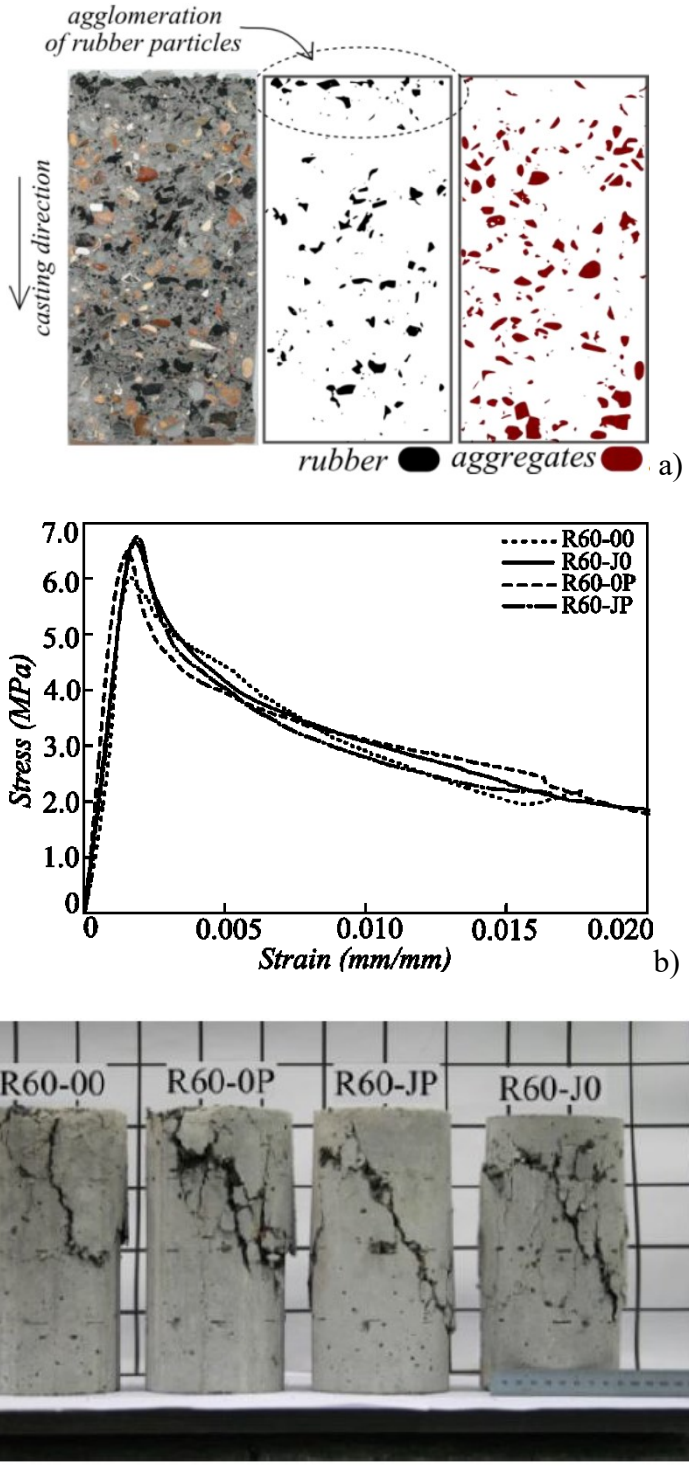


Figure 3.8 a) Longitudinal cross section through a rubberised concrete cylinder, b) Stress-strain response of pilot tests with 60% replacement, c) Failure of pilot cylindrical samples

As observed in Figure 3.8b, all cylindrical samples from the pilot tests had similar stiffness, strength and post-peak behaviour. Table 3-3 shows that the variance between recorded strengths f_{cr} and the dissipated energy G_c after crushing was minimal. On the other hand, the elastic stiffness E_{cr} and crushing strain $\varepsilon_{cr1,1}$ showed some scatter, yet within reasonable limits for such material. Close

examination of the failure pattern depicted in Figure 3.8c shows that members without jubilee clips developed end failures, whereas others had sliding failures which are typically expected for concrete specimens. This indicates that in cylindrical samples made of concrete with significant rubber content, end confinement combined with ground and capped loading surfaces are required to achieve expected failure modes under compression. Additionally, the use of low friction bearing systems had a minor influence on the stress-strain characteristics and failure mode. Consequently, the pilot tests suggested the suitability of test set-ups in which samples are provided with end confinement and connected directly to the loading plates.

Table 3-3 Results of the pilot tests

Sample	f_{cr} (MPa)	$\varepsilon_{cr1,1}$ (mm/mm)	E_{cr} (MPa)	G_c (N/mm)*
R60-00	5.97	0.00165	4208	9.8
R60-0P	6.43	0.00148	6351	10.9
R60-JP	6.62	0.00208	3855	10.2
R60-J0	6.52	0.00176	4305	10.2
Dev.	±0.28	±0.000253	±1130	±0.45

* The crushing energy G_c was calculated as the area below the post-peak stress-displacement curve as demonstrated in detail in Figure 3.10f.

3.3.2 Stress-strain response

Material characterisation tests on rubberised concrete and normal concrete cylinders were carried out to assess the influence of rubber content on the constitutive behaviour. The investigated rubber replacement ratios were 20%, 40% and 60% of the total aggregate volume, as described before. Figures 3.9a–d depict three axial and lateral stress-strain recorded test curves and their average. The stress-strain curves include both pre-peak and post-peak behaviour as recorded in the tests. The post-peak response is plotted down to 30% of the compressive strength f_{cr}. Beyond this value, an approximate response band is plotted with reference to the negative stiffness of the descending branch.

The comparative assessment of σ-ε curves from Figure 3.9a–d shows clear reductions in strength and stiffness with the increase of rubber content. The strength is approximately halved with each 20% increment increase of aggregate replacement. The compressive strength of concrete f_{cr} with $\rho_{vr} = 0.6$ (R60) is about 10% of the normal concrete R00. The elastic modulus E_c is also significantly affected with R60 exhibiting 20% of the modulus from R00. On the other hand, the reduction in the

crushing axial strain ε_{cr1} is comparatively less with about 40% reduction from R00 to R60. A stronger influence on mechanical properties is typically observed for small replacement ratios and tends to stabilise as the rubber content increases.

Beyond the peak, the stiffness response in the lateral direction, governed by the sliding behaviour of the two bodies separated by the macro-crack, flattens with the increase of rubber replacement. In addition to the interlock of mineral aggregates, this is produced by the intrinsic deformability of the interfacial clamping rubber particles which enable higher dilation of the sample at lower sliding displacements. In contrast to the average test measurements for normal concrete, in which a distinct peak lateral strain is observed as the rubber content increases, the peak lateral strain takes the form of a plateau, rather than a discrete point. On the other hand, the post-peak axial compression behaviour exhibits increased softening with the decrease in strength. Tests showed more flexible post-crushing behaviour which typically leads to similar or higher energy dissipation in the post-peak regime.

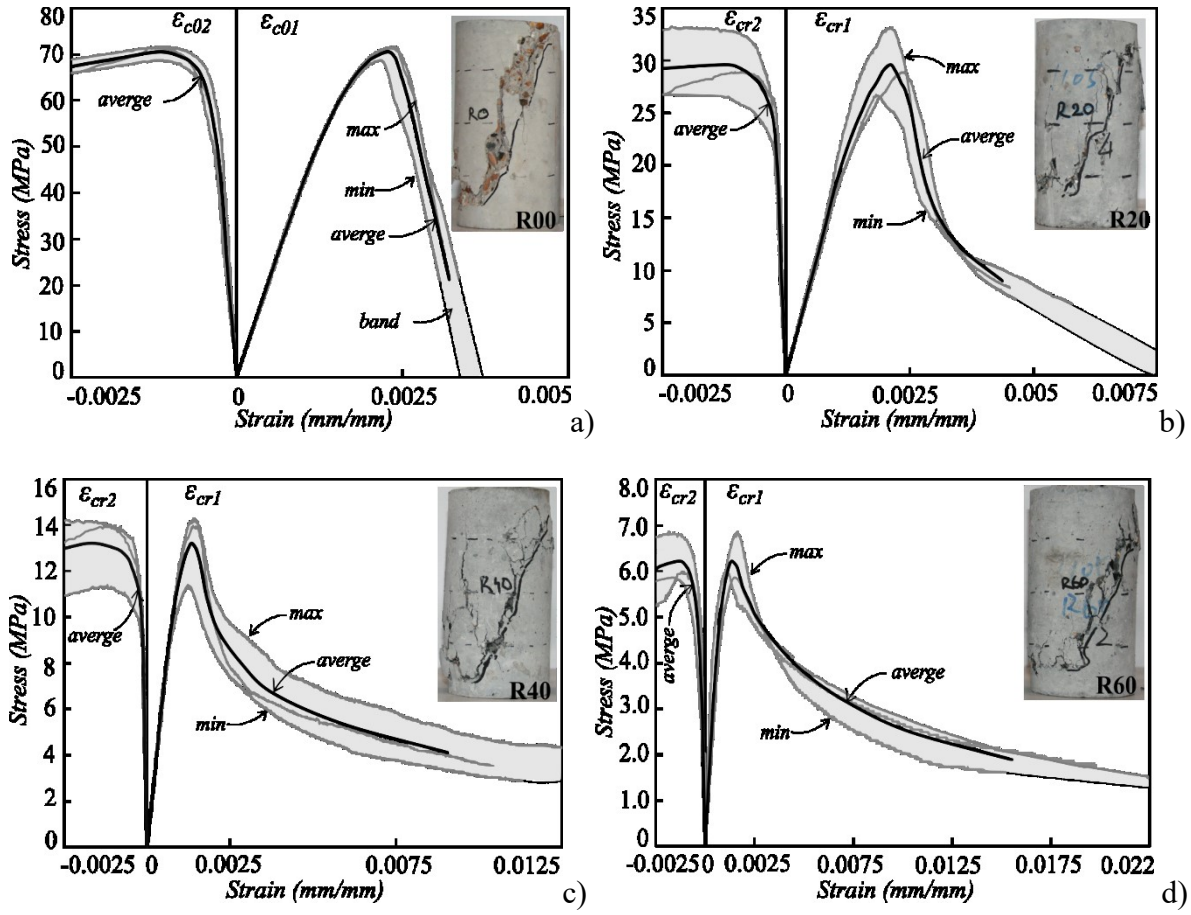


Figure 3.9 Stress-strain relationships for a) normal concrete R00, b) rubberised concrete with 20% replacement R20, c) rubberised concrete with 40% replacement R40, d) rubberised concrete with 60% replacement R60

The pre-peak behaviour of the concrete tests was strongly influenced by the rubber replacement of the mineral aggregates. As illustrated in Figure 3.9, the elastic stiffness E_{cr} degraded with the increase in rubber content. Naturally, the rubber aggregates are softer and lighter in weight compared to mineral aggregates. In this case, the matrix, comprised of binders, water and admixtures, is much stronger than the rubber aggregates but may be weaker than the mineral aggregates. Hence, for the rubberised concrete materials, the reduction in stiffness is a function of the stiffness ratio between the cement matrix and inclusions (rubber particles and voids).

Around the peak, the tangent modulus decreases to zero and crushing occurs, which is generally triggered by de-bonding of the aggregates from the cement paste. As the bond capacity of rubber particles is lower than that of mineral aggregates, this effect is activated at earlier stages (Xue and Shinozuka 2013). Tensile cracks therefore typically occur around the crack which eventually produces visible macro-cracks. At the peak, the macro-crack, in the form of the sliding crack, governs the behaviour and results in significant lateral expansion and volume increase even with an increase in axial compaction.

3.3.3 Influence of rubber content

As depicted in Figure 3.10a–c and Table 3-4, similarly to the stiffness E_{cr} degradation with rubber content as described above, test measurements of compressive strength f_{cr} and axial strain at crushing ε_{cr1} showed similar decreasing trends. For the concrete samples without rubber, the average E_{cr} for R00 = 42.3 GPa, f_{cr} for R00 = 70.2 GPa and the corresponding average ε_{cr1} for R00 = 0.228%. The average E_{cr} for samples with rubber was 19.6 GPa, 14.1 GPa and 9.03 GPa for R20, R40 and R60, respectively. The recorded f_{cr} and ε_{cr1} were 29.7 MPa and 0.213%, respectively, for 20% replaced mineral aggregates, 13.3 MPa and 0.138% for 40% replacement, and 7.06 MPa and 0.137% for the material with the highest rubber content (60%). Although an evident decrease was recorded for axial compaction, the lateral dilation in Figure 3.10d exhibited a rather constant average response for the rubberised concrete samples with lateral strains ε_{cr2} that varied between 0.12% and 0.13%. In the post-peak response, the shape of the descending branch showed flatter inclination and the ultimate recorded strain increased (at 30% of $f_{cr,Rij}$) as the rubber content increased.

In addition to the cylindrical samples used for the stress-strain assessments, 100 mm cubes were tested in compression and cylinders with 100 mm diameter were subjected to splitting (Figure 3.7a, b). This enables a direct comparison of the compressive strength loss as a function of sample type (Figure 3.10b) and provides information on the tensile strength of rubberised concrete (Figure

3.10e). Material strengths assessed on cubes are higher than the corresponding cases on cylinders. Smaller cylinder-to-cube strength ratios were obtained for rubberised concrete in comparison with typical cases of normal concrete (about 0.8 for normal strength concrete). The average cylinder-to-cube test strength $f_{cr}/f_{cr,cube}$ was 0.91, 0.58, 0.54 and 0.59 for 0%, 20%, 40% and 60% replacement, respectively. The splitting strength decreased nearly in proportion to the rubber content from 4.99 MPa for normal concrete to 1.20 for rubberised concrete with the highest amount of rubber content.

Table 3-4 Summary of test results

ρ_{vr} (-)	f_{cr} (MPa)	$f_{cr,cube}$ (MPa)	$f_{ctr,sp}$ (Mpa)	$\varepsilon_{cr1,1}$ (mm/mm)	$\varepsilon_{cr2,1}$ (mm/mm)	E_{cr} (Mpa)	G_c (N/mm)
0	70.2	77.0	4.99	0.002277	-0.00115	42302	9.13
0.20	29.7	50.7	3.12	0.002130	-0.00120	19608	7.63
0.40	13.3	24.6	1.98	0.001373	-0.00128	14124	9.86
0.60	7.06	11.8	1.20	0.001366	-0.00130	9028	10.5

The curve in the top left corner of Figure 3.10f describes the post-peak stress decrease with the increase of crushing crack displacement w_{cr} up to the test recorded residual value of $0.3f_{cr}$ and the corresponding $w_{cr,test}$. The area below the curve is referred to as the crushing energy G_c and may be defined as the energy dissipated during crushing. Based on this assumption, the test recorded stress-strain curves were analysed and the energy released during crushing was assessed. The samples with the lowest amount of rubber (ρ_{vr} = 0.2) seem to be governed by a rather brittle response in comparison to those with ρ_{vr} = 0.4–0.6. For ρ_{vr} = 0.2, the concrete seems to govern the post-crushing behaviour since the assessed energy G_c is smaller than the assessed crushing energy for R00. As shown in Figure 3.10f, for the cases with 40% and 60% replacement, the released energy increases and a more ductile response is observed, with the rubber having a significant influence on the behaviour.

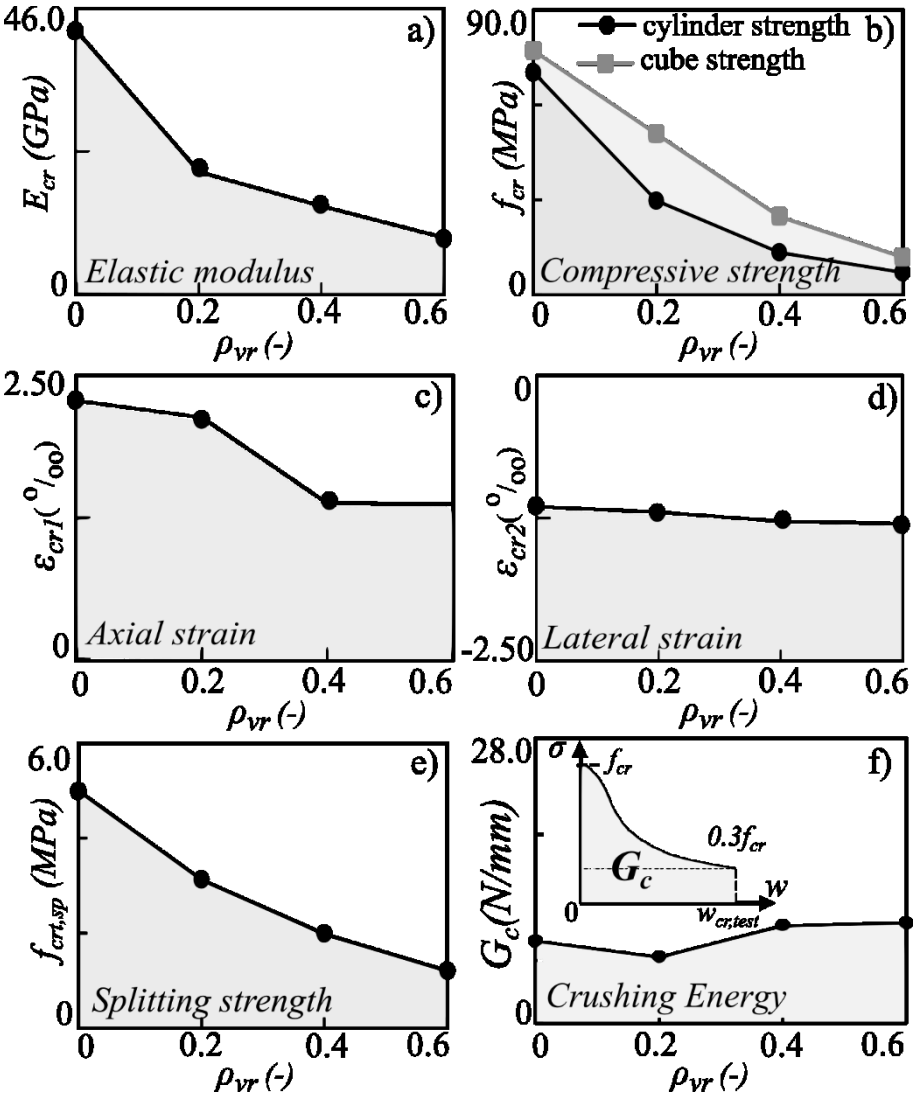


Figure 3.10 Influence of rubber content ρ_{vr} on the mechanical properties of concrete: a) elastic modulus E_{cr}, b) compressive strength f_{cr}, c) peak axial strain ε_{cr1}, d) peak lateral strain ε_{cr1}, e) splitting strength $f_{ctr,sp}$, f) crushing energy G_c

The material tests described in this section on cylinders and cubes (Figure 3.11) allowed direct assessment of the complete compressive constitutive behaviour of concrete materials with embedded rubber particles. Additional considerations regarding the strength degradation both in compression and tension were included as well as an evaluation of the energy released during crushing. Key observations from the resulting stress-strain and failure characteristics described above are used further in the following section for proposing relationships for predicting the mechanical properties of rubberised concrete material as a function of the rubber content.

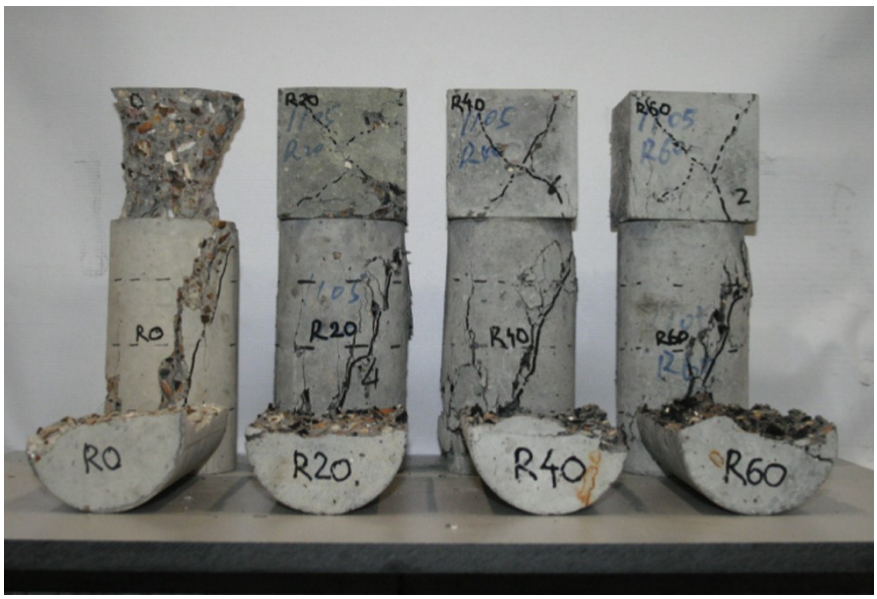


Figure 3.11 Comparative view of tested samples

3.4 Prediction of mechanical properties

In addition to the experimental results presented in Section 3.3 on the three rubberized concrete mixes and the reference normal concrete mix, the prediction equations proposed in this section incorporate an extensive database from previous studies of a further 238 concrete mixes of which 198 embed rubber particles and 40 corresponding reference ones. Thus, the entire database includes average mechanical properties from 238 concrete mixes, each determined from a minimum of three material tests, which leads to a total of over 714 samples. Expressions to assess the compressive strength, tensile strength and modulus of elasticity are proposed herein, followed in the subsequent section by suggested representations for the complete constitutive behaviour of rubberised concrete materials.

Table 3-5 Predictions of Equation 3.2

Author	n_{mixes} (-)	f_{c0} (MPa)	$\rho_{vr,min}$ (-)	$\rho_{vr,max}$ (-)	$d_{r,max}$ (mm)	$d_{g,max}$ (mm)	$f_{cr,test}/f_{cr,pred}$ (-)	
							Average	COV
Test in this research	3	70.2	0.200	0.600	14	10	1.04	0.08
Guneyisi et al. (2004)	60	61-87.9	0.025	0.500	40	20	1.05	0.08
Hernandez et al. (2002)	4	97.2	0.030	0.080	22	20	0.88	0.09
Khatib and Bayomy (1999)	8	39.6	0.025	0.500	50	20	0.78	0.17
Naito et al. (2014)	3	46.8	0.100	0.300	9.5	12	1.31	0.13
Su et al. (2015)	4	61.1	0.072	0.082	5.0	20	1.26	0.03
Xue and Shinozuka (2013)	8	38.2	0.032	0.128	6.0	12	0.91	0.11
Total (CA+FA)	90						1.03	0.1
Aiello and Leuzzi (2009)	4	27.8	0.023	0.112	20	18	0.91	0.04
Azevedo et al. (2012)	9	71.1	0.028	0.153	4.8	9.5	0.80	0.21
Bignozzi and Sandrolini (2006)	2	33.9	0.137	0.205	2.0	20	1.30	0.06
Cairns et al. (2004)	3	51.3	0.050	0.250	5.0	10	1.13	0.22
Eldin and Senouci (1993)	4	35.3	0.090	0.360	6.0	19	1.17	0.17
Ghaly and Cahill (2005)	9	12.7-27.7	0.081	0.256	2.0	20	1.05	0.07
Khatib and Bayomy (1999)	8	39.6	0.022	0.434	5.0	20	0.76	0.30
Liu et al. (2013)	3	44.5	0.015	0.045	2.0	12	0.80	0.13
Raffoul et al. (2016)	5	63.3	0.045	0.600	20	20	0.97	0.07
Taha et al. (2008)	4	27.4	0.176	0.352	20	20	1.30	0.09
Topcu (1995)	3	35.3	0.052	0.156	1.0	18	0.79	0.10
Total (FA)	54						1.00	0.13
Aiello and Leuzzi (2009)	3	47.0	0.062	0.188	20	20	0.67	0.08
Atahan and Sevim (2008)	5	38.2	0.045	0.222	-	-	0.77	0.11
Bing and Ning (2014)	8	37.6-63.5	0.156	0.622	20	20	1.40	0.14
Cairns et al. (2004)	3	51.3	0.050	0.250	5.0	10	1.06	0.13
Eldin and Senouci (1993)	4	34.9	0.160	0.640	38	25	1.10	0.12
Ganjian et al. (2009)	3	33.9	0.024	0.049	25	16	0.95	0.09
Khatib and Bayomy (1999)	8	39.6	0.028	0.566	50	20	0.50	0.20
Naito et al. (2014)	2	46.8	0.133	0.267	10	40	1.06	0.14
Taha et al. (2008)	4	27.4	0.088	0.648	20	20	1.34	0.16
Topcu (1995)	3	35.3	0.098	0.294	4.0	10	0.74	0.13
Toutanji (1996)	4	32.0	0.150	0.600	13	16	1.25	0.15
Turatsinze and Garros (2008)	4	44.1	0.102	0.254	10	19	0.76	0.15
Zheng et al. (2008)	3	56.0	0.096	0.289	32	20	1.27	0.09
Total (CA)	54						0.99	0.13

3.4.1 Compressive strength

The compressive strength assessments for mixes reported in the database and Table 3-5 were carried out on both cylinders of 100 mm × 200 mm and 150 mm × 300 mm dimensions, as well as on cubes of 50 mm, 100 mm or 150 mm sizes. Fattuhi and Clark (1996) noted however that it is difficult to make an accurate comparison between the results of various investigations on rubberised concrete since the shape and size of specimens influence the compressive strength of concrete, which is also the case for normal concrete. Due to specimen geometry, the volumetric expansion of cylinders is distinctive of a cube made of the same material resulting in dissimilar failure patterns and consequently different nominal strength.

Several previous studies dealt with size effects in concrete material testing. For example, Neville (1993) proposed conversion factors to account for the size effect in compression based on the volumetric dimensions of the samples. Mansur and Islam (2002) and Yi et al. (2006) used regression analyses to obtain correlation functions between various sample sizes and shapes. Nielsen and Hoang (2010) reported that size effects in concrete can be described by a Weibull distribution, in which the reference sample is characterised by its strength $f_{cr,ref}$ and volume $V_{cr,ref}$, and the element that requires conversion is defined by the strength $f_{cr(d)}$ and volume $V_{cr(d)}$, related through Equation (3.1) (where m = 30 for compression). To harmonize the test results in the database considered in this investigation, the compression strength results are adjusted in relation to reference cylindrical samples of 100 mm × 200 mm and a reference age of 28 days.

$$f_{cr,ref} = f_{cr(d)}(V_{cr(d)} / V_{cr,ref})^{1/m} \tag{3.1}$$

Figure 3.12 illustrates the relationship between the compressive strength degradation (CSD) as a function of rubber replacement. On the ordinate axis, the rubberised concrete strength f_{cr} is normalised against the reference strength of the conventional concrete f_{c0}, whereas on the abscissa the rubber content is reported as volumetric ratio ρ_{vr}. The volumetric ratio ρ_{vr} is the volume of rubber that replaces the mineral aggregates regardless of its size and type. The plot includes the results of the tests described in Section 3.3, used as a reference, results from the database in Table 3-5, and the exponential trend lines for the results. Close inspection of the influence of the type of rubber on the strength degradation indicates that for replacements of only coarse mineral aggregates, the scatter between results is relatively large and the database trend line deviates from the reference tests trend line. In contrast, for replacement of fine or both fine and coarse aggregates, the trends are nearly identical.

The strength of concrete is typically influenced by the cement type, water-cement ratio, mineral aggregate type, source and size, the presence of admixtures (e.g. plasticizers, retarders), the

presence of other cementitious materials (e.g. fly ash, micro-silica, metakaolin). Additionally, for rubberised concrete mixes, the rubber type, size and replacement proportions also have a significant influence on the achieved strength. A detailed examination of the results from Section 3.3, as well as from the database, show that the main parameters governing the strength of rubberised concrete are the volumetric replacement ratio, the size of replaced aggregate and size of rubber particles. It was also observed that strength degradation can be affected by the testing arrangement, control and instrumentation, which increases the uncertainty in modelling.

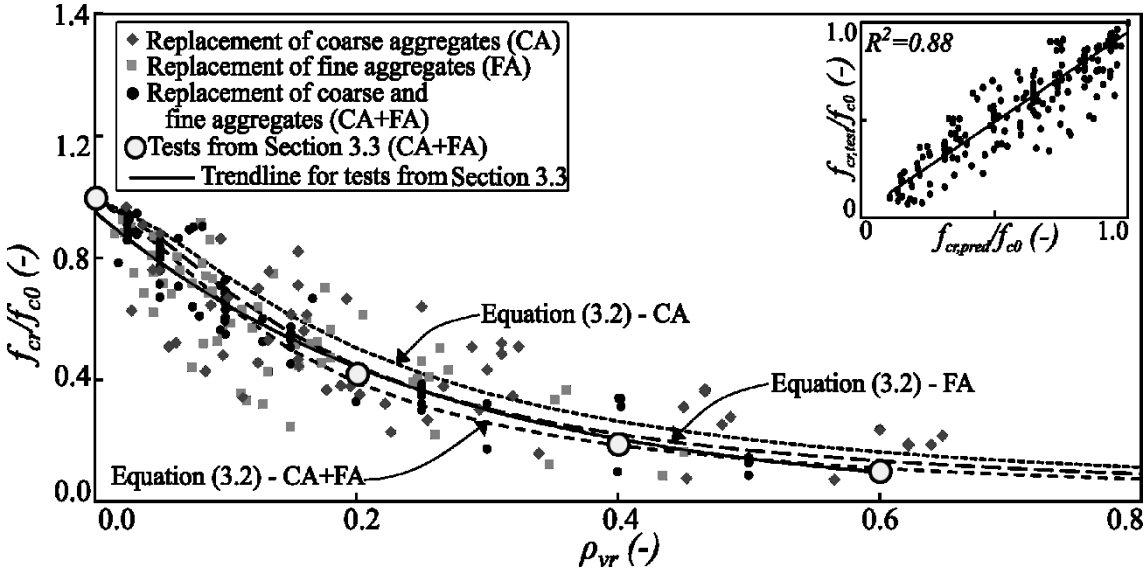


Figure 3.12 Compressive strength degradation as a function of volumetric rubber ratio ρ_{vr}

Close inspection of the database indicates that the rubber and mineral aggregate sizes have a relatively insignificant influence on strength degradation. In contrast, the volumetric rubber ratio ρ_{vr} strongly affects the compressive strength, while the type of mineral aggregate replaced also has an influence. The results for the coarse aggregate replacement also indicate a comparatively greater level of dispersion. On the other hand, no clear trend exists with regard to the influence of the aggregate size factor.

To represent the compressive strength degradation (CSD) for practical application, a parametric equation was developed. The functional form for this semi-empirical model is shown in Equation (3.2). The function passes through (ρ_{vr}, f_{c0}/f_{cr}) = 0.1, and captures the rapid reduction in strength shown by the data. The volumetric rubber ratio ρ_{vr} and the type of replaced aggregate are incorporated in the formulation. The latter is represented by a factor λ which accounts for the size range of the mineral aggregate replaced; i.e. fine (FA), coarse (CA) or coarse and fine (CA + FA).

The values for λ were inferred from the database after classifying the data into bins according to the replaced aggregate size. The λ factor was chosen separately for each type of aggregate replaced in order to obtain the best estimates for f_{cr}. Considering the 238 mixes from the database (Table 3-5), which also includes the test results from the current investigation and described in Section 3.3, Equation (3.2a) may be used for assessments of f_{cr}. As shown in Equation (3.2b), λ = 2.43 for fine mineral aggregate (FA) replacement, λ = 2.90 for both fine and coarse aggregates (CA + FA) replacement, and λ = 2.08 if rubber replaces coarse aggregates (CA).

$$f_{cr} = \frac{1}{1+2(\frac{3\lambda\rho_{vr}}{2})^{3/2}} f_{c0} \tag{3.2a}$$

where k is function of the replaced mineral aggregate size

$$\lambda = \begin{cases} 2.43 \rightarrow d_{g.repl} \in (0,5) \\ 2.90 \rightarrow d_{g.repl} \in (0, d_{g,\max}) \\ 2.08 \rightarrow d_{g.repl} \in (5, d_{g,\max}) \end{cases} \tag{3.2b}$$

The database in Table 3-5 contains rubberised concrete mixes with volumetric replacement factors ρ_{vr} up to 0.65. This is approximately equivalent to total replacement of the fine and coarse aggregates or 60% replacement of the fine and coarse aggregates. There is very limited data on mixes in which $\rho_{vr} > 0.6$, primarily since above this limit the physical characteristics are strongly governed by the rubber and because the concrete workability and slump decrease drastically (Raffoul et al. 2016). The strength results used for validation of Equation (3.2a) are average strengths on a minimum of three samples. Hence, the analytical model is validated using a minimum of 714 tests, which involve a wide range of material variations, as follows:

– Fine mineral aggregate replacement by mass up to 100% (average = 14.62%)
– Coarse mineral aggregate replacement by mass up to 100% (average = 16.27%)
– Total mineral aggregate replacement by total aggregate volume up to 64.8% (average = 16.03%)
– Average rubber size $d_{r,avg}$ = 1.05–27.5 (average = 12.6)
– Maximum rubber aggregate size $d_{r,max}$ = 50mm
– Maximum mineral aggregate size $d_{g,max}$ = 10–40 mm
– Volumetric replacement factor ρ_{vr} = 0.015–0.648
– Reference concrete compressive strength f_{c0} = 12.70 – 97.2 MPa

The results from the database and the reference results from Section 3.3 are plotted against average exponential trend lines and the proposed Equation (3.2a) accounting for λ factors from Equation (3.2b) in Figure 3.12. Table 3-5 depicts the main characteristics of the mixes used for the calibration

of Equation (3.2). For a target total average test-to-predicted strength ratio of 1.00, the coefficient of variation (COV) increases from 10.1% for CA + FA, to 12.1% for FA, and to 13.4% for CA. Although the COV for each group of mixes is rather small in the majority of the cases, low average test-to-predicted values are obtained particularly for the case of replacement with coarse aggregates CA (Table 3-5). Predictions for rubberised concrete materials in which fine aggregates (FA, CA + FA) are replaced show a more uniform response, both in terms of individual average and COV. Additionally, as observed in Figure 3.12 and Table 3-5, combined aggregate replacements may lead to an optimal mix and a more stabilised compressive behaviour in comparison with cases with only fine or coarse aggregates replaced.

As noted before, testing arrangements may also have an influence on the mechanical characteristics. For controlled set-ups in which displacement control is combined with detailed instrumentation, the predicted-to-test compressive strengths show an average of 1.04 and a COV of 0.08. Neville (1959) and Himsworth (1945) investigated the variability of concrete and its effect on mix design. They showed that higher dispersion between results is typically obtained for low concrete strengths, noting that very low COV values are attainable in well-controlled laboratory tests (~5%), with excellent results are referred to when the COV is less than 12%. The control is fair when COV is about 18% and situations of poor control are when COV values are above 25%.

Based on the database results, a relationship between the cube and cylinder strength of rubberised concrete could not be proposed since there are very few reports in which both cubes and cylinders were tested. The $f_{cr}/f_{cr,cube}$ ratios reported in Section 3.3 may be used as approximate conversion factors for rubberised concrete mixes that have very similar characteristics to those reported here.

3.4.2 Modulus of elasticity

Using available data from the tests undertaken in this study as well as those available from the database, Equation (3.3) is suggested for predicting the elastic modulus of rubberised concrete as a function of the compressive strength assessed by means of Equation (3.2).

$$E_{cr} = 12\left(\frac{f_{cr}}{10}\right)^{2/3} \text{ (GPa)} \tag{3.3}$$

Figure 3.13a depicts the relationship between f_{cr} and the E_{cr} obtained from tests using 110 concrete mixes and the tests described in Section 3.2, as well as the analytical representation of Equation (3.3). Figure 3.13b illustrates the stiffness degradation as a function of ρ_{vr}. For the validation, all tests are treated in a similar manner disregarding the type of aggregate since limited results exist for rubberised concrete materials with fine aggregate replacement. Relatively more variation is

observed in comparison with the predictions for compressive strength, with an average reported-to-predicted elastic modulus of 1.04 and an associated COV of 0.21.

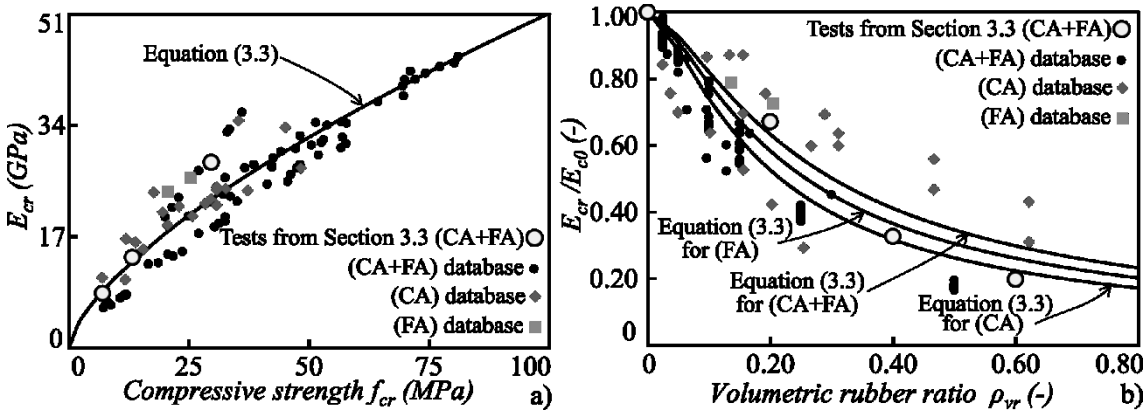


Figure 3.13 a) Relationship between modulus of elasticity E_{cr} and compressive strength f_{cr} for rubberised concrete, b) degradation of stiffness as a function of volumetric rubber ratio ρ_{vr}

3.4.3 Splitting strength

As above, a relationship between the splitting tensile strength $f_{ctr,sp}$ and rubberised concrete strength f_{cr} is suggested herein. The results from 89 rubberised concrete mixes from available databases and the test results from Section 3.3, are used in deriving Equation (3.4). Figure 3.14a illustrates the relationship between $f_{ctr,sp}$ and f_{cr}, as obtained from the test results and Equation (3.4). Figure 3.14b depicts the splitting strength $f_{ctr,sp}$ degradation as a function of ρ_{vr}. The predictions show good agreement with tests with an average test-to-predicted strength ratio of 1.01 and COV of 19%.

$$f_{ctr,sp} = 0.24 f_{cr}^{2/3} \tag{3.4}$$

To sum up, a series of expressions to predict the compressive strength f_{cr}, modulus of elasticity E_{cr} and splitting strength $f_{ctr,sp}$ of concrete materials incorporating embedded rubber particles are proposed in this section. The analytical equations are validated against the test results described in Section 3.3 and an extensive database of rubberised concrete mixes with a wide range of parameter variations. The suggested expressions account for the influence of rubber content ρ_{vr} and type of mineral aggregate replaced. They offer a reliable prediction of the basic mechanical properties and enable the development of equations to assess the full constitutive behaviour of rubberised concrete materials, as discussed in the following section.

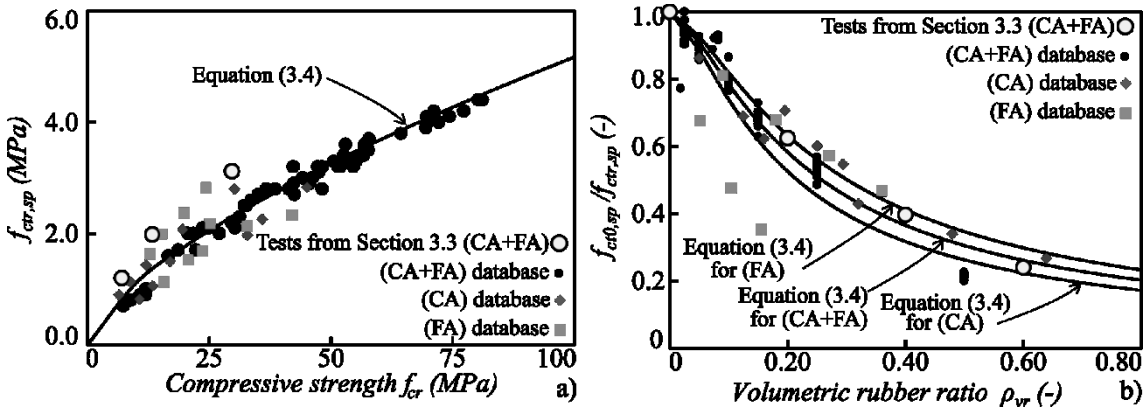


Figure 3.14 a) Relationship between splitting strength $f_{ctr,sp}$ and compressive strength f_{cr} for rubberised concrete, b) degradation of $f_{ctr,sp}$ as a function of volumetric rubber ratio ρ_{vr}

3.5 Uniaxial Unconfined constitutive relationships

3.5.1 Proposed model

Based on the test results and observations described above, this section proposes a uniaxial unconfined constitutive model for rubberised concrete materials. The model uses the equations proposed in Section 3.4 to estimate the elastic modulus E_{cr}, compressive strength f_{cr} and splitting tensile strength $f_{ctr,sp}$ as a function of the mechanical properties of the reference concrete without rubber (i.e. $\rho_{vr} = 0$). The crushing strain $\varepsilon_{cr1,1}$ of rubberised concrete is a function of the crushing strain of the reference concrete $\varepsilon_{c01,1}$, determined using Equation (3.5) (EN 1992-1-1) and ρ_{vr}. With reference to Figure 3.15, the uniaxial behaviour is divided into three stages: initial, degraded and post-crushing. In the initial stage, the material is defined by Equation (3.6) up to stress ratios below the elastic limit $\sigma/f_{cr} \leq 0.3$ (Equation (3.7)). The second stage is defined by a second degree polynomial function, depicted by Equation (3.8), which is bounded by the proportionality limit $\varepsilon_{cr1,el}$ and the crushing strain $\varepsilon_{cr1,1}$ which can be determined from Equation (3.9). The post-crushing stage (Equation (3.10)) is dependent on the post-peak crushing energy ($g_{c,2}$) in Equation (3.11), represented by a triangular distribution (Figure 3.15).

$$\varepsilon_{c01,1} = 0.7 f_{c0}^{0.31} \tag{3.5}$$

$$\sigma = E_{cr}\varepsilon_{cr1} \rightarrow \varepsilon_{cr1} \leq \varepsilon_{cr1,el} \tag{3.6}$$

$$\varepsilon_{cr1,el} = 0.3 f_{cr} / E_{cr} \tag{3.7}$$

$$\frac{\sigma}{f_{cr}} = \frac{5}{3}\left(\frac{\varepsilon_{cr1} - \varepsilon_{cr1,el}}{\varepsilon_{cr1,1}}\right) - \left(\frac{\varepsilon_{cr1} - \varepsilon_{cr1,el}}{\varepsilon_{cr1,1}}\right)^2 + \frac{0.3 f_{cr}}{f_{cr}} \rightarrow \varepsilon_{cr1} \in (\varepsilon_{cr1,el}, \varepsilon_{cr1,1}) \tag{3.8}$$

$$\varepsilon_{cr1,1} = (1 - \rho_{vr})\varepsilon_{c01,1} \tag{3.9}$$

$$\frac{\sigma}{f_{cr}} = \frac{1}{8}\left(\frac{f_{cr}}{g_{c,2}} - 1\right)^2 \left(\frac{\varepsilon_{cr1} - \varepsilon_{cr1,1}}{\varepsilon_{cr1,1}}\right)^2 - \frac{6}{8}\left(\frac{f_{cr}}{g_{c,2}} - 1\right)\left(\frac{\varepsilon_{cr1} - \varepsilon_{cr1,1}}{\varepsilon_{cr1,1}}\right) + \frac{f_{cr,2}}{f_{cr}} \rightarrow \varepsilon_{cr1} \geq \varepsilon_{cr1,1} \tag{3.10a}$$

where $$\frac{f_{cr,2}}{f_{cr}} = \frac{5}{3}\left(\frac{\varepsilon_{cr1,1} - \varepsilon_{cr1,el}}{\varepsilon_{cr1,1}}\right) - \left(\frac{\varepsilon_{cr1,1} - \varepsilon_{cr1,el}}{\varepsilon_{cr1,1}}\right)^2 + \frac{0.3 f_{cr}}{f_{cr}} \tag{3.10b}$$

$$g_{c,2} = [(1 + \rho_{vr}) f_{cr}]^{2/3} \tag{3.11}$$

The lateral strain ε_{cr2} is a function of the axial strain ε_{cr1}, stress ratio σ/f_{cr} and ρ_{vr}. It is assumed that prior to crushing ε_{cr2} follows a bi-linear representation depicted by two regimes as a function of the volumetric rubber ratio. Assessment of lateral response requires the uniaxial σ-ε relationship (Equation (3.6) – (3.11)) and the lateral strain at crushing $\varepsilon_{cr2,1}$. Based on results and observations from Section 3.3, $\varepsilon_{cr2,1}$ corresponding to the crushing strain of rubberised concrete $\varepsilon_{cr1,1}$ can be estimated by Equation (3.12).

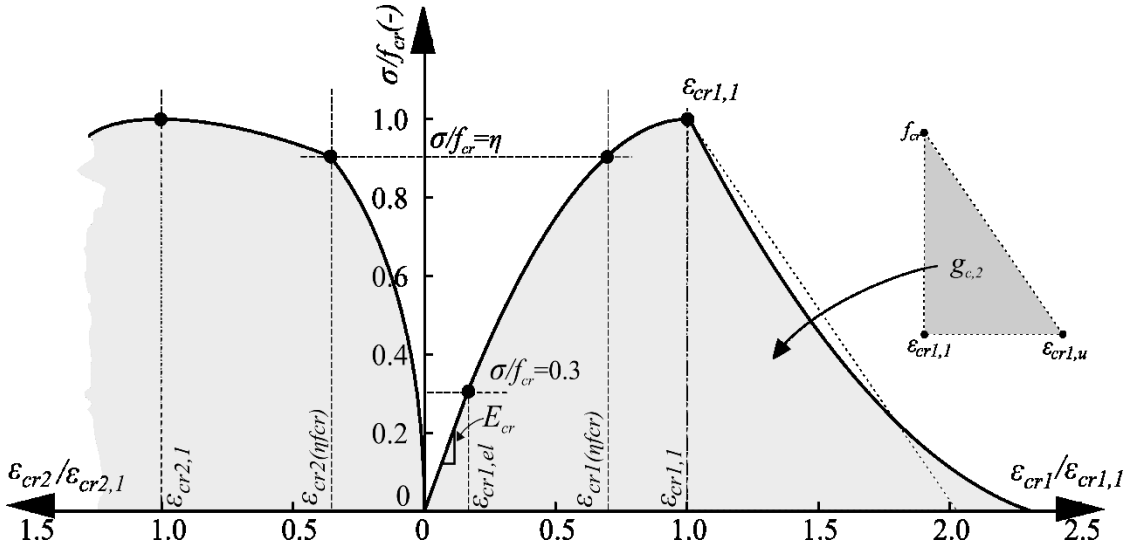


Figure 3.15 Uniaxial constitutive model for rubberised concrete

Figure 3.16 depicts the relationship between the stress factor σ/f_{cr} and the strain ratio $\varepsilon_{cr1}/\varepsilon_{cr2}$ as obtained from the tests. It can be observed that as the rubber content increases, the curve becomes softer, in a bi-linear representation; the slope change occurs at lower axial stress levels for high rubber replacements. This shows that the lateral-to-axial deformation behaviour is strongly governed by rubber deformation. In the analytical approach, this aspect is captured by Equation (3.13) which may be used to estimate the axial stress ratio η at which the lateral behaviour starts to be governed by the rubber. Up to η, the lateral strain may be assessed using Equation (3.14), and beyond η it can be estimated through Equation (3.15). Beyond crushing, the lateral response of

rubberised concrete is a function solely of the axial stress ratio (Equation (3.16)). The proposed equations predict the σ-ε response in absolute values.

$$\varepsilon_{cr2,1} = \frac{4}{3(1-\rho_{vr})}\varepsilon_{cr1,1} \tag{3.12}$$

$$\eta = 1-3\rho_{vr}^2/2 \tag{3.13}$$

$$\frac{\varepsilon_{cr2}}{\varepsilon_{cr1}} = (\frac{\sigma}{f_{cr}})\frac{1}{3(\rho_{vr}^2+1)} \rightarrow 0 \geq \varepsilon_{cr1} > \varepsilon_{cr1(\eta f_{cr})} \tag{3.14}$$

$$\frac{\varepsilon_{cr2}}{\varepsilon_{cr1}} = (\frac{\sigma}{f_{cr}})\frac{4}{3(1-\rho_{vr}^3)} + \varepsilon_{cr2(\eta f_{cr})} \rightarrow \varepsilon_{cr1(\eta f_{cr})} \geq \varepsilon_{cr1} > \varepsilon_{cr1,1} \tag{3.15a}$$

where $\varepsilon_{cr2(\eta f_{cr})} = \eta\frac{\varepsilon_{cr1(\eta f_{cr})}}{3(\rho_{vr}^2+1)}$ (3.15b)

$$\frac{\varepsilon_{cr2}}{\varepsilon_{cr1}} = 10(1-\frac{\sigma}{f_{cr}}) \rightarrow \varepsilon_{cr1} \geq \varepsilon_{cr1,1} \tag{3.16}$$

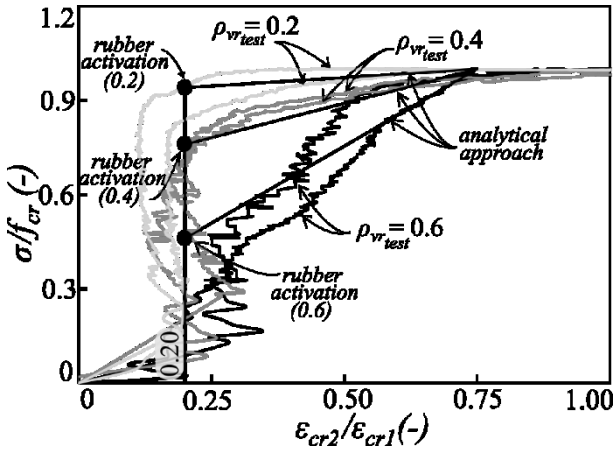


Figure 3.16 Relationship between stress ratio and lateral-to-axial strain ratio

Direct uniaxial tensile tests on rubberised concrete are lacking, and existing information about tensile behaviour is derived from indirect splitting or flexural tensile tests. The database of tests described in Section 3.4 as well as tests carried out in this study were employed to assess the splitting strength (Equation (3.4)) of rubberised concrete as a function of the compressive rubberised concrete strength (Equation (3.2)). Although the exact ratio between the tensile and splitting strength of rubberised concrete may differ, Equations (3.17a) and (3.17b) (Model Code 2010) can be further used for assessing the tensile strength. The tension behaviour before cracking can be accounted for by assuming the elastic stiffness determined using Equation (3.3).

$$f_{ctr,sp} = 0.9 f_{ctr} \tag{3.17a}$$

$$f_{ctr} = 0.26 f_{cr}^{2/3} \tag{3.17b}$$

Limited research currently exists regarding the post-cracking response of members provided with rubber particles. The maximum crack mouth opening as directly reported in the literature, or determined by means of rigid plastic assumptions on tests reported by Liu et al. (2013), Toutanji (1996) and Turtansize and Garros (2008), indicate values below those reported for normal concrete which vary between 160 and 180 μm (Reinhardt and Cornelissen 1986). In the tests carried out by Taha (2008) as well as Najim and Hall (2013) on 13 mixes with replacement ratios ρ_{vr} of 0–0.65, the maximum crack displacement $w_{max,r}$ varied between 144 and 366 μm (Figure 3.17a), with an average of 229 μm. Accounting for a linear relationship between ρ_{vr} and $w_{max,r}$, the latter can be estimated by Equation (3.18) as a function of the base maximum crack width ($w_{max,0}$ = 180 μm for $\rho_{vr} = 0$).

$$w_{\max,r} = w_{\max,0} + 0.3\rho_{vr} \tag{3.18a}$$

$$w_{\max,0} = 0.18\,\text{mm} \tag{3.18b}$$

For simplicity, as illustrated in Figure 3.17b, a bi-linear tensile stress-strain diagram may be assumed. Alternatively, an exponential representation (Hordijk 1992) can also be employed on the condition that the fitting parameters of the model are used in order to obtain the lowest bound of G_f.

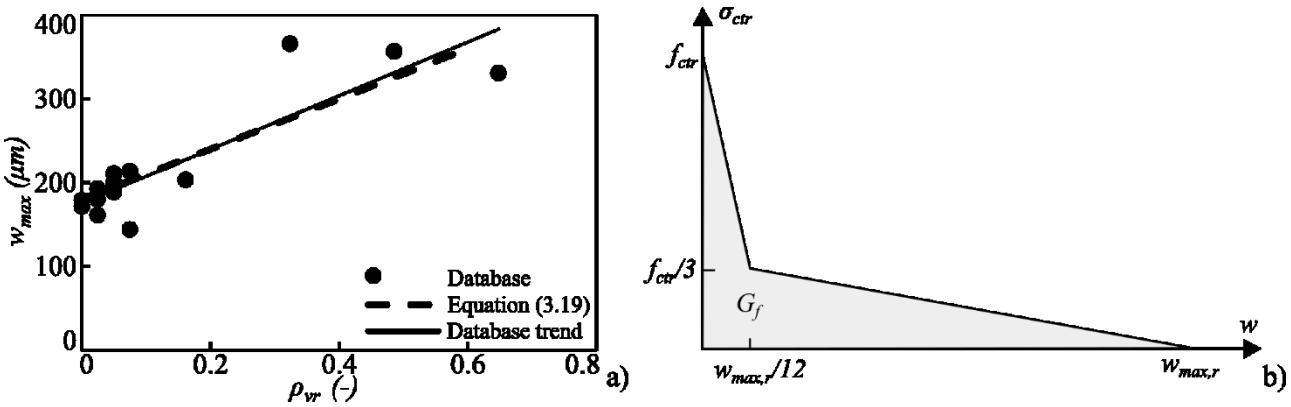


Figure 3.17 a) Relationship between maximum crack width and rubber content, b) assumed stress-strain diagram in tension

3.5.2 Validation against test results

Figure 3.18 depicts the predicted compressive constitutive behaviour using Equation (3.5–3.16) against the stress-strain relationships obtained from the tests described in Section 3.3. The comparative assessment between predicted and experimental constitutive response shows good

agreement. For the case without rubber, the crushing strain $\varepsilon_{cr1,1}$ corresponds to the crushing strain of normal concrete $\varepsilon_{c01,1}$ as determined from Equation (3.5) (EN 1992-1-1) since $\rho_{vr} = 0$. This illustrates a rather flexible response in comparison with that obtained from tests, and a lower compressive strength f_{cr} since the polynomial coefficients in Equation (3.10) were selected to predict a lower bound value.

For the case with low rubber content ($\rho_{vr} = 0.2$), the predicted response corresponds to the lower bound of σ-ε curves from tests. Although the predicted compressive strength shows the highest variance with respect to the test average, both the lateral and axial strains exhibit the best estimates in comparison with the average strain from the tests. For higher amounts of rubber ($\rho_{vr} = 0.4$–0.6), the predicted constitutive response is similar to that assessed from experimental results in terms of stiffness, strength and strains. Additionally, the assumptions regarding the amount of energy dissipated in the post-peak regime lead to good estimates of the descending branch for all the cases investigated.

The results from Equation (3.6–3.18) show a test-to-predicted compressive strength average of 1.04 and a COV of 6.7%, whereas the average ratio for axial crushing strains is 1.00 with a COV of 17.6%, and the average ratio between lateral strains at crushing is 1.11 with a COV of 18.5%. The predictions in Figure 3.18, combined with previous statistical results, show that the proposed uniaxial constitutive model may be used to assess the detailed characteristic behaviour of concrete materials incorporating rubber particles. The above-proposed model offers a reliable and practical approach, in terms of determining the target mechanical properties of rubberised concrete for analysis and design purposes, as well as for detailed assessments of axial and lateral stress-strain responses.

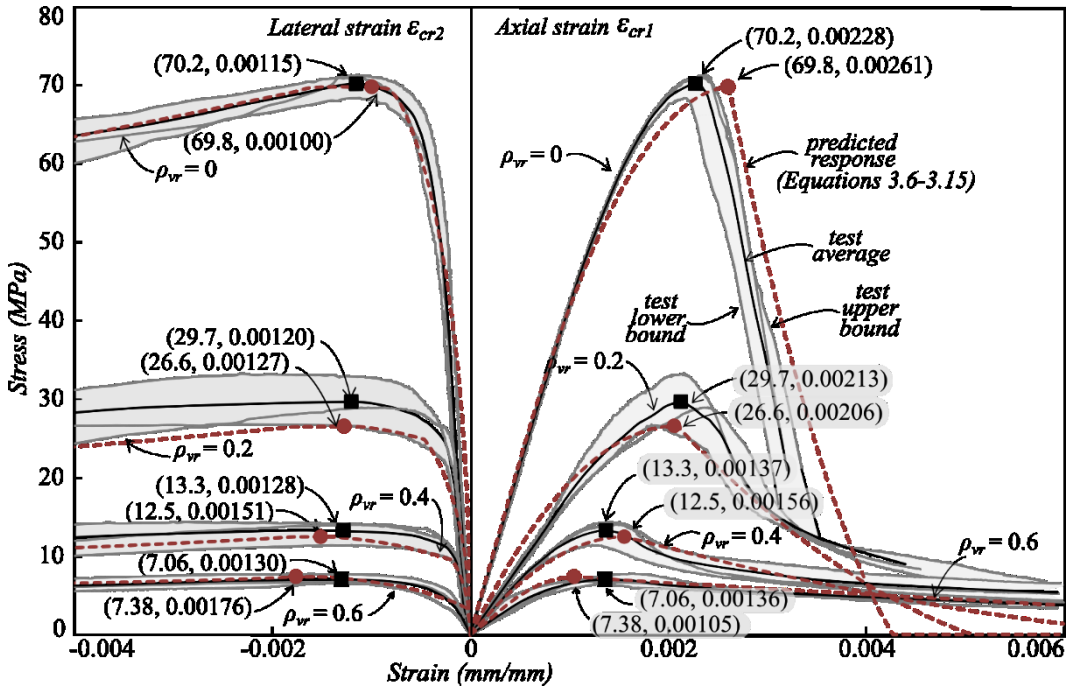


Figure 3.18 Comparison between test and predicted stress-strain responses (black and red curves represent experimental and predicted response, respectively)

Figure 3.19 plots a comparison between the Eurocode 2 stress-strain σ-ε relationship for non-linear analysis against predicted responses for ρ_{vr} = 0 and f_{c0} = 50 MPa from Equation (3.5–3.11) by accounting for four cases at which Equation (3.10a,b) activates at a fraction of the crushing strain $\varepsilon_{c01,1}$. It may be observed that the elastic E_{cr} and secant stiffness, crushing strain $\varepsilon_{c01,1}$ and compressive strength f_{c0} show a close match with the Eurocode 2 σ-ε relationship. It is also worth noting that Equation (3.8) in this chapter, which predicts the compressive behaviour between $0.3f_{cr}$ and $1.0f_{cr}$, also shows good agreement with the Eurocode 2 in the post-peak branch if Equation (3.10a,b) is activated for stages beyond $\varepsilon_{c01,1}$. However, to obtain a lower bound of the crushing energy and as well as a close σ-ε response for high strength concrete (ρ_{vr} = 0) in the predictions of the model from Figure 3.18, the activation of Equation (3.10 a,b) begins at $\varepsilon_{c01,1}$ for normal concrete and at $\varepsilon_{cr1,1}$ for rubberised concrete.

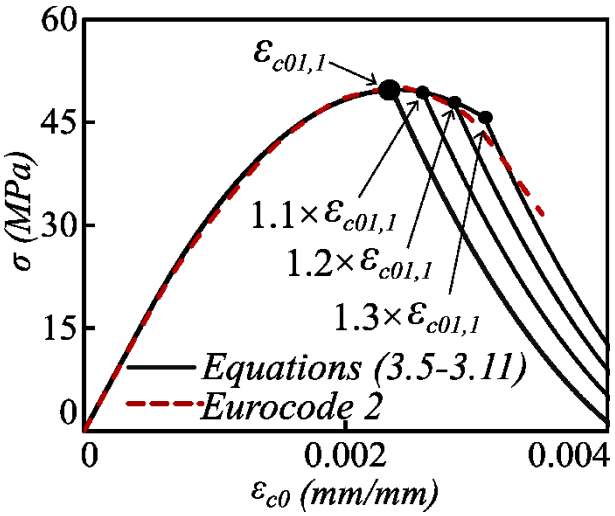


Figure 3.19 Comparison between stress-strain responses predicted by EC2 and the proposed model

3.6 Effect of AFRP confinement

3.6.1 Stress-strain behaviour of confined tests

As introduced in Section 3.2, 14×100 mm×200 mm cylindrical specimens, with rubber replacement ratio of 0, 45% and 60%, were wrapped with 2-3 layers of AFRP jackets. In total, 2 normal concrete specimens were wrapped with 2 layers of AFRP jackets (R00F2), as well as 3 rubberised concrete specimens with 45% rubber contents (R45F2) and 2 specimens with 60% rubber replacement (R60F2). An additional 7 specimens with 60% rubber contents were wrapped with 3 layers of AFRP (R60F3). The tests were performed using the same "sandwich" setup as introduced in Section 3.2 under a displacement rate of 0.5mm/min.

The failure modes of all specimens are demonstrated in Figure 3.20. The failure mode of AFRP confined specimens was dominated by rupture of the jackets around mid-height followed by the jacket de-bonding at the overlapping area due to the lateral expansion of the specimen. One of the specimens (R00F3-1) failed by disconnection between the AFRP layers due to bond failure between AFRP sheets and concrete while R40F2-2 crushed at the top of the cylinder as the end jubilee clip was ruptured during the test; therefore, these two tests showed relatively low compression and deformation capacities.

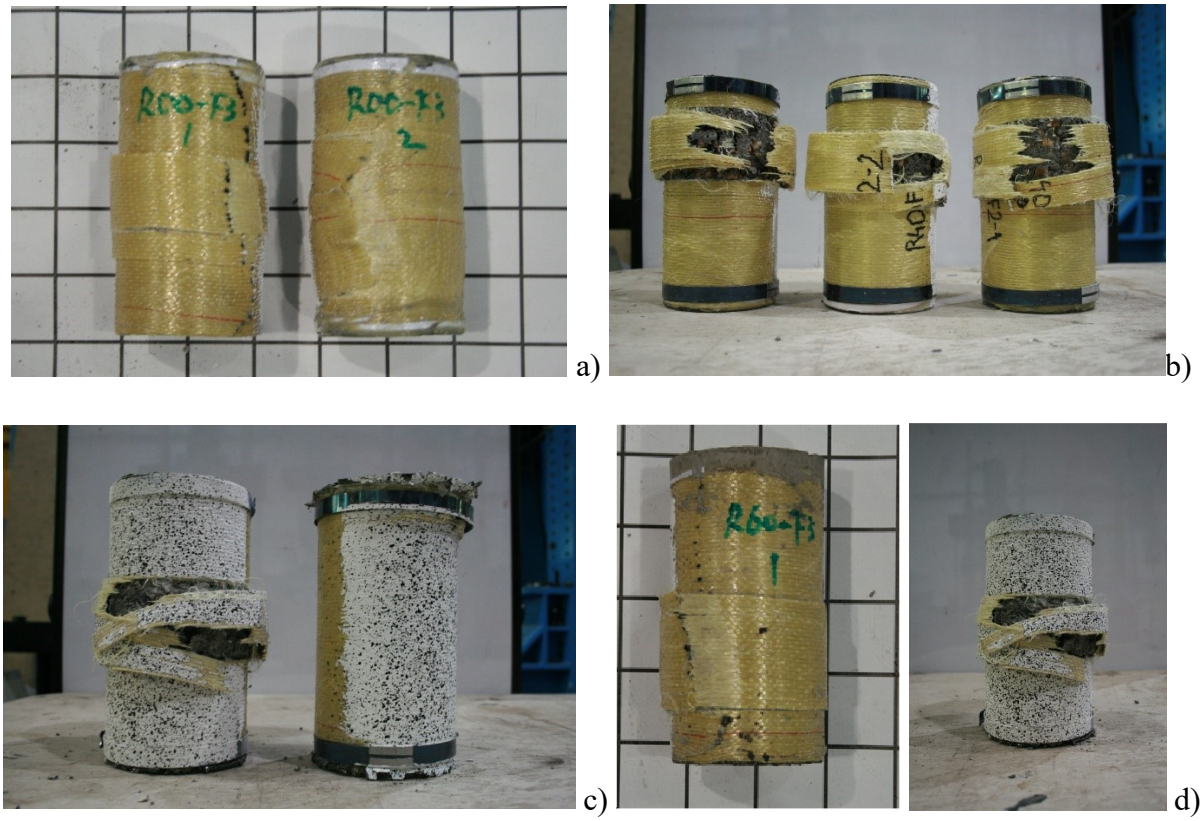
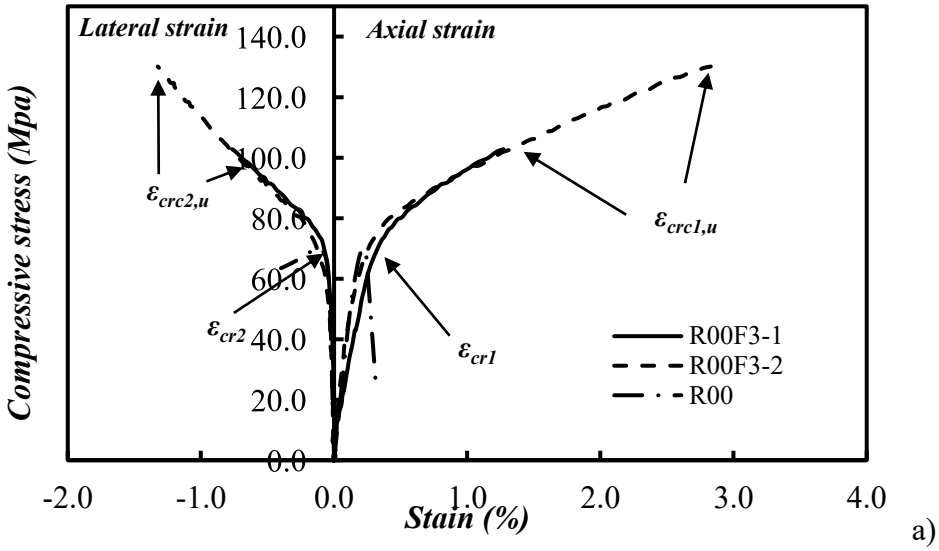
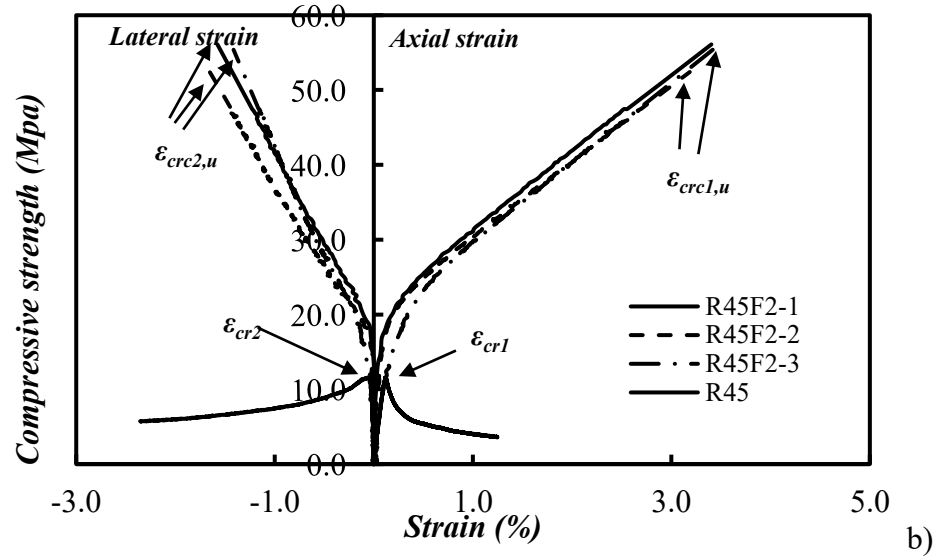


Figure 3.20 Typical failure modes of confined rubberised concrete specimens: a) R00F3, b) R40F2, c) R60F2, d) R60F3

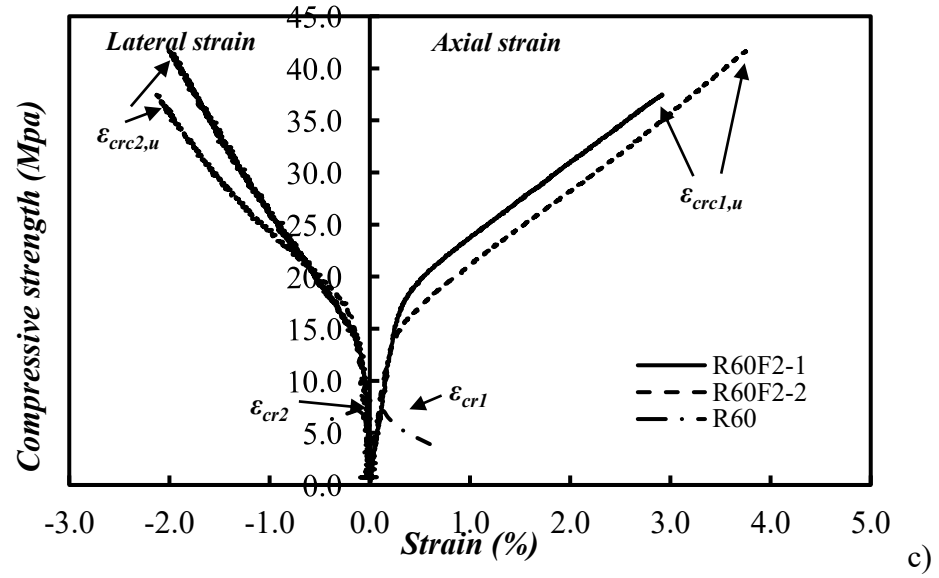
The stress-strain curves of all specimens are shown in Figure 3.21. All specimens experienced typical bilinear stress-strain behaviour with two independent slopes (E_{c1}, E_{c2}) in addition with a transition zone. It is clear that the slope of the initial linear elastic parts (E_{c1}) for the confined concrete specimens show no difference from the reference unconfined cylinders which indicates that the initial linear section is controlled by the unconfined behaviour of concrete. Due to the passive confinement nature of FRP jackets used herein, the external confinement needs to be activated under sufficient deformation, hence the stress-strain behaviour of confined concrete is controlled by the unconfined material under low level of axial loads. The nonlinear transition zone following the first linear section indicates the interaction between concrete and confinement jackets. The lateral expansion of concrete activates the external confinement followed by the second linear part until the rupture of confinement jackets. The concrete part is progressively crushed during this period which contributes to the lateral expansion of the AFRP jacket hence the effectiveness of the confinement is enhanced.



a)



b)



c)

Figure 3.21 Compression test stress-strain behaviour for AFRP confined and unconfined concrete specimens: a) R00F3, b) R40F2, c) R60F2, d) R60F3 (continued)

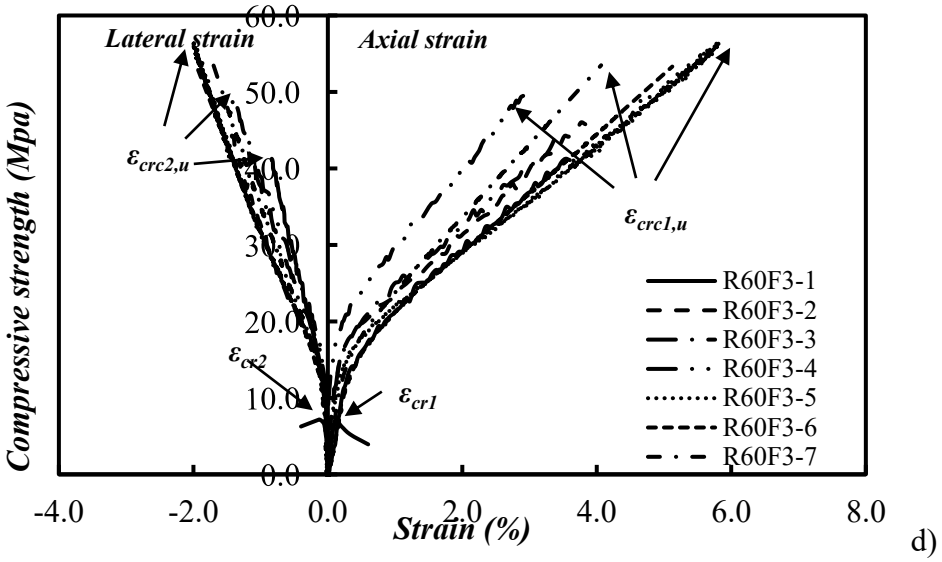


Figure 3.21 Compression test stress-strain behaviour for AFRP confined and unconfined concrete specimens: a) R00F3, b) R40F2, c) R60F2, d) R60F3

3.6.2 Influence of AFRP jacket on the mechanical properties

The specimen details and test results as well as the corresponding unconfined concrete strengths are listed in Table 3-6. The ultimate strengths of the specimens were significantly increased by the external confinement. Although the confined concrete specimens showed explosive type failure at the ultimate state, showing a sudden loss of loading capacity, the ultimate axial and lateral deformations (strains) of these specimens were also enhanced. Normal concrete specimens with 3 layers of AFRP jackets (R00F3) failed at an average ultimate strength of f_{crc}=116.5 MPa with axial ultimate strain of $\varepsilon_{crc1,u}$=0.02051 and lateral strain of $\varepsilon_{crc2,u}$=-0.01044. Compared to the reference unconfined concrete specimens, the peak strength was increased by 166%. R45F2 specimens failed at the peak strength of f_{crc}=54.6 MPa and strains of $\varepsilon_{crc1,u}$=0.04258, $\varepsilon_{crc2,u}$=0.01548. The ultimate state of R60F2 specimens corresponded to f_{crc}=39.6 MPa and $\varepsilon_{crc1,u}$=0.03563, $\varepsilon_{crc2,u}$=0.02060 while R60F3 specimens failed at a slightly higher strength of f_{crc}=49.2 MPa with the similar strain levels of $\varepsilon_{crc1,u}$=0.03663, $\varepsilon_{crc2,u}$=0.01508. The strength enhancement of R45F2, R60F2 and R60F3 specimens compared to the corresponding unconfined concrete with the same rubber content were 476%, 60% and 625%, respectively.

Table 3-6 AFRP confined test results

No.	ρ_{vr} (-)	n_{frp} (-)	t_{frp} (mm)	f_{cr} (MPa)	f_{crc} (MPa)	f_l/f_{cr} (-)	$\varepsilon_{cr1,u}$ (mm/mm)	$\varepsilon_{cr2,u}$ (mm/mm)	E_{c1} (Mpa)	E_{c2} (Mpa)	f_{crc} / f_{cr} (-)
R00F3-1	0	2	0.4	70.2	102.8	0.27	0.01272	-0.00764	43685	2630	1.46
R00F3-2					130.1		0.02829	-0.01324	49789	1930	1.85
Ave.					116.5		0.02051	-0.01044	46737	2280	1.66
Dev.					19.3		0.01101	0.00396	4316	495	0.28
R45F2-1	0.45	2	0.4	11.5	56.1	1.67	0.03402	-0.01577	15483	1033	4.88
R45F2-2					52.4		0.03185	-0.01654	15802	1000	4.57
R45F2-3					55.4		0.03416	-0.01414	15774	1064	4.82
Ave.					54.6		0.03334	-0.01548	15686	1032	4.76
Dev.					2.0		0.00130	0.00123	177	32	0.16
R60F2-1	0.60	2	0.4	7.06	37.5	2.72	0.03445	-0.02138	6230	716	5.31
R60F2-2					41.6		0.03765	-0.01982	6698	751	5.89
Ave.					39.6		0.03765	-0.02060	6464	734	5.60
Dev.					2.9		0.00226	0.00110	331	25	0.41
R60F3-1	0.60	3	0.6	7.87	56.9	3.66	0.05821	-0.01995	7352	730	7.23
R60F3-2					53.3		0.02122	-0.01948	3577	774	6.77
R60F3-3					53.5		0.04064	-0.01701	6957	970	6.80
R60F3-4					41.3		0.03597	-0.00834	4590	710	5.25
R60F3-5					46.0		0.03768	-0.01448	12180	780	5.84
R60F3-6					43.7		0.03362	-0.01188	11050	820	5.55
R60F3-7					49.5		0.02905	-0.01443	50690	3930	6.29
Ave.					49.2		0.03663	-0.01621	7618	797	6.25
Dev.					5.7		0.01145	0.00415	3423	1187	0.73

Considering the two factors (rubber content ρ_{vr} and number of AFRP layers n_{frp}) influencing the mechanical properties of confined rubberised concrete, the term of nominal confinement ratio (f_l/f_{cr}) is used to perform the comparative assessment. As noted before in Chapter 2, the lateral confining pressure f_l is defined as

$$f_l = \frac{2E_f t_f \varepsilon_{fu}}{D} \tag{3.19}$$

where E_f, t_f and ε_{fu} stand for the elastic modulus (E_f=116000 MPa), thickness and ultimate strain (ε_{fu} =0.02 mm/mm) of external confinement, while D indicates the diameter of the concrete specimen.

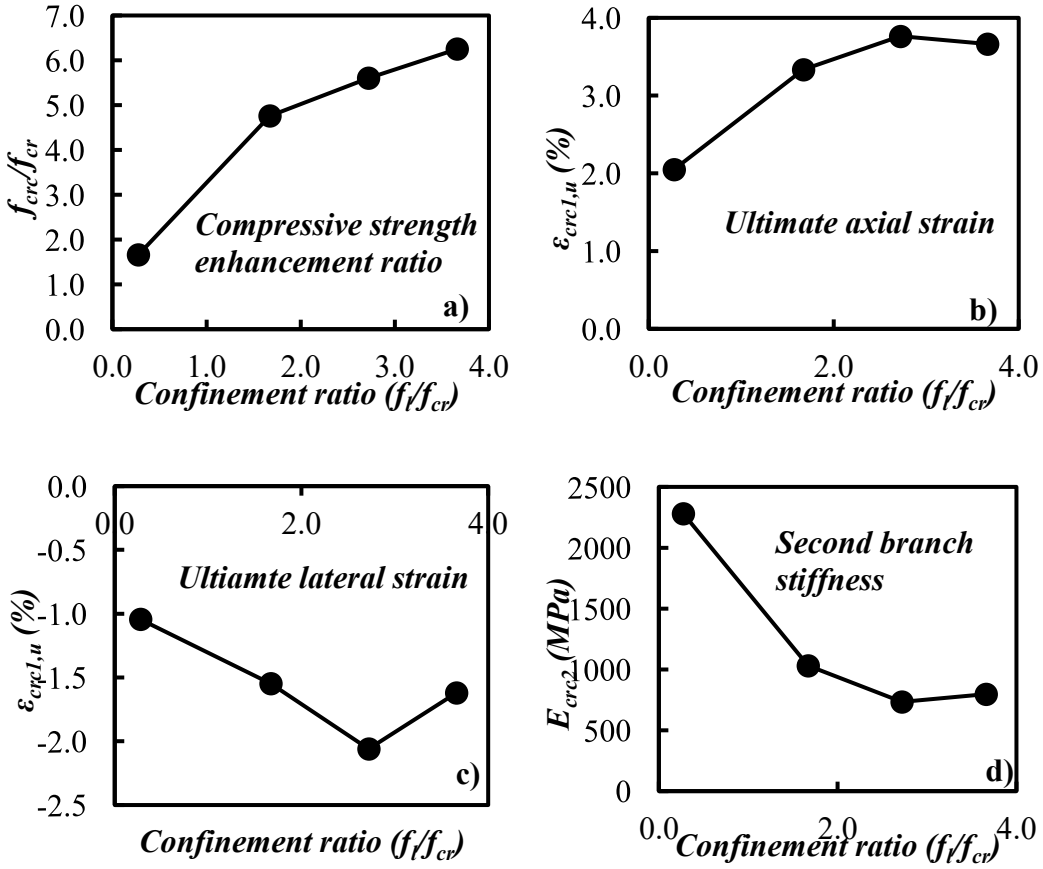


Figure 3.22 Influence of confinement ratio f_l/f_{cr} on the mechanical properties of confined rubberised concrete: a) compressive strength f_{crc}, b) ultimate axial strain $\varepsilon_{crc1,u}$, c) ultimate lateral strain $\varepsilon_{crc2,u}$, d) stiffness of second linear branch E_{crc2}

It is evident that with the increase of confinement ratio, the compressive strength enhancement ratio is increased significantly (Figure 3.22a). Figures 3.22b, c illustrate the influence of confinement ratio on the deformation capacity. Generally, both axial and lateral ultimate strains increase with the

confinement ratio. In the case of R60F3, nevertheless, the specimens fail at lower axial and lateral strains. In this case, the inner rubberised concrete failed at a relatively early stage due to its low strength as the load resistance and ductility rely more on the lateral expansion of AFRP confinement. The bond failure between AFRP sheets played an important role at the ultimate state, hence the stiffness of R60F3 specimens failed with relatively lower deformation. Consequently, the bond properties as well as the specimen preparation process can have a more significant influence on the failure state of the specimens. It can be noted from Figure 3.22d that E_{c2} decreases significantly with the increase of the confinement ratio (f_l/f_{cr}). The initial strength and stiffness of the concrete core decreases with the increase of rubber content which contributes to the reduction in E_{c2}. On the other hand, the stiffness of R60F3 specimens are higher than of R60F2 which indicates that the material stiffness of the second linear stress-strain branch is controlled by the combination of both the concrete core and external confinement.

The tests indicated that using AFRP jackets is an effective way for providing external confinement in terms of enhancing the strength and ductility of rubberised concrete. In addition to the uniaxial compression tests described in this chapter, AFRP sheets were chosen for external confinement for the shear and beam-column member tests described in Chapter 4-6.

3.7 Concluding remarks

The tests described in this chapter focused on examining the uniaxial behaviour of concrete materials incorporating rubber particles obtained from recycled end-of-life tyres as replacement of mineral aggregates. A detailed account of a set of 110 material tests, including experimental assessments of the complete stress-strain response of rubberised concrete carried out on cylindrical samples, was presented. The main parameter investigated in the tests was the rubber replacement ratio for both fine and coarse mineral aggregates in equal volumes by rubber particles with various sizes. Moreover, 14 AFRP confined cylindrical specimens with different rubber content and aramid sheets were prepared for the investigation of uniaxial behaviour of confined rubberised concrete. Additionally, a detailed analysis of a database on average test results from 238 rubberised concrete mixes and their reference concrete mixes, including tests undertaken in this study, was carried out. The test results and observations described in this chapter enabled the definition of a series of prediction expressions to estimate the mechanical properties of rubberised concrete materials as well as the development of an analytical model for detailed assessment of the complete stress-strain response of the material as a function of its volumetric rubber ratio. The experimental and analytical investigations in this chapter, allow the following key observations to be highlighted:

- The experimental results showed that the rubber particles influenced the mechanical properties as a direct function of the volume of the mineral aggregates replaced. Additionally, the database analysis showed that, besides the volumetric replacement ratio, the type of mineral aggregate replaced also affects the behaviour, with relatively less influence from the type and characteristics of the rubber added.
- Uniaxial compression tests, carried out on cylindrical samples to assess the complete stress-strain response, showed that the compressive strength, elastic modulus, and crushing strain decrease with the increase in rubber content. On the other hand, the lateral strain at crushing and the energy released during crushing is enhanced due to the presence of rubber.
- The tests showed that the reduction in elastic stiffness is mainly a consequence of the flexibility and light weight of rubber aggregates in comparison with mineral aggregates. The presence of rubber particles with inherently low bond capacity leads to premature crushing, in comparison with normal concrete, as a function of the rubber content. This initiates tensile cracks within the material that eventually leads to a sliding macrocrack which produces large lateral expansion and volume increase.
- Beyond peak, the stiffness response in the lateral direction, governed by the sliding behaviour of the two bodies separated by the macro-crack, flattens with the increase of rubber content due to the intrinsic deformability of the interfacial clamping rubber particles which enables higher dilation of the sample at lower sliding displacements. The experimental response typically exhibited more flexible post-crushing behaviour and similar or higher energy dissipated in the post-peak regime.
- The proposed expressions for estimating the mechanical properties, which have been validated using an extensive database of 198 rubberised concrete mixes, offer significant improvements for design purposes in comparison with existing analytical models. Existing strength prediction relationships have only been validated for a limited number of concrete mixes incorporating similar rubber particle sizes and types of mineral aggregate replaced.
- A novel uniaxial constitutive analytical model for rubberized concrete is proposed and validated against the test results carried out within this study. The model provides a reliable representation, which has been lacking to date, for assessing the complete axial and lateral stress-strain response for rubberized concrete.
- The compression tests carried out on AFRP confined conventional and rubberised concrete showed that the external confinement significantly enhanced the compressive strength and axial deformation capacity with the increase of confinement ratio. On the other hand, this

enhancement also relies on the manufacturing process which can influence the bond properties between the confinement and concrete hence the mechanical behaviour of test specimens.

- The AFRP confined concrete specimens showed typical bilinear stress-strain behaviour. The behaviour in the first linear branch is dominated by the properties of concrete since the confinement jacket is not activated under low compression load. The following nonlinear transition area correspond to the interaction between the concrete and the confinement jacket. The second linear branch, on the other hand, is controlled by the combination of both materials. It is noted that the stiffness of this branch decreased with the reduction of concrete strength, and also increased when an additional layer of confinement was provided for the same type of rubberised concrete.

Chapter 4

4 Asymmetric shear tests

Nomenclature

Greek letters

δ - displacement
δ_{Pu} - displacement at failure
ε - strain
$\varepsilon_{rc,el}$ - strain proportionality limit
ε_{rc1}- uniaxial crushing strain
ε_{cru} - ultimate compressive strain
ε_u - ultimate tensile strain
σ - stress
σ_{pu} - cement matrix strength
ρ_{vr} - rubber replacement ratio
τ - shear stress
τ_{res} - residual shear strength
τ_u - shear resistance

Lowercase latin letters

$d_{g,repl}$ - size of the replaced mineral aggregate
$d_{g,max}$ - maximum aggregate size
f_c - cylinder concrete compressive strength
f_{ct} - tensile concrete strength
f_{rct} - tensile rubberised concrete strength
f_{rc} -compressive rubberised concrete strength
f_{c0} - compressive reference concrete strength
s - crack slip
s_{lim} - slip limit
w - crack width
w_{bot} - crack width at the bottom notch
w_{top} - crack width at the top notch
$w_{max,0}$ - maximum crack size for normal concrete
$w_{max,r}$ - maximum crack size for rubberised concrete

Uppercase latin letters

A_f - area of the critical section
E_{rc} - elastic modulus of rubberised concrete
P_2/P_1 - load ratio
P - load
P_{cr} - cracking load
P_u - maximum load
T_s – toughness

4.1 General

As explained before in Chapter 2, a number of studies investigating the mechanical properties of rubberised concrete under uniaxial compression and tension have been carried out, and several analytical approaches for predicting these properties have been proposed. In particular, in recognition of the potential improved performance in terms of ductility and post-crushing energy dissipation in comparison to conventional concrete, more recent applications have focused on the use of rubberised concrete as a structural material. These have varied from studies on unconfined and FRP confined beam-column members (Elghazouli et al. 2017; Youssf et al. 2015; Youssf et al., 2016), rubberised concrete filled steel tubes (Silva et al. 2016; Abendeh et al. 2016), push-off specimens provided with shear studs replicating composite beams (Han et al. 2015), beam members (Ismail and Hassan 2016; Ismail and Hassan 2016), standard wall panels used as exterior cladding

for buildings (Naito et al. 2014), and wall panels subject to blast load and ballistic impact (Bewick et al 2010; Naito et al 2013).

Some of the above-mentioned studies simulated extreme actions on members such as blast load, ballistic impact and seismic loading. Amongst the fundamental requirements in terms of ductility, energy dissipation and damping, structural materials have to be provided with sufficient shear resistance which may play an important role for verifications at ultimate or may govern the local or total collapse of structural systems. As mentioned in previous investigations, shear fractures occur in RC slabs subjected to short-pulse blast, from penetration of projectiles into concrete members and may also govern the failure mode for seismic loading of nuclear containments or multi-storey structures (Bazant and Pfeiffer 1986; Luong 1990). Although some studies focused on the impact behaviour and ductility of rubberised concrete at the material level (Ismail and Hassan 2016; Xue and Shinozuka, 2013; Naito et al. 2014), investigations on rubberised concrete under pure shear are lacking.

To obtain an insight into the shear behaviour of rubberised concrete, this chapter describes an experimental programme carried out on members subjected to asymmetric four-point loading. A full account of 18 prismatic members made of conventional concrete, as well as rubberised concrete with 20%, 45% and 60% replacement of both fine and coarse mineral aggregates with rubber particles, as well as 3 tests in which aramid fibre polymers sheets are used to restrained member dilation, is given. To capture crack kinematics and crack patterns at failure, a digital image correlation (DIC) monitoring system was used to track the member displacements throughout the tests. After characterising the members according to their failure modes, a comparative assessment is carried out on members developing shear-governed failures, with focus on the influence of the rubber content on the shear capacity and resistance to cracking. The main observations related to the shear transfer across the cracked interfaces are also discussed.

4.2 Experimental programme

A total of 18 specimens, of which 3 were provided with AFRP confinement, were prepared to assess the relationship between the shear behaviour of normal concrete and rubberised concrete with various replacement ratios of both fine and coarse aggregates. Two normal concrete types were considered (C35 Grade and C70 Grade) and three rubberised concrete mixes with volumetric replacement ratios varying in the range of $\rho_{vr} = 0\text{-}0.6$ were considered (Xu et al. 2018). The binders, aggregates, rubber particles and admixtures were identical to those described in Chapter 3.

4.2.1 Mix design and specimen details

The rubberised concrete mixes, referred to in the research as R20, R45 and R60, prepared for the assessment of shear behaviour had 20%, 45% and 60% volumetric replacement of both fine and coarse aggregates. Detailed mix proportions are listed in Table 4-1.

Table 4-1 Concrete mixes

		R20	R45	R60
Compressive strength per mix (MPa)	Reference	73	59	73
	Rubberised concrete	20.8	9.6	7.3
Binders (kg)		425	314	425
Aggregates (kg)	5-10 mm	800	740	400
	0-5 mm	656	479	328
Rubber (kg)	0/5 mm	49.5	110	149
	5/10 mm	11.0	24	33.0
	10/20 mm	49.45	110	148
Admixture (l)	(PL+SPL)	7.6	7.6	7.6
w/c (-)		0.35	0.35	0.35

Prismatic samples of 150×150×600 mm dimensions were prepared for testing. As shown in Figure 4.1a**,** the specimens were provided with 5 mm wide notches at the top and bottom surfaces to create a weak section at the middle of the member. Cylindrical samples of Ø100×200 mm and 100 mm cube samples were also prepared according to codified provisions (EN 206-1:2000, 2000; ASTM C39/C39M, 2015) to assess the compression strengths of concrete. Additionally, Ø100×254 mm samples were prepared to assess the splitting strength of the investigated concretes. All the prisms, cylinders and cubes were cast in plastic or cast-iron forms in the sizes required for testing and covered with plastic sheets for 48 hours before de-moulding. Afterwards, all the specimens were cured in water tanks up to 28 days. Prior to testing, the cylinders were ground and capped to ensure full contact between the samples and loading platens. The exact dimensions of each sample (prisms, cylinders and cubes) were measured before the tests on at least three different locations. The exact dimensions of fracture planes were measured using a calliper device on both the front and back surfaces of the prisms. The cross-sectional areas of the fracture planes A_f are listed in Table 4-2. For the restrained dilation tests, one layer of AFRP was bonded to the specimen after notches were cut and measurements were carried out (Figure 4.1b). The wrapping procedure was the same as introduced in Chapter 3 of this thesis.

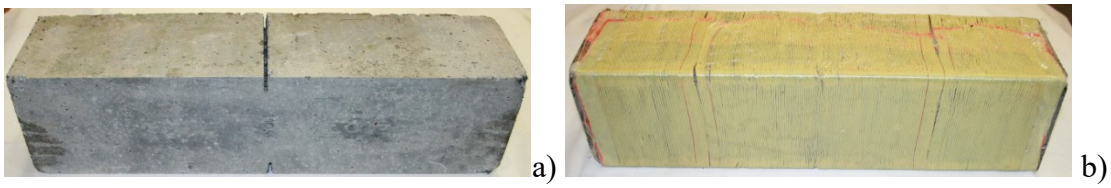


Figure 4.1 a) Rubberised concrete sample, b) Confined rubberised concrete sample

4.2.2 Testing arrangement

Concrete material testing under pure shear stress is not straightforward since there is no agreement on the ideal approach for assessment. As discussed in Chapter 2, existing studies on the pure shear behaviour of concrete materials have proposed several testing arrangements. It is therefore important to firstly discuss the possible testing arrangements before describing the procedure adopted in this research investigation.

Direct shear test

This type of shear test is most widely used to determine the shear strength of granular materials in geotechnical engineering such as soil and rock. As shown in Figure 4.2, the sample should be fixed in the shear box which consists of an upper part that can move under horizontal actions and a fixed lower part. The main disadvantage of this test is related to the shrinkage of concrete. The change of shape of the sample can create a gap between the walls of the shear box and the sample which can cause an inaccuracy in the test results. Besides, the additional friction between the two crack surfaces caused by the self-weight of the material or the confinement normal force can lead to a higher shear resistance than actual results (Boulifa et al. 2012).

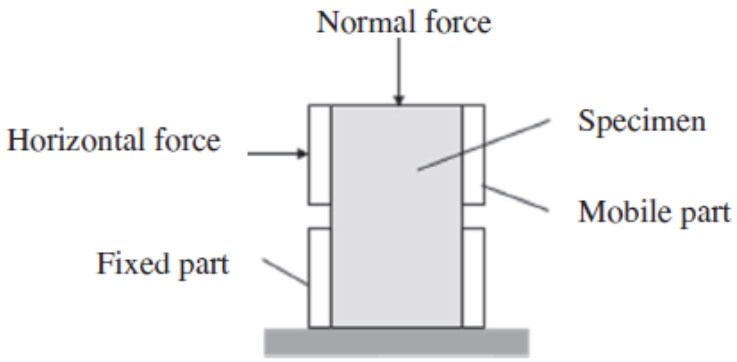


Figure 4.2 Configuration of direct shear test

This type of test can also be inaccurate for aggregate interlock dominant materials since the sample can dilate under shear forces and the instrument cannot provide sufficient axial forces to constrain the expansion (Wong et al. 2007). Accordingly, this type of test may provide relatively poor results and has not been considered herein.

Cutting shear test

The most conventional concept for shear loading is that the shear actions can be produced by a pair of cutting instruments acting on the same cross section as shown in Figure 4.3a, which is in accordance with the practical cutting of all materials using scissors. However, this arrangement cannot create shear stress along the cross-section as desired. Since the test is under symmetric loading, the stress condition of the sample should also be symmetric providing that no shear stress can be produced along the cross-section. The failure of the sample initiates from the contact points due to the concentrated normal stresses and gradually forms as the cutting edges penetrate into the material. The final failure is due to the principle tension effect acting on the cross section as shown in Figure 4.3b.

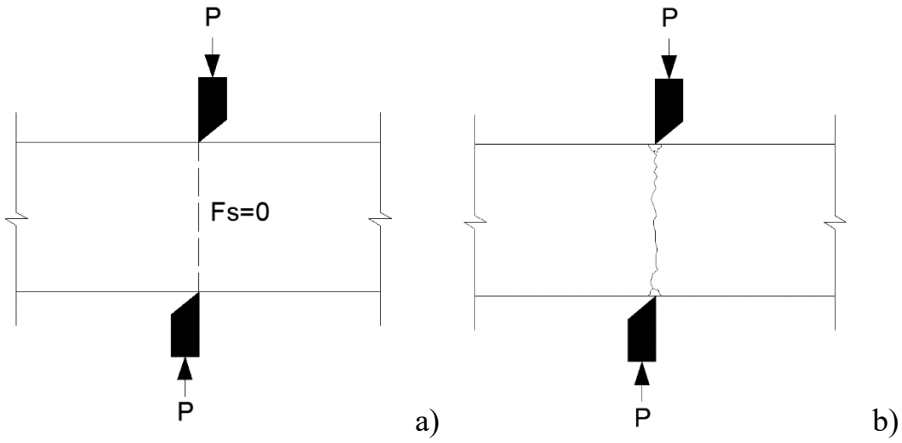


Figure 4.3(a) Prototype and (b) failure pattern of cutting shear test (no shear stress produced)

S-shape shear test

The general idea of this type of test is to create a shear force zone by loading the tested samples with a couple of forces which can equilibrate each other without the application of additional boundary conditions.

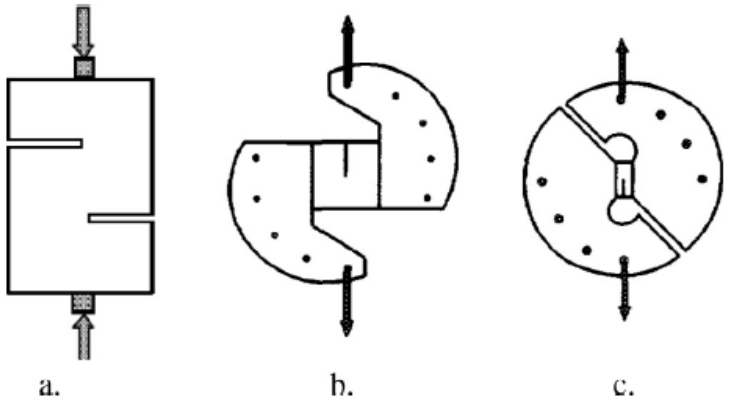


Figure 4.4 Different shear test configurations (Boulifa et al. 2012): (a) push-off test; (b) mixed mode device (Richard 1981); (c) mixed device (Bank-Sills and Arcan 1983).

The push-off test was first designed for the investigation of the interaction between the reinforcement and the concrete as shown in Figure 4.4a which was first proposed by Mattock and Hawkins (1972) to investigate the shear behaviour of reinforced concrete. However, finite element analysis showed that tensile stress occurs around the tips of the notches and the values of these stresses are of the same magnitude of the shear stress. As a result, the sample was under a mixed state of stress rather than pure shear action. Figure 4.4b, c show the S-shape shear tests which were designed for mixed action failure type tests on ductile materials, which can also be designed for a pure shear test by adjusting the loading angles (Boulifa et al. 2012). To create a pure shear failure, the S-shape test also requires the curvatures of the loading plates to be within a certain value in order to avoid other types of failures caused by compressive (or tensile) stress. In addition, the connections between the loading plates and concrete materials are also difficult to design. Consequently, this type of test may not be suitable for brittle material such as concrete.

Double shear test for cylindrical specimens

The double shear test proposed by Luong (1990) aims at measuring the shear strength of concrete and rock materials through cylindrical specimens as shown in Figure 4.5. The tested cylinder is manufactured with a relative small height and concentric notches on both top and bottom surfaces. The load is applied in the central area of the top surface (inside the perimeter of the notch) and in the external area of the bottom surface (outside the perimeter of the notch) as shown in Figure 4.5a, b. In order to reduce the normal stresses perpendicular to the shear faces induced by the sliding between the inner and outer parts of specimen, four symmetric notches are prepared, distributing uniformly around the cylinder, perpendicular to the upper and bottom surface of the specimen.

Consequently, the axial load is applied on the central cylinder of the specimen which is retained by the four concentric tubular parts.

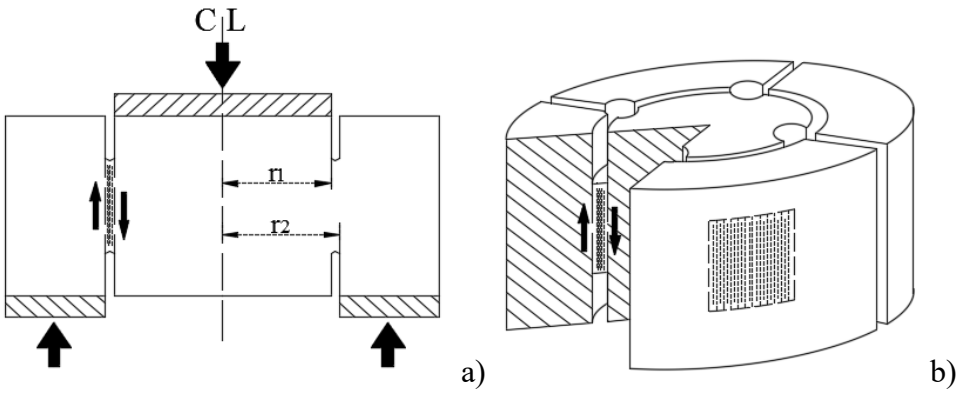


Figure 4.5 Double shear test layout by Luong (1992): a) elevation view, b) shear area

It has however been shown that the double shear test setup introduces non-negligible bending actions within the failure surfaces. Typical types of failure, as shown in Figure 4.6, occur in this test (Garcia et al. 2016). The distributed load leads to cracking outside the vertical notched, since the distances between the equivalent loading points and the support points are relatively wide, hence the failure of the specimen occurs due to combination of bending and shear effects.

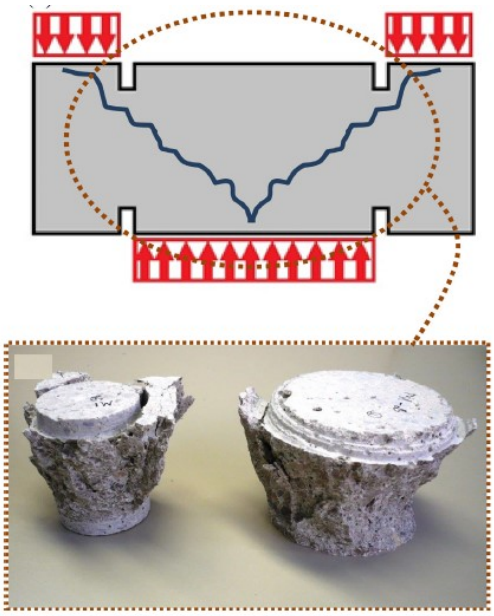


Figure 4.6 Failure pattern of double shear test by Garcia et al. (2016)

JSCE-SF6 shear test (JSCE-SF6 1990)

The Japanese standard JSCE-SF6 specifies the double shear test method for shear strength of steel fibre reinforced concrete by direct double shear. The standard test apparatus as shown in Figure 4.7a provides perpendicular loads on the specimens at all times. The deviation at the upper and lower edges should be in a range between 0 and 1 mm. The spacing (H) between the edges is the same as the specimen height and the width of the upper and lower cutting edges should be 1/10 of the edge spacing.

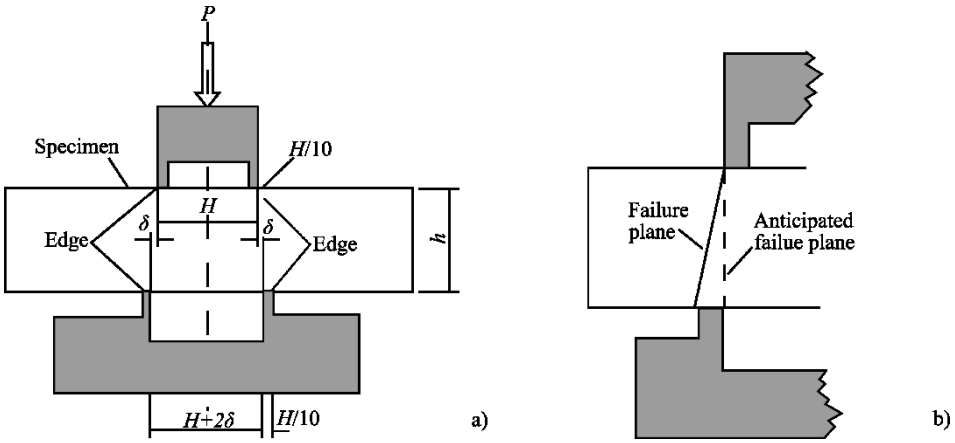


Figure 4.7 JSCE-SF6 shear test: a) layout, b) anticipated and unusable failure types

The idea of this test setup is to create a shear force within a short shear band, therefore the shear action is concentrated within the span between the upper and lower cutting plates. Since the shear span is sufficiently short, minor bending actions occur within the critical region. All-round notches around the two anticipated failure planes with equal depth are also required to guarantee proper shear failure. The double shear test has been shown to be a suitable method to determine the shear behaviour of concrete materials (Mirsayah and Banthia 2002; Tuan et al. 2006). On the other hand, failure patterns as shown in Figure 4.7b generally occur in the case of an eccentric loading indicating bending actions within the critical sections. According to JSCE-SF6, damage patterns that occur along the anticipated failure plane cannot be used for the prediction of the shear capacity. In addition, since the double shear test requires two identical shear planes, it brings more potential deficiency and eccentricity within the test setup. Consequently, the configurations and dimensions of apparatus and tested specimens need to be prepared rigorously to guarantee desirable results.

Asymmetric four-point shear test (Iosipescu shear test)

The asymmetric four-point shear test (Iosipescu shear test) was originally designed (Iosipescu and Negoita 1969) for the determination of shear behaviour of ductile materials such as steel, as shown

in Figure 4.8a. When performing normal shear tests on a beam specimen, bending moments always occur simultaneously along with shear actions. The proposed model and the corresponding shear force and bending moment diagrams are shown in Figure 4.8b below. The tested sample is simply supported at the bottom and two compression forces are applied from the top two points which are anti-symmetrical to the loading points. The symmetrical beam specimen is loaded under anti-symmetrical loads which creates a constant shear force and a zero bending moment around the centre point. Load P1 should be considerably larger than P2 to ensure the stability of the specimen and maximum shear force in its middle part. Besides, in order to ensure a zero bending moment along the middle cross-section, the relationship between the loads P_1, P_2 and loading spans L_1, L_2 should be set as $P_2 = P_1 L_1/(2L_2 + L_1)$.

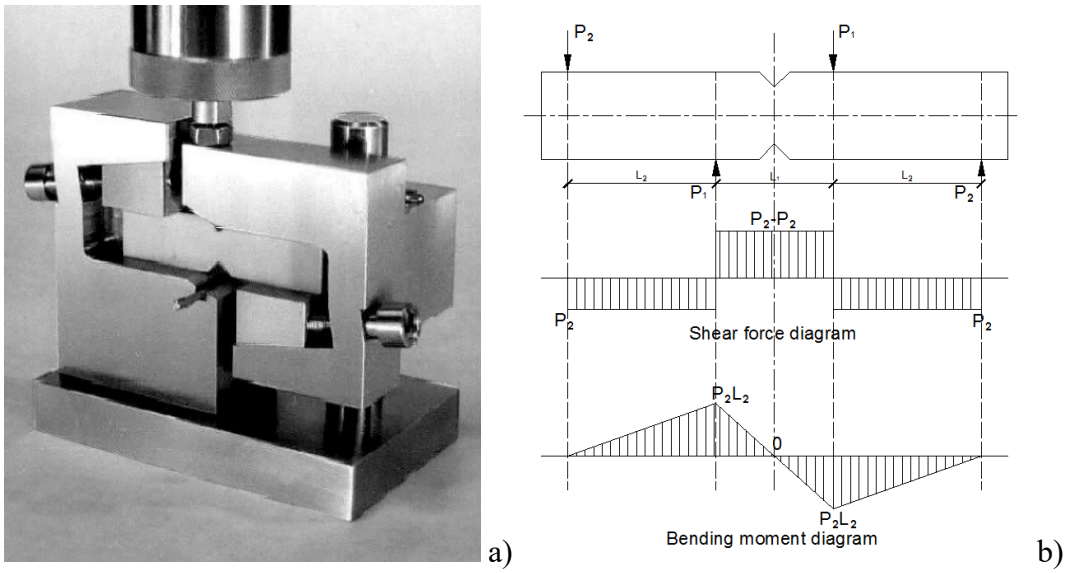


Figure 4.8 a) Iosipescu shear test setup, b) corresponding shear and bending diagrams

Since the loading pattern and boundary conditions can be created conveniently for brittle materials, this type of test can also be used in concrete material shear tests (Bažant and Pfeiffer 1986). Depending on the length of the shear band, fracture may initiate from the tips of the notches and propagate along the direction normal to the maximum compressive principle stress, which would exhibit a tension governed failure type as show in Figure 4.9a, b. In this case, the cracks propagate due to tensile actions, hence the test fails to create a pure shear governed type of failure. Further improvements has been made by decreasing the distance between the shear force couple (Bažant and Pfeiffer 1986), which minimizes the shear span and tensile actions. For the test with a narrower shear band, the fracture propagates vertically through the notch until the sample finally ruptures, representing a shear governed failure. Figure 4.9c shows the improved test design and fracture

mode. Finite element simulations have shown that fracture cracks can propagate sideway when the shear force band is wide while vertically when the shear force zone is sufficiently narrow. Bažant and Pfeiffer (1986) also reported that the test results from single and double notched specimens should be the same.

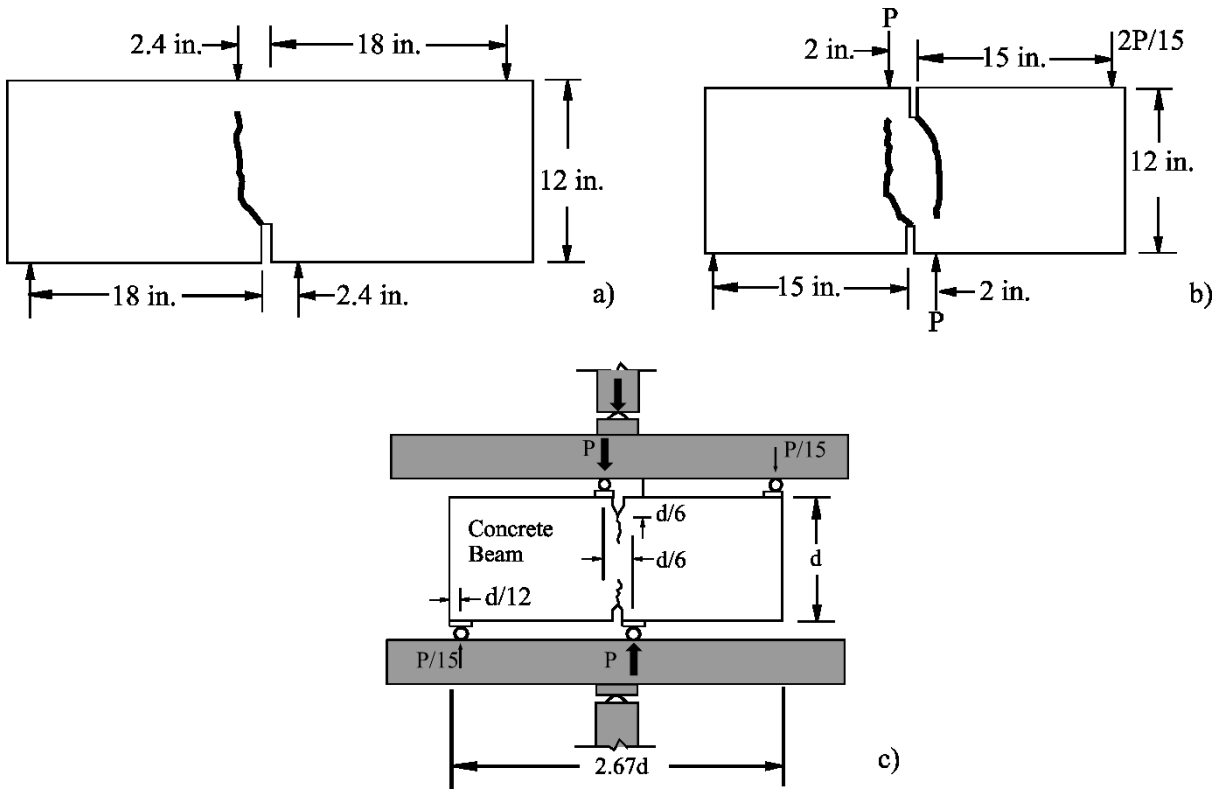
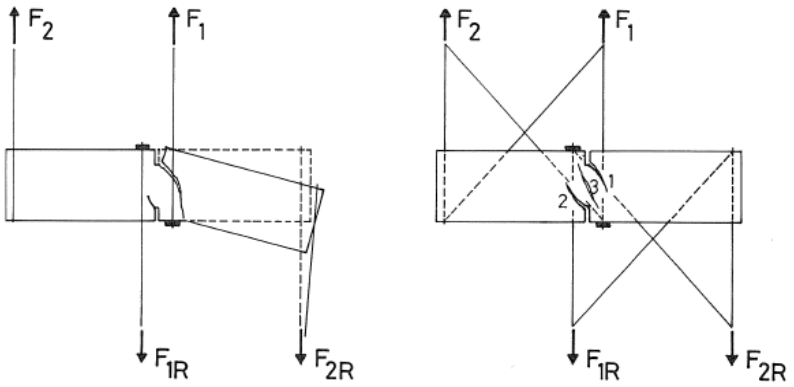


Figure 4.9 Fracture modes: (a) and (b) Mode 1 (tensile) failure and (c) Mode 2 (shear) failure (Bažant and Pfeiffer, 1986)

Studies have shown that the rotation of the sample during loading would have an influence on the test results (Schlangen 1993). As shown in Figure 4.10, the rotation of the specimen led the fracture to occur away from the shear plane which finally ended up with tension governed failure, while a fixed arrangement led to a failure type much closer to a shear governed type.



a) b)

Figure 4.10 Failure mechanism for 4-point shear test with: (a) freely rotating supports and (b) fixed supports (Schlangen 1993)

In all the testing methods discussed above, the key factor was to create a pure shear force on the cross section without any other action. Despite efforts to obtain pure shear (referred to as Mode II) situations in testing, in all cases, mixed-mode behaviour in which tensile crack growth (referred to as Mode I) takes over before Mode II failure occurred. Some testing arrangements may favour shear crack propagation against tensile in comparison to others. However, as mentioned, there is no common agreement on the most appropriate technique for obtaining pure shear behaviour. Hence, the choice of the testing arrangement and specimen geometry is typically made based on practicality regarding ease of preparation and the stress conditions at the fracture plane. An attractive option, which is employed in this research, is the asymmetric four-point test since constant shear action and zero bending moment develops at the fracture plane (Iosipescu and Negoita 1969). The symmetrical beam specimen is simply supported at the bottom and two compression forces are applied from the top two points which are anti-symmetrical to the loading points. To ensure beam failure along the middle section, notches are required at top and bottom, without creating additional stress concentrations.

The asymmetric four-point tests on prism specimens were carried out in a stiff four-post Instron Satec machine with maximum load capacity of 3500kN as illustrated in Figure 4.11a,b. The specimens and supports were placed on the bottom platform of the testing machine. A stiff load transfer beam was bolted directly to the actuator. Two roller sets were placed on the top of the test specimen without being connected to the transfer beam for load distribution to the two loading points. The side roller was placed at the very end of the specimen whereas the middle roller was placed on the other half of the specimen near the notch. The top roller assemblies consisted of a stiff 90 mm-wide top plate hinged to the rollers, and the rollers with a diameter of 40 mm and 50 mm

wide plates were in direct contact with the specimen. The distance between the displacement application points was around $P_2/P_1 = 1/11$ in order to enforce shear action at the critical section (Figure 4.11b).

The bottom support rollers were connected to 200×210 mm steels girders. These girders were also bolted together to avoid rotation of the supports. The prismatic specimens were connected to supports through two 50 mm wide steel plates. All 50 mm plates connecting the test rig to the samples were positioned to prevent any local crushing. A displacement rate of 0.05mm/min was applied by the machine to the transfer beam. In the absence of a standard test procedure, the displacement rate was chosen to allow detailed recording of crack width during loading. Besides the load cells located at each of the four posts of the testing machine, that recorded the load corresponding to applied displacement, two 600kN load cells were located between each support (200 mm girder) and the testing machine bed to record the reactions at the bottom. For all tests, the back face of the members was instrumented with linear potentiometers to record crack mouth opening displacement (CMOD) and crack mouth shear displacement (CMSD) as shown in Figure 4.11c. Two other transducers were placed on the left and right sides of the samples to check the member expansion during the test.

As shown in Figure 4.11d, a Digital Image Correlation (DIC) system, consisting of two 5MP cameras provided with 35mm f/2D lenses positioned 2.0 m away from the specimen and 0.65 m apart, as well as a controller, was used to capture crack propagation and member displacements (Lavision). High contrast black/white patterns were provided to the front face of the specimens by applying two layers of water-based white paint and, subsequently, a fine black speckle pattern with dots of size 0.5-2.0 mm was used to ensure smooth detection of surface deformations during testing. This was also required to allow the post-processing software to compute surface strain vector fields. The monitored area (field of view) was clear of obstacles so that both cameras could record surface deformations, and the test environment was vibration-free over the testing time to avoid recording of spurious data. A recording rate of 1Hz was used throughout testing to achieve a balance between the amount of collected data and required post-processing time. Before the start of the recording, a calibration procedure was performed to ensure measurement accuracy as required by the testing recommendations (Lavision). Throughout calibration and testing, homogenous illumination of the monitored surface of the specimen (150 mm × 600 mm) was guaranteed.

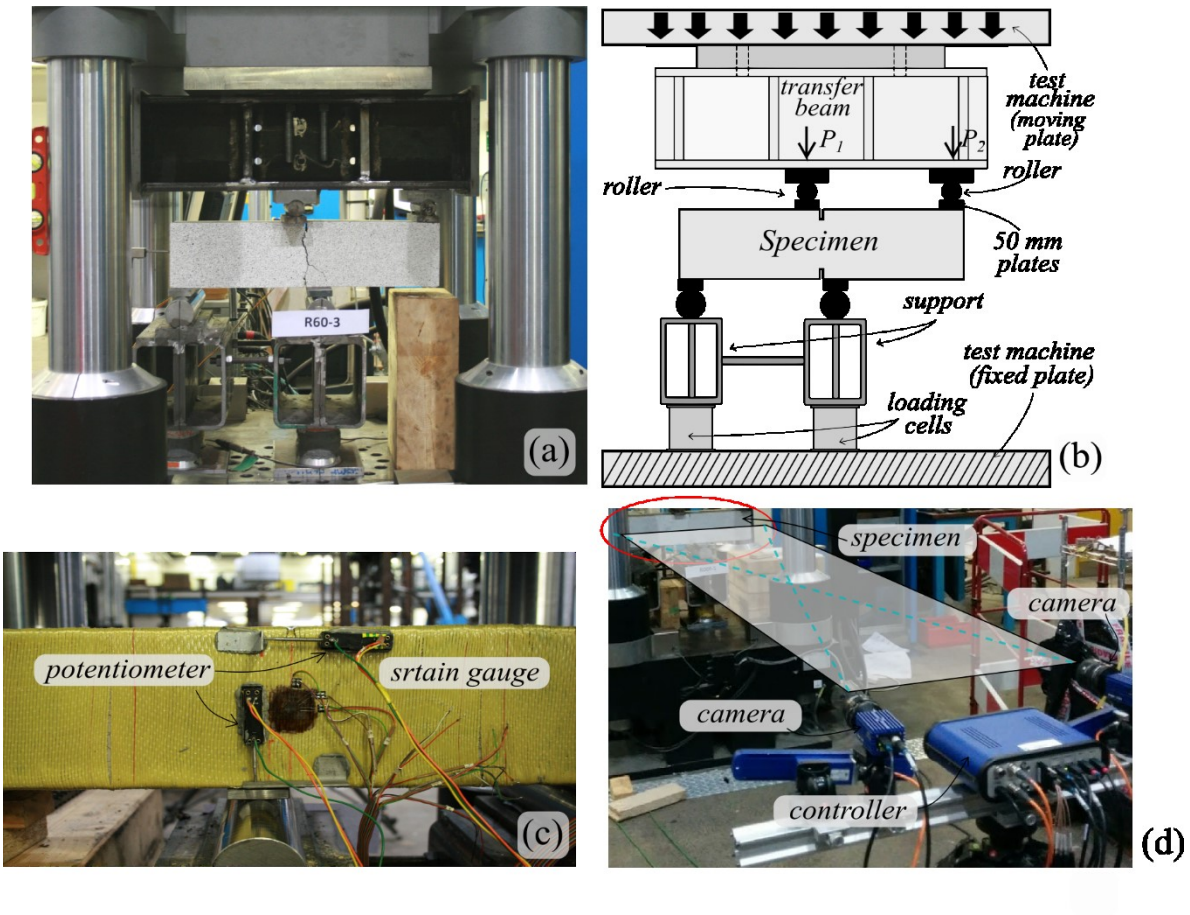


Figure 4.11 Testing arrangement: a) General view, b) Layout; Instrumentation c) devices, d) digital image correlation system (DIC)

The resulting surface deformations are also dependent on the input parameters in the post-processing software (Lavision), especially parameters such as subset size that directly influences the level of accuracy. For instance, when the subset size is set as 9 pixels, the accuracy is 0.02 pixels and the uncertainty is 1.5%, whereas when the subset size is increased to 121 pixels, the accuracy becomes 0.0012 pixels with an uncertainty of 0.0035%. For assessment of the strain vectors from the recorded images for the tests described here, the chosen subset size was 21 pixels which cover an area in the range of 1.50 mm^2; hence, the accuracy was in the range of 0.007 pixels (0.4μm), whilst the uncertainty was around 0.15%. For the assessment of CMOD and crack widths, the DIC is preferred to linear potentiometers as it could detect fine cracks and offer detailed information about the crack pattern and growth.

4.3 Test results

Asymmetric four-point tests were carried out to assess the influence of rubber content on the shear resistance and crack kinematics. In the first phase, the shear bandwidth represented by edge-to-edge distance between loading plates in the vicinity of the notches, was varied from l_s = 5mm to l_s = 50 mm to obtain an optimal testing configuration, with a focus on the crack kinematics rather than member strength. The results of these comparative tests are shown in Figure 4.12 which illustrates both the crack pattern at failure and the load-displacement response (P-δ) as recorded by the testing machine. The P-δ responses of the remaining tests of unconfined specimens are depicted in Figure 4.13, whereas the crack patterns prior to failure, as obtained from the digital image correlation system, are shown in Figure 4.14. The specimens described here are defined by a notation of the form R*xxy-z* in which *xx* is the rubber content in percentage, *y* is used to show the type of concrete in members without rubber (N – normal strength, H – high), whilst *z* is the sequence of member testing. Detailed specimen geometries and test results are shown in Table 4-2.

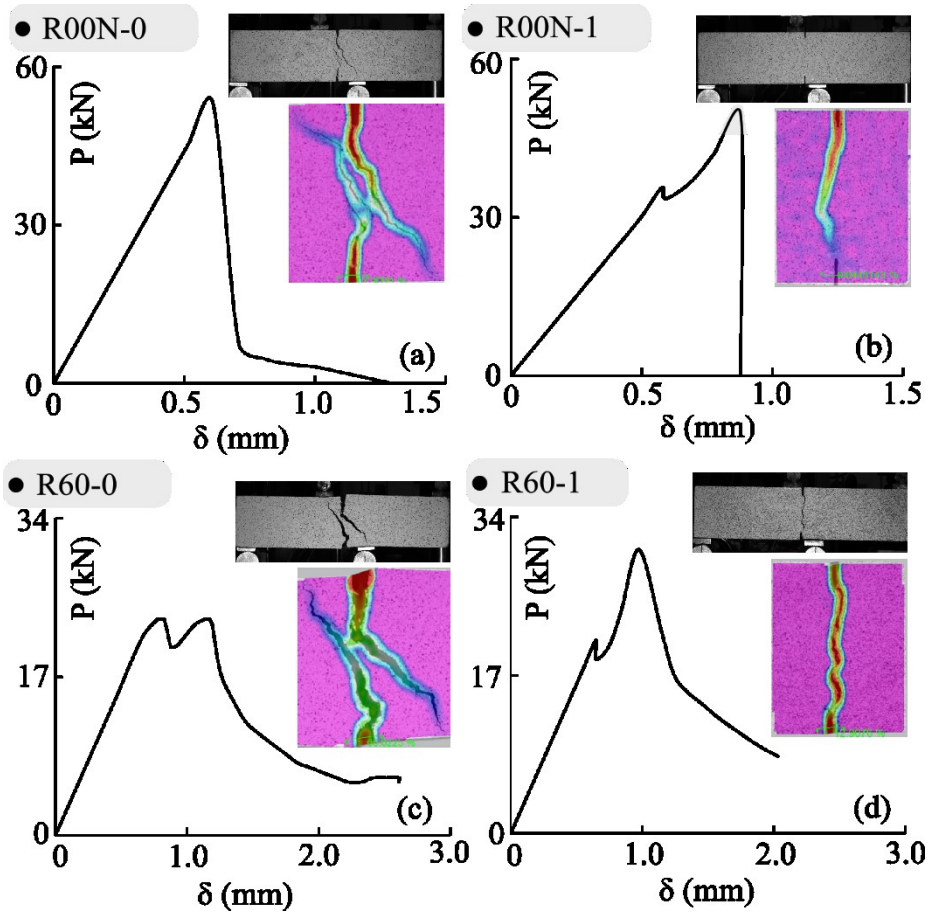


Figure 4.12 Pilot tests: a) R00N-0, b) R00N-1, c) R60-0, d) R60-1

Table 4-2 Specimen details and results

Specimen	P_u (kN)	P_{cr} (kN)	δ_{Pu} (mm)	$f_{c,28d}$[1] (MPa)	Age	$f_{c,test}$[2] (MPa)	Critical section ($\times 10^3$) mm	τ_u (MPa)	Failure Mode[3]
R00H-1	63.1	59.5	0.65	72.9	29	73.2	16.0	3.94	MM
R00H-3	84.0	78.9	0.57	72.9	30	73.4	16.1	5.21	MM
R00H-2	50.8	49.7	0.45	72.9	30	73.4	16.1	3.16	MM
R00N-0[4]	53.4	-	-	42.6	224	46.1	16.0	3.35	M-I
R00N-1	49.4	35.5	0.88	42.6	224	46.1	15.9	3.11	M-II
R00N-2	49.9	46.9	0.91	42.6	229	46.3	16.2	3.07	MM
R20-1	39.4	37.8	0.75	20.8	31	21.0	15.4	2.55	M-II
R20-2	52.4	29.8	0.70	20.8	31	21.0	15.1	3.46	M-I
R20-3	50.7	46.2	0.71	20.8	31	21.0	14.9	3.41	M-I
R40-1	26.0	-	1.76	9.6	72	10.2	15.8	1.64	MM*
R40-2	32.8	29.1	0.72	9.6	78	10.3	16.4	2.00	M-II
R40-3	50.2	47.3	0.82	9.6	78	10.3	16.2	3.10	M-I
R60-0[4]	23.2	-	-	6.6	219	7.5	15.9	1.46	M-I
R60-1	30.1	20.7	0.94	7.3	28	7.3	15.0	2.01	M-II
R60-2	22.2	17.2	1.38	7.3	28	7.3	15.2	1.46	MM
R60-3	24.1	22.2	1.2	7.3	28	7.3	15.4	1.56	MM
R60F-1	39.1	27.3	1.34	6.6	223	12.0	16.2	2.16	M-II
R60F-2	59.1	58.0	1.06	6.6	224	12.0	15.8	3.88	M-II
R60F-3	45.3	44.8	1.44	6.6	224	12.0	16.5	2.97	M-II

1) 28 days compressive strength on Ø100×200 mm cylinders

2) assessed by means of Eurocode 2 equations for unconfined members and by means of testing on 150×150×300 prisms for R60F specimens

3) M-I – tensile governed Mode I, M-II – shear governed Mode II, MM – mixed mode pilot tests with the width of the shear band of 50 mm

4) Pilot tests with the band width of l_s= 50 mm.

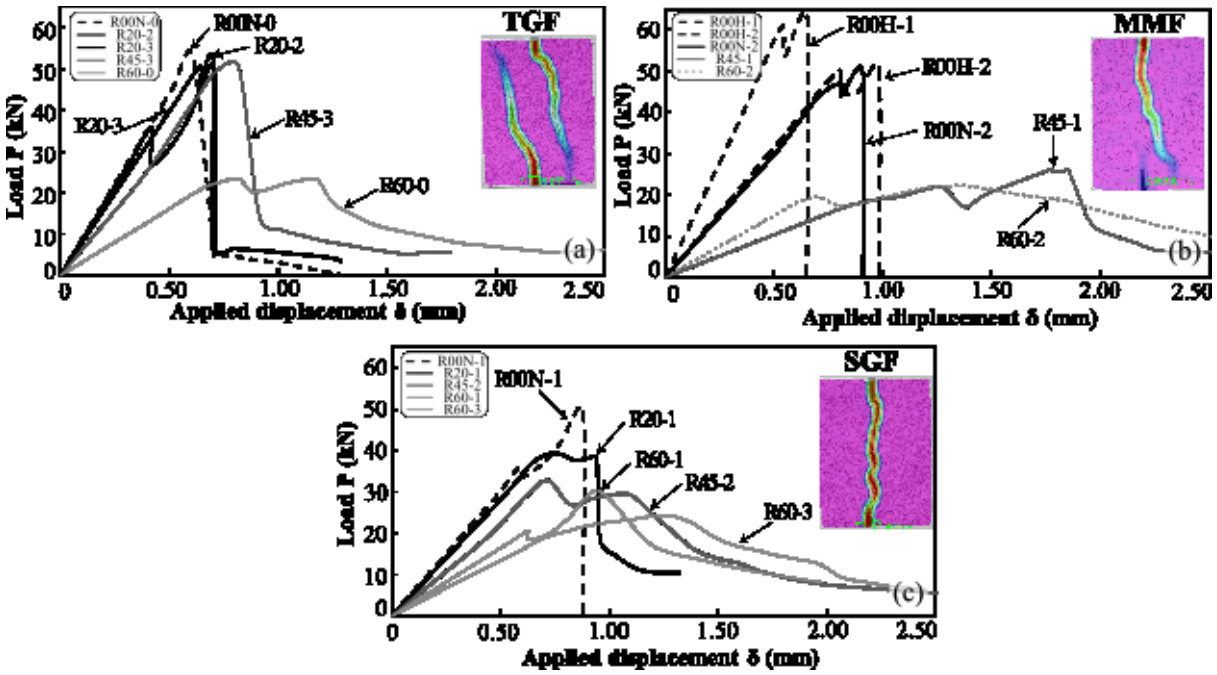


Figure 4.13 Load–displacement response for: a) Tensile-governed failures (TGF), b) Mixed-mode failure (MMF), c) Shear-governed failures (SGF)

For Specimens R00N-0 and R60-0, the width of the shear band l_s, defined as the distance between the edges of the 50 mm wide transfer plates, was set to 50 mm. In contrast, in Specimens R00N-1 and R60-1, the edges of the 50 mm transfer plates were placed at the notches (l_s=5mm). The former specimens had tensile-dominated behaviour with failure due to the formation of double inclined cracks that propagated outside the support, showing that the wider shear band introduces extra bending at the critical region. In contrast, Specimens R00N-1 and R60-1 had shear-governed failures, in which a critical crack formed directly between the top and bottom notches, which is in agreement with other investigations, confirming that such failures occur only for very small l_s (e.g. Ingraffea and Panthaki 1985). Hence, l_s = 5mm was considered for the remaining tests.

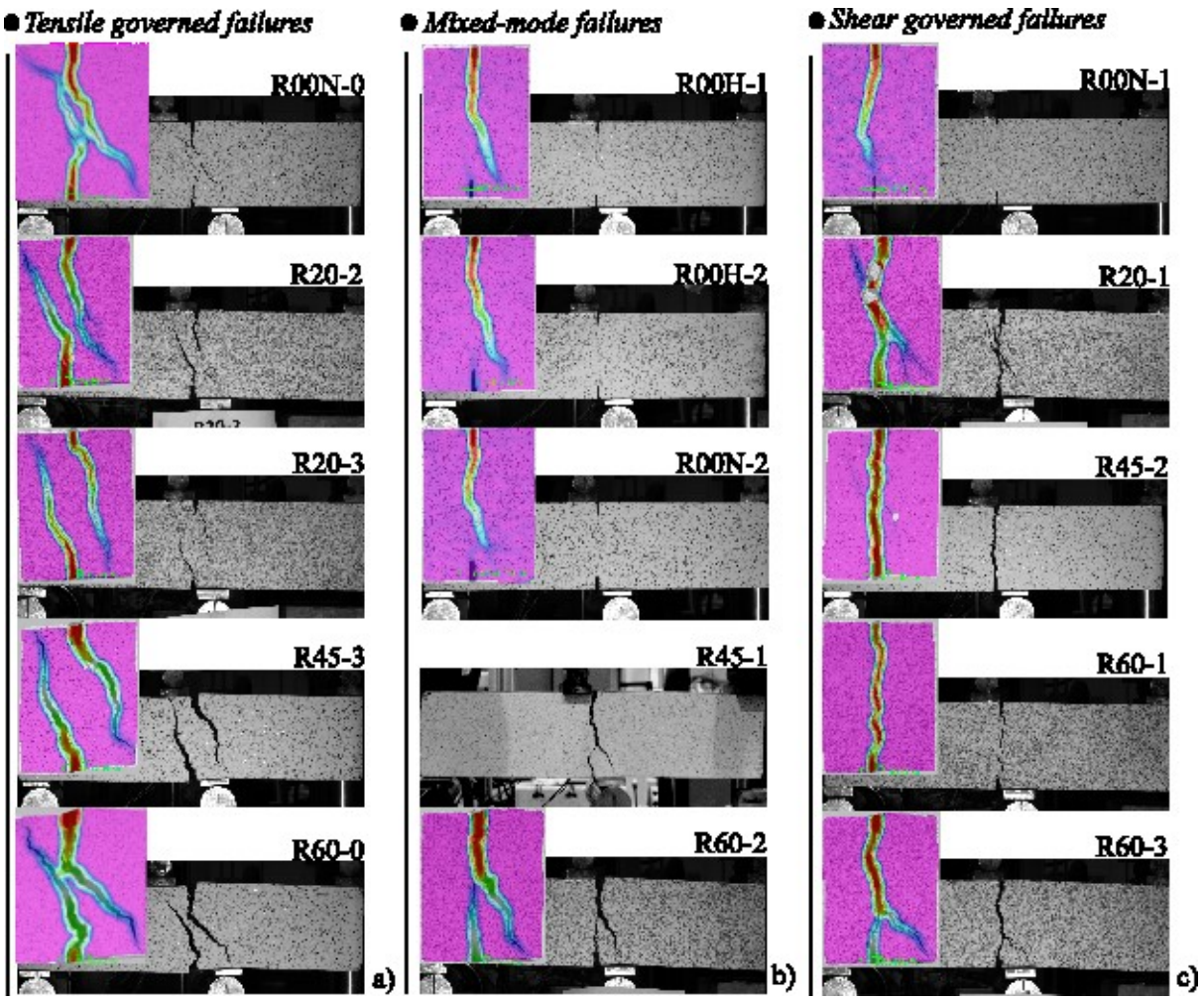


Figure 4.14 Crack patters prior to failure as obtained from the DIC system: a) Tensile governed failures (TGF), b) Mixed mode failures (MMF), c) Shear governed failures (SGF)

For the remaining members with l_s = 5mm, the response obtained may be divided into three categories: (i) Tensile-Governed Failure (TGF) with the formation of two independent cracks at both notches that propagated towards the supports on the opposite side was recorded for 5 specimens (R00N-0, R60-0 with l_s = 50 mm and R20-2, R20-3, R45-3 with l_s = 5mm); (ii) Mixed Mode Failure (MMF) which initiates with the formation of a single crack, dominated by shear action, but deviating from the fracture plane due to the influence of tensile actions, was obtained for 5 specimens (R00H-1, R00H-2, R00N-2, R45-1, R60-2); (iii) Shear-Governed Failures (SGF) with the formation of a single crack along the critical section were observed in 5 specimens (R00N-1, R20-1, R45-2, R60-1 and R60-3). The response and crack kinematics of these members are described below. It should be noted that all the AFRP confined specimens (R60F) showed SGF behaviour as discussed subsequently in a separate section.

4.3.1 Tensile-governed and mixed-mode responses

Figure 4.13a shows the *P-δ* relationships recorded from the actuator at mid-point of Specimens R20-2, R20-3 and R45-3 with TGF. In this case, flexural actions produced two inclined fracture planes resulting from crack propagation from both notches to the supports (Figure 4.14). The failure of the two R20 specimens was sudden without post-peak softening, resembling that in the shear-governed normal concrete Specimen R00N-1 described in the following section. These had a similar response in terms of stiffness *K*, maximum load P_u and displacement at failure δ_{Pu} (P_u = 52.4 kN, δ_{Pu} = 0.70 mm and P_u = 50.7 kN, δ_{Pu} = 0.71 mm, respectively). From the three R45 specimens, only R45-3 developed TGF, showing increased stiffness and strength (P_u = 50.2 kN at δ_{Pu} = 0.82 mm) in comparison to other R45-1 and R45-2 members.

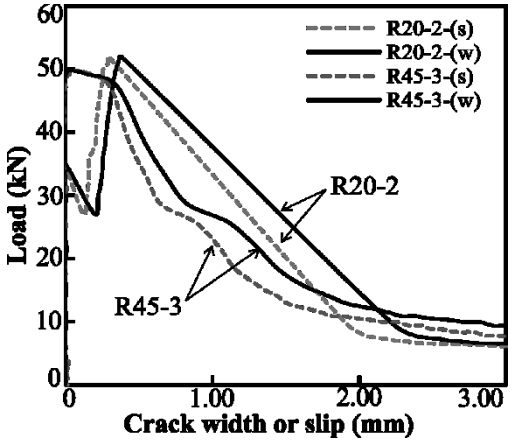


Figure 4.15 Crack with and slip for R20-2 and R45-3 with tensile-governed failures (TGF)

Crack slips and average crack widths as processed from DIC data using virtual gauges are plotted for Specimens R20-2 and R45-3 in Figure 4.15. In several cases, the crack width of the bottom notch w_{bot} was larger than the width of the top notch w_{top}, in which the behaviour was generally governed by the crack width at the top notch only. Hence, the crack widths are reported as average values of the top and bottom notch separations $w=(w_{top}+w_{bot})/2$. The crack slip *s* is determined from the sliding of the two crack faces between the right edge of the top notch and the left edge of the bottom notch, to obtain the slip vector component from the DIC virtual gauge. Although the crack slip *s* and opening *w* exhibited similar trends, the width *w* precedes the slip *s* through the loading process, after crack initiation. For R20-2 and R20-3, w_{top} was always positive indicating a continuous expansion up to failure, whereas the bottom notches were closing. On the other hand, for R45-3, w_{top} was negative while the bottom w_{bot} was positive in tension up to $0.7\times P_u$, followed by compression until failure.

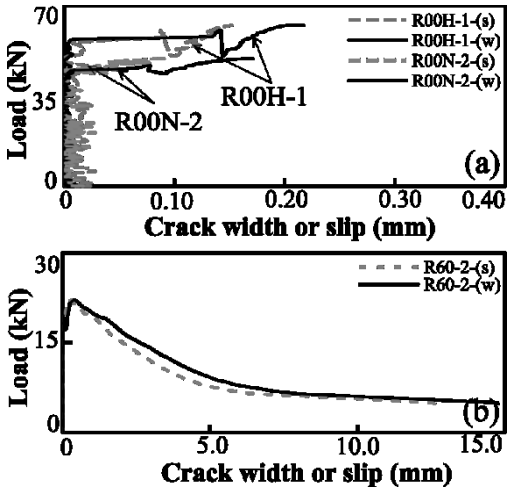


Figure 4.16 Crack with and slip for: a) R00H-1, R00N-2, b) R60-2 with mixed-mode failures (MMF)

Figure 4.13b shows the *P-δ* relationships of the specimens exhibiting MMF (R00N-2, R00H-1, R00H-2, R45-1 and R60-2). Both R00H members failed in MMF with notable scatter in terms of P_u and $\delta_{Pu,}$ mostly due to significant brittleness of the high strength concrete employed in these specimens, in comparison to other members within the same group. R00H-1 reached P_u = 63.1 kN and δ_{Pu} = 0.65 mm, whilst R00H-2 showed the lowest stiffness and failed at the lowest P_u = 50.8 kN at corresponding δ_{Pu} = 0.98 mm. R00N-2 had a similar behaviour to R00H-2 which failed at a peak load of P_u = 49.9 kN with δ_{Pu} = 0.91 mm. Similarly to specimens failing in the other two modes, all specimens with no rubber content showed a sudden drop in strength after their P_u was attained. R60-2 showed slightly higher stiffness compared to R45-1 and failed at similar loads and displacements. R60-2 reached P_u = 26.0 kN and δ_{Pu} = 1.76 mm, whilst R45-1 failed at P_u = 22.2 kN and a corresponding δ_{Pu} = 1.38 mm. The crack widths and slips derived from the DIC data for R00H-1 and R00N-2 in Figure 4.16a indicate behaviours governed by slip prior to failure, followed by a response dominated by tensile cracking. On the other hand, for R60-2 in Figure 4.16b, crack opening dominates the response after initiation around $0.86 \times P_u$.

As illustrated Figure 4.13a, the increase of rubber content from 20% to 45% did not influence significantly the *P-δ* response of the specimens with TGF illustrating minimal contribution from the rubber content to the post-peak softening and energy dissipation. After reaching P_u, these showed a sudden loss of strength and fractured in three parts without exhibiting a ductile response post-fracture. This allowed free rotation of the two extreme bodies, hence limiting the influence of secondary shear actions such as aggregate interlock and rubber particle clamping on the post-peak response. Besides the free rotation of the fractured parts, TGF and MMF may occur due to the slight

misalignment of the top and bottom notches that produce a non-symmetric testing configuration in which the bending moment at the extremities of the shear bands is not negligible, allowing supplementary tensile actions to develop. Hence, the shear mode crack growth is in this case followed by tensile cracking which eventually dominates the post-cracking and ultimate response.

4.3.2 Shear-governed response

Specimens R00N-1, R20-1, R45-2, R60-1 and R60-3 exhibited SGF failures in which the fracture occurred at the critical section (Figure 4.14). As depicted in Figure 4.13c, Specimen R00N-1 showed a stepped behaviour in which the P-δ response was characterised by a slight decrease in strength at the crack opening, followed by an increase, primarily due to the stress redistribution and aggregate interlock. Specimen R00N-1 reached P_u = 49.4 kN at a corresponding δ_{Pu}= 0.88 mm. This was followed by a sudden drop in strength when the specimen fractured in two parts. Specimen R20-1 also failed in a similar manner. Since it had the lowest rubber replacement ratio from the tested range, R20-1 had stiffness similar to that of the normal concrete specimen R00N-1.

Similar to R00N-1, the strength of R20-1 dropped when the crack opened, increasing slightly afterwards until it reached P_u = 39.4 kN at δ_{Pu}= 0.75 mm. After failure, the strength dropped instantaneously showing that 20% of rubber replacement did not significantly influence the overall behaviour. The specimen with ρ_{vr}=0.45, R45-2, showed a lower P_u and stiffness compared with R00N-1 and R20-1. It failed at an applied δ_{Pu}= 0.72 mm and a corresponding load of P_u = 32.8 kN. The post-peak curve of Specimen R45-2 had a much more ductile behaviour than R00N-1 and R20-1 since it showed a more gradual decrease in strength and relatively soft response. With further increase in rubber content, R60-1 and R60-3 members showed the lowest stiffness, yet significant post-peak energy dissipation, compared to other shear-governed members by reaching P_u = 30.1 kN at δ_{Pu}= 0.94 mm and P_u = 24.1 kN, δ_{Pu} = 1.2 mm, respectively. As for R20-1, Specimen R60-3 also had a second branching crack propagating towards the supports, and its width was consistently smaller than that of the notch-to-notch critical crack (Figure 4.14c).

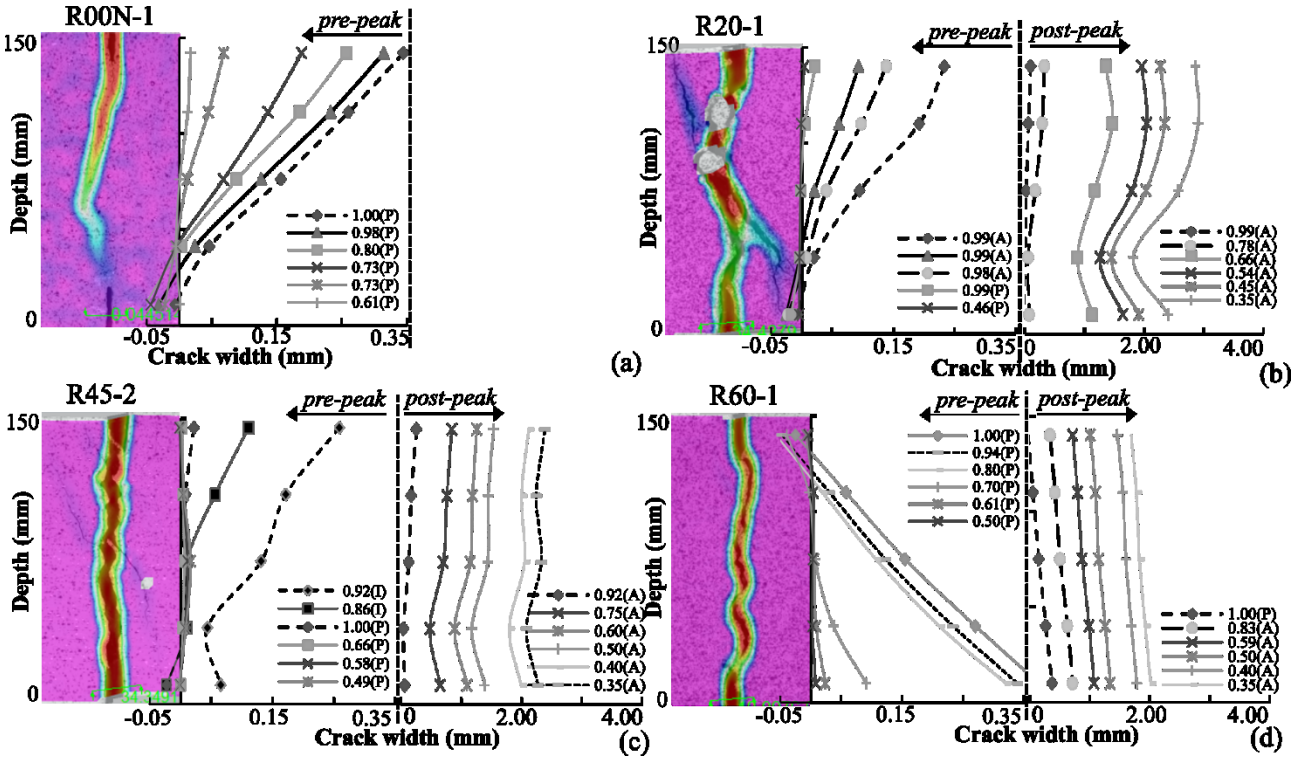


Figure 4.17 Crack kinematics for shear-governed members (SGF): a) R00N-1, b) R20-1, c) R45-2, d) R60-1; The legends represent the ratio between the load at which the measurement is assessed and the maximum load P/Pu, with (P)=pre-peak, (I)=inter-peak and (A)= post peak represent the stage on the P-δ curve

In Figure 4.17, the crack widths are plotted at five locations of the critical section at various fractions of the load P corresponding to an applied actuator displacement δ as indicated in the plots. These allow detailed observation of the crack kinematics throughout the loading procedure, and enables comparative assessments between the responses of the investigated normal and rubberised concrete materials. Specimens R00N-1, R20-1 and R45-2 had responses in which the top notch separated constantly, while the bottom notch was closing for maximum top crack widths of about 0.30-0.35mm (Figure 4.18a, b). This corresponds to a load level near ultimate. For R45-2, such crack widths were obtained in the post-peak regime at a load corresponding to 92% of P_u, representing the second peak of the stepped P-δ recorded (Figure 4.13c). The second ascending branch represents strength enhancement due to secondary shear actions. Specimen R60-1 had a similar response. Specimen R60-3 had a comparable response to the other SGF rubberised concrete specimens, hence for compactness, the kinematics are not described in detail. As seen in Figure 4.13c, for all the specimens developing SGF, consistent reductions of P_u developed with the increase of ρ_{vr}.

For R60-1, the bottom notch had crack widths of 0.35mm, whilst the top notch was in compression. This contrasting behaviour occurs due to the difficulty in achieving perfect symmetry in the testing

arrangement. For R00N-1, R20-1, R45-2, the right-hand side of the specimen acted more like a cantilever with the extreme load application point, including the self-weight of the supports, taking more of the actuator load. In contrast, for R60-1, the left-hand side of the member was subjected to higher load through the central load application point. However, the post-peak response of all rubberised concrete shear-governed members had post-peak responses with crack propagations with similar ductile kinematics (Figures 4.17b-d). Specimen R00N-1 had no recorded information regarding the crack kinematics in the post-peak regime since its failure was brittle.

The crack slips and average crack widths of the shear-governed members are plotted in Figure 4.18a,b. They show an increase in the crack opening before the peak, up to values of 0.1 mm, while the slip had a largely linear behaviour. The gradual shift in the *P-w* curves between R00N-1, R20-1, R45-2 and R60-1 in Figure 4.18a may be directly linked to the increase in rubber content and the clamping effect of the crack interfaces. Except in R60-3, for the same level of load in the post-peak range, members with higher rubber content had smaller crack widths in comparison to specimens with little or no rubber content.

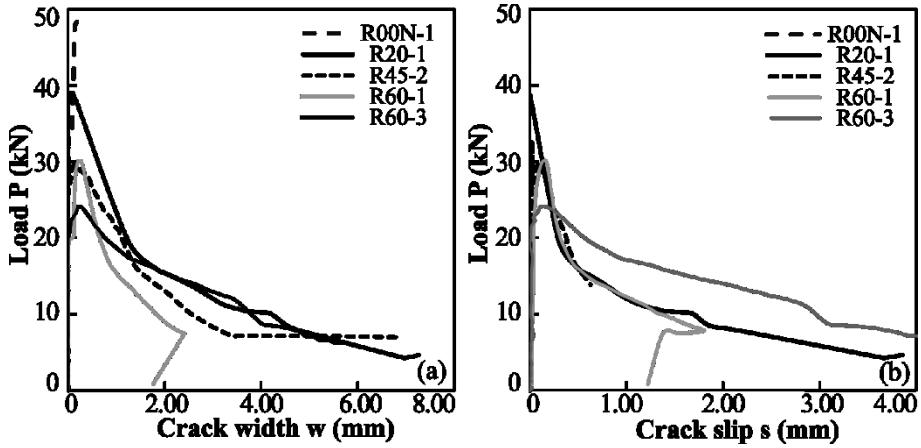


Figure 4.18 SGF members: a) Average crack width, b) Crack slip

It is worth noting that the post-peak behaviour typically exhibits increased ductility with the increase of rubber content and the rubber particles contribute to the more ductile post-fracture. Except for R60-3, the *P-δ* curves show a stepped behaviour, indicating an increase in strength (R00N-1, R60-1) or in residual strength (R20-1, R45-2) after the crack initially opened and prior to fracture. From a kinematics point of view, it seems that the fracture of the concrete matrix was followed by secondary effects such as the interlock of mineral aggregates and, for rubberised concrete members, by an additional clamping effect between the two crack interfaces. Due to

aggregate interlock-rubber clamping actions, some enhancement in behaviour is observed for specimens with higher amounts of ρ_{vr}.

4.3.3 Restrained dilation tests (AFRP confined tests)

As described in the previous sections, asymmetric four-point bending tests may have responses other than shear-governed ones. Although the reduced member cross-section is located in the maximum shear band, the internal microstructure of the materials combined with imperfect symmetric testing configurations, tensile cracking may take over and govern member behaviour. To overcome member dilation due to potential crack propagation outside of the notch-to-notch cross-section, three members with a high amount of rubber ρ_{vr}=0.6 (R60F-1, R60F-2, R60F-3) were externally confined with one layer of AFRP and subjected to the same testing procedure. All these tests showed considerable scatter in their P-δ response (Figure 4.19a), yet they all had shear-governed failures (Figure 4.19b).

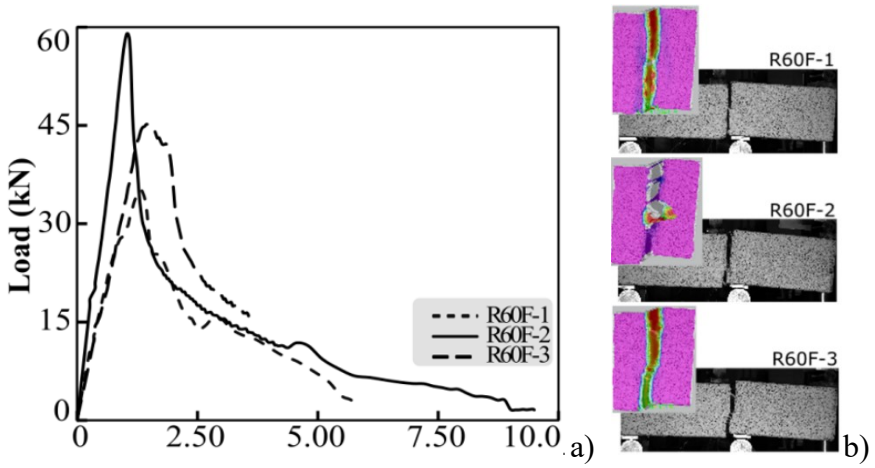


Figure 4.19 a) Load-displacement response for AFRP confined tests, b) shear-governed failure types

The ultimate capacity for R60F-1, R60F-2, R60F-3 were P_u = 35.1 kN, P_u = 59.0 kN and P_u = 45.2 kN, respectively, with an average value of 46.4kN. The displacements δ_u at peak were 1.34, 1.06 and 1.44 mm, respectively. The strongest specimen, R60F-2 had also the highest stiffness in comparison with the other two specimens. In a direct comparison to R60-1 without confinement, these had increased ultimate capacity and δ_u at failure. Also, their post-peak response was characterised by a soft ductile fracture with displacements at fracture twice that of R60-1. The external FRP confinement also limited the crack expansion and growth outside the notch-to-notch reduced cross-section, allowing only shear-governed modes to develop.

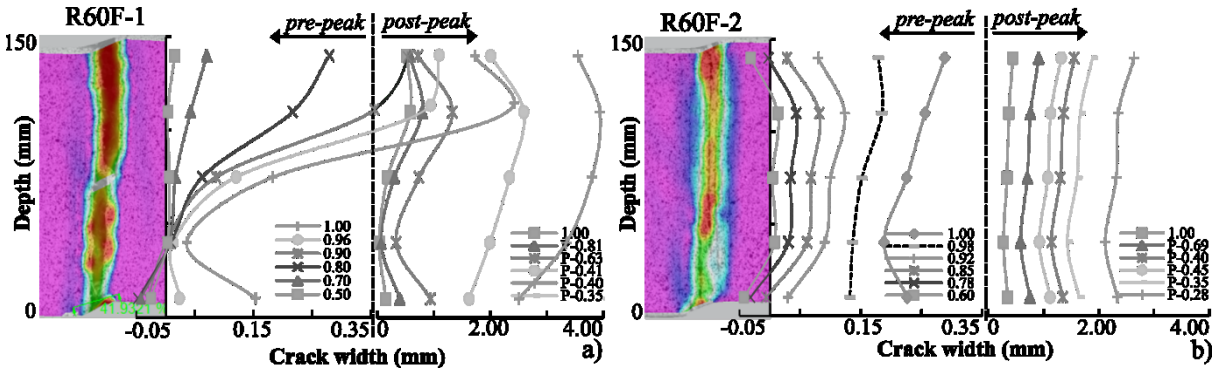


Figure 4.20 Crack kinematics for confined R60F members: a) R60F-1, b) R60-2

The crack widths depicted in Figure 4.20a indicate a similar response for R60F-1 to the unrestrained shear-governed specimens, with one of the notches closing and the other expanding. The top-notch width at failure was in the range of 0.7 mm, which is twice the maximum crack width for R60-1. Specimen R60F-2 had more stable crack propagation with crack widths within the same ranges as the unrestrained R60-1. The post-peak response showed considerably more energy dissipation leading to crack widths of about 4 mm, twice as in the case of R60-1 (i.e. around 2mm). From the crack slips and average crack widths in Figure 4.21, it can be observed that sliding occurred prior to crack opening. For R60F-1, slip is observed at 56% of P_u, whilst significant opening occurs at 64% of P_u. For the other two confined specimens, R60F-2 and R60F-3, the sequence for crack kinematics was similar. For R60F-2 sliding activated at $0.72\times P_u$ and opening at $0.85\times P_u$, whereas for R60F-3, both actions developed at similar ultimate load fractions ($0.88\times P_u$). In the post-peak range, the crack propagation was characterised by a simultaneous increase, both in terms of slip and width. As shown in Figure 4.21, instead of enhancing the shear strength, crack opening and sliding capacities of rubberised concrete in the same way as for its compressive behaviour, the AFRP jackets only restrained the lateral expansion of the specimens while shear behaviour was dominated by the concrete itself.

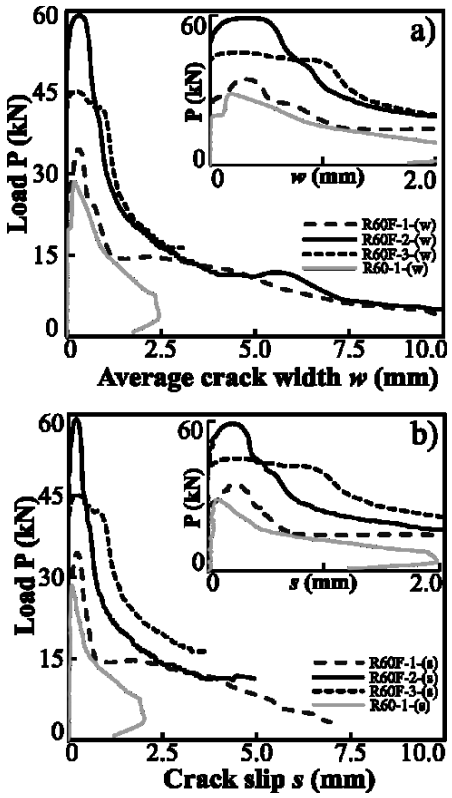


Figure 4.21 a) Average crack width, b) Crack slip for shear governed confined members

In contrast to the lateral confining mechanism applied in the uniaxial compression tests, the external FRP sheet prevented the lateral dilation of the test specimens in the horizontal direction perpendicular to the loading direction and also provided enhancement to the shear strength of concrete from the FRP matrix and adhesive mix. The restrained dilation tests carried out on prisms provided with external confinement depict cases in which crack propagation due to tensile action is restricted, whilst direct shear behaviour is favoured. This testing configuration allows isolation of the shear action since unidirectional FRP sheets were parallel to the notch-to-notch weak cross-section, indicating that the shear behaviour of the specimen is not restrained. Based on the results discussed above, this specimen and testing arrangement ensure shear failures which can assess actual shear strength of the material, rather than shear-governed failures in which minimal tensile action exists. However, such tests require supplementary investigation since only 3 specimens with single layer of AFRP, included in this test series were not sufficient to quantify the influence of external confinement on the shear behaviour of rubberised concrete. Consequently, further assessments of shear strength are carried out only from unrestrained tests. To this end, a comparative assessment on the influence of rubber content on the shear strength is described below.

4.4 Comparative assessments

As discussed before in Chapter 2, the term 'shear strength' is used in previous studies to refer to several concepts ranging from the resistance of a material subjected to pure shear stress to the capacity of a reinforced concrete beam under external shear action. On the other hand, shear resistance τ_u refers to the ultimate shear stress imposed on the plane of fracture A_f in the absence of a normal force (Everling 1964). In this study, shear strength is defined as the ratio between the ultimate load P_u and the corresponding fracture surfaces, where A_f, is used as a metric for comparison. From the tested specimens, members having shear-governed failures (SGF) are considered for comparison in terms of the influence of ρ_{vr} on τ_u, material toughness, as well as qualitative observations regarding the shear transfer between cracked concrete interfaces.

Figure 4.22a illustrates the relationship between the ultimate shear stress τ_u against the rubber replacement ratio ρ_{vr}, whilst Figure 4.22b depicts the influence of the concrete compressive strength f_c on τ_u. It can be observed that with the increase of ρ_{vr}, τ_u decreases in a non-linear manner. When ρ_{vr} is increased from 0 to 20% and 45%, the τ_u decreases considerably, while the rate of strength loss reduced when moving to ρ_{vr}=45-60%. This stands mostly for members which developed SGF in the tests. As indicated in Figure 4.22b, τ_u increases with f_c for all failure cases including both normal and rubberised concrete members.

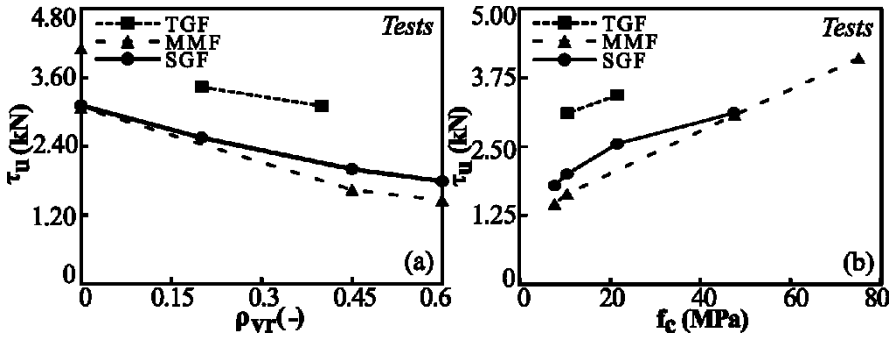


Figure 4.22 a) τ_u vs ρ_{vr} from tests, b) τ_u vs f_c from tests

The material toughness T_s is a property representing the resistance to crack propagation, directly governed by mechanical properties of the material and its geometry. The flexural toughness of the members, as illustrated in Figure 2.10 defining the material ability to resist flexural cracks, is typically determined from the P-δ relationship obtained from flexural loading tests (e.g. ASTM C1609, 2013). Flexural toughness and material toughness indices are defined as ratios between the areas under the P-δ curve at deflection limits as defined by the codified procedure (Gopalaratnam

and Gettu 1995). This approach was recently employed for the assessment of toughness in shear failures of push-off fibre reinforced tests (Barragan et al. 2006). In this experimental programme, the results from the DIC measurements in terms of load-slip (*P*-*s*) are used to assess the absolute toughness T_s defined as the area below the shear stress-slip (τ-*s*) curve considering slip limits s_{lim} of 0.25, 0.5, 1.0, 2.0 (Equation 4.1).

$$T_{s_{\lim}} = \int_0^{s_{\lim}} \tau(s)\, ds \tag{4.1}$$

Table 4-3 Residual shear strength and equivalent shear strength

Specimen	Residual shear strength (MPa)				Equivalent shear strength (MPa)		
	τ_u	$\tau_{res0.25}$	$\tau_{res0.50}$	$\tau_{res1.0}$	$\tau_{0.25}$	$\tau_{0.50}$	$\tau_{1.0}$
R20-1	2.55	1.04	0.94	0.67	1.54	1.77	1.28
R45-2	2.00	1.44	0.96	0.00	1.53	1.41	1.30*
R60-1	2.01	1.35	1.01	0.75	1.58	1.42	1.19
R60-3	1.56	1.55	1.37	1.10	1.42	1.45	1.32

* assessed at s_{lim}=0.63

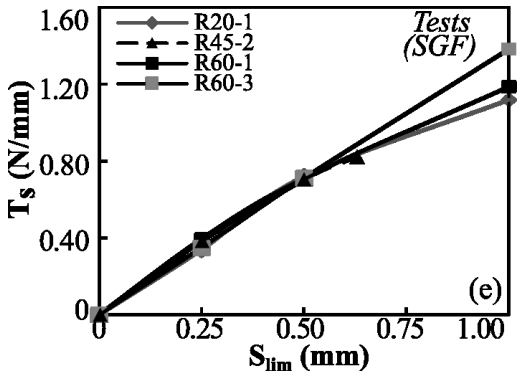


Figure 4.23 member toughness T_s

Table 4-3 depicts the T_s values obtained for the s_{lim} described previously for rubberised concrete members with SGF, residual shear strengths τ_{res}, and equivalent shear strengths τ_{eq} as a ratio between T_s at a slip limit, and the s_{lim} ($s_{0.25}$, $s_{0.5}$, $s_{1.0}$, $s_{2.0}$). The normal concrete specimen R00N-1 reached slip values below the minimum s_{lim} considered. Figure 4.23 illustrates the capacity of the member to resist cracking. From the T_s-s_{lim} curves, it can be observed that all members had an essentially identical response up to s_{lim}=0.50, with R60-1 and R60-3 showing higher toughness at s_{lim}=1.0 as all plotted series are showed an increase in T_s with the increase in s_{lim}.

For R45-2, the lack of data for s>0.62 did not permit an assessment of T_s. However, at s=0.62, it had the same T_s as R20-1. Specimen R20-1, with ρ_{vr}=0.2, had similar T_s with R45-2 and R60-1 at s_{lim}=0.25, with a slight enhancement for higher slip limits. In addition to the crack kinematics illustrated in Figure 4.17, the results of the T_s assessment indicated minimal influence on ρ_{vr} hence on the crack growth of shear-governed rubberised concrete members.

Key observations from the tests show notable impact of the ρ_{vr} on τ_u and the post-peak response of rubberised concrete in comparison with the reference normal concrete. Experimental results showed that, while normal concrete and rubberised concrete with low rubber content (ρ_{vr}=0.2) are typically represented by rather brittle shear responses with low or no energy dissipated in the post-peak regime, the rubberised concrete with higher amounts of rubber (ρ_{vr} =0.4-0.6) exhibits increased post-peak softening response with rubber particles contributing to the softer post-fracture. The rubberised concrete cracked interfaces are inherently subjected to other forms of friction than cracked interfaces in normal concrete, with the clamping effect of the rubber particles offering different energy dissipation mechanisms in addition to the conventional interlock of the mineral aggregates.

In the case of SGF members developing vertical cracked interfaces as those described in Section 4.3.2, the load transfer is limited to aggregate interlock and the concrete residual stresses, whilst the vertical component of the shear force transferred through the concrete compressive zone tends to be negligible as the crack inclination is around 90° (Bompa and Elghazouli 2015). The residual stresses transferred through the fracture process zone are a function of the tensile strength of the concrete f_{ct} and the maximum crack opening $w_{max,r,}$ both being a function of ρ_{vr}. On the other hand, in conventional concrete, the aggregate interlock is a function of the maximum aggregate size $d_{g,max}$, strength of the cement matrix σ_{pu} and aggregate distribution within the cracked interface (Walraven and Reinhard 1981). For rubberised concrete, $d_{g,max}$ and σ_{pu} are the same as for the reference conventional concrete from which it is derived, since both the mineral aggregate gradation and the water-to-binder ratios are the same.

Based on the above discussion, the forces transferred through interlocking particles clearly depend on their distribution at the cracked interfaces. As this distribution is fairly proportional to the rubber content ρ_{vr} and the ratio between mineral aggregates to rubber particles, ρ_{vr} effectively determines the forces transferred through the crack interfaces including the level of post-peak softening. These observations and assumptions, combined with the obtained test load-deformation responses, suggest that both at cracking and in the post-cracking regime, a higher amount of rubber at the cracked interface produces a softer response due to a notable clamping effect of the rubber particles, whilst low amounts of rubber are linked to aggregate interlock resulting in a less ductile response.

4.5 Concluding remarks

This chapter described tests carried out on rubberised concrete members subjected to asymmetric four-point loading to obtain a detailed insight into the shear behaviour of rubberised concrete. A full account of 15 prismatic members made of conventional concrete as well as concrete with relatively high replacement ratios of both fine and coarse mineral aggregates with rubber particles, in addition to 3 AFRP confined specimens, was given. After describing the materials, mix designs and member details, key observations resulting from detailed measurements of the crack kinematics, with focus on members developing shear governed responses, were reported. Moreover, comparative assessments focusing on the unconfined specimens in terms of shear resistance, toughness and force transfer across the cracked interfaces, were presented. Based on the findings and discussions, the following concluding remarks can be drawn:

- Asymmetric four-point tests may be used to obtain shear-governed failures, yet these are very sensitive to the alignment of the predefined fracture planes and characteristics of testing arrangement, with slight non-symmetry often leading to tensile-governed response.
- The tested specimens showed three distinct types of ultimate behaviour: (i) tensile-governed failures (TGF) with the formation of two independent cracks at both the top and bottom notches that propagated towards supports on the opposite sides; (ii) mixed mode failures (MMF) that initiate with the formation of a single crack, dominated by shear action, but deviating from the predefined fracture plane due to the influence of the tensile actions; and (iii) shear-governed failures (SGF) with formation of a single crack along the critical section.
- The results indicated a decrease of around 20% in the estimated member strengths for 20% of rubber content, 40% reduction for 40% rubber content and about 60% less strength for 60% rubber content, in comparison with strengths obtained for the reference SGF cases, suggesting a decreasing member strength-rubber content relationship similar to that for compressive strength-rubber content.
- Typical load-deformation curves showed stepped responses characterised by a slight decrease in strength at the crack opening, followed by an enhancement, primarily due to the interlock of mineral aggregates and clamping of rubber particles.
- Detailed measurements of the crack kinematics showed that the fracture of the concrete matrix is followed by secondary effects such as the conventional interlock of mineral aggregates. For rubberised concrete members, this included an additional rubber clamping effect between the two crack interfaces, directly influencing the post-cracking range, with members including higher rubber content having smaller crack widths in comparison to specimens with no or low rubber content.

- A relatively high amount of rubber at the cracked interface produces a comparatively softer post-peak response due to the clamping effect of the rubber particles. In contrast, low amounts of rubber are linked to aggregate interlock governing a less ductile response. However, the assessed resistance to cracking through toughness parameters showed similar responses for all tested rubberised members with a slight enhancement for cases with 60% rubber content.
- The AFRP confinement restrained the dilation of rubberised concrete specimens, hence the tension-governed crack propagation was restricted, and the shear-governed failure was favoured. It indicates that external AFRP confinement can be a suitable method to enhance the shear behaviour of rubberised concrete such that potential tensile cracks are restricted.
- Although rubberised concrete with AFRP confinement showed higher shear strength and corresponding failure displacement compared with unconfined specimens, the enhancement is due to the restraint of crack propagation due to other effects. The tests described herein indicate that AFRP confinement can enhance the shear resistance of rubberised concrete yet further studies on this aspect with different rubber contents and level of confinements are needed to identify appropriate shear resistance models for externally confined rubberised concrete.

Chapter 5

5 Experimental methodology for member tests

Nomenclature

δ_y – lateral deformation at flexural yielding
l_{col} – column length
l_{rub} – length of the rubberised concrete region
l_{conf} - length of the externally confined region
s_w – stirrup spacing
D – column diameter
F – FRP confinement layers
Ø – diameter
R – rubber content

5.1 General

Studies on the structural behaviour of reinforced rubberised concrete (RRuC) members have pointed out that the presence of rubber reduces the compressive strength but enhances ductility and energy dissipation. Existing experimental investigations have, however, focused on members with concrete materials incorporating relatively low rubber content. There is therefore a need for further research on the inelastic performance of structural members incorporating rubber particles, particularly for cases in which relatively large proportions of rubber replacement for mineral aggregate are used.

As shown in Chapter 3 for rubberised concrete materials, the loss of strength is significant up to replacement levels of 10-15%, but the rate of reduction decreases with higher replacement ratios. It was also shown that the rubber content has a less detrimental influence on the bond properties in comparison with its influence on the uniaxial compressive strength, with bond coefficients exhibiting largely constant trends irrespective of the rubber content up to replacement ratios of 60% (Bompa and Elghazouli 2017). This suggests that higher replacement ratios may offer an improved balance between the environmental benefits of using rubber as well as enhanced ductility, energy dissipation, and reliable bond behaviour on the one hand, and the loss in concrete strength on the other hand.

This chapter describes the experimental methodology adopted in this research in order to assess the behaviour of reinforced rubberised concrete beam-column members subjected to inelastic lateral cyclic deformations and different levels of co-existing axial loads. The test series includes specimens that employ concrete materials incorporating rubber particles representing relatively large replacement proportions of mineral aggregates. Two series of large-scale circular reinforced rubberised concrete column specimens with different geometries. In total 14 reinforced beam-column members were examined, in which the rubber content varied in the range ρ_{vr}=0-0.60 while

the reinforcement ratio was maintained. All specimens were confined with circular steel stirrups, while 5 columns were also externally confined with AFRP sheets. The details of the beam-column specimens are described in this chapter together with the details of the test rigs employed as well as the instrumentation adopted.

5.2 Specimen details

Table 5-1 Specimen details

Specimen	Geometry [1)]			Rubber content (%)	No. AFRP layers	Rebar layout	Stirrup layout
	l_{col} (mm)	l_{rub} (mm)	l_{conf} (mm)				
D250-R00-F0-N2	1000	-	-	R00	0	8 Ø12	Ø10 at 100 mm
D250-R00-F0-N1	1000	-	-	R00	0	8 Ø12	Ø10 at 100 mm
D250-R60-F0-N1	1000	450	-	R60	0	8 Ø12	Ø10 at 100 mm
D250-R60-F3-N1	1000	450	500	R60	3	8 Ø12	Ø10 at 100 mm
D350-R45-F0-N0	1350	450	-	R45	0	8 Ø16	Ø10 at 100 mm
D350-R45-F0-N1	1350	450	-	R45	0	8 Ø16	Ø10 at 70 mm
D350-R60-F0-N0	1350	470	-	R60	0	8 Ø16	Ø10 at 70 mm
D350-R60-F0-N1	1350	470	-	R60	0	8 Ø16	Ø10 at 70 mm
D350-R60-F0-N2	1350	470	-	R60	0	8 Ø16	Ø10 at 70 mm
D350-R60-F0-N2S	1350	470	-	R60	0 [2)]	8 Ø16	Ø10 at 40 mm
D350-R45-F2-N0	1350	450	500	R45	2	8 Ø16	Ø10 at 70 mm
D350-R45-F2-N2	1350	450	450	R45	2	8 Ø16	Ø10 at 70 mm
D350-R60-F3-N0	1350	470	600	R60	3	8 Ø16	Ø10 at 70 mm
D350-R60-F3-N2	1350	470	600	R60	3	8 Ø16	Ø10 at 70 mm

Notes:

1) l_{col}, l_{rub} and l_{conf} stand for the effective column height, length of rubberised concrete and length of AFRP confinement from bottom of the column.

2) denser stirrup arrangement (s_w=40mm)

Considering the effectiveness of confinement in circular sections, fourteen specimens of circular cross-section of which four were with a diameter of Ø250 mm and ten were with a diameter of Ø350 mm were prepared as described in detail in Table 5-1. The reinforcement cages of all specimens were constructed first and located in wooden moulds while plastic moulds were used for the column parts as shown in Figure 5.1 and Figure 5.2. Ready-mix normal concrete was used for the foundation and top parts of specimens while rubberised concrete was mixed in the laboratory. The AFRP sheets were wrapped around the member in the bottom part. Constant pressure was applied using sponge roller and plastic squeegee (see Figure 5.3) to ensure adequate bonding. The specimen reference used the format of D*vvv*-R*xx*-F*y*-N*z* which indicate the column diameter (D) in mm, the rubber content (R) in percentage, the number of confining layers (F) and the level of axial

load (N: N0 for members without axial load, N1 for ‘low’ axial loads below 10% of the nominal cross-section axial capacity, and N2 for ‘high’ axial loads above 10% of the nominal cross-section axial capacity). The geometric details of all the Ø250 and Ø350 specimens are given in Table 5-1.


a)

b)

Figure 5.1 a) Foundation steel cage, b) column steel cage and moulds of Ø250 specimens


a)

b)

Figure 5.2 a) Foundation steel cage, b) column steel cage and moulds of Ø350 specimens



Figure 5.3 AFRP sheets wrapping

Ø250 mm diameter specimens

For comparison purposes, the experimental assessment presented herein includes four specimens of Ø250 mm diameter that were tested as part of an initial study (Elghazouli et al. 2017). All specimens were constructed in three parts from the bottom: foundation block, circular column span and head block as shown in Figure 5.4.

The geometry and reinforcement layout of the four specimens are identical as shown in Figure 5.5. As illustrated in Figure 5.5, these three specimens were provided with 8×Ø12 mm bars as longitudinal reinforcement and Ø10 mm circular stirrups with a spacing s_w=100. All specimens had a circular cross-section with a diameter 250 mm, and an effective cantilever height of 1000 mm. Each specimen had a rectangular foundation of 800×400×514 mm^3 which was bolted to the test rig plate, and a rectangular cap of 400×300×300 mm^3 connected to the vertical and lateral actuators with load transfer box. Two of the specimens (D250-R00-F0) were made of conventional concrete (as in Figure 5.4a) while another specimen (D250-R60-F0) had rubberised concrete replacement (RRuC) over a length of 450 mm from the footing-to-column interface (as in Figure 5.4b). In addition, the fourth rubberised concrete specimen was provided with rubberised concrete at the bottom and external AFRP confinement (CRRuC) as shown in Figure 5.4c. Three layers of AFRP confinement were provided from the bottom of the column part up to a length of 500 mm which ensured sufficient confinement of the rubberised concrete part.

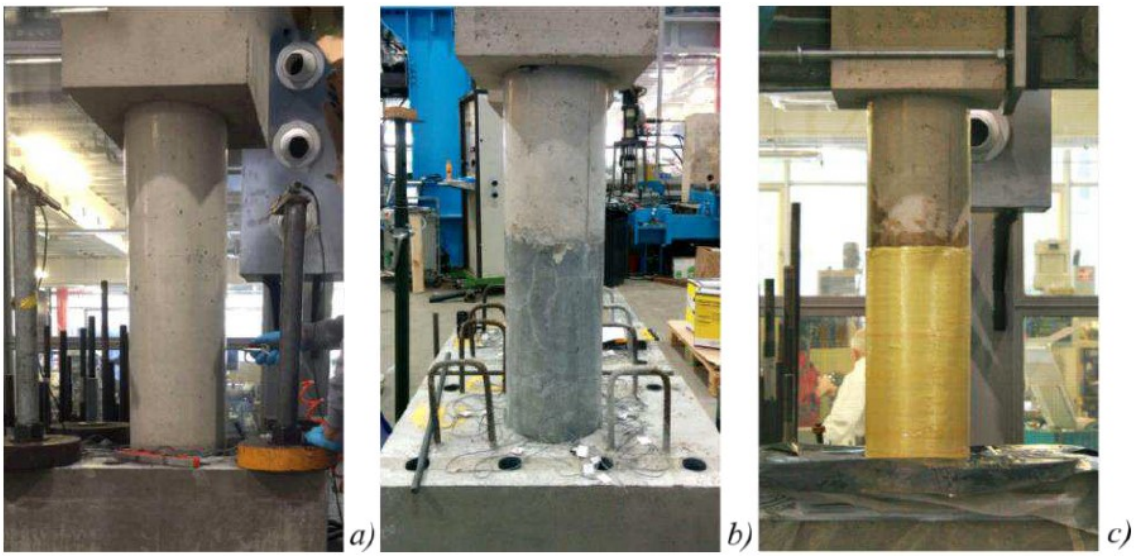


Figure 5.4 a) Typical Ø250 reinforced conventional concrete specimen (RC), b) Ø250 reinforced rubberised concrete specimen (RRuC), c) Ø250 AFRP confined reinforced rubberised concrete member (CRRuC)

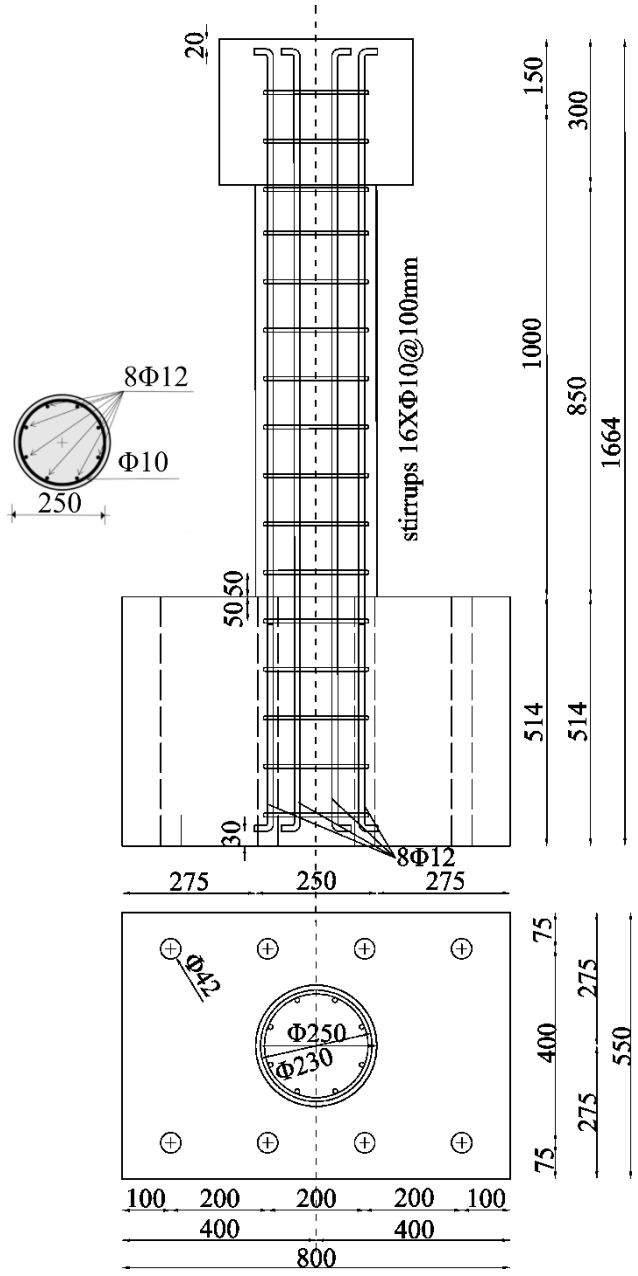


Figure 5.5 Ø250 specimens geometry and reinforcement layout

Ø350 mm diameter specimens

In total ten Ø350 specimens were constructed which were provided with identical longitudinal reinforcement detailing consisting of 8×Ø16 mm symmetrically positioned rebars (Figure 5.6). All members had transverse circular stirrups of Ø10 mm at a spacing s_w=70 mm except D350-R60-F0-N2S which had s_w=40 mm. Six of the Ø350 specimens were provided with rubberised concrete (RRuC) on a length of approximately 450 mm from the footing-to-column interface as depicted in Figure 5.7a. Four of these six members were externally confined (CRRuC) with two or three layers

of Aramid fibre reinforced polymer (AFRP), with confined lengths measured from the bottom of the column as illustrated in Figure 5.7b. Each Ø350 specimen had a rectangular footing (2100×600×400 mm) at its base, and a rectangular cap (400×400×300 mm) at the top. The effective cantilever height of all Ø350 specimens was 1350mm. The geometry and reinforcement layout of all Ø350 specimens are shown in Figure 5.6. The footing and column caps were designed to remain relatively rigid in comparison with the beam-column specimen.

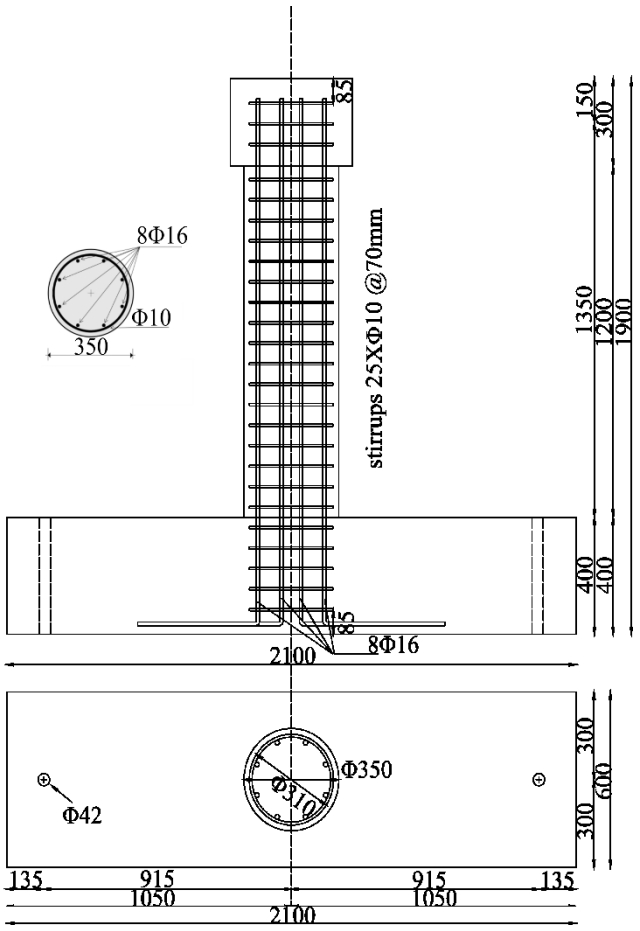


Figure 5.6 Ø350 specimens geometry and reinforcement layout

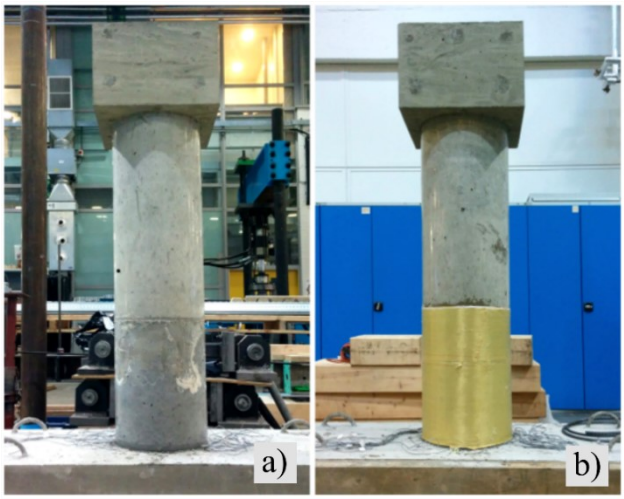


Figure 5.7 a) Typical Ø350 reinforced rubberised concrete specimen (RRuC), b) typical Ø350 AFRP confined reinforced rubberised concrete member (CRRuC)

5.3 Testing arrangements

Two test rigs were used for the beam-column experiments considering the geometries of specimens with Ø250 and Ø350 mm diameters. Both rigs were designed to apply lateral cyclic displacements and co-existing axial loading on the upright placed specimens. After the application of a constant axial load, the lateral cyclic deformations were applied based on one cycle at 0.25, 0.5, and 0.75×δ_y, followed by three cycles at 1.0δ_y, 2.0 δ_y and (2+2n)×δ_y up to fracture of the flexural reinforcement where δ_y is the estimated lateral yield deformation and n=1, 2, 3, 4, etc. The displacement rate was controlled at the rate of 0.3mm/s. The tests continued until fracture of at least one logitudinal reinforcement bar occurred or the lateral actuator displacement limit was reached. The typical lateral displacement sequence applied for all the specimens is shown in Figure 5.8. Detailed information of both rigs is described in this section.

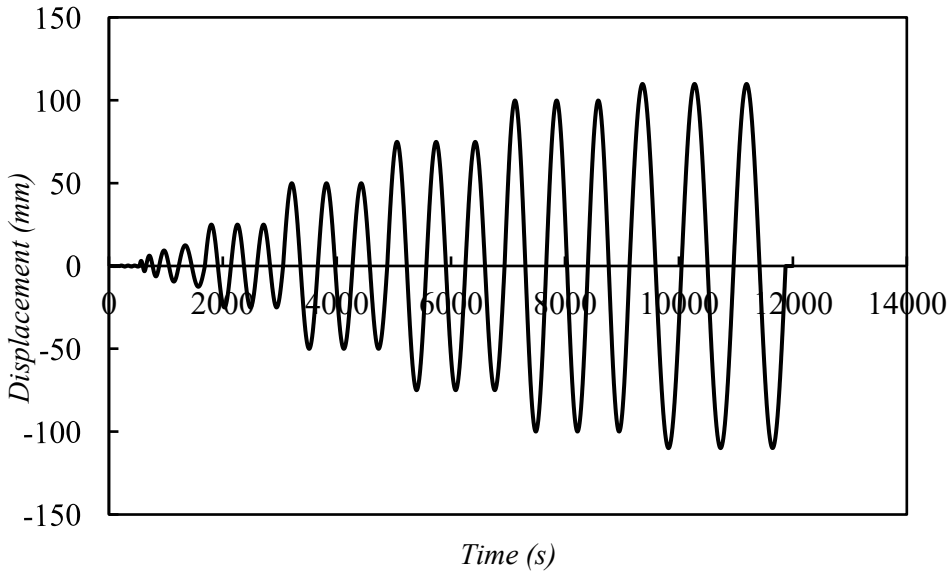


Figure 5.8 Typical lateral displacement sequence

5.3.1 Self-reaction test rig for Ø250 members

The test set-up employed for the Ø250 mm members is shown in Figure 5.9 while a schematic is given in Figure 5.10. The specimens were tested in an upright position, with the horizontal and vertical actuators allowing lateral cyclic deformations and coexisting gravity loading, respectively, to be applied. The specimen was connected to the 130mm base plate through four high tensile 33 mm bolts, which were prestressed up to a load of 180 kN. The 1200×1200×130 mm base plate was also connected to the frame using 20 bolts of 24 mm diameter.

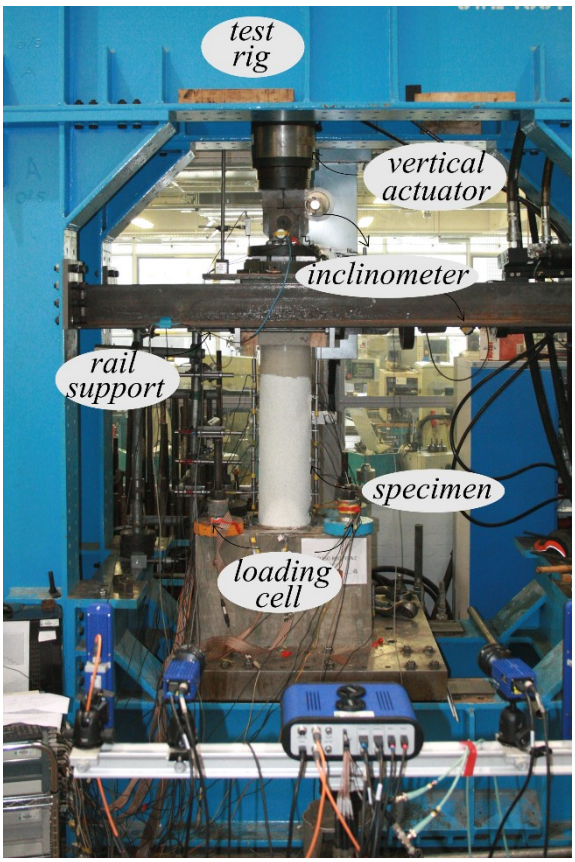


Figure 5.9 General view of the self-reacting test rig

The vertical and horizontal actions were applied to the specimen through hydraulic actuators. The vertical actuator had a static load capacity of 500 kN and maximum stroke of ± 50 mm, while the lateral actuator had a static capacity of 250 kN with a stroke of ± 125 mm. Load cells were directly mounted on both actuators. The backs of the actuators were stressed to low friction swivel joints which were connected to 1200×1200 mm reaction plates through 6 bolts of 24 mm diameter. The reaction plates were directly connected to the test frame through bolts of 24 mm diameter as shown in Figure 5.10.

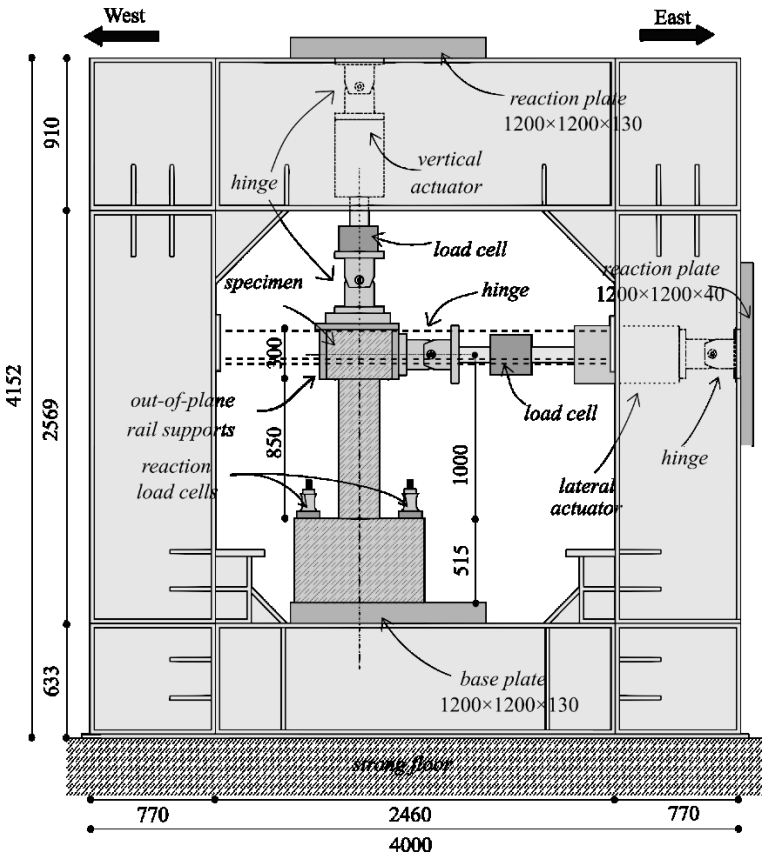


Figure 5.10 Schematic of self-reacting test rig

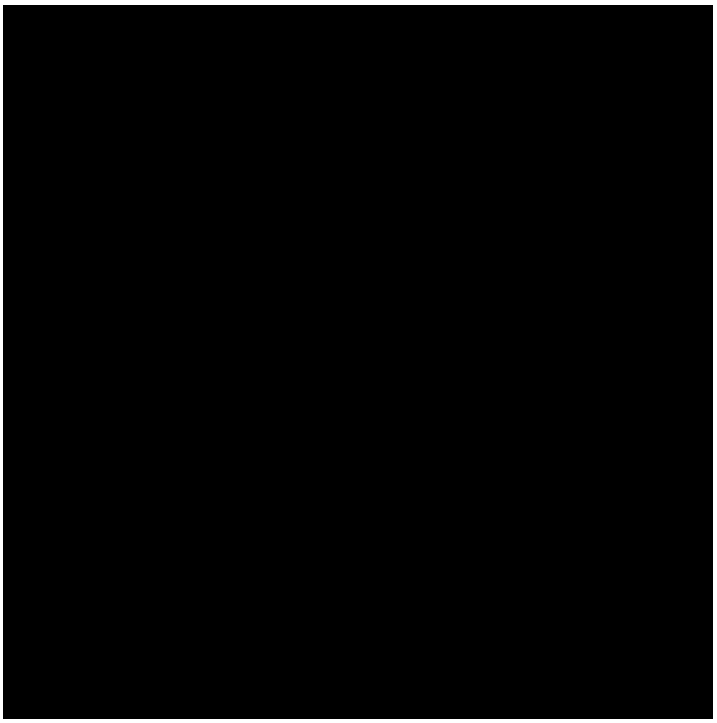


Figure 5.11 Detailed dimensions of load transfer box

Two low friction swivel joints were used to connect each actuator to both the test frame and the specimen to allow free in-plane movement (see Figure 5.10). A load transfer box was built using steel plates around the column cap providing connection between the vertical and horizontal loading devices and the column. As shown in Figure 5.11, the two 600×300×30 mm steel plates were stressed as a pair through four bolts with the diameter of 30 mm. The top plate of 600×600×30 mm was connected to the side plates through two screws along each side. The actuators were also stressed to the transfer box on the cap of the specimen through swivel joints using four 24 mm bolts.

In order to restraint the out of plane movement, a pair of angle steel rail supports were connected to the frame using 8 bolts with diameter of 24 mm on both the front and back side of the specimen. As shown in Figure 5.9, the rails were located along the cap of the specimen. Wood blocks were provided between the support rails and member cap to avoid direct contact between the steel components. The contact face of the rail and wood block were fully greased to reduce additional friction. Detailed geometry of the rail is provided in Figure 5.12.

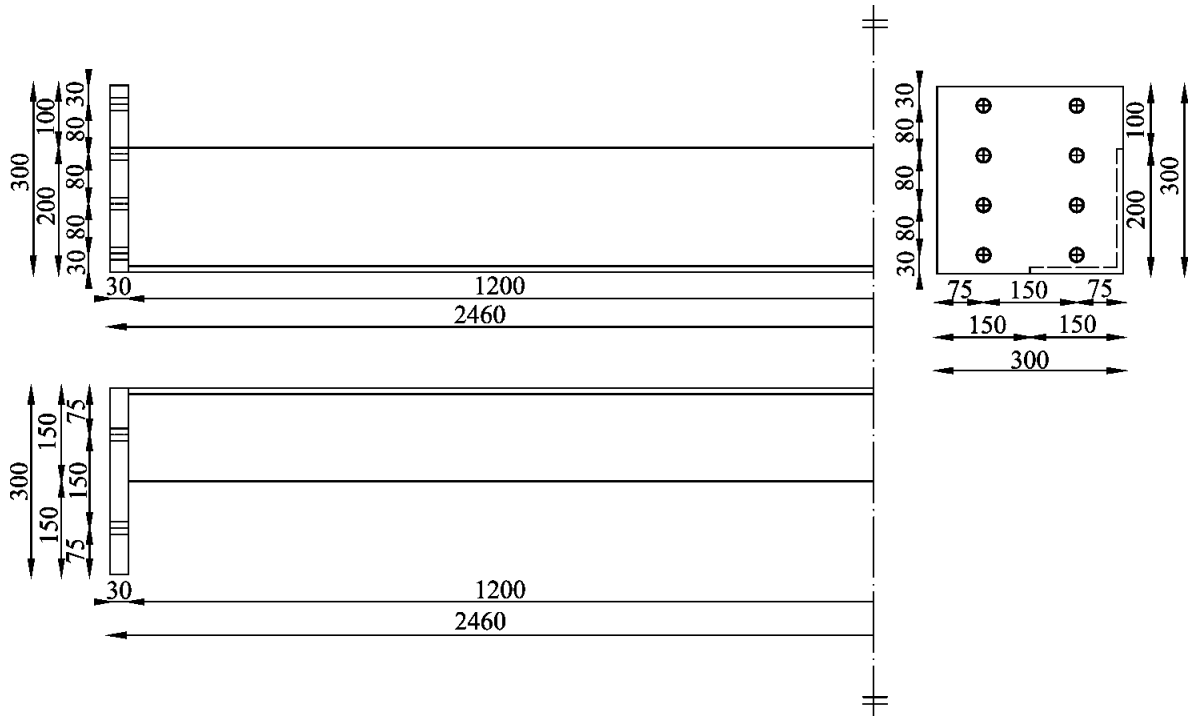


Figure 5.12 Dimensions of out-of-plane rail support

5.3.2 Large-scale test rig for Ø350 members

Similar to the self-reaction rig described above, the large-scale rig allowed the Ø350 beam-column members to be subjected to lateral cyclic displacements and co-existing axial loading. The general

views of the testing arrangement for the large-scale test rig are shown in Figure 5.13. The vertical reaction frame was fixed to the strong floor. Two side braces were added to ensure the out of plane stability of the frame as shown in Figure 5.14. A separate horizontal reaction frame was also employed which was connected to the horizontal loading devices. The reaction frame was fully fixed to the strong floor through 6 pre-stressed Ø33 mm ties (see Figure 5.14).

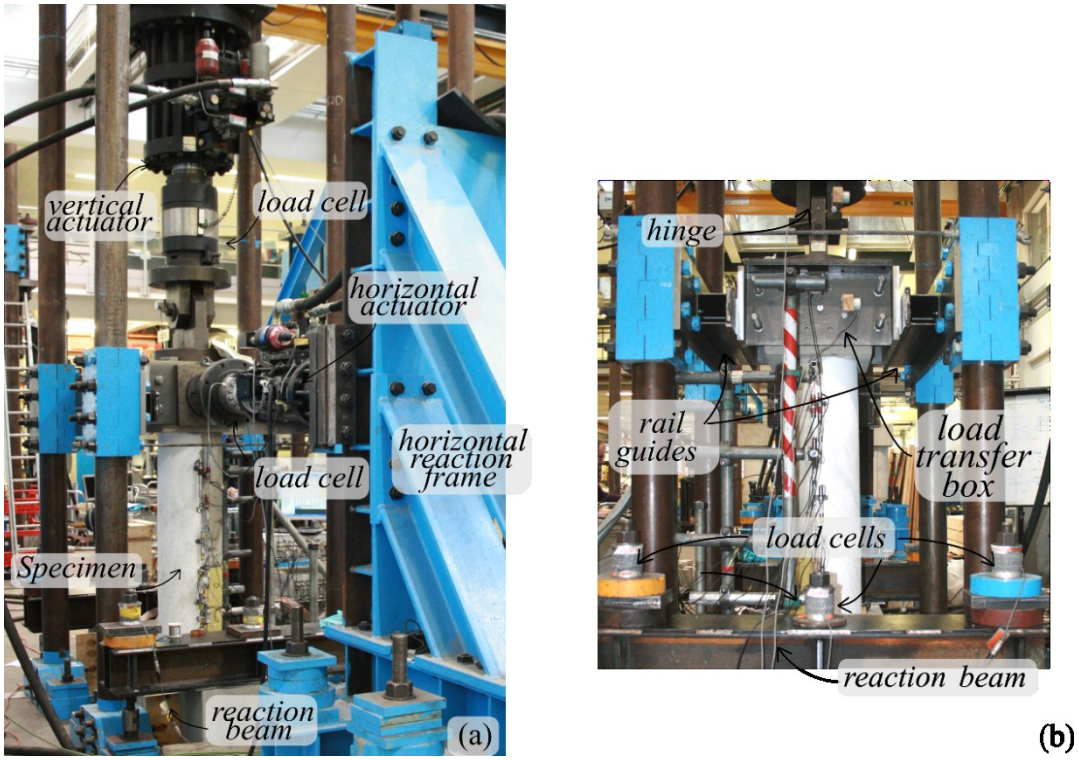


Figure 5.13 General view of the large-scale test rig: a) skew view, b) side view

The footing of the Ø350 specimens was directly supported and connected by means of 4 pre-stressed Ø33 mm ties and transfer beams to the strong floor of the laboratory to avoid potential sliding and overturning under lateral loads. Pre-stressing loads were recorded by means of 600 kN load cells positioned at each tie (see Figure 5.14). The vertical and horizontal loads applied on the Ø350 members were generated through the same loading system as for the Ø250 members. The vertical actuator with a static loading capacity of 1000 kN and maximum stroke of ± 50 mm was fixed on the top of the loading frame through 4 bolts of 33 mm in diameter, while the horizontal actuator had a static capacity of 250 kN with a stroke range of ± 125 mm was connected to the horizontal reaction frame with 6 Ø24 mm bolts. Both actuators incorporated load cells as well as two low friction swivel hinges allowing in-plane rotation. The same loading transfer box as in Figure 5.11 was used in the large-scale test rig which was bolted to the vertical and horizontal loading system. The out-of-plane movement of the column members was also restrained in the test set-up with a pair of steel rail guides as shown Figure 5.13b and Figure 5.14. The steel rails with a

hollow square cross-section were bolted to the steel frame which was fixed onto the floor through 4 Ø60 mm bolts. PTFE (Polytetrafluoroethylene) sheets were provided and fully greased between the contact faces of the steel rails and loading box to avoid additional friction.

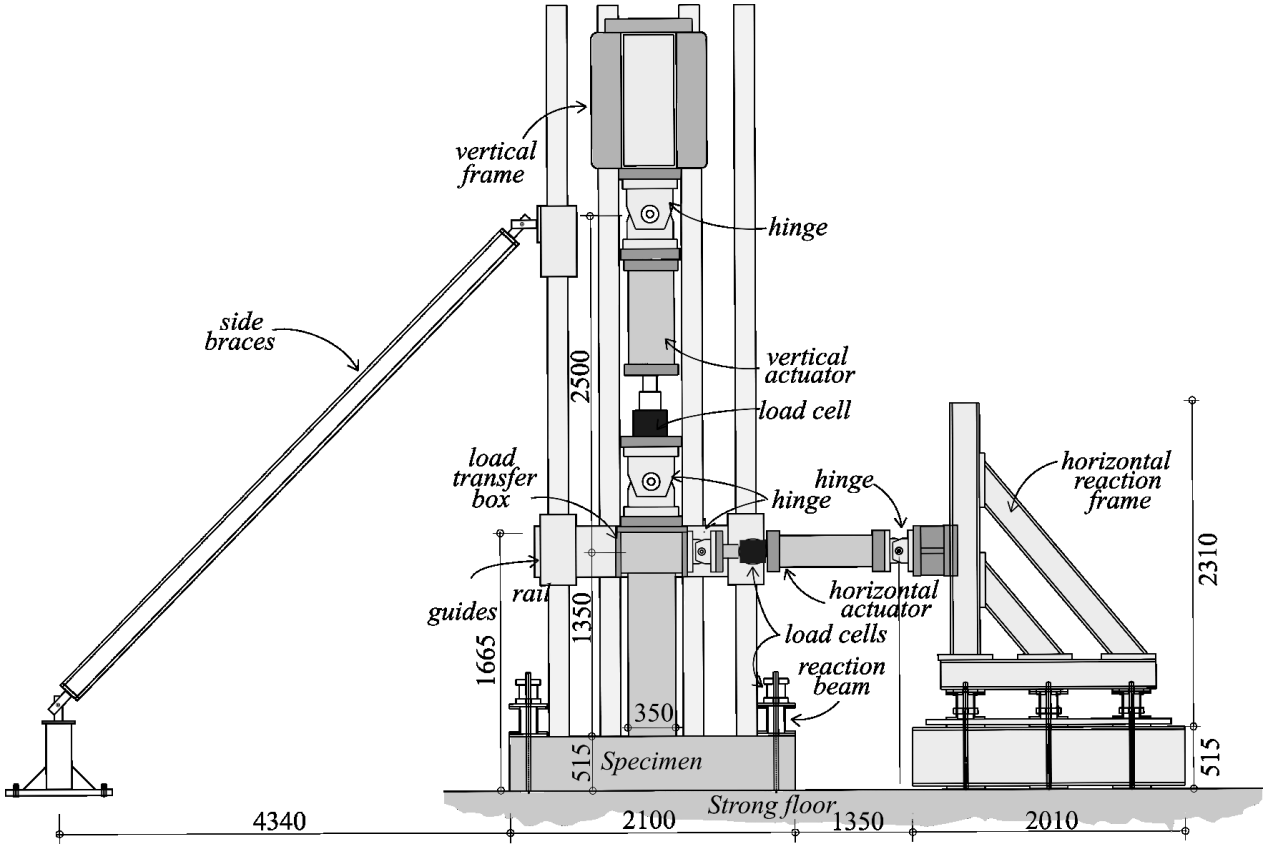


Figure 5.14 Schematic of large-scale test rig

5.4 Instrumentation

Detailed instrumentations were used for each of the 14 specimens to measure the response at each loading stage. The vertical and horizontal loads and displacements applied through the actuators were obtained directly from load cells. In additionally, the following types of instrumentation were used:

- Strain gauges on reinforcement and AFRP sheets.
- Linear variable displacement transducers (LVDT) on column surface.
- Inclinometers.
- Digital image correlation (DIC) system.

All the strain gauges, LVDTs and inclinometers were connected to the data logger which recorded the readings throughout the test automatically.

5.4.1 Strain gauges

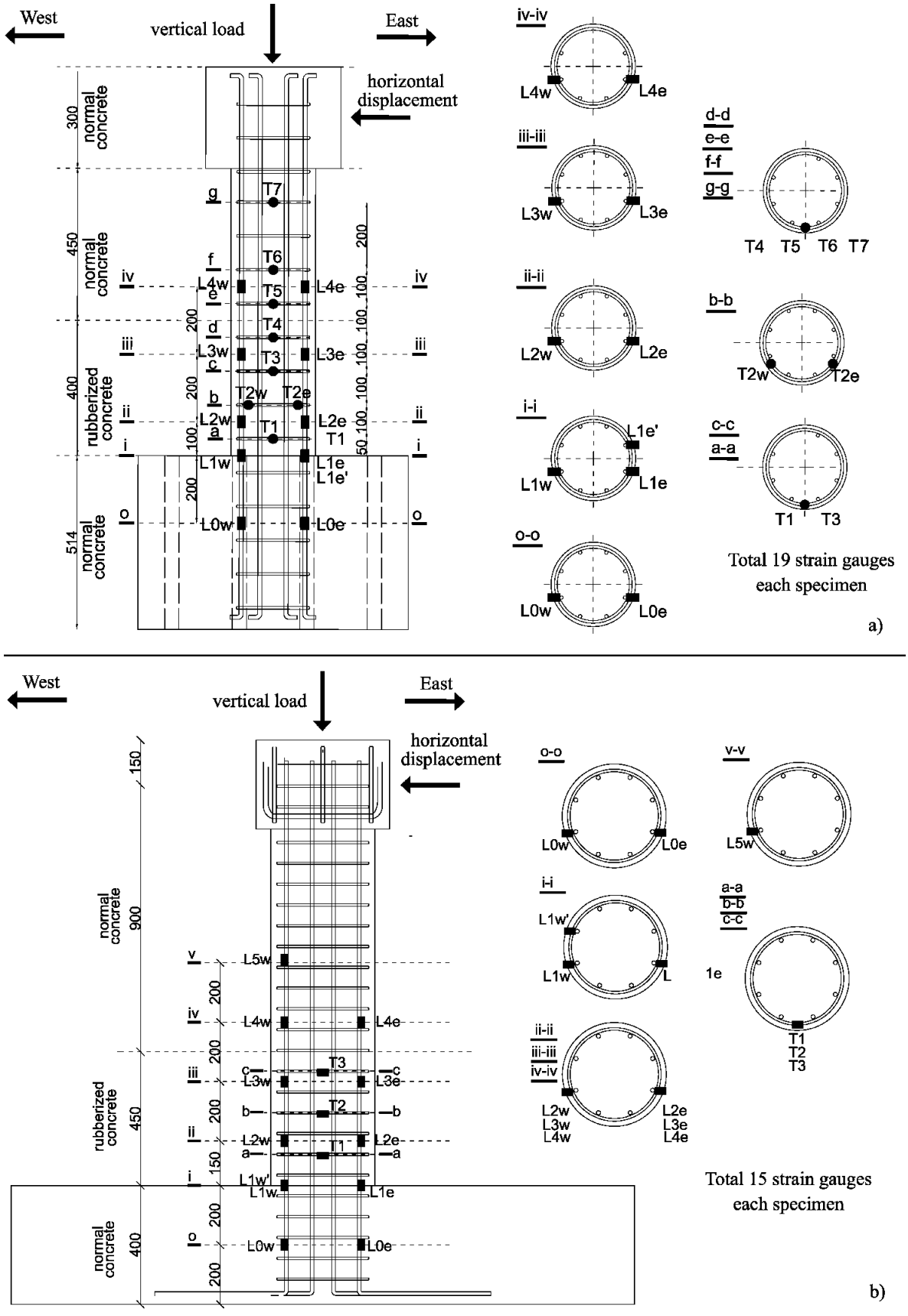


Figure 5.15 Detailed strain gauge locations for: a) Ø250 specimens, b) Ø350 specimens

In order to assess the stress and strain distribution along the stirrups and longitudinal reinforcement, electrical resistance strain gauges were mounted on the surface of the steel reinforcement in the critical area of the columns. Detailed strain gauge locations of Ø250 and Ø350 members are shown in Figure 5.15a and b. Type FLAB-5 strain gauges with gauge length of 5 mm were adopted. The gauge factor was 2.1±1% and the electrical resistance was 120±0.5Ω.

As noted in Figure 5.15, strain gauges were glued along the directions of the rebars as a pair on the furthest west and east longitudinal rebars at each level of the member height. The strain distributions in stirrups along the member were also recorded by strain gauges in the horizontal directions. The strain gauges were located on the outer face of the rebars at selected locations (see Figure 5.16). The surfaces of the strain gauges were protected by waterproof material afterwards.

The labels for strain gauges adopted in Figure 5.15, L*n*W/ L*n*E and T*n*W/ T*n*E, indicate strain gauges along longitudinal (L) or transverse (T) direction, and level of the specimen height (*n*=0, 1, 2…) and the sides of locations (W=west, E=east). It should be noted that gauges L1W/L1E represent the longitudinal strain gauges at the interface of the column and foundation block of each specimen and L0W/L0E indicate gauges recording the reinforcement stains in the foundation block. In addition, strain gauges were also provided on the surface of AFRP jackets for the specimens with external confinement. Gauges were mounted on the AFRP jackets both transversely and vertically along the west and east axes of the member (see Figure 5.17) to obtain the strain distribution in the confinement in both directions. The vertical gauges were attached at the same locations as L1W/L1E and L3W/L3E, while the transverse gauges were located at the same position as T1 and T2.

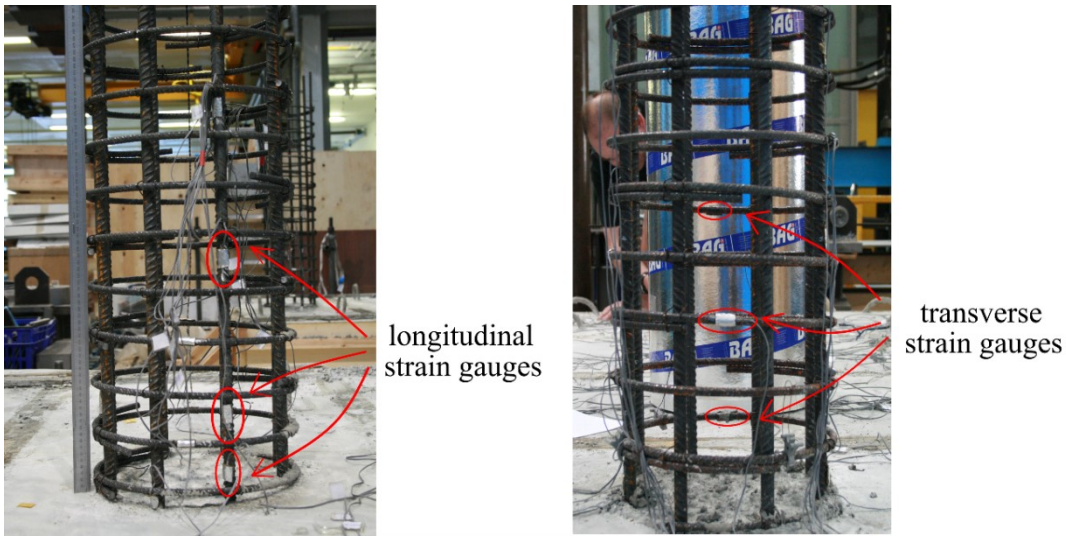


Figure 5.16 Strain gauges on: a) longitudinal reinforcement, b) stirrups with waterproof material

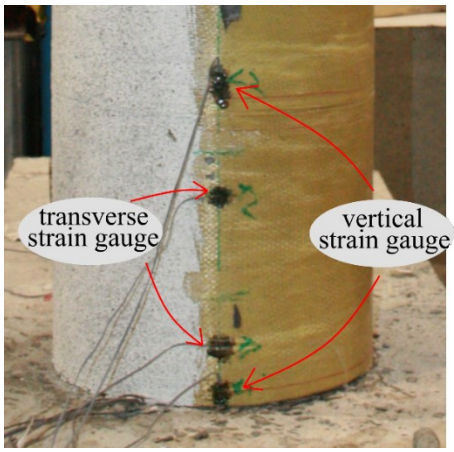


Figure 5.17 strain gauges on external confinement

5.4.2 Linear variable displacement transducers (LVDT) and inclinometers

In addition to the load cells and displacement transducers incorporated within the horizontal and vertical actuators, a series of displacement transducers were positioned along the height of the column as shown in Figure 5.18.

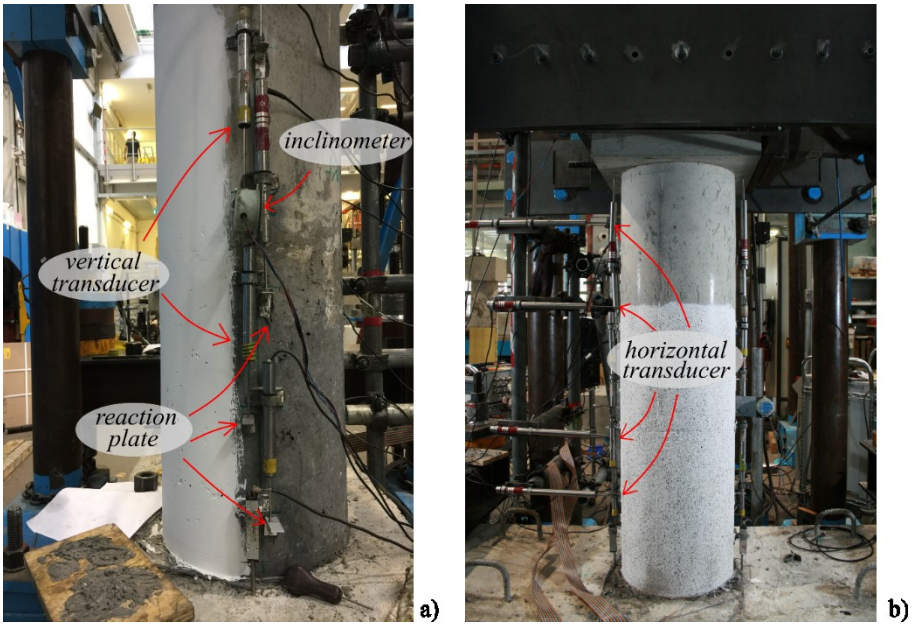


Figure 5.18 General view: a) vertical LVDTs layout, b) horizontal LVDTs layout

As shown in Figure 5.19, the horizontal transducers H1-H6 recorded the lateral displacement of the specimen at each level of the column height. Vertical transducers W1-W9/E1-E9 and the

corresponding reaction plates were mounted directly on the column surface along the west and east axes of test specimens. These measurements represented the concrete surface strains under cyclic displacements. In addition, transducers H0 and W0/N0 were also placed at the foot block of each specimen to check any overall displacement or rocking effects.

Two inclinometers were placed at the vertical and horizontal actuators (see Figure 5.9) to obtain the rotation of the actuators during the test. As shown in Figure 5.14, another two inclinometers (INC1/INC2) were mounted at the specimen top and the interface of the rubberised concrete and normal concrete.

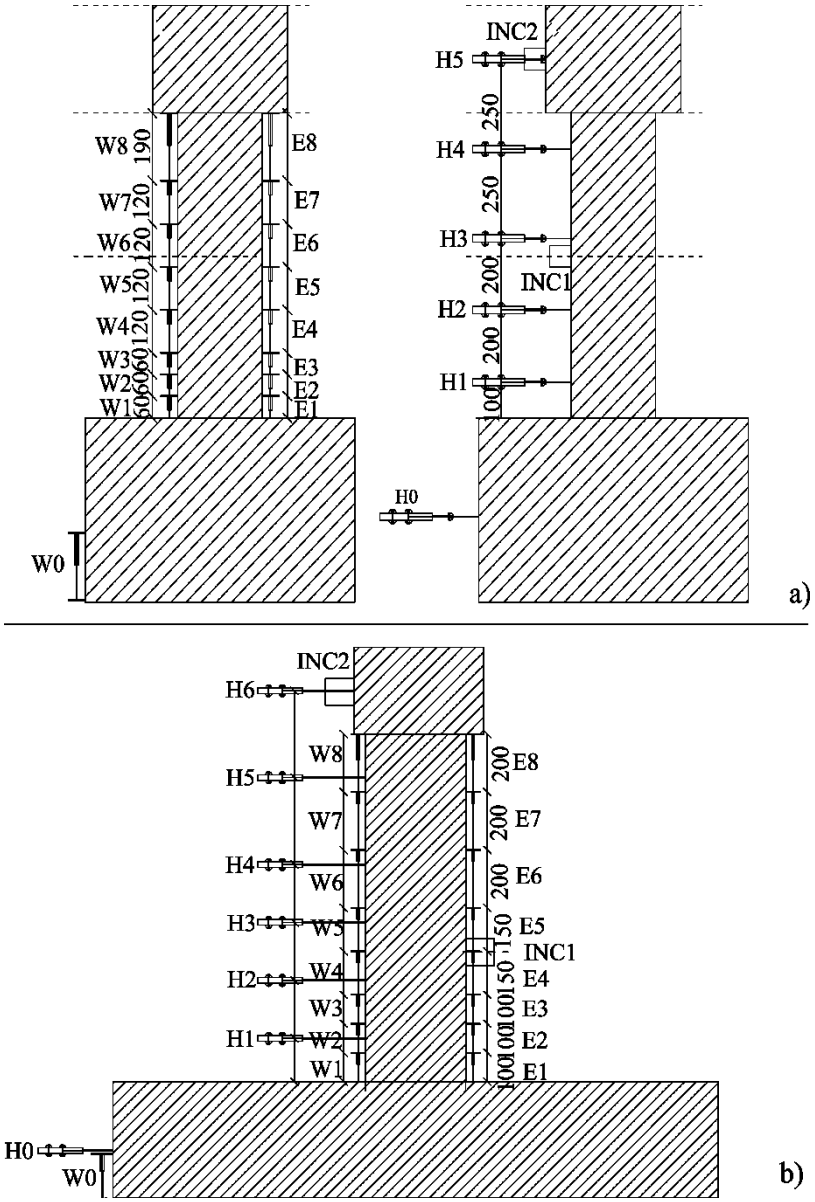


Figure 5.19 Locations of LVDTs and inclinometers: a) Ø250 specimens, b) Ø350 specimens

5.4.3 Digital image correlation (DIC) system

The DIC system, discussed in more detail in Section 4.2, was also adopted in the beam-column member tests, and was used to capture the concrete surface crack propagation and member displacements (see Figure 5.20). The front surfaces of the test specimens were painted with two layers of water-based white paint and a black speckle with dots of size 0.5-2.0 mm to create high contrast black/white patterns for the post-processing sequence. The accuracy of the resulting surface deformation, based on the pre-set parameters, as discussed in Section 4.2, had a range of 0.4μm, whilst the uncertainty was within a range of 0.15%.

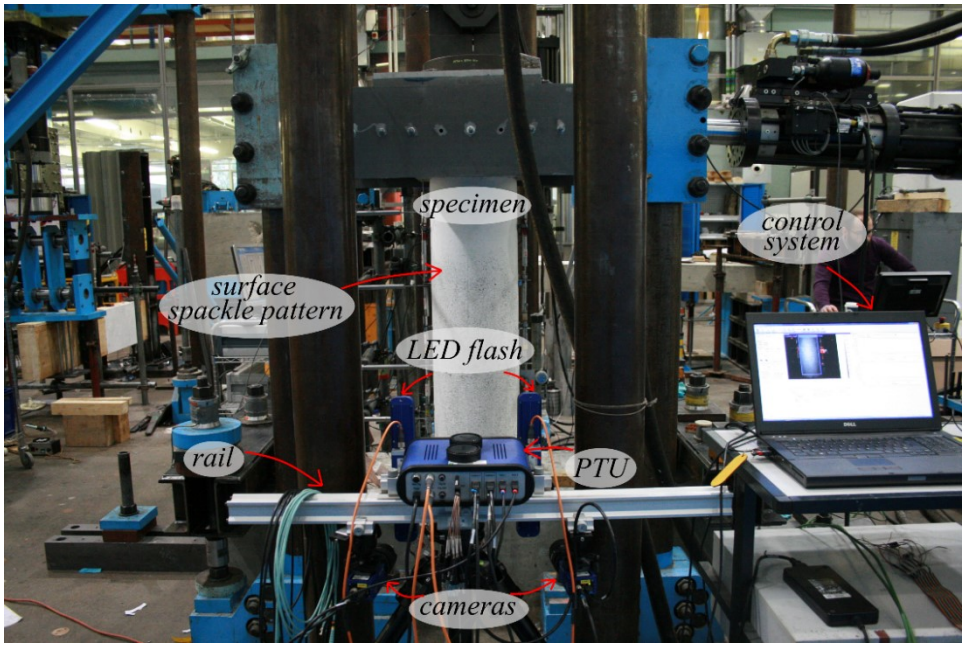


Figure 5.20 DIC system setup

5.5 Concluding remarks

This chapter provides a general overview of the experimental methodology used for the reinforced rubberised concrete (RRuC) beam-column member tests. In total 14 member specimens were tested to investigate the cyclic behaviour of reinforced concrete beam-column members incorporating a significant proportion of recycled rubber particles as a replacement for mineral aggregates. Tests were carried out on large scale members of circular cross-section, with and without external confinement, and with different proportions of rubber content and axial loads. Two test rig arrangements were used for specimen diameters of 250 and 350 mm. Two specimens 250 mm diameter were made of normal concrete while the other specimens contained rubberised concrete in

the lower half of the members. Five RRuC specimens were externally confined with two or three layers of aramid fibre reinforced polymer (AFRP) sheets.

In order to monitor the member behaviour, detailed instrumentations system were employed. LVDTs were used to obtain the overall displacements of the specimens, while inclinometers measured the corresponding rotations. The strain distributions along longitudinal and transverse reinforcement as well as the external confinement were recorded by strain gauges at various selected locations. Detailed concrete surface deformation and crack propagation were captured by the DIC system. The detailed test results and observations are presented in the following chapter.

Chapter 6

6 Results of beam-column member tests

Nomenclature

Greek letters

δ – lateral deformation
Δ– lateral drift ratio
δ_f – lateral deformation at rebar fracture
δ_y – lateral deformation at yielding
δ_u – lateral deformation at ultimate load corresponding herein to 20% decrease in capacity
ε – strain
ε_1 – axial strain
ε_2 – lateral strain
$\varepsilon_{c0,1}$ – crushing strain of conventional reference concrete
ε_{cu} – ultimate concrete strain
ε_{cu2} – ultimate concrete strain for simplified design
ε_{c0u2} - ultimate concrete strain of reference concrete for simplified design
ε_{rcu2} – ultimate concrete strain of rubberised concrete for simplified design
ε_{2u} – ultimate lateral strain
$\varepsilon_{rc1,1}$ – axial crushing strain
$\varepsilon_{rc2,1}$ – lateral strain at crushing
ε_{rcc1} – axial strain for confined rubberised concrete
ε_{rcc2} – lateral strain for confined rubberised concrete
ε_{rccu} – ultimate strain for confined rubberised concrete
ε_{sy} – steel yield strain
θ – slope
λ - factor for the size of mineral aggregate replaced
ρ_{vr} – volumetric rubber ratio
μ_ψ / $\mu_{\psi+1}$ - rotation ductility
ν – axial load ratio
σ – stress
τ – plasticity length parameter
Δ_y – drift at yielding
ψ – rotation
ψ_y - rotation at yielding
ψ_p – plastic rotation
ψ_u - ultimate rotation

Lowercase latin letters

d_b – longitudinal rebar diameter
e – eccentricity
f_{c0} – cylinder reference concrete strength
f_c – cylinder concrete strength
$f_{c,cube}$ – cube concrete strength
f_{ct} – concrete splitting strength
f_{cc} – confined concrete strength
$f_{c,top}$ - cylinder concrete strength above the rubberised region
f_{rc} – rubberised concrete strength
f_{rcc} – confined concrete strength
f_t/ f_{tw} – fracture strength of the longitudinal/ transverse steel
f_y/f_{yw} –yield strength of the longitudinal/ transverse steel
h_f– footing depth
$k_{cr,test}$ – test member inelastic stiffness
l_f– footing length
l_{rub} – rubberised concrete region length
l_{conf} - externally confined region length
s_w – stirrup spacing

Uppercase latin letters

D – column diameter
E_d – energy dissipation
E_s – steel elastic modulus
L – moment length
$L_{pl,test}$ – test assessed plasticity length
L_{tot} – total member length
M – bending moment
M_y – bending moment at yield
M_u – bending moment at ultimate
N – axial load
N_{max} – maximum axial capacity
Ø – diameter
P – applied lateral load
V – shear force
V_{max} – maximum lateral force
V_y – yielding lateral load

This chapter provides the results and observations from experimental study on reinforced concrete beam-column members subjected to inelastic lateral cyclic deformations and different levels of co-existing axial loads. A detailed account of the test results from 14 large-scale tests on 350 mm and 250 mm diameter circular reinforced rubberised concrete members, with or without external FRP confinement, is given. As mentioned in the previous chapter, the specimen reference adopts the format of D*vvv*-R*xx*-F*y*-N*z* which indicatse the column diameter (D) in mm, the rubber content (R) in percentage, the number of confining layers (F) and the level of axial load (N: N0 for members without axial load, N1 for 'low' axial loads below 10% of the nominal cross-section axial capacity, and N2 for 'high' axial loads above 10% of the nominal cross-section axial capacity).

6.1 Material properties

6.1.1 Concrete characteristics

Ready-mix concrete was used in the footing and top parts of the members, whilst concrete with high rubber content mixed in the laboratory was placed in the bottom regions. Two rubberised concrete mixes with volumetric replacement ratios of ρ_{vr}=0.45 and ρ_{vr}=0.60, described below in detail and referred to here as R45 and R60, were considered. The constituents used in the materials prepared in the laboratory were mineral aggregates, rubber particles, binders, tap water and admixtures with the quantities as provided in Table 6-1.

Table 6-1 Concrete mix

		R45	R60
Binders (kg)		314	425
Aggregates (kg)	5-10 mm	740	400
	0-5 mm	479	328
Rubber (kg)	0/5 mm	134	149
	5/10 mm	24	33
	10/20 mm	110	148
Admixture (l)	(PL+SPL)	7.6	7.6
w/c (-)		0.35	0.35

The rubberised concrete mix methodology was the same as introduced in Section 3.2 previously. Both ready-mix normal concrete and rubberised concrete materials were poured in the prepared member forms and compacted using concrete vibrators. The casting was performed in three phases, namely the normal concrete in the footing in wood forms, the rubberised region of the column in plastic circular forms (BAG column formers) and, ultimately, the remaining region of the column and column cap with normal concrete. After casting, these were covered with plastic sheets to

ensure concrete hydration. The column forms were removed from the members approximately one week after casting. The sampling of concrete materials was made according to EN206-1. The compressive strength was determined using Ø100×200 mm cylinders and 100 mm cubes, and the splitting strength was measured using Ø102×254 mm cylinders following the same procedure as described in Section 3.2 before. Material tests were carried out at 28 days and at the time of testing.

The complete compressive stress-strain σ-ε responses were assessed by means of testing for the rubberised concrete (R45 and R60), confined rubberised concrete (R45F2 and R60F3), as well as for the reference conventional concrete (R00) from which the rubberised concrete materials were derived (see Figure 6.1). These are plotted in a normalised form in relation to the strength f_{rc} as well as axial and corresponding lateral crushing strain of the rubberised concrete ($\varepsilon_{rc1,1}$ and $\varepsilon_{rc2,1}$, respectively).

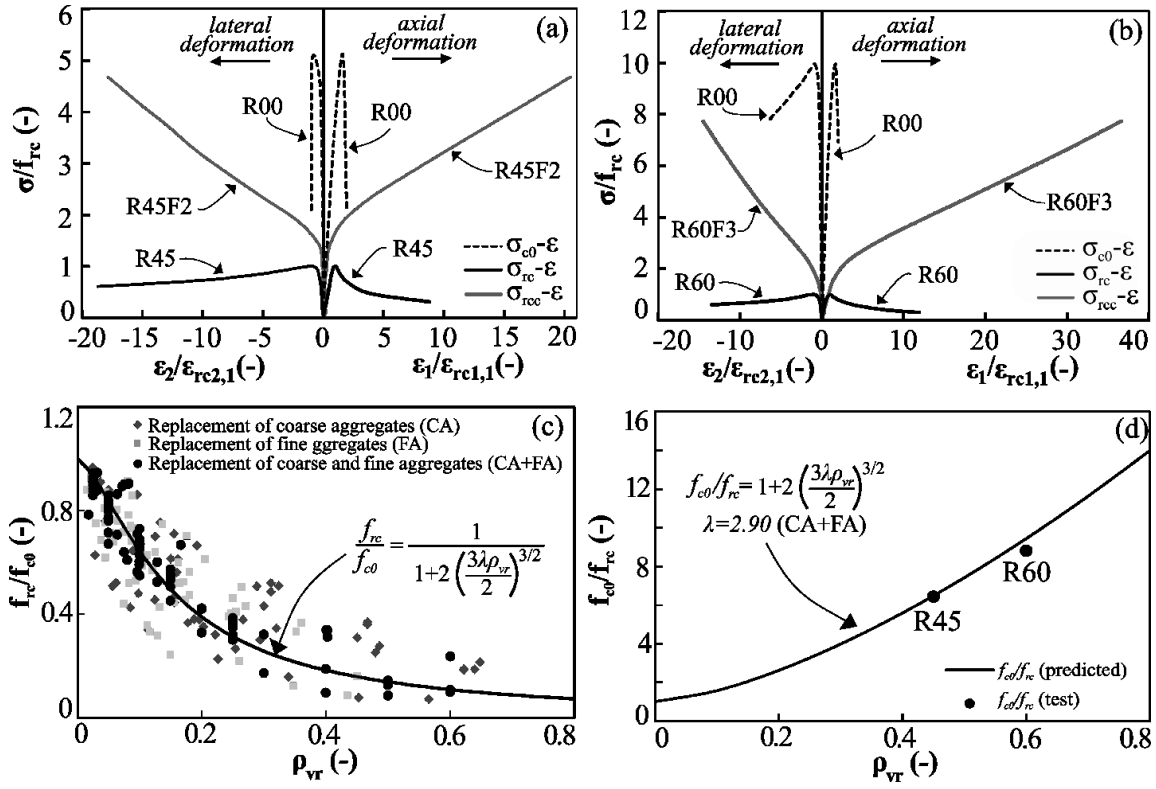


Figure 6.1 Constitutive σ-ε response: a) R45 Ø100 cylinders, b) R60 Ø100 cylinders, c) strength degradation curve (Section 3.4), d) strength degradation curve and properties of rubberised concrete materials

As shown in Figures 6.1a,b, the compressive strengths of the reference concrete materials f_{c0} are about 5 times that of the rubberised R45 counterpart and about 10 times of the R60 counterpart. These values are in good agreement with predictions using the rubberised-to-reference concrete compressive strength degradation curve (f_{rc}/f_{c0}), as described in Chapter 3 (see Figure 6.1c). As

observed in Figure 6.1d, for λ=2.90 that corresponds to the replacement of both coarse and fine mineral aggregates, the predicted values (f_{c0}/f_{rc}) are in good agreement with data points representing the σ/f_{rc} ratios at peak for the cases described above for the curves in Figures 6.1a,b.

For the five externally confined specimens, two (F2) or three (F3) layers of aramid fibre reinforced polymer (AFRP) sheets oriented perpendicular to the longitudinal axis of the member were used as external confinement, as indicated in Table 6-2. The same arrangement was also used in the corresponding Ø100×200 mm cylinders for material testing in order to determine the confined properties (see Table 6-2). Aramid sheets S&P Grade A120/290 with 0.2 mm design thickness, mean sheet elastic modulus 116 kN/mm^2, mean tensile strength of sheet 2400 N/mm^2 and mean strain capacity of sheet 2-10%, were used. A 100-mm overlapping length for the member specimens, and 50 mm for material cylinders, was adopted to ensure sufficient transfer length. Two-component epoxy resin bonding adhesive from the same producer as the aramid sheets, conforming to BS EN 1504-4 was applied to the fibre sheets prior to their application to the specimen.

Table 6-2 Concrete properties for each specimen

Specimen	Age of testing	Concrete strength						
		Bottom region						Top region
		at 28 days			at testing		confined	at 28 days
		f_c or f_{rc} (MPa)	$f_{c,cube}$ or $f_{rc,cube}$ (MPa)	f_{ct} or f_{rct} (MPa)	f_c or f_{rc}(MPa)	$f_{c,cube}$ or $f_{rc,cube}$ (MPa)	f_{rcc} (MPa)	$f_{c,top}$ (MPa)
D250-R00-F0-N2	87	70.2	77.0	4.99	74.1	89.7	-	74.1
D250-R00-F0-N1	27	70.2	77.0	4.99	72.0	86.8	-	72.0
D250-R60-F0-N1	54	6.58	11.8	1.14	7.54	-	-	73.0
D250-R60-F3-N1	68	6.58	11.8	1.14	9.17	-	54.6	72.9
D350-R45-F0-N0	111	9.17	16.1	1.58	10.7	18.3	-	76.0
D350-R45-F0-N1	98	9.17	16.1	1.58	10.5	18.1	-	75.8
D350-R60-F0-N0	27	7.95	11.5	1.22	7.91	11.6	-	55.4
D350-R60-F0-N1	34	7.95	11.5	1.22	7.97	13.4	-	59.7
D350-R60-F0-N2	56	7.95	11.5	1.22	8.14	12.9	-	61.9
D350-R60-F0-N2S	63	7.95	11.5	1.22	7.99	11.6	-	65.0
D350-R45-F2-N0	117	9.17	16.1	1.58	10.7	18.3	54.6	76.1
D350-R45-F2-N2	85	9.17	16.1	1.58	10.4	17.9	54.6	75.6
D350-R60-F3-N0	48	7.95	11.5	1.22	7.94	11.7	43.7	62.4
D350-R60-F3-N2	42	7.95	11.5	1.22	7.94	11.7	43.7	60.9

6.1.2 Steel reinforcement

In all specimens, hot rolled deformed bars with diameters of Ø10 mm, Ø12 and Ø16 mm, made of steel Grade B500C, were used without any surface treatment for stirrups and longitudinal reinforcement, depending on the specimen, as indicated in Table 5-1. In total, three batches of steel bars were tested for D250 (Ø10_B1 and Ø12 bars), D350-R45 (Ø10_B2 and Ø16_B2 bars) and D350-R60 (Ø10_B3 and Ø16_B3 bars) specimen groups, among which Ø10 bars were used for transverse hoops while Ø12 and Ø16 bars were used for longitudinal reinforcement. The properties of the steel materials were different for each of the casting groups. The reinforcement tests were carried out under displacement control with the rate of 3 mm/min using the arrangement shown in Figure 6.2. The average stress-strain diagrams of all rebars are shown in Figure 6.3a,b. It can be noted that longitudinal bars Ø12, Ø16_B2 and Ø16_B3 showed clear yield plateaus at around f_y =526 Mpa, 551 MPa and 574 MPa respectively, whilst the yield strengths of Ø10 bars were determined using 0.2% offset (see Figure 6.3b) which resulted in yield strengths f_{yw} of 496 Mpa, 507 Mpa and 588 MPa for each of the three batches respectively. The detailed reinforcement properties are given in Table 6-3 based on the average results from steel coupon tests on a minimum of three samples.

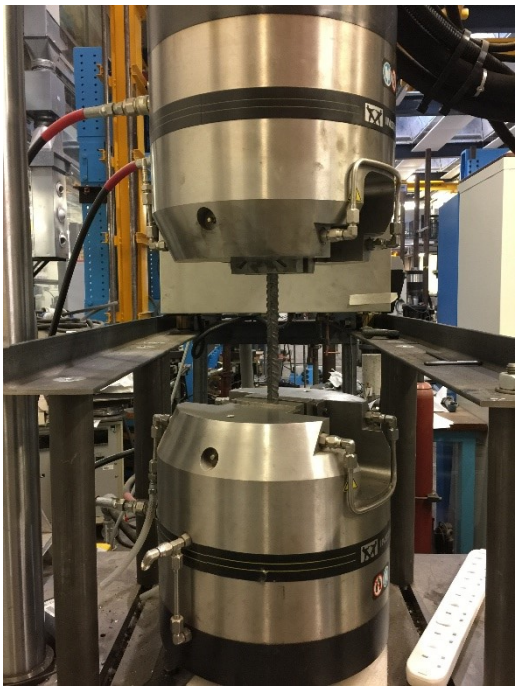


Figure 6.2 Steel rebar testing

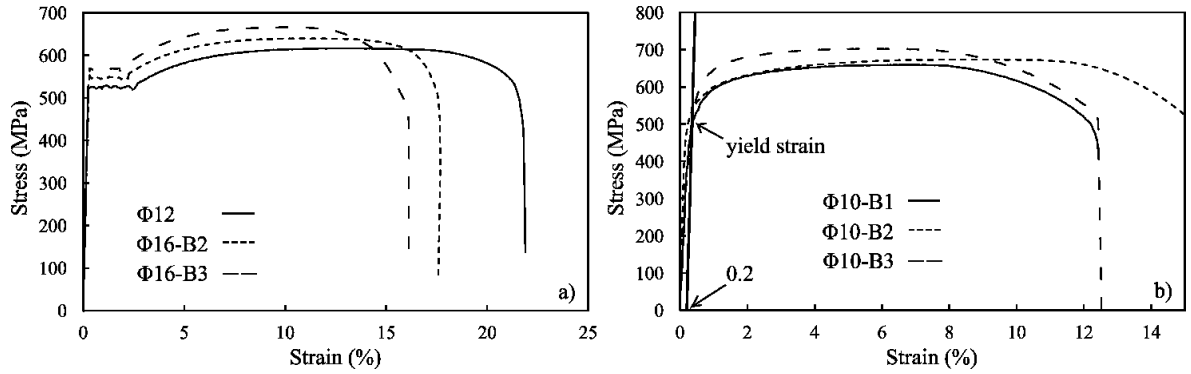


Figure 6.3 Typical stress-strain characteristics of reinforcement

Table 6-3 Summary of reinforcement properties

Specimen	E_s (GPa)	Longitudinal (Ø12, Ø16)		Transverse (Ø10)	
		f_y/f_t (MPa)	ε_u (%)	f_{yw}/f_{tw} (MPa)	ε_{uw} (%)
D250-R00 (R60)	200	526/619	12.0	496/603	6.9
D350-R45	200	574/675	10.1	507/636	7.9
D350-R60	200	551/640	10.9	588/713	5.4

6.2 Test results and observations

As noted before, the experimental assessment included ten Ø350 and four Ø250 diameter beam-column members. Out of these 14 specimens, and as shown in Table 5-1 in Chapter 5, seven were Reinforced Rubberised Concrete (RRuC) members provided with only stirrup confinement (D250-R60-F0-N1, D350-R45-F0-N0, D350-R45-F0-N1, D350-R60-F0-N0, D350-R60-F0-N1, D350-R60-F0-N2, D350-R60-F0-N2S), two were conventional Reinforced Concrete (RC) (D250-R00-F0-N2, D250-R00-F0-N1), whilst the remaining five were Confined Reinforced Rubberised Concrete (CRRuC) specimens which were provided with stirrups and external AFRP confinement (D250-R60-F3-N1, D350-R45-F2-N0, D350-R45-F2-N2, D350-R60-F3-N0, D350-R60-F3-N2). As indicated in Table 6-4, the axial load applied to the members varied between zero and 800 kN which corresponds to about 15% of the nominal axial capacity accounting for the concrete strength and the contribution of the longitudinal reinforcement. In all cases, the axial load was first applied and maintained throughout the test, followed by application of the lateral cyclic displacements up to failure using a displacement rate of about 0.3mm/sec. It should be noted that the influence of the horizontal component of the axial load at large lateral deformations was accounted for in determining the lateral loads. Specimen D250-R00-F0-N2 with conventional reinforced concrete was tested first under high level of axial load as the pilot test followed by the remaining 13 specimens (Elghazouli et al. 2018).

Table 6-4 Summary of test results

Specimen	N (kN)	V_y (kN)	V_{max} (kN)	δ_y (mm)	δ_u (mm)	δ_f (mm)	M_y (kNm)	M_u (kNm)	ψ_y ×1000 (rad)	ψ_u ×1000 (rad)
D250-R00-F0-N2[1)]	400	54.1	73.7	11.0	24.8	N/F[2)]	85.3	86.1	11.0	24.8
D250-R00-F0-N1	200	54.0	57.3	10.8	41.5	62.5	56.0	61.2	10.8	41.8
D250-R60-F0-N1	20	29.8	38.5	10.8	63.4	87.5	30.1	39.0	10.8	63.4
D250-R60-F3-N1	200	39.9	43.4	10.8	59.8	87.5	42.1	47.0	10.8	59.8
D350-R45-F0-N0	0	63.9	80.1	12.4	96.6	110	86.3	108.2	9.2	71.5
D350-R45-F0-N1	140	70.4	84.9	14.6	96.0	100	96.1	116.7	10.8	71.1
D350-R60-F0-N0	0	60.3	74.0	12.7	96.9	112	81.5	100.1	9.4	71.8
D350-R60-F0-N1	140	66.5	77.0	15.1	101.9	100	91.2	106.6	11.2	75.5
D350-R60-F0-N2	280	67.5	79.2	15.8	72.9	100	95.6	111.4	11.7	54.0
D350-R60-F0-N2S	280	65.9	73.9	14.6	79.5	100	91.6	104.9	10.8	58.9
D350-R45-F2-N0	0	63.7	84.4	12.4	107.4	113	86.2	114.3	9.2	79.5
D350-R45-F2-N2	800	82.6	94.4	12.0	76.4	N/F[2)]	115.5	140.7	8.9	56.6
D350-R60-F3-N0	0	55.0	78.1	12.2	102.6	100	68.9	105.7	9.0	76.0
D350-R60-F3-N2	800	57.9	78.1	12.0	72.5	N/F[2)]	83.9	119.0	8.9	53.9

[1)]Specimen D250-R00-F0-N2 was the pilot test specimen

[2)]N/F – specimens for which fracture of flexural reinforcement was not observed

6.2.1 Rubberised concrete members

D250-R00-F0-N2 (pilot test)

Specimen D250-R00-F0-N2 was tested under a high axial load of P= 400 kN (Figure 6.4b) as a pilot test. As shown in Figure 6.4a, the yield of longitudinal reinforcement occurred at the displacement of δ_y= 11.0 mm with a corresponding lateral load V_y= 42.4 kN. The lateral capacity was V_{max}= 73.7 kN with a corresponding displacement of 17.2 mm. Concrete crushing under caused severe loss of stiffness after the peak point and the failure mode of this member, consequently, was the total crushing of the concrete core at the column-foot interface followed by fracture of reinforcement as shown in Figure 6.4c.

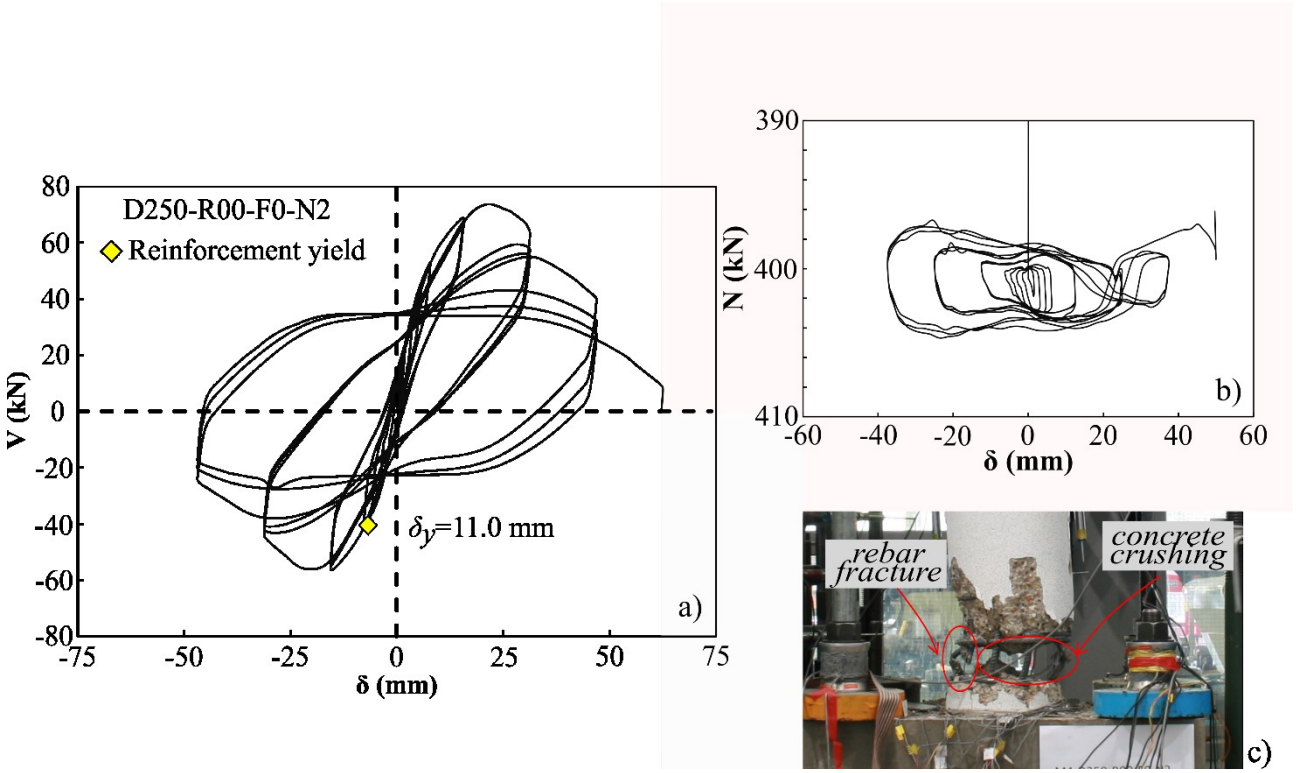


Figure 6.4 D250-R00-F0-N2: a) hysteric load-deformation response, b) vertical load applied, c) reinforcement fracture

D250-R00-F0-N1

The reinforced conventional concrete (RC) specimen (D250-R00-F0-N1) was first tested as a control specimen under the vertical load of 200 kN after the pilot test. The hysteretic load-displacement response of the specimen as well as the vertical load variation are shown in Figure 6.5.

As indicated in Figure 6.5a, the first yield of longitudinal reinforcement occurred at δ_y= 10 mm and lateral load V_y =54.0 kN. The peak load V_{max}=57.3 kN was reached at a displacement of 16.5 mm.

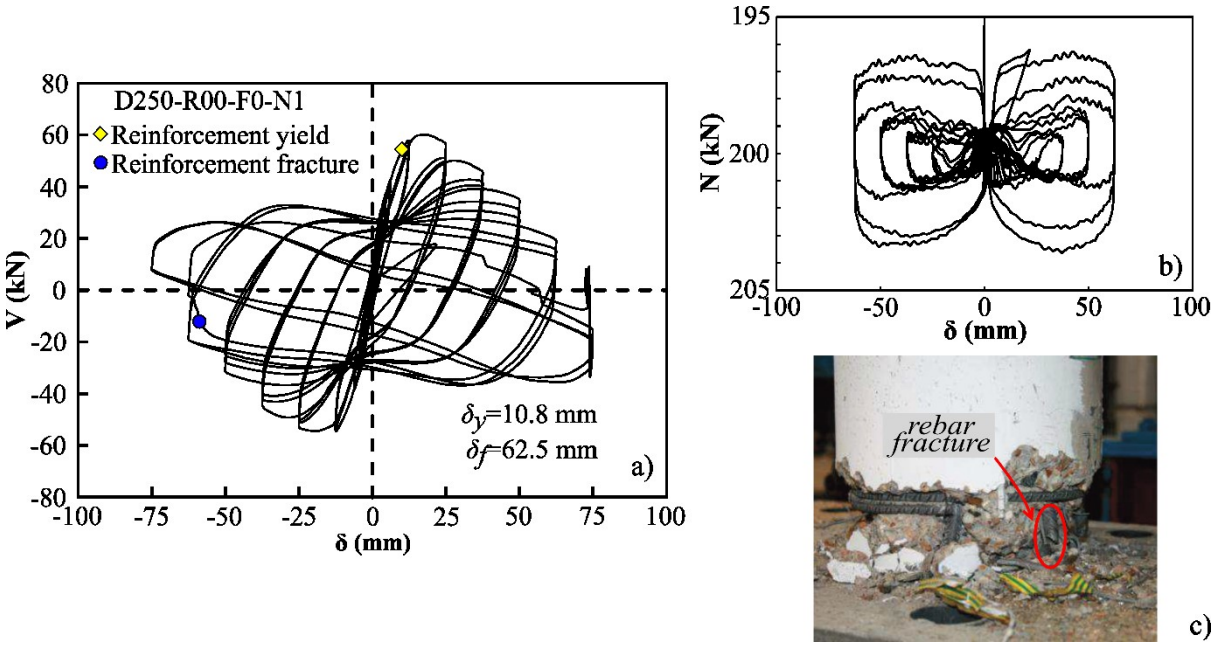


Figure 6.5 D250-R00-F0-N1: a) hysteric load-deformation response, b) vertical load applied, c) reinforcement fracture

Beyond the peak load point, the specimen showed a relatively rapid strength reduction with the increase of lateral displacement reaching an ultimate displacement δ_u =41.5 mm (corresponding to 20% reduction in lateral capacity). The vertical load applied on the specimen was constant during the test procedure with less than 5% variation as shown in Figure 6.5b. Concrete spalling was localised above the column-footing interface followed by rupture of the reinforcement at a lateral displacement of 62.5 mm (i.e. approaching Δ=6.4% drift with respect to the specimen height) as shown in Figure 6.5c.

D250-R60-F0-N1

For the Ø250 rubberised reinforced concrete (RRuC) specimen (D250-R60-F0-N1), the vertical load applied was 20 kN. The hysteretic load-displacement response of the specimen as well as the vertical load applied are shown in Figure 6.6a,b. In this specimen, yielding of the main reinforcement occurred at δ_y of about 10 mm with a corresponding lateral load V_y of 29.8 kN. The peak load of V_{max}=38.5 kN was reached at 22.6 mm and was followed by a relatively gradual compressive crushing behaviour of the concrete in comparison to the conventional RC member (D250-R00-F0-N1) which led to a higher ultimate displacement of 63.4 mm. Instead of full spalling of the concrete cover, the rubberised concrete were still held after crushing. The fracture of the

longitudinal reinforcement occurred in the third cycle with displacement amplitude of 87.5 mm (9% drift) as indicated in Figure 6.6c.

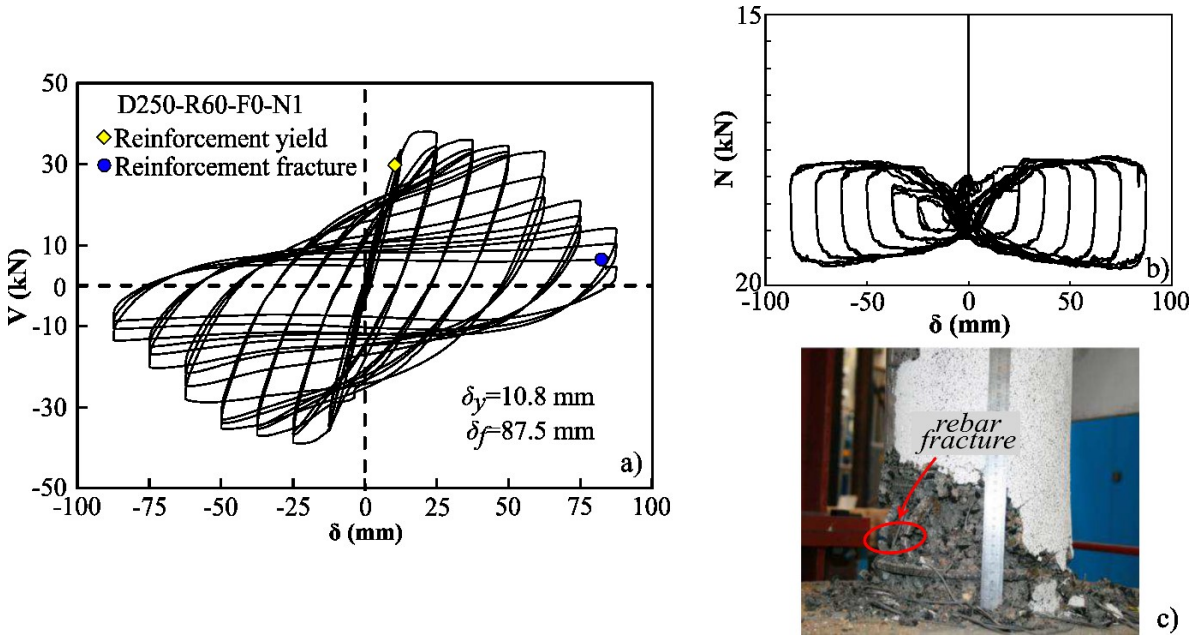


Figure 6.6 D250-R60-F0-N1: a) hysteric load-deformation response, b) vertical load applied, c) reinforcement fracture

D350-R45-F0-N0

The Ø350 RRuC member D350-R45-F0-N0 was tested as a cantilever without axial load. Cracking was followed by flexural yielding at δ_y = 12.4 mm, with corresponding drift levels of about Δ_y=1.0% as recorded by strain gauges positioned at the column-to-footing interface (L1W). The lateral load at yield V_y was 63.9 kN as indicated in Figure 6.7a. The ultimate lateral load V_{max} reached was 80.1 kN at a displacement of 48.1 mm. The reinforcement fractured at a lateral displacement of 110 mm as shown in Figure 6.7b. The maximum lateral load V_{max} was reached at an ultimate displacement of 96.6 mm

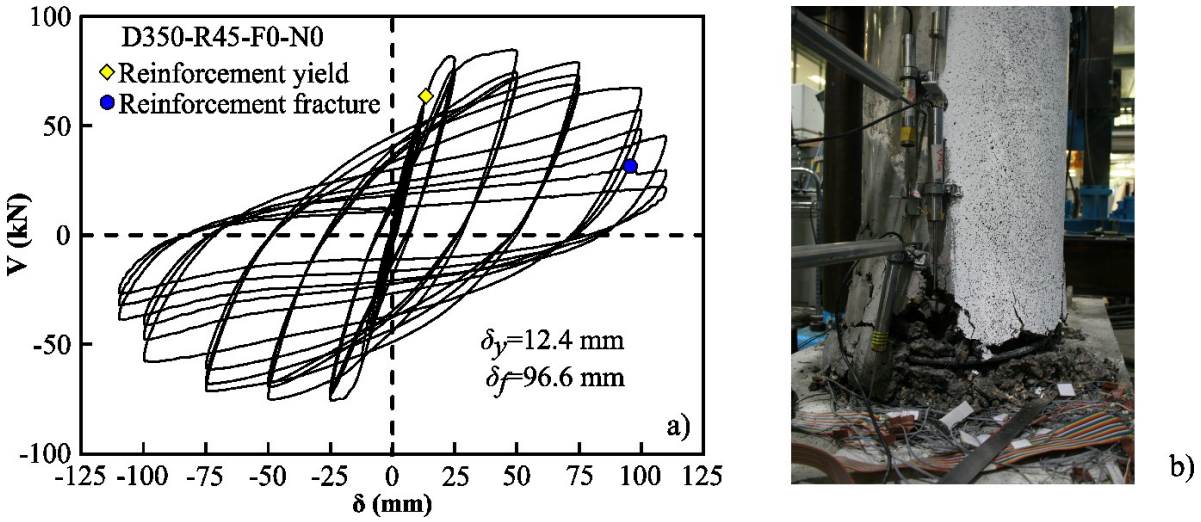


Figure 6.7 D350-R45-F0-N0: a) hysteric load-deformation response, b) reinforcement fracture

D350-R45-F0-N1

The axial load applied for Specimen D350-R45-F0-N1 was P=140 kN. Compared to the previous member without axial load, the yield load V_y and yield displacement δ_y were slightly increased (70.4 kN and 14.6 mm respectively as shown in Figure 6.8a). Although the ultimate load V_{max} also increased slightly to 84.9 kN, the corresponding displacement was about 25 mm. The ultimate displacement showed similar value of δ_u =96.0 mm. The fracture of reinforcement also occurred at a lateral displacement δ_f =100 mm as indicated in Figure 6.8c. The applied vertical load had a variance about 7% throughout the test (Figure 6.8b). It can be noted that the presence of axial load delayed the yielding of longitudinal reinforcement, and increased the initial stiffness of the member leading to a higher lateral load capacity with lower lateral drift.

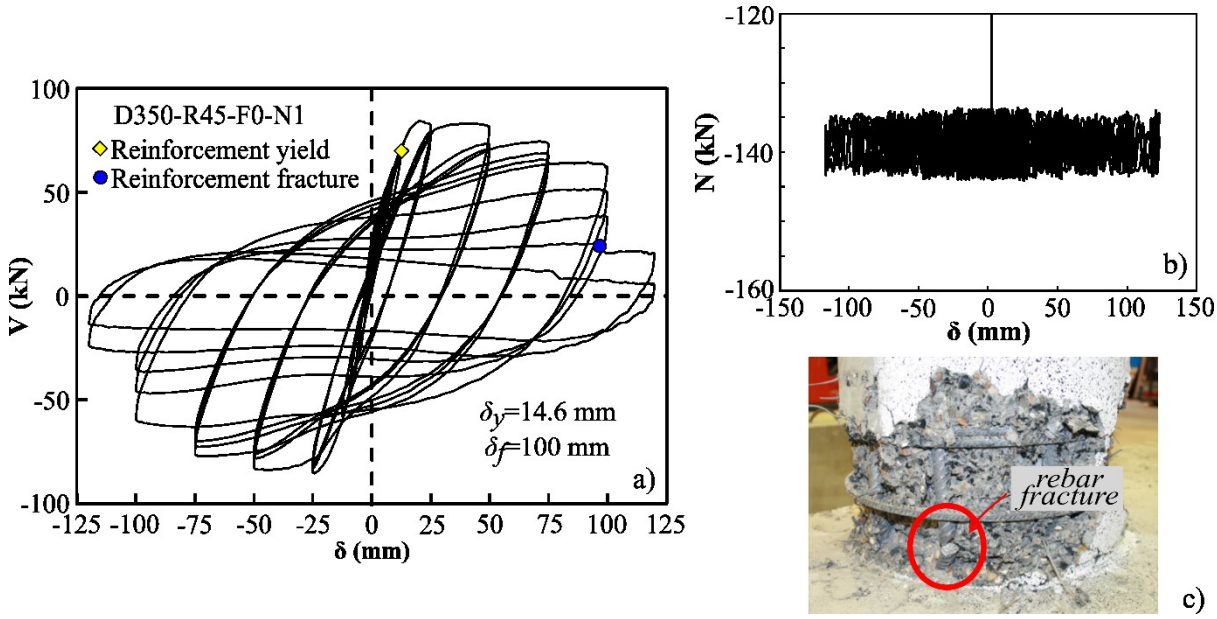


Figure 6.8 D350-R45-F0-N1: a) hysteric load-deformation response, b) vertical load applied, c) reinforcement fracture

D350-R60-F0-N0

Due to the reduction of rubberised concrete strength in this specimen compared to the first cantilever member (D350-R45-F0-N0), the yield and peak lateral loads of D350-R60-F0-N0 were both reduced to V_y =60.3 kN and V_{max} =74 kN with corresponding displacements of 12.7 mm and 45.1 mm. The ultimate displacement was δ_u =96.9 mm as for the previous Ø350 members. The load-displacement response and failure mode are shown in Figure 6.9a,b.

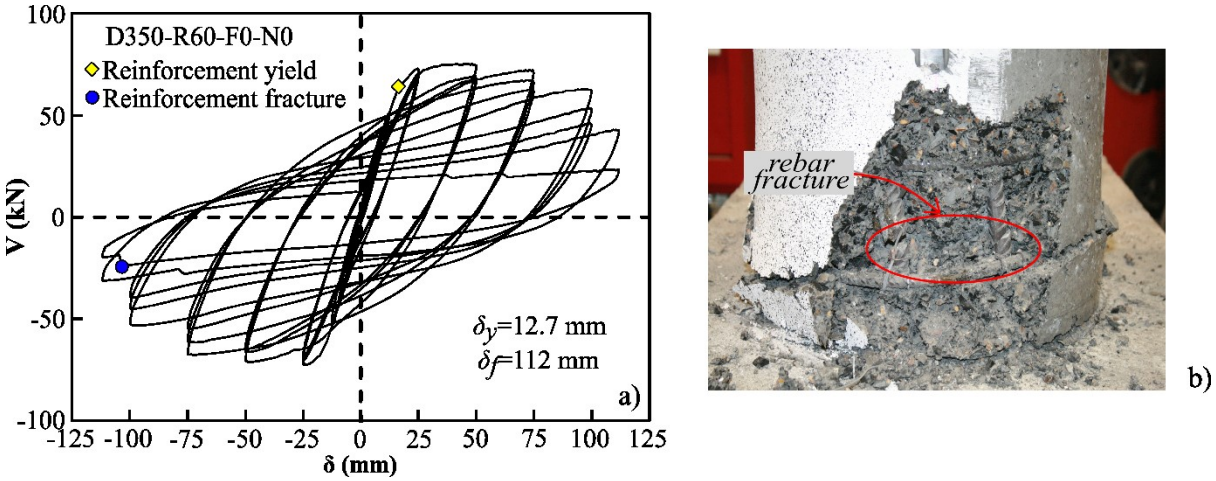


Figure 6.9 D350-R60-F0-N0: a) hysteric load-deformation response, b) reinforcement fracture

D350-R60-F0-N1

Similar to the previous cases, the higher vertical load of P=140 kN applied on D350-R60-F0-N1 increased its yield load V_y, yield displacement δ_y and the peak load V_{max} to 66.5 kN, 15.1 mm and 77.0 kN, respectively, with a reduced peak load displacement of 25 mm as shown in Figure 6.10a. The vertical load was also stable with only 7% variation (Figure 6.10b). The ultimate displacement (δ_u =101.9 mm) was slightly higher while the lateral displacement when the longitudinal reinforcement fractured was lower (δ_u =100 mm) as shown in Figure 6.10c.

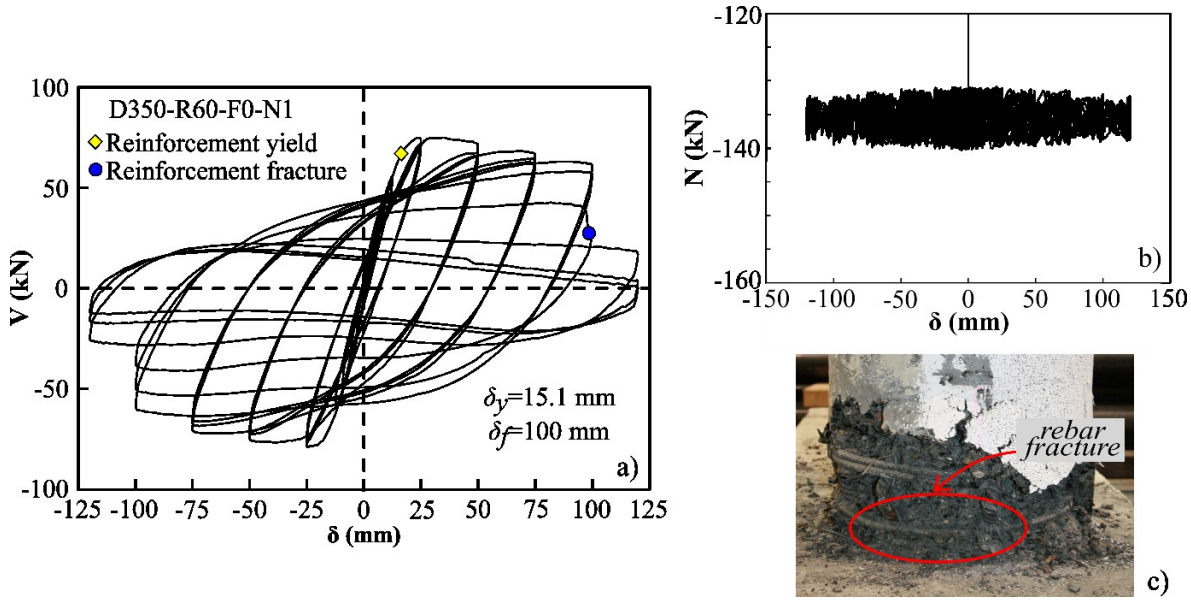


Figure 6.10 D350-R60-F0-N1: a) hysteric load-deformation response, b) vertical load applied, c) reinforcement fracture

D350-R60-F0-N2

Specimen D350-R60-F0-N2 with double the axial load P=280 kN (Figure 6.10b) showed further increase of member stiffness and lateral load capacity. The yield displacement was δ_y =15.8 mm with the lateral load V_y=67.5 kN. The peak lateral load V_{max}=79.2 kN occurred at a lateral displacement of 24 mm. On the other hand, it can be noted from Figure 6.11a that the increase of axial load caused more significant degradation compared to previous cases. The first fracture of reinforcement occurred at a displacement δ_f=100 mm in the first cycle (Figure 6.11c).

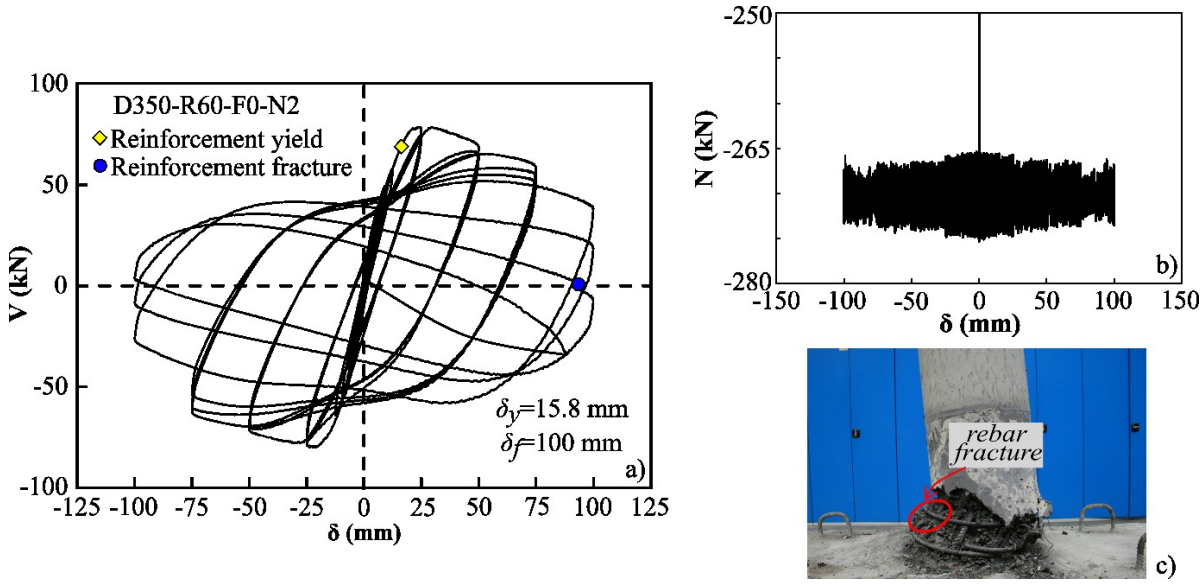


Figure 6.11 D350-R60-F0-N2: a) hysteric load-deformation response, b) vertical load applied, c) sliding failure

D350-R60-F0-N2S

Specimen D350-R60-F0-N2S with additional stirrups was tested under the same level of axial load (P=280 kN, Figure 6.12b) and exhibited similar response to the previous member. Yielding of reinforcement occurred at V_y=65.9 kN and δ_y=14.6 mm, while the peak axial load was reached at a displacement of 25 mm corresponding to V_{max}=73.9 kN (Figure 6.12a). Instead of the sliding failure, the member with high ratio of stirrup confinement showed stable behaviour after the fracture of reinforcement at a displacement of δ_f=100 mm (Figure 6.12c).

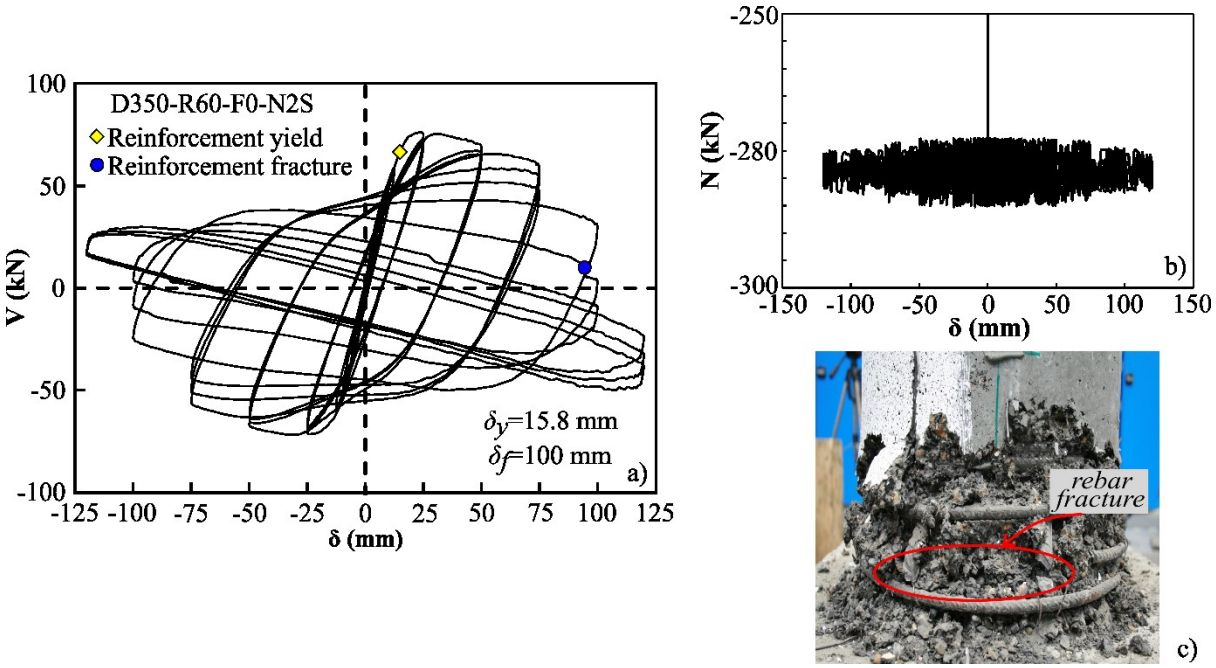


Figure 6.12 D350-R60-F0-N2S a) hysteric load-deformation response, b) vertical load applied, c) reinforcement fracture

The degradation in the Ø350 members was generally similar. Figure 6.13 shows the typical degradation state of two Ø350 RRuC columns as obtained from the DIC recordings at δ = 50, 75 and 100 mm (corresponding to drift ratios Δ = 3.7, 5.5 and 7.4%, respectively). A relatively soft crushing behaviour was observed at the compression zone of the members leading to the first signs of spalling at applied lateral displacements exceeding 75 mm. Although the bottom part of the rubberised concrete zone was subjected to considerable dilation, up to this level of displacement the rubber particles kept the concrete cover clamped to the member core. After the cover separated from the specimen, generally after or at the 1st cycle at δ = 100 mm (Δ = 7.4%), the member rotation was combined with some sliding at the reverse lateral loading direction. Prior to fracture, notable pinching was observed at high inelastic deformations due to the significant deterioration in the plastic hinge region.

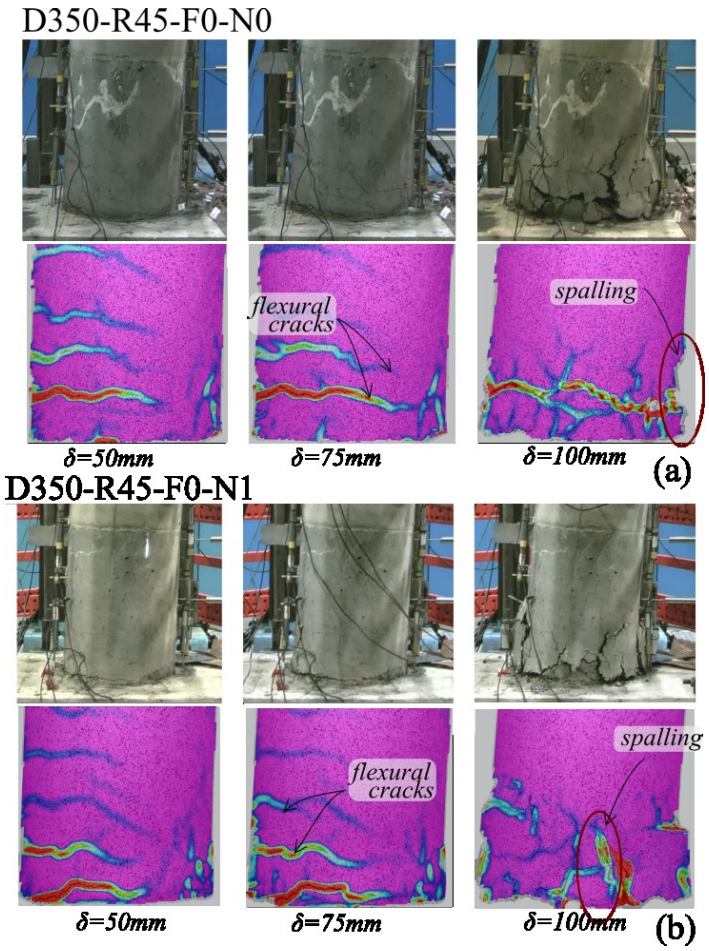


Figure 6.13 RRuC member kinematics from camera and DIC: a) D350-R45-F0-N0 with no axial load, b) D350-R45-F0-N2 with high axial load

Although cyclic degradation affected all members, this behaviour was more pronounced for members with high axial load. After reaching V_{max}, the loss in lateral capacity between the first and subsequent cycles was up to 17% prior to fracture of the flexural reinforcement. In addition, the higher level of axial load generally increased the lateral load capacity and delayed the yield of reinforcement, comparing members with the same rubber content.

With increasing cycles and more accumulation of damage, for all Ø350 RRuC members the longitudinal reinforcement fracture occurred at δ_f of at least 100 mm (Δ = 7.4%). For example, for D350-R45-F0-N1, D350-R60-F0-N1, D350-R60-F0-N2 and D350-R60-F0-N2S, the rebar fracture was recorded at δ_f = 100 (Δ = 7.4%). For the remaining specimens (D350-R45-F0-N0 and D350-R60-F0-N0), fracture occurred at δ marginally higher than 110 mm (Δ > 8.1%). The displacements at fracture δ_f are observed on the V-δ curves for all members and reported in Table 6-4. In contrast to the longitudinal rebars at ultimate, in most cases the circular stirrups remained in the elastic range up to the 2nd cycle of δ = 100 mm (Δ = 7.4%) with some yielding occurring afterwards due to degradation. Figure 6.14 shows the strain gauge readings of the transverse stirrups at the column-

footing interface for all Ø350 RRuC members. It can be noted that the strain growth in the bottom hoop was stable within a drift of Δ = 5.5% in most cases but increased significantly at higher displacements. As shown in Figure 6.14e and f, the large lateral expansion of the rubberised concrete core, especially under high level of axial load, led to excessive dilation of the transverse stirrups.

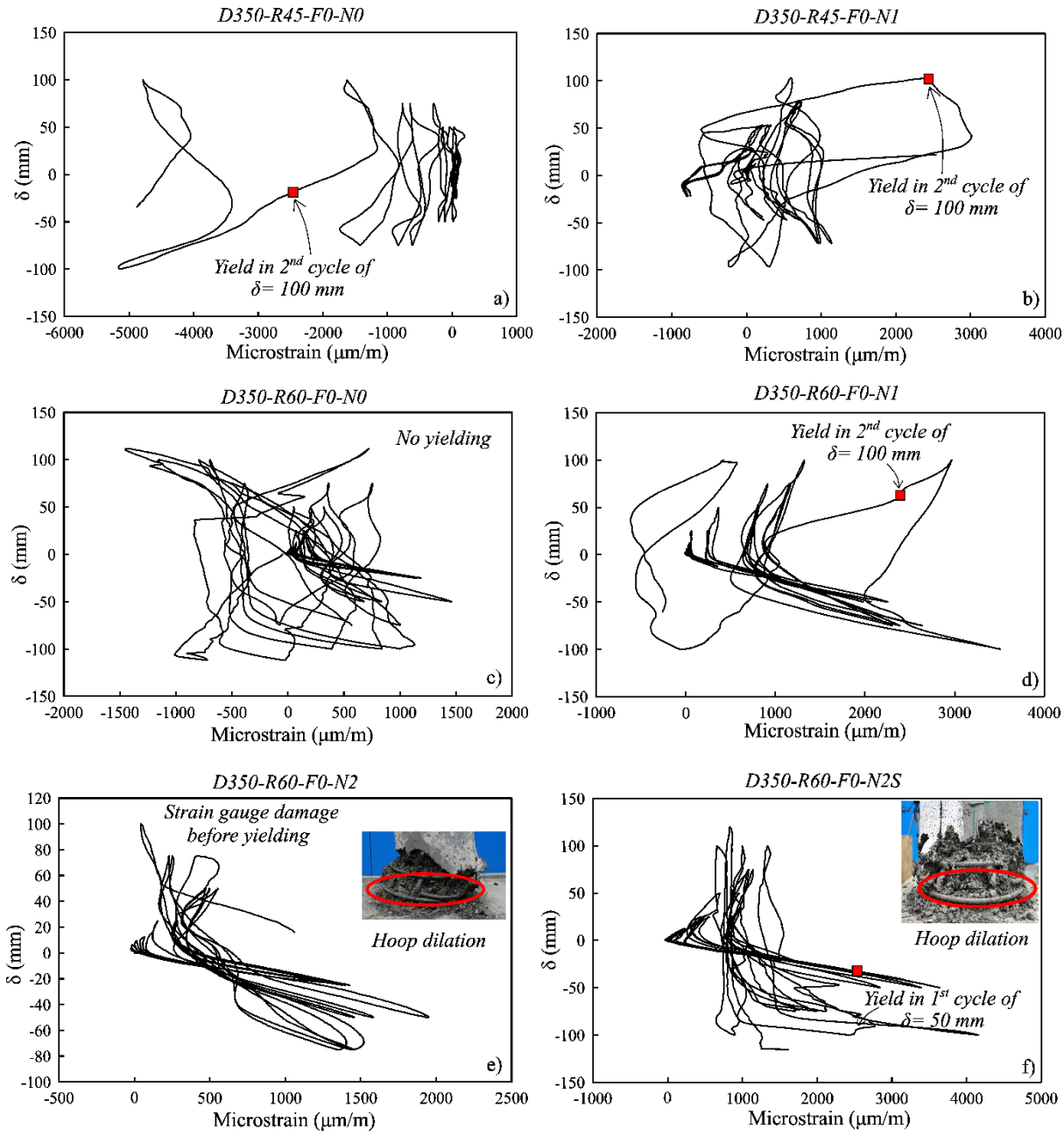


Figure 6.14 Bottom transverse stirrup strains: a) D350-R45-F0-N0, b) D350-R45-F0-N1, c) D350-R60-F0-N0, d) D350-R60-F0-N1, e) D350-R60-F0-N2, f) D350-R60-F0-N2S

6.2.2 Confined rubberised concrete members

D250-R60-F3-N1

The Ø250 CRRuC specimen (D250-R60-F3-N1) had a vertical load of 200 kN, representing the same level of axial load applied on Specimen D250-R60-F0-N1, considering the compressive strength of confined rubberised concrete. The behaviour of this specimen was characterised by a relatively soft crushing behaviour due to the presence of rubber particles, combined with an elastic response of the external AFRP confinement. The maximum lateral force V_{max} reached was about 52 kN, at a lateral displacement about 18 mm. The yield of longitudinal reinforcement occurred at δ_y =10.8 mm which was the same as that of the unconfined member. This specimen had a highly stable cyclic response and significant energy dissipation, as demonstrated by the shape of the hysteretic loops in Figure 6.15a, particularly when compared with its unconfined rubberised counterpart (D250-R60-F0-N1 in Figure 6.6a) as well as its RC counterpart (D250-R00-F0-N1 in Figure 6.5a). The AFRP sheets remained in the elastic regime, although some stretched regions were observed as shown in Figure 6.15c. Rebar fracture occurred at a lateral displacement of 87.5 mm (drift Δ<9%).

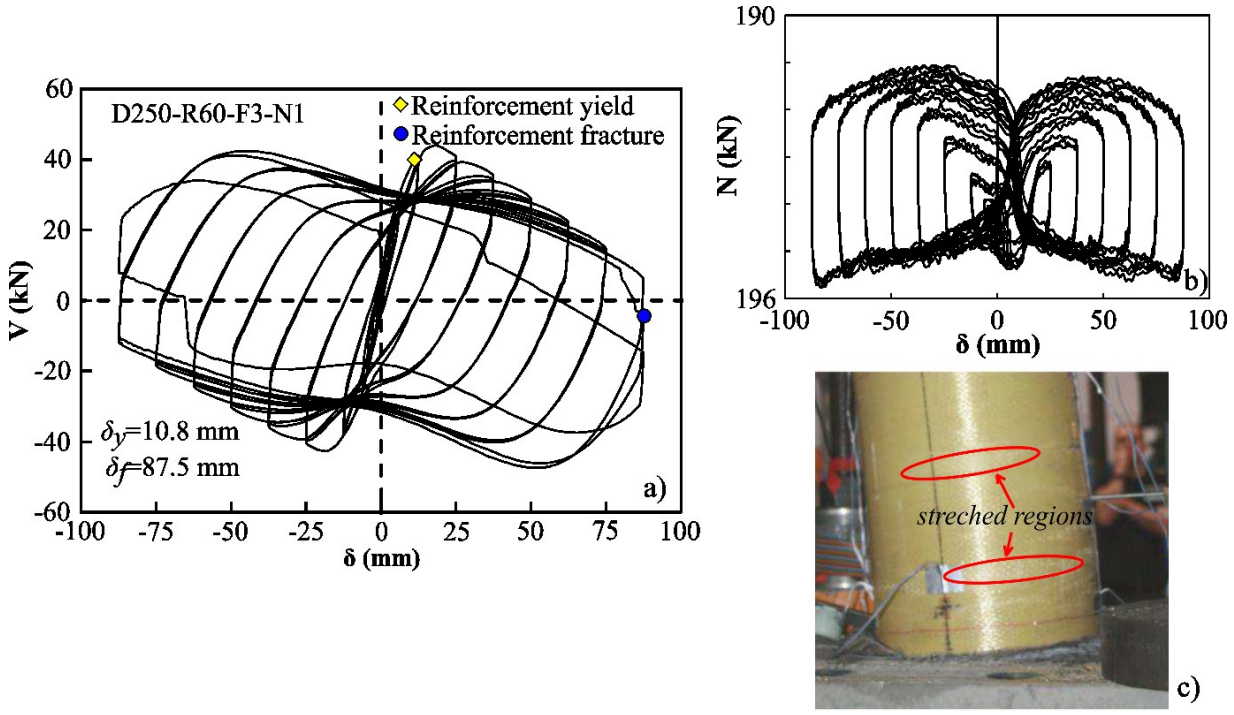


Figure 6.15 D250-R60-F3-N1: a) hysteric load-deformation response, b) vertical load applied, c) undamaged AFRP at failure

D350-R45-F2-N0

For the externally confined rubberised concrete (CRRuC) Ø350 members, for each of the two rubberised concrete types (i.e. R45 and R60), one member had no axial load, whilst the other was subjected to 800kN, representing a relatively high level of axial load.

For Specimen D350-R45-F2-N0 with no axial load, yielding of flexural reinforcement was recorded at δ_y of 12.4 mm, with a corresponding lateral force V_y of 63.7 kN. The maximum lateral force for D350-R45-F2-N0 was V_{max}=84.4 kN occurring at a displacement of 50 mm as shown in Figure 6.16a. Fracture of reinforcement occurred at the same level of displacement compared to the unconfined members (2nd cycle of δ_f= 113 mm). Only some stretched regions were found on the AFRP jacket without any rupture, and the main damage of the specimen was localised at the footing-member interface where a gap was formed as shown in Figure 6.16b.

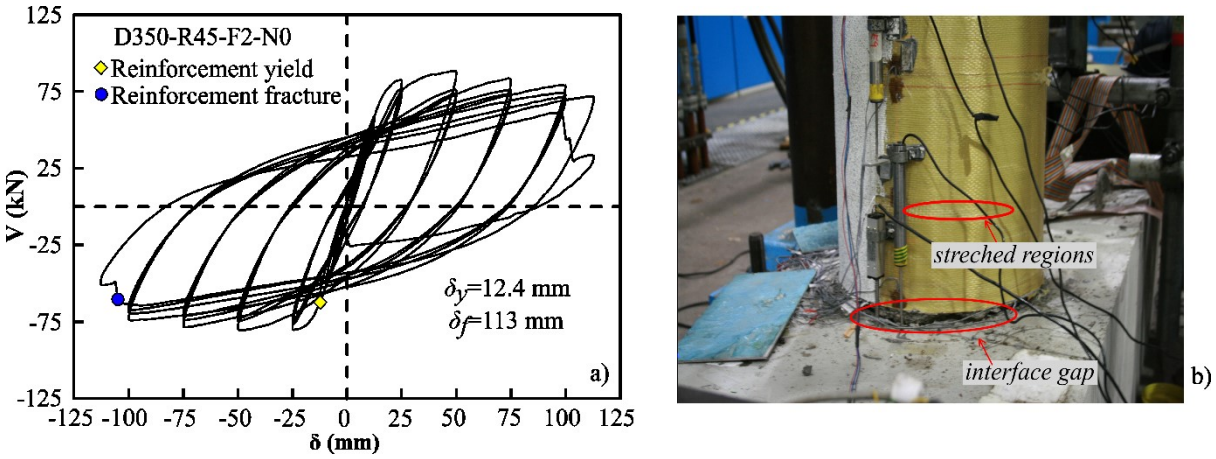


Figure 6.16 D350-R45-F2-N0: a) load-deformation response, b) AFRP stretches and interface gap

D350-R45-F2-N2

Compared with the previous specimen without axial load, Specimen D350-R45-F2-N2 showed higher lateral load capacity of V_{max}= 94.4 kN (at a displacement of 20.2 mm) and corresponding yield load V_y=82.6 kN (at δ_y=12.0 mm) as shown in Figure 6.17a. Due to the high axial load (P= 800 kN as in Figure 6.17b). This member behaved similarly to the previous confined specimens as notable stretched regions and a gap at the member-footing interface formed with the increase in displacement. Compared with Figure 6.16a, the specimen with high axial load showed more notable degradation in lateral capacity which was the same as the unconfined cases. On the other hand, the presence of axial load increased the area enclosed in each hysteric loop indicating higher energy dissipation, as discussed further in Section 6.3 below.

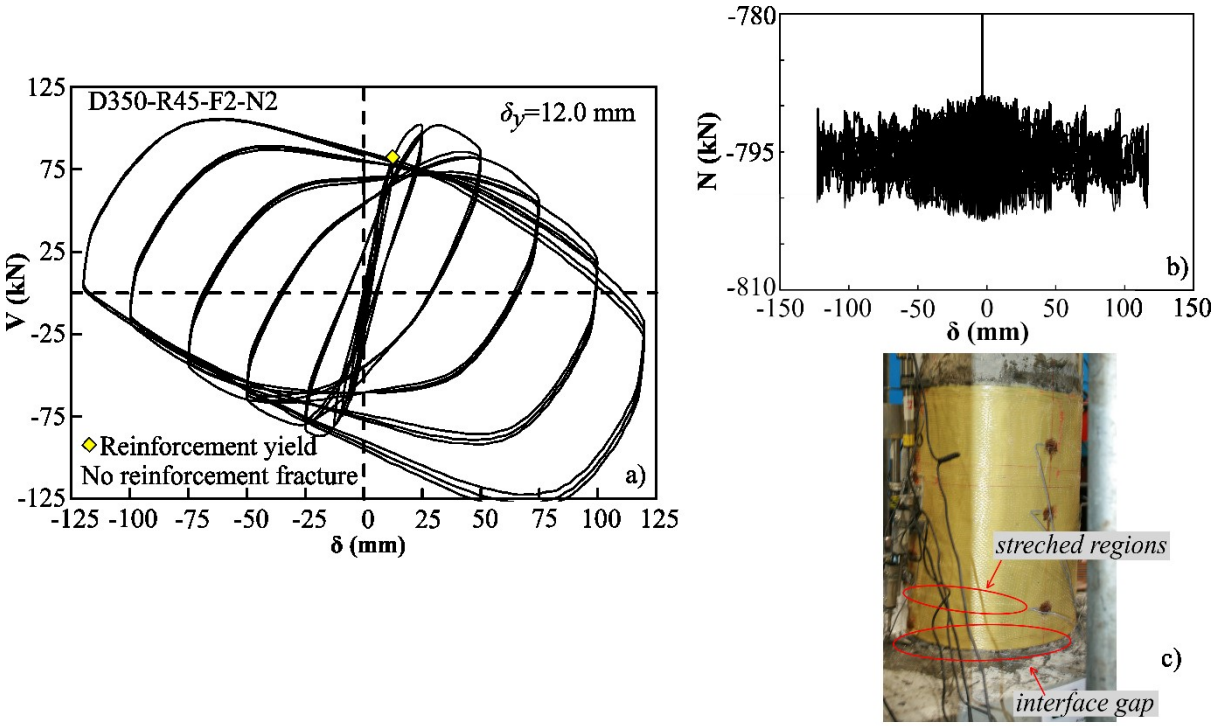


Figure 6.17 D350-R45-F2-N2: a) load-deformation response, b) vertical load applied, c) AFRP stretches and interface gap

D350-R60-F3-N0

Specimen D350-R60-F3-N0 showed a peak lateral load capacity of V_{max}=78.1 kN at adisplacement of 48.52 mm which was 8.1% lower than that of D350-R45-F2-N0. The yield displacement was δ_y= 12.2 mm with a corresponding lateral force V_y of 55.0 kN as shown in Figure 6.18a. Rupture of the longitudinal reinforcement occurred at the first cycle at a displacement of δ_f= 100 mm. Figure 6.18b shows the the AFRP confinement and the concrete core after removing the jacket. Similar to previous CRRuC members, only horizontal stretches were observed on the AFRP jacket without damage and the concrete core remained intact. It also can be seen from Figure 6.18b that the damage in the CRRuC member was localised at the bottom area of the column, including cracks on concrete surface, reinforcement rupture and the disconnection between the column and footing.

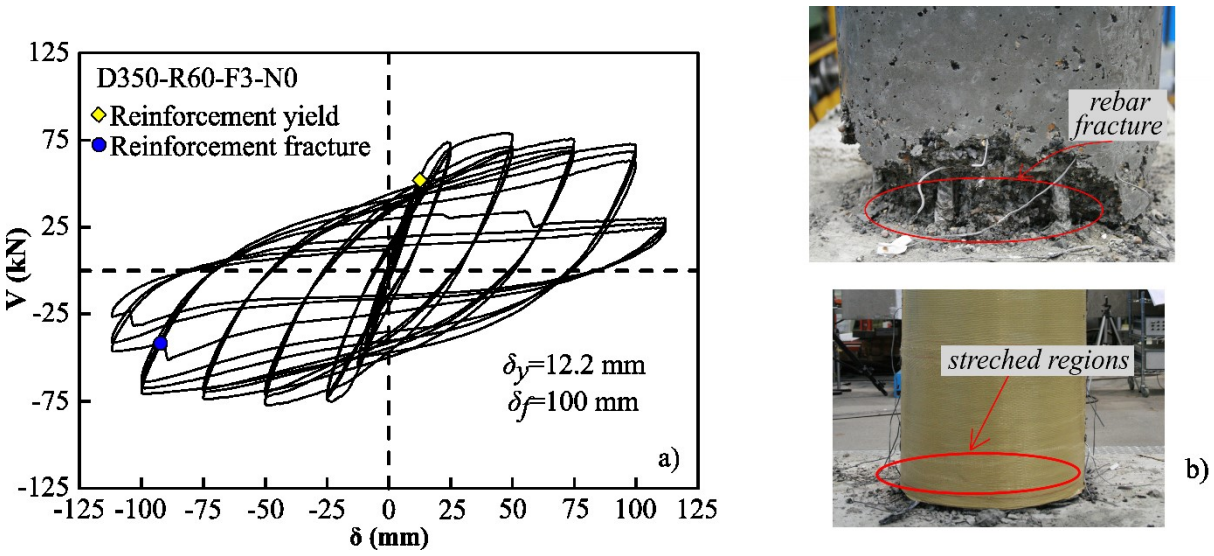


Figure 6.18 D350-R60-F3-N0: a) load-deformation response, b) failure of AFRP and concrete core

D350-R60-F3-N2

Specimen D350-R60-F3-N2, with an axial load of P= 800 kN (Figure 6.19b), reached a lateral load of V_{max}=78.1 kN at a lateral displacement of about 23 mm. The yield force and corresponding displacement (V_y= 57.9 kN, δ_y= 12.0 mm) were similar to its counterpart specimen without axial load (D350-R60-F3-N0) as indicated in Figure 6.19a. Similar to D350-R45-F2-N2 subjected to the same level of axial load was applied, no rupture of longitudinal reinforcement was reached. The failure of D350-R45-F2-N2 is illustrated in Figure 6.19c.

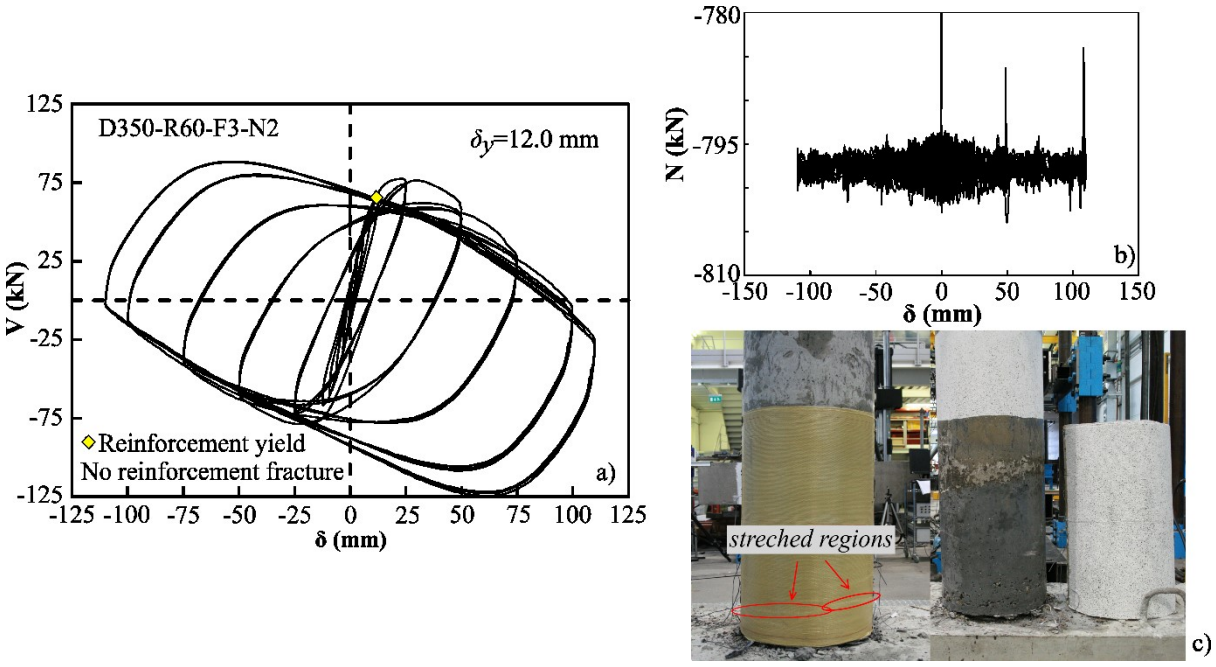


Figure 6.19 D350-R60-F3-N2: a) load-deformation response, b) vertical load applied, c) failure of AFRP and concrete core

It can be noted from all the CRRuC member behaviour discussed above that the external confinement maintained the integrity of concrete at significant inelastic deformation levels. Two typical softening behaviour captured by the DIC measurements is illustrated in Figure 6.20.

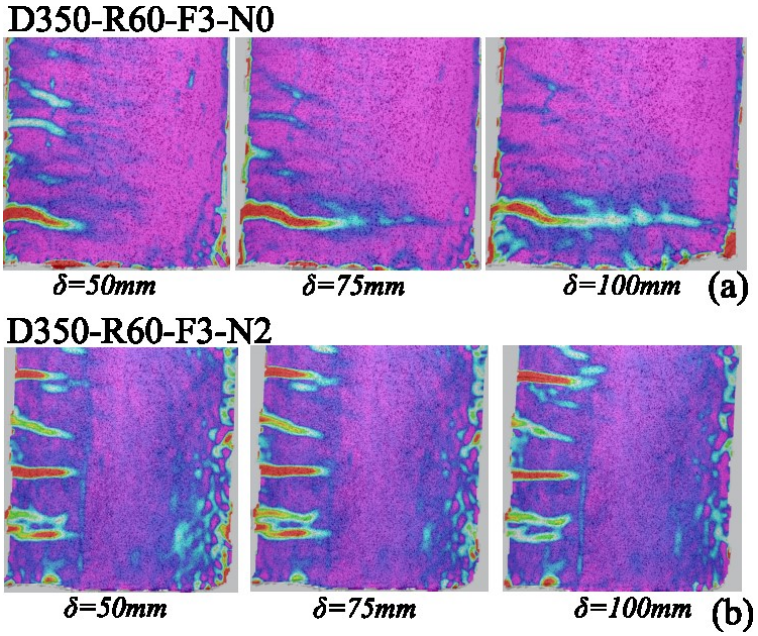


Figure 6.20 CRRuC member kinematics as obtained from the DIC: a) D350-F60-F3-N0, b) D350-R60-F3-N2

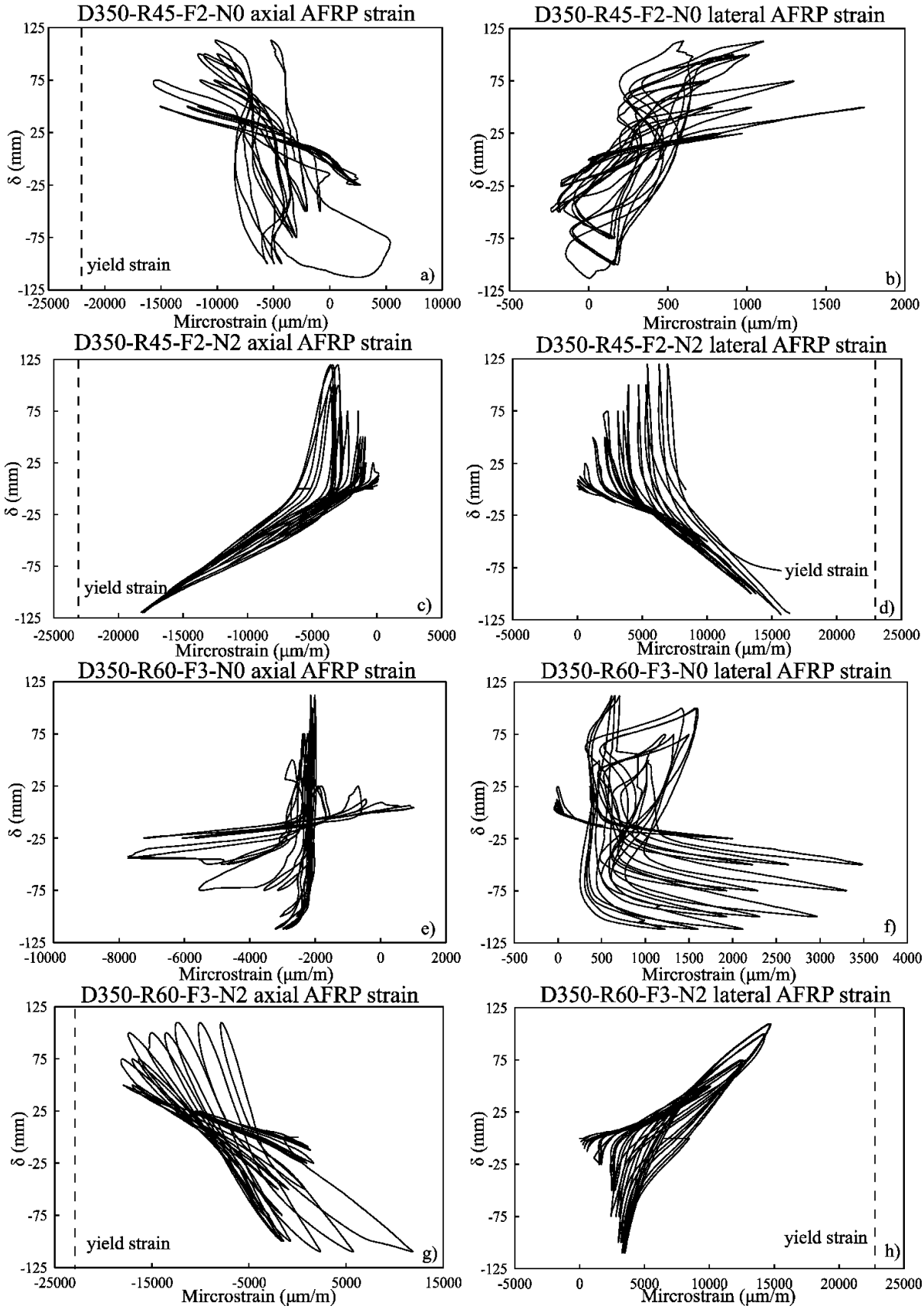


Figure 6.21 Maximum strain reading on AFRP jackets of all the Ø350 CRRuC members

A relatively soft crushing behaviour, due to the presence of rubber particles, as in the case of the RRuC members, was observed. Combined with the effect of the external AFRP confinement, this resulted in a highly stable cyclic response and significant enhancement in energy dissipation for the CRRuC members subjected to axial load in comparison with the corresponding RRuC members. This is demonstrated by the shape of the hysteretic loops in Figures 6.19a for D350-R60-F3-N2 and in Figure 6.11a for D350-R60-F0-N2, respectively. As discussed in Section 2.3, sufficient level of compression was required on the concrete core to activate the lateral deformation hence the external confinement. As a result, for the CRRuC members with no axial load (D350-R45-F2-N0 and D350-R60-F3-N0), the hysteretic responses in Figures 6.16a and Figure 6.18a resemble those of their RRuC counterparts without AFRP confinement (D350-R45-F0-N0 and D350-R60-F0-N0) as depicted in Figures 6.7a and Figure 6.9a, indicating insignificant contribution from the external confinement to the energy dissipation. Figure 6.21 shows the maximum readings of the strain gauges on AFRP jackets along both axial and lateral directions.

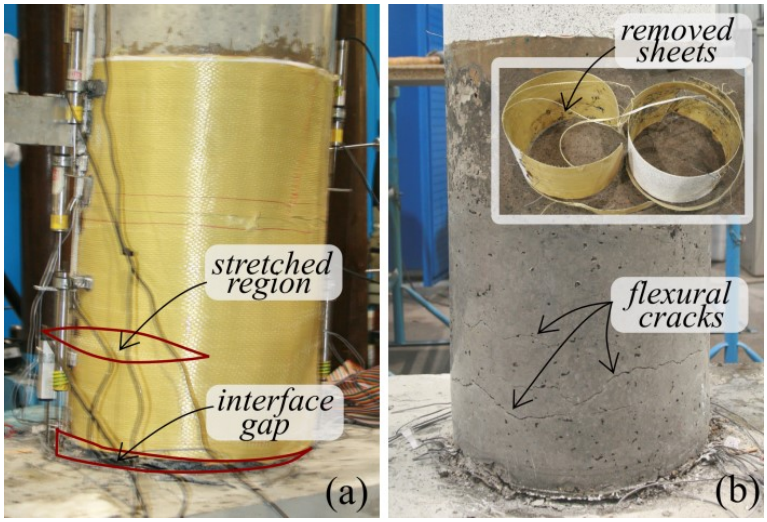


Figure 6.22 Views of Specimen D350-R45-F2-N0 after testing: a) stretched regions and interface gap, b) damage state after removal of external confinement

The strain measurements showed that the AFRP sheets remained in the elastic range in both the axial and lateral directions indicating sufficient level of confinement was provided, although some stretched regions, corresponding to locations of flexural cracks, were observed as shown in Figure 6.22a. Figure 6.22b shows the typical plastic hinge region after removal of the confinement sheets in Specimen D350-R45-F2-N0. The presence of the external confinement restricted the member lateral dilation, limiting concrete damage in compression and keeping the concrete core and cover intact. Although some cracks formed within the confined length of the member, most of the energy

was dissipated at the footing-to-member interface where a gap was formed at reversed cycles (Figure 6.22a).

6.2.3 Moment-rotation response

The envelope lateral moment-rotation curves, depicted in Figure 6.24, were determined from the peak values of the first cycle for each lateral deformation level. The calculated bending moment at the column foot cross-section consisted both the lateral load-displacement and the P-delta effects induced by the applied axial load. As shown in Figure 6.23, the total bending moment was calculated as $M = PX + VL$ .In this expression, P was the applied axial load; X was the tangential distance between the axial load and column foot, calculated based on the summation of hinge length of the vertical actuator S (as shown in Figure 5.9 in Chapter 5) and the column height L, with the expression of $X = (L+S)\sin\theta$; V was the applied lateral load and the column height. The rotation angle ψ was the angle between in the lateral displacement δ and the column height L.

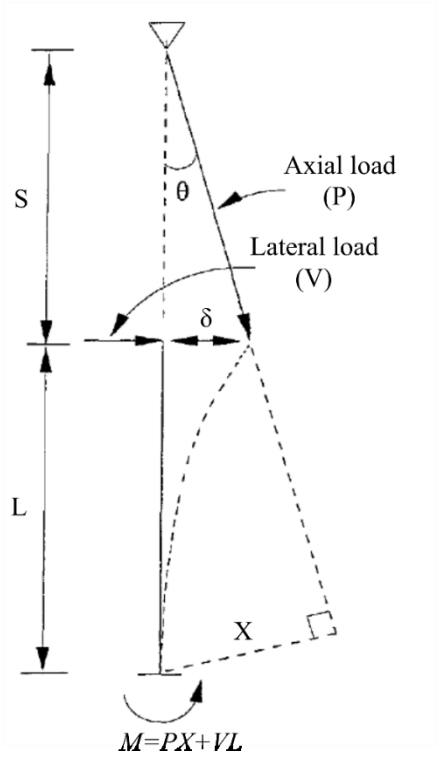


Figure 6.23 Calculation of bending moment considering P-delta effect

As observed in Figure 6.24a, the RC member (D250-R00-F0-N1) showed higher lateral strength in comparison with the RRuC (D250-R60-F0-N1) and CRRuC (D250-R60-F3-N1) members, yet accompanied by an increased deterioration with higher lateral deformation. The R45 RRuC members (D350-R45-F0-N0 and D350-R45-F0-N1) with low and no axial load, respectively, showed similar levels of ductility with some enhancement in strength for the axially loaded member

(Figure 6.24b). On the other hand, as depicted in Figure 6.24c for the Ø350 R60 RRuC members, for cases with high axial load (D350-R60-F0-N2), an observed increased in capacity was combined with more notable deterioration with increase in lateral deformation in comparison with their counterparts with low or no axial load (D350-R60-F0-N1 and D350-R60-F0-N0, respectively). Similarly, as shown in Figure 6.24d, for CRRuC members, the presence of axial load produced a combined effect of enhancement in V_{max} with more rapid degradation in comparison with the CRRuC members without axial load.

Comparing the envelope curves for the Ø350 RRuC members in Figures 6.24b,c with the Ø350 CRRuC members in Figure 6.24d, shows that for both R45 and R60 materials, the influence of the external confinement on the capacity and inelastic degradation of the members without axial load is minimal. In contrast, the presence of axial load combined with external confinement leads to higher stiffness and capacity in comparison with specimens with no axial loads.

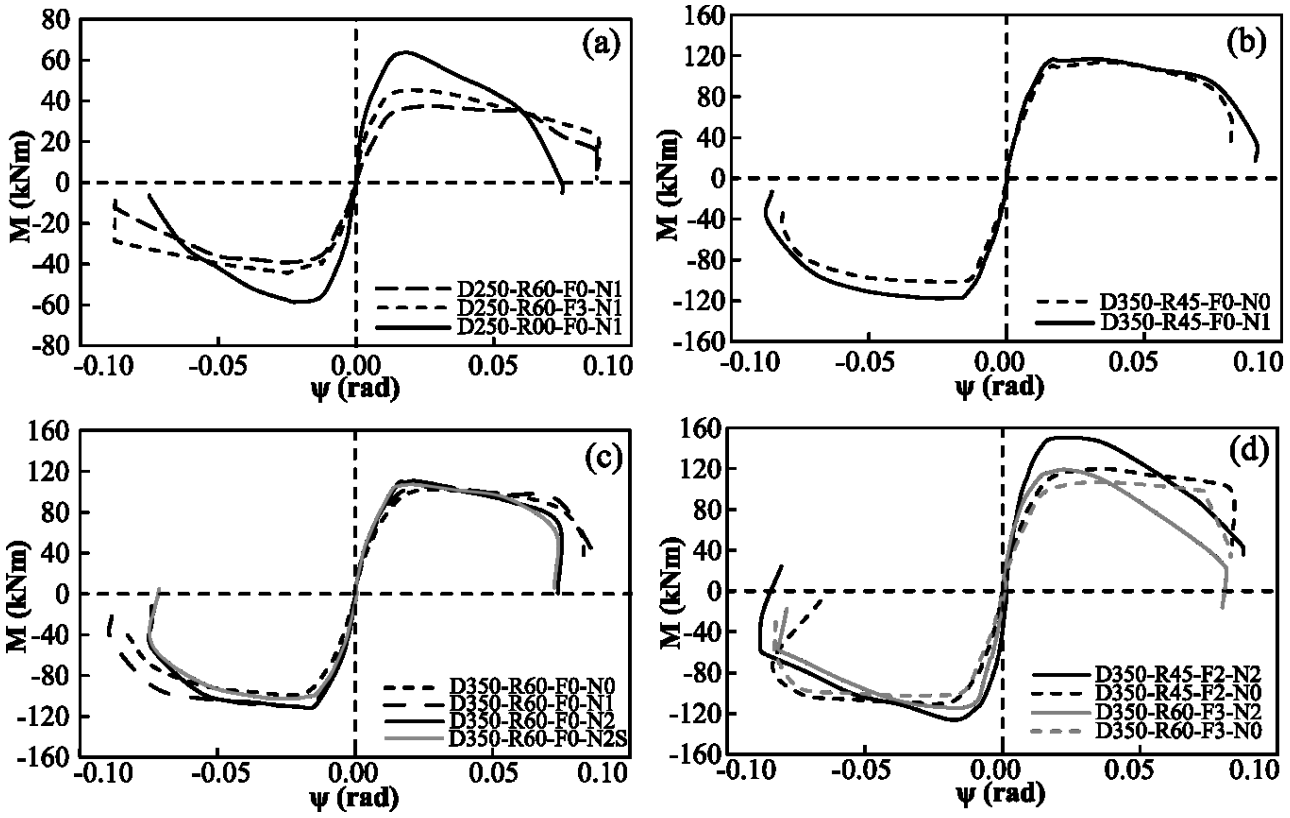


Figure 6.24 Envelope moment-rotation (M-ψ) curves: a) Ø250 members, b) Ø350 R45 RRuC members, c) Ø350 R60 RRuC members, d) Ø350 CRRuC members

The envelope curves in Figure 6.24 and member stiffness $k_{cr,test}$ values in Table 6-5 (determined in the post-cracking regime from the ratio of the lateral load at 40% of V_{max} and the corresponding lateral deformation δ) indicate varying stiffness with concrete type and level of axial load. The RRuC member with R45 and no axial load (D350-R45-F0-N0) had 30% higher stiffness in

comparison with the R60 member (D350-R60-F0-N0), whilst the R45 member with low axial load (D350-R45-F0-N1) had 10% higher stiffness compared to the corresponding R60 member (D350-R60-F0-N1). Additionally, D350-R60-F0-N2 subjected to high axial load showed about 21% and 37% proportional enhancement in stiffness in comparison to D350-R60-F0-N1 and D350-R60-F0-N0, respectively.

Irrespective of the concrete type, externally confined CRRuC members without axial load (D350-R45-F2-N0 and D350-R60-F3-N0) developed an initial stiffness similar to the equivalent RRuC specimens within about 10% (D350-R45-F0-N0 and D350-R60-F0-N0, respectively). The axially loaded CRRuC members (D350-R45-F2-N2 and D350-R60-F3-N2) had the stiffest elastic response with $k_{cr,test}$ 2.16 and 1.76 times higher than the CRRuC R45 and R60 counterparts with no axial load (D350-R45-F2-N0 and D350-R60-F3-N0), respectively. The above observations, in conjunction with the envelopes in Figure 6.24, indicate that members with higher rubber content develop lower stiffness as expected, whilst the axial load produces an enhancement in stiffness up to two folds in the presence of axial confinement.

The experimental observations described above also show that AFRP confined members (CRRuC) typically exhibit relatively high levels of energy dissipation and low cyclic degradation, with the confinement also leading to enhancement in lateral capacity in comparison with the rubberised specimens (RRuC). Both RRuC and CRRuC members show gradual compressive crushing of concrete, due to the presence of flexible rubber particles as compared to conventional concrete. Generally, members subjected to a lower axial load had lower flexural strength and stiffness, whilst those with higher axial load with or without external confinement showed enhancements in terms of both stiffness and strength. Also, CRRuC members sustained considerable levels of lateral deformation before fracture of the longitudinal reinforcement and developed significant ductility, as discussed below.

Table 6-5 Stiffness and ductility characteristics

Specimen	*Axial load (-)*	*v (-)*	*N (kN)*	$k_{cr,test}$ (N/mm)	M_y *(kNm)*	M_u *(kNm)*	ψ_y *(mrad)*	ψ_u *(mrad)*	μ_ψ (-)	$\mu_{\psi+1}$ (-)	$L_{p,test}$ *(mm)*
D250-R00-F0-N1	Low	0.05	200	11338	56.0	61.2	10.8	41.8	2.9	3.9	280
D250-R60-F0-N1	Low	0.03	20	3888	30.1	39.0	10.8	63.4	4.9	5.9	303
D250-R60-F3-N1	Low	0.06	200	5844	42.1	47.0	10.8	59.8	4.5	5.5	365
D350-R45-F0-N0	No	0	0	7623	86.3	108.2	9.2	71.5	6.8	7.8	388
D350-R45-F0-N1	Low	0.07	140	8157	96.1	116.7	10.8	71.1	4.4	5.4	410
D350-R60-F0-N0	No	0	0	5865	81.5	100.1	9.4	71.8	6.6	7.6	400
D350-R60-F0-N1	Low	0.08	140	7382	91.2	106.6	11.2	75.5	5.7	6.7	478
D350-R60-F0-N2	High	0.16	280	9291	93.9	111.4	11.7	54.0	3.6	4.6	427
D350-R60-F0-N2S	High	0.17	280	7994	91.6	104.9	10.8	58.9	4.4	5.4	415
D350-R45-F2-N0	No	0	0	6747	86.2	114.3	9.2	79.5	7.7	8.7	445
D350-R45-F2-N2	High	0.13	800	14599	115.5	140.7	8.9	56.6	5.4	6.4	525
D350-R60-F3-N0	No	0	0	6225	74.3	105.7	9.0	76.0	7.4	8.4	418
D350-R60-F3-N2	High	0.16	800	11015	82.5	119.0	8.9	53.9	5.1	6.1	390

6.2.4 Ductility considerations

Table 6-5 provides the member rotations at yield as well as at ultimate (assumed herein to correspond to 20% reduction in lateral capacity) as illustrated in the envelope curves in Figure 6.24. As observed from Table 6-5, the lowest rotation at ultimate (ψ_u=41.8 mrad) was obtained for the conventional RC member (D250-R00-F0-N1) due to the comparatively sudden compressive crushing behaviour and more visible inelastic deterioration in comparison to other members. Considerably larger rotations at ultimate were obtained for the RRuC and CRRuC members in comparison with the RC member, for both the Ø250 and Ø350 specimens. These vary between ψ_u=53.9 mrad for CRRuC with high axial load (D350-R60-F3-N2) and ψ_u=79.5 mrad for CRRuC without axial load (D350-R45-F2-N0). In most cases, specimens with no axial load developed higher ultimate rotation capacities in comparison to those with axial load. The CRRuC Ø350 members (D350-R45-F2-N0 and D350-R60-F3-N0) had an average of 8.50% increase in ψ_u in comparison with their RRuC counterparts (D350-R45-F0-N0 and D350-R60-F0-N0, respectively). On the other hand, the Ø250 mm CRRuC member (D250-R60-F3-N1) had 5.7% lower ψ_u when compared to the Ø250 mm RRuC member (D250-R60-F0-N0), whilst the R60 Ø350 mm CRRuC specimen subjected to a relatively high axial load (D350-R60-F3-N2) exhibited nearly the same ψ_u as its RRuC counterpart (D350-R60-F0-N2). Overall, the test results show that rubberised concrete members provide significant levels of inelastic deformation and energy dissipation as discussed in more detail in subsequent sections.

6.3 Comparative assessment

Based on the test results and observations, a number of performance characteristics can be examined. These include axial-bending strength interaction as well as ductility and energy dissipation properties, as discussed in more detail in this section.

6.3.1 Strength interaction

Moment-axial (M-N) strength interaction diagrams are typically adopted to characterise the cross-sectional strength under combined loading (Hognestad 1951). For members provided with rubberised concrete, the assessment of M-N interaction may be considered using a simplified parabola-rectangle constitutive stress-strain σ-ε relationship for rubberised concrete with a crushing strain ε_{cr1} defined in Equation (6.1a) and the concrete compressive strength f_{rc} in Equation (6.1b), derived from the closed-form non-linear σ-ε proposed previously (Equation 3.5-3.11) in Section 3.5 (Figure 6.25). The crushing strain $\varepsilon_{c0,1}$ (EN 1992-1-1), and compressive strength f_{c0} from Equation (6.1a,b) are material properties for the conventional reference concrete from which the rubberised

concrete is derived, whilst ρ_{vr} and λ in Equation (6.1b) are the rubber content and a factor dependent on the size of the mineral aggregate replaced, respectively.

$$\varepsilon_{rc1} = \left(1-\rho_{vr}\right)\varepsilon_{c0,1} \text{ and } \varepsilon_{c0,1} = 0.7 f_{c0}^{\ 0.31} \tag{6.1a}$$

$$f_{rc} = \frac{f_{c0}}{1+2\left(1.5\lambda\rho_{vr}\right)^{3/2}} \text{ and } E_{rc} = 12\left(f_{cr}/10\right)^{2/3} \tag{6.1b}$$

in which $\lambda = \left\{2.43 \rightarrow d_{g,repl} \in (0,5); 2.90 \rightarrow d_{g,repl} \in (0, d_{g,max}); 2.08 \rightarrow d_{g,repl} \in (5, d_{g,max})\right\}$

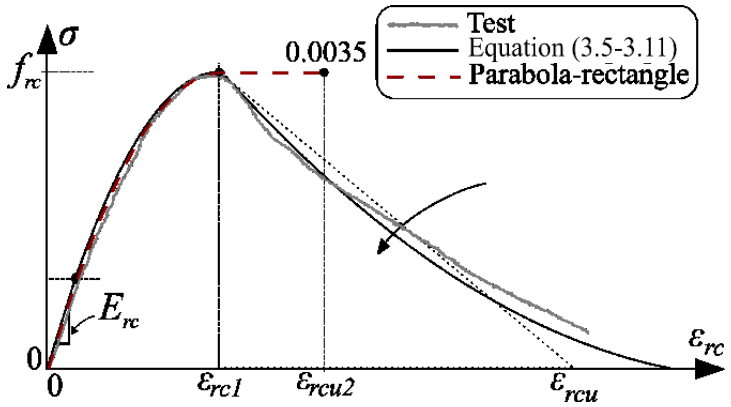


Figure 6.25 Typical stress-strain response of rubberised concrete materials

Implicitly, for the Ø250 RC member (ρ_{vr}=0), the material properties considered are those of normal concrete. For this member, the ultimate compressive strain (referred to herein as ε_{cu2} for conventional concrete or ε_{c0u2} for conventional reference concrete) was determined using the Eurocode 2 recommendations for concrete with f_c > 58 MPa (Equation 6.1c). On the other hand, for RRuC members, rubberised concrete may be considered as a low-strength concrete according to Eurocode 2 guidelines (EN 1992-1-1). Hence, the ultimate compressive strain for rubberised concrete may be considered as in Equation (6.1d). For the members considered in this study, the test strengths given in Table 6-2 were accounted for in the assessments, whilst the remaining parameters were determined as described above. The steel yield strain ε_{sy} is determined from the yield strengths f_y, given in Table 6-3 by considering an elastic modulus E_s=200 GPa.

$$\varepsilon_{cu2} = \varepsilon_{c0u2} = \begin{cases} 0.0035 \rightarrow f_c < 58MPa \\ 0.0026 + 0.035\left[\left(98 - f_c\right)100\right]^4 \rightarrow f_c \geq 58MPa \end{cases} \tag{6.1c}$$

$$\varepsilon_{rcu2} = 0.0035 \tag{6.1d}$$

For externally-confined AFRP specimens, the same procedure as for RC and RRuC members are used, except that the σ-ε in compression accounts for the external confinement (Rocca et al. 2009) and the influence of the eccentricity on the prediction of the compression governed failure region in

the axial-bending interaction diagram (Fam et al. 2003). Fibre polymer sheets exhibit a linear-elastic response up to failure, without cumulative damage and largely constant lateral strains at successive loading cycles (Rocca et al. 2009). For conventional concrete members, previous tests showed that the determined dilation strains on the fibre jacket were typically around ε_2 of up to 0.0048 (i.e. 0.48%) (Priestley et al. 1996; Seible et al. 1997).

For the rubberised concrete materials employed in this study, Ø100 cylinder tests indicated ε_{2u}=1.78% for R60-F3, and ε_{2u}=1.55% for R45-F2. Strain gauges located on the Ø350 externally confined CRRuC members with axial loading reached lateral strains of ε_2=0.6-0.7% at the ultimate moment M_u and ε_2=1.47-1.64% at maximum deformation δ_u, reflecting a more significant activation of the fibre polymer sheets in comparison to previous FRP confined RC tests (Priestley et al. 1996). For CRRuC members without axial load, these strains were on average about ε_2=0.25%. This is in line with results from the literature indicating that for the same level of confinement, by two layers of carbon FRP, rubberised concrete columns with ρ_{vr}=0.09 subjected to axial load and lateral deformation, developed maximum dilation strains. At maximum deformation δ_u, these strains were in the range of ε_2=0.80% which were larger than the dilation strains recorded for reference RC counterpart (ε_2=0.59) (Youssf et al. 2016).

The above remarks suggest that the level of dilation affecting the lateral confinement is a function of the transverse strain generated by the concrete material, and implicitly, the rubber content ρ_{vr} and confinement thickness. To this end, Figure 6.26a shows a decreasing trend of ε_2 in relationship to ρ_{vr} which corresponds to an increase in lateral strains with an increase in rubber content for members from this investigation as well as others from the literature (Youssf et al. 2016; Priestley et al. 1996). As observed in the figure, the strain ε_2 at M_u is about half in comparison to the strain ε_2 at δ_u for members with high rubber content (ρ_{vr}=0.45-0.60*),* whilst for ρ_{vr}*=0,* ε_2 at δ_u should be similar to ε_2 at M_u. Although the strains at ultimate deformation δ_u are of importance for ductility considerations, for M-N strength interaction, the lateral strain ε_2 at M_u should be employed as discussed further below.

In previous studies on concrete-filled FRP tubes subjected to bending and axial loading, it was shown that the gradual change in the state of stress in the jacket with eccentricity influences the level of confinement activated (Fam et al. 2003). The effect of confinement becomes more significant for high axial loads (i.e. when the eccentricity $M/N=e\rightarrow 0$) and there is no notable effect from confinement on the pure bending strength (i.e. when $e\rightarrow\infty$) (Teng et al. 2002). The test observations described in Section 6.2 of this chapter indicated similar trends. There is minimal influence from the external confinement on the response of both RRuC and CRRuC members without axial loads, with similar hysteretic response and energy dissipation. In contrast, for RRuC

and CRRuC members with axial loads, a significant difference was observed in terms of both capacity and energy dissipation.

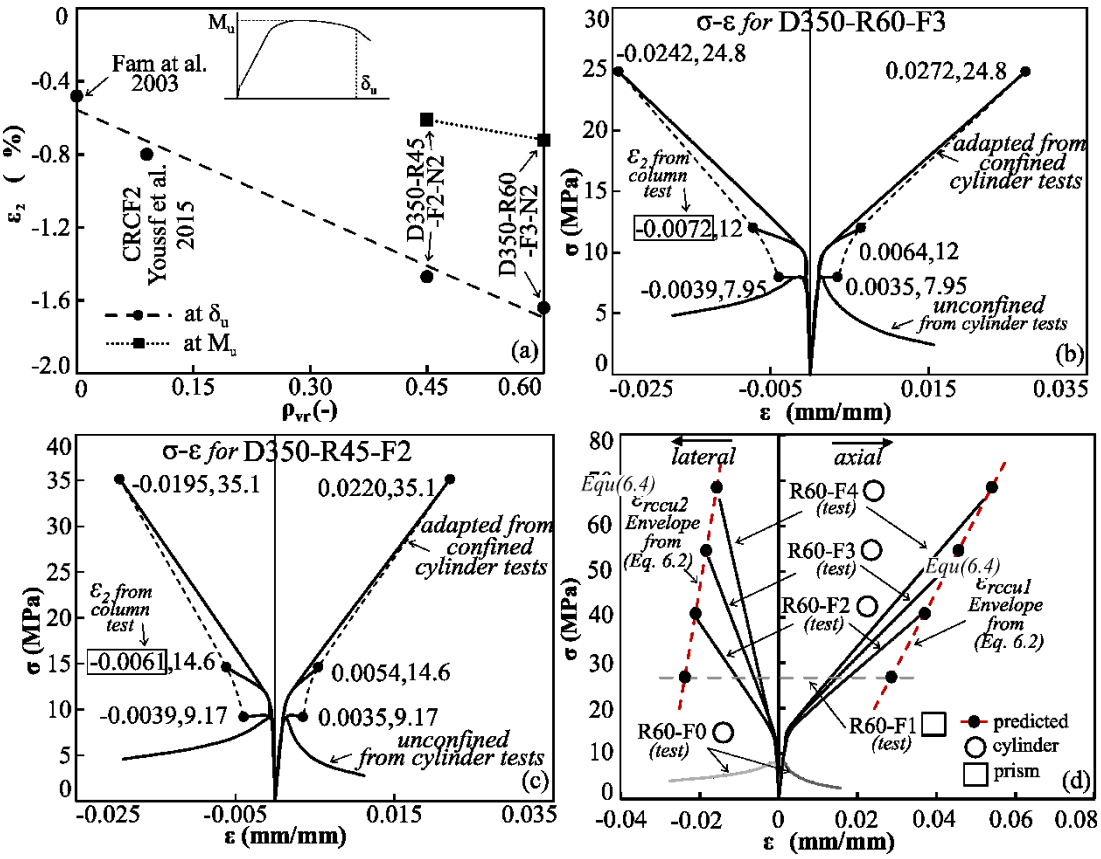


Figure 6.26 a) Influence of ρ_{vr} on ε_2; stress-strain σ-ε curves for assessment of M-N interaction diagram for: b) D350-R60-F3 columns, c) D350-R45-F2 columns; d) regression analysis for assessment of proportionality factors in Equation (6.2)

Figures 6.26b,c shows the compression σ-ε employed for the assessment of M-N curves for CRRuC members. For cases of bending without axial load (v=0, $e\rightarrow\infty$), the compressive σ-ε follows the unconfined shape for rubberised concrete (RuC) as illustrated in Figure 6.25. On the other hand, for concentric loading, it follows the σ-ε obtained from material testing (v=max, e=0) with the corresponding influence of the member diameter and jacket thickness using proportionality factors obtained from the material tests described in Section 6.1 and in other complementary material tests, as presented in Figure 6.26d (Anagennisi).

The proportionality factors were obtained from a regression analysis on the limited test results for the materials investigated in this research. For such configurations, as illustrated in Figure 6.26d, Equations (6.2a-c) (represented by dashed red lines and solid black points) offer good agreement between the ultimate strengths f_{rcc} and strains (ε_{rcc1} and ε_{rcc2}) obtained from Ø100×200 mm cylinder

tests for R60-F0 to R60-F4 and 150×150 mm vertical prisms for R60-F1. For the R45 members, a similar approach was used by maintaining the slope of Equations (6.2a-c), but adapted to the corresponding material test results illustrated in Figure 6.1a. Although the estimated properties of the confined material (f_{rcc}, ε_{rcc1}, ε_{rcc2}) are in good agreement with the test results, Equations (6.2a-c), noting that this is only validated within the range of materials considered in this study.

$$f_{rcc} = \left[870\left(t/D\right)+1.63\right] f_{rc} \tag{6.2a}$$

$$\varepsilon_{rcc1} = 4.25\left(t/D\right)+0.0200 \tag{6.2b}$$

$$\varepsilon_{rcc2} = 1.35\left(t/D\right)-0.0265 \tag{6.2c}$$

For intermediate cases of M-N interaction, σ-ε was determined using the lateral strains ε_2 obtained from strain gauges at M_u, as discussed above, and assuming the same $\varepsilon_2/\varepsilon_1$ weighting function as obtained from Ø100 cylinder tests. The obtained ε_{crcu} values for the three cases (namely: pure bending, intermediate eccentricity $e=M_u/N$ represented by Specimens D350-R45-F2-N2 or D350-R60-F3-N2, and concentric loading without bending) were used to determine the M-N interaction curve at three characteristic points (i.e. $e\rightarrow\infty$, $e=M_u/N$, $e\rightarrow 0$, respectively).

Figures 6.27a-g illustrate the predicted M-N interaction curves, using the above-discussed assumptions, for the test members, with the figures also indicating the experimentally obtained strengths. The test results, represented by a pair of (M_u,N) values, as given in Table 6-4, consistently lie just outside or coincide with the M-N curves. For the M-N curves of RRuC members (Figure 6.27a,b,f), the balance point (corresponding to the largest moment capacity), occurs at relatively low axial loads, indicating a wider compression-governed domain in comparison to the interaction curve of the RC member in Figure 6.27e. The latter shows a wider domain in which reinforcement tension yielding governs up to eccentricity levels of about e=0.08, while for the former cases the balance point is at about e=0.25.

The predictions of the idealised M-N curves for CRRuC members show similar values to those for RRuC members in the low axial load regions below the balance point, since the confinement plays a minimal role in capacity enhancement, and the behaviour of the concrete reduces to the unconfined compressive σ-ε. In contrast, for the case of concentric loading (e=0), the squash capacity of CRRuC members is about two-folds of the RRuC members. The balance points of the interaction curves in Figure 6.27c-d are determined using the σ-ε for partial confinement with intermediate levels of eccentricity ($e=M_u/N$). As described above, the effect of confinement becomes more pronounced with an increase in axial load and a corresponding decrease in eccentricity. However, for the regime of compression governed failures (i.e. above the balance point), no member test data

is available. Accordingly, the interaction curve in that region was conservatively determined by linearly joining the capacity at the balance point and at concentric axial loading (i.e. at e=0). These are represented by the dashed lines in Figure 6.27c-d for the externally confined members.

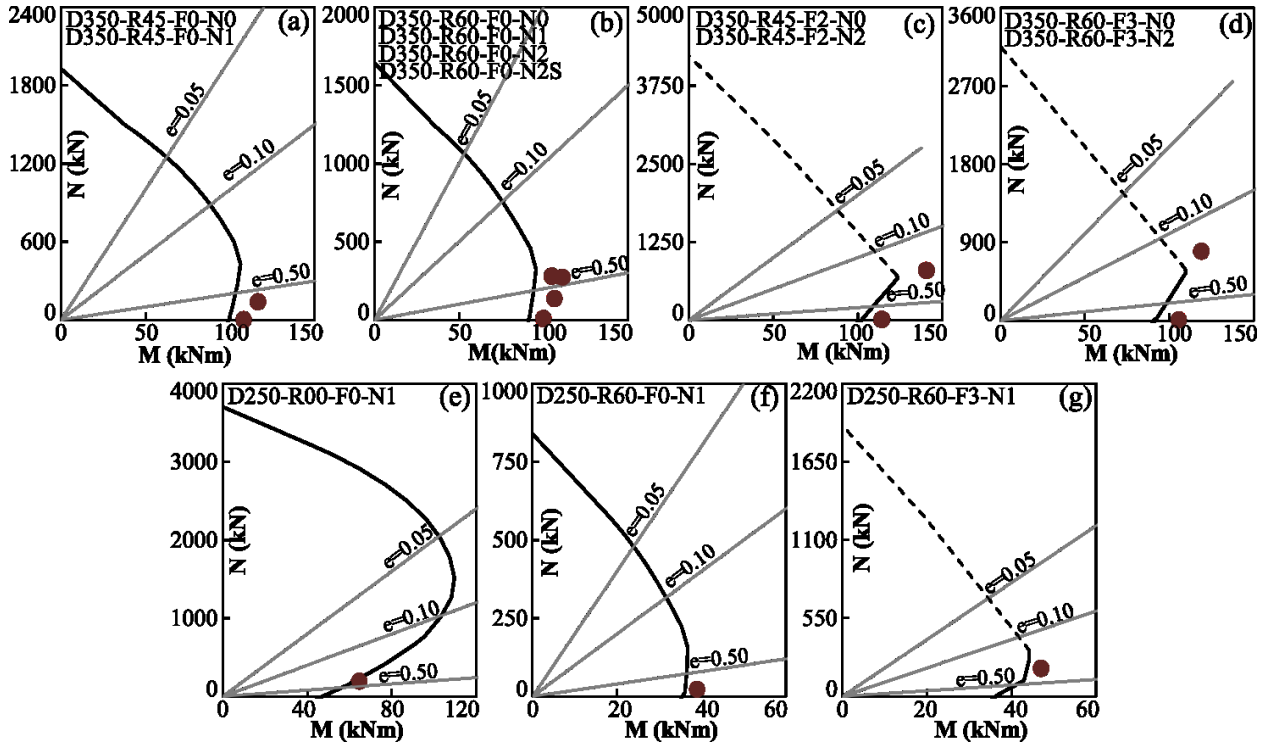


Figure 6.27 Bending-axial interaction curves for Ø350 RRuC members a) D350-R45-F0, b) D350-R60-F0; Ø350 CRRuC members c) D350-R45-F2, d) D350-R60-F3; Ø250 members e) RC - D350-R00-F0-N1, f) RRuC – D350-R60-F0-N1, g) CRRuC – D350-R60-F3-N1

6.3.2 Ductility considerations

Based on observations from the test results, the rubberised members developed a relatively soft post-peak response, indicating a more ductile response in comparison with conventional RC. It is therefore important to assess the influence of this local material behaviour on the overall ductility of members. To this end, the member rotational ductility $\mu_\psi/\mu_{\psi+1}$ was examined by considering the rotation at yield ψ_y (corresponding to the first yield of longitudinal reinforcement, as obtained from strain gauges located above the member-to-footing interface), and the ultimate rotation ψ_u as represented by Equation (6.3), in which ψ_u is the ultimate rotation as illustrated in Figure 6.28 (Elghazouli and Treadway 2008). The ultimate rotation ψ_u is assumed herein to correspond to a reduction of 20% from the ultimate moment M_u.

$$\mu_{\psi} = \frac{\psi_p}{\psi_y} = \frac{\psi_u}{\psi_y} - 1 \tag{6.3a}$$

$$\mu_{\psi+1} = \frac{\psi_u}{\psi_y} = \frac{\psi_p}{\psi_y} + 1 \tag{6.3b}$$

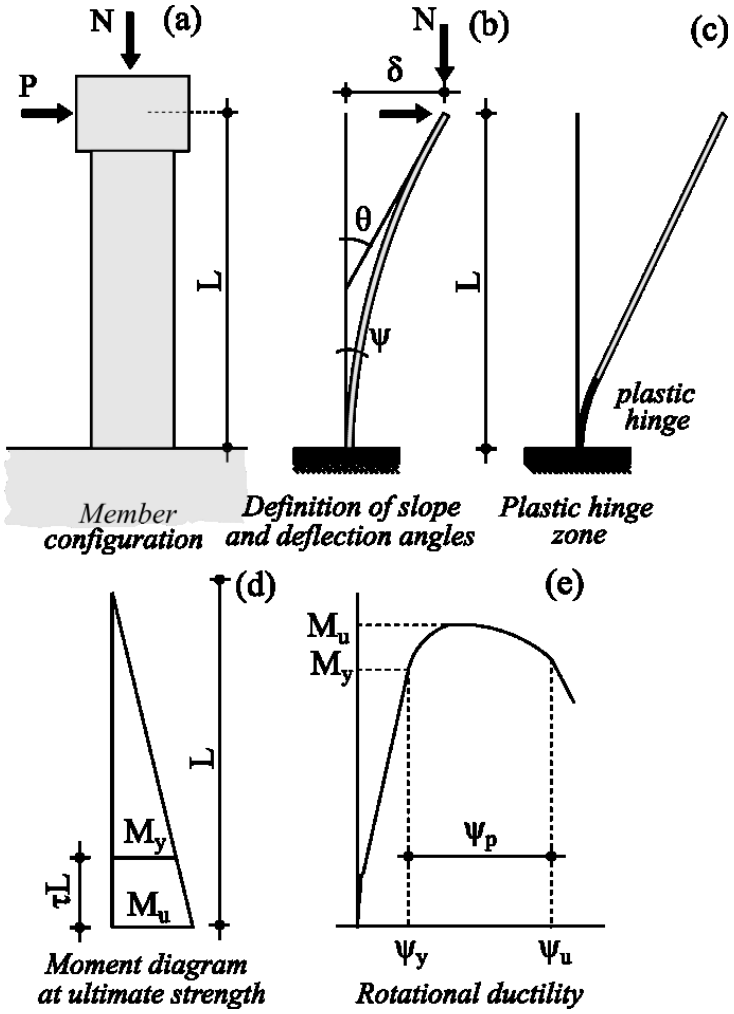


Figure 6.28 Inelastic response assessment: a) member configuration, b) definitions of slope and deflection angle, c) plastic hinge zone, d) moment diagram at ultimate, e) rotational ductility

Figure 6.29a illustrates the ultimate rotation ψ_u as obtained from the member tests. For the Ø250 members, the RC member had the lowest ψ_u, whilst the rubberised and confined rubberised member had consistently higher values (Table 6-5). As the yield rotation ψ_y was nearly identical for all Ø250 members, the rotation ductility $\mu_{\psi+1}$, plotted in Figure 6.29b, followed the same trend as ψ_u. From Figure 6.29b, it may be observed that the Ø250 RC member with low axial load (D250-R00-F0-N1) had the lowest rotation ductility with $\mu_{\psi+1}$=3.9. The Ø250 RRuC and CRRuC specimens (D250-R60-F0-N1 and D250-R60-F3-N1), had $\mu_{\psi+1}$ of 5.5-5.9 which represents more than 50%

improvement in rotational ductility in comparison with the RC specimen subjected to a similar axial load ratio.

As mentioned in Section 6.2, the presence of axial load reduces ψ_u for both RRuC and CRRuC members in comparison to the pure bending specimens. A similar trend is observed for the Ø350 RRuC members in Figure 6.29b in terms of rotation ductility $\mu_{\psi+1}$, with higher values up to $\mu_{\psi+1}$ = 7.8 obtained for cantilever members (e.g. D350-R45-F0-N0) and a minimum of $\mu_{\psi+1}$ = 4.6 for members with high axial load (i.e. D350-R60-F0-N2). The increase in confinement pressure due to the denser stirrup arrangement of s_w=40mm in Specimen D350-R60-F0-N2S led to enhanced ductility with 22% in comparison with its counterpart (D350-R60-F0-N2) with wider stirrup spacing (s_w=70 mm).

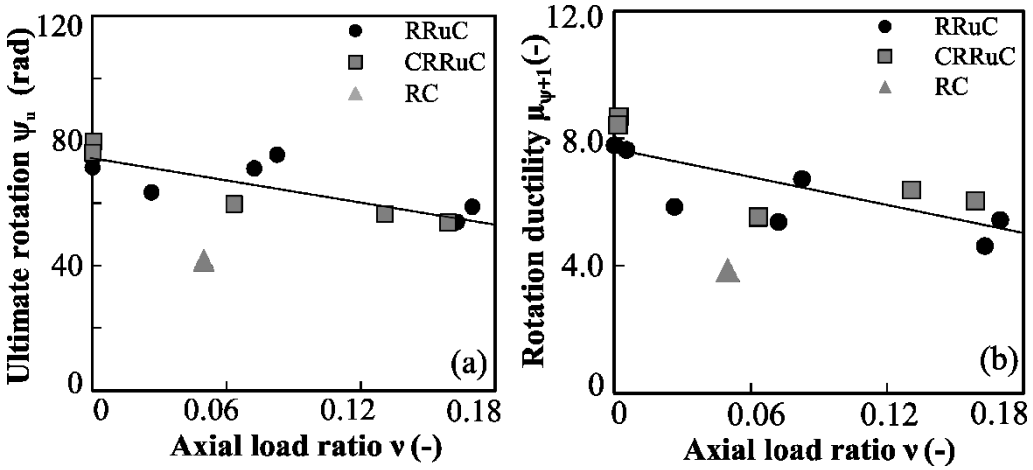


Figure 6.29 Ductility considerations: a) ultimate rotation ψ_u, b) rotation ductility $\mu_{\psi+1}$

The Ø350 CRRuC members indicated improved ductility characteristics in comparison with the Ø350 RRuC specimens. For the Ø350 CRRuC members, $\mu_{\psi+1}$ varied in the range of $\mu_{\psi+1}$=6.1-8.7 with higher values for non-axially loaded members (D350-R45-F2-N0 and D350-R60-F3-N0) and lower bounds for members subjected to high axial loads (D350-R45-F2-N2 and D350-R60-F3-N2). Externally confined members D350-R45-F2-N0 and D350-R60-F2-N0 without axial load reached $\mu_{\psi+1}$ levels 43% higher than their RRuC counterparts without external confinement ($\mu_{\psi+1}$=8.4-8.7). As described in Section 6.2, the hysteretic response of the two groups with no axial load was similar. Hence, in such cases, the external confinement was only partly activated since the level of concrete lateral dilation was relatively low. In contrast, D350-R60-F3-N2 had a $\mu_{\psi+1}$ about 41% higher than D350-R60-F0-N2 since the external confinement contributed in a more significant manner as the lateral dilation of the concrete increases in comparison to cantilever cases.

As discussed above and depicted in Figure 6.29a,b and Table 6-5, it is clear that for both RRuC and CRRuC members, the ultimate rotation ψ_u is reduced with the increase in axial load. The rotational ductility μ_ψ and $\mu_{\psi+1}$ typically reduces as well, but is sensitive to the actual yield rotation ψ_y. An increase in confinement by stirrups has a positive influence on μ_ψ, reducing the detrimental effect of axial loads. In the same manner, external confinement by means of AFRP sheets enhances μ_ψ, with a minimal increase for cantilever members and a more significant increase when axial loading is present as the external sheets develop larger strains due to the more pronounced lateral concrete dilation.

6.3.3 Plasticity length of reinforcement

Figure 6.30 shows the reinforcement strain levels plotted along the length of the member as recorded in selected tests at various drift ratios. The typical strain profiles corresponding to various drift ratios show concentrations of strains near the member-to-footing interface. The dashed black line shows the yield strain of the flexural reinforcement $\varepsilon_{s,y}$, as obtained from the material tests described in Section 6.1. The intersection between the maximum strain ε_s and the $\varepsilon_{s,y}$ line shows the limit between inelastic-to-elastic deformations, and implicitly, the plasticity region of the member $L_{pr,test}$. As observed, $L_{pr,test}$ has the smallest value for the Ø250 RC member (D250-R00-F0-N1), followed by the Ø250 RRuC member (D250-R60-F0-N1) and the Ø250 CRRuC specimen (D350-R60-F3-N1). These values are also given in Table 6-5. On the other hand, for the Ø350 RRuC R60 members, $L_{pr,test}$ was in the range of 400-480 mm, whilst for the Ø350 RRuC R60 $L_{pr,test}$ was in the range of 390-418 mm, with typically lower values obtained for members subjected to higher axial load.

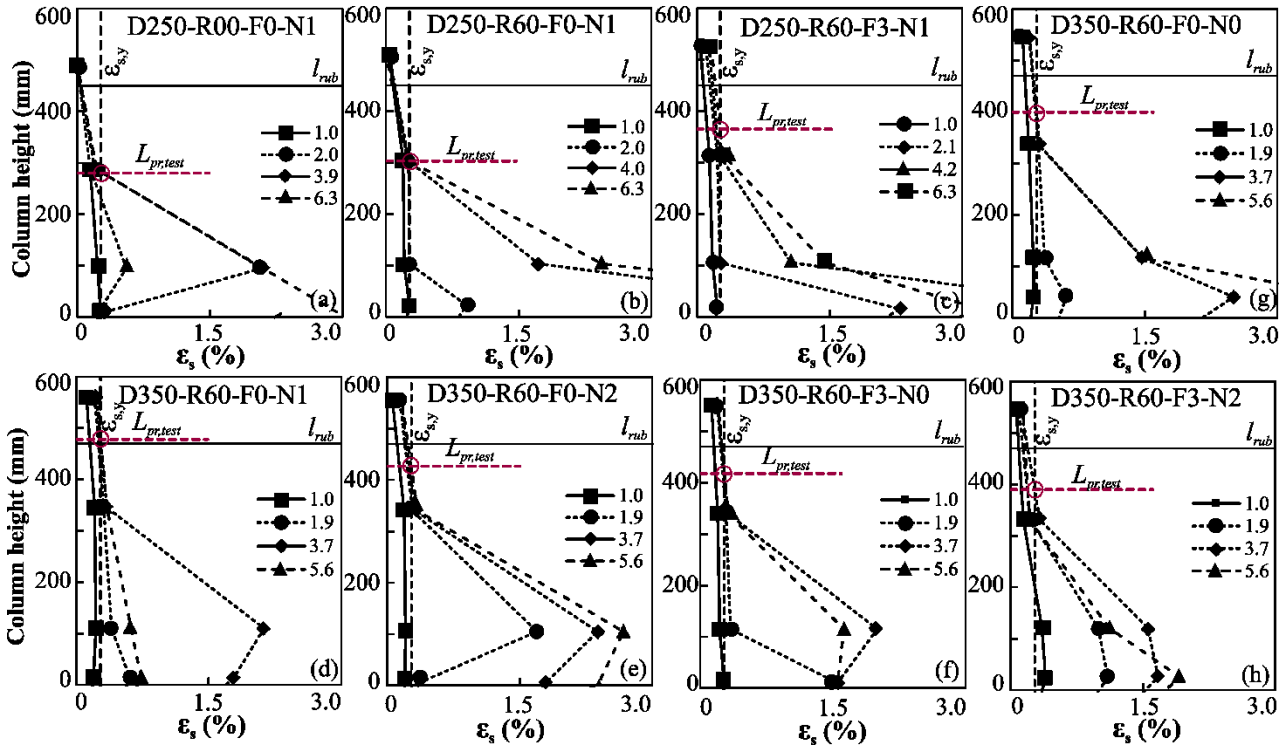


Figure 6.30 Reinforcement strains and plasticity distribution

Figure 6.31 depicts the plasticity region τ obtained in the tests as a ratio between $L_{pr,test}/l_{col}$.. As in Figure 6.30, the shortest plastic hinge length is obtained for the RC member in comparison with the remaining members. Additionally, regardless of the section size, the RRuC and CRRuC members exhibit τ values in the range of 0.31-0.34 due to the more significant spread of plasticity throughout the member length in comparison with the RC member.

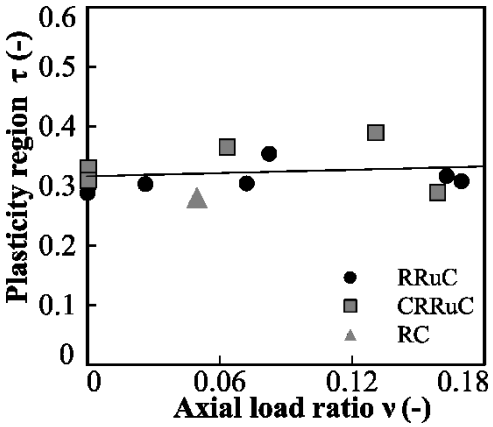


Figure 6.31 Estimated plasticity region

6.3.4 Energy dissipation

For comparison purposes, the energy dissipation of the test members is estimated from the hysteretic behaviour shown in Figures 6.4a-6.19a as the enclosed areas from the first and third cyclic loops at each deformation level, which are represented in Figure 6.32 by continuous and dashed lines, respectively. The difference between the two lines at the same deformation level may be regarded as the inter-cycle degradation. Firstly, Figure 6.32a compares the energy dissipation of the three Ø250 specimens. As expected, the CRRuC specimen D250-R60-F3-N1 had the highest energy dissipation of the Ø250 specimens (by a factor of 2.7 compared to the RRuC member - D250-R60-F0-N1). The RC specimen (D250-R00-F0-N1) dissipated the same amount of energy up to δ=60 mm (Δ=6%) in comparison with the CRRuC specimen. The energy dissipated by this member was 25% less than of the CRRuC member. The RRuC specimen D250-R60-F0-N1 also behaved reasonably well, despite the low concrete strength, and was able to dissipate energy even at higher displacements.

Figure 6.32b-e shows the energy dissipation at each applied lateral deformation level for the Ø350 members. For members with v=0, the behaviour up to displacement levels of δ=75 mm (Δ=5.5%) is essentially the same (Figure 6.32b,c). At higher displacement levels, the RRuC members degrade faster than other members. After δ=75 mm, the energy dissipation in externally-confined members increases linearly since the confinement maintains the concrete strength. The sudden drop in the energy dissipation versus lateral displacement curve at around δ=100 mm (Δ=7.4%) is attributed to rebar fracture. In contrast, for RRuC members without external confinement, the energy dissipation decreases with the accumulation of damage after the δ=75 mm point and drops significantly at δ=100 mm. This shows that externally-confined members have a more stable response with an increase of lateral deformations in comparison to non-laterally confined members.

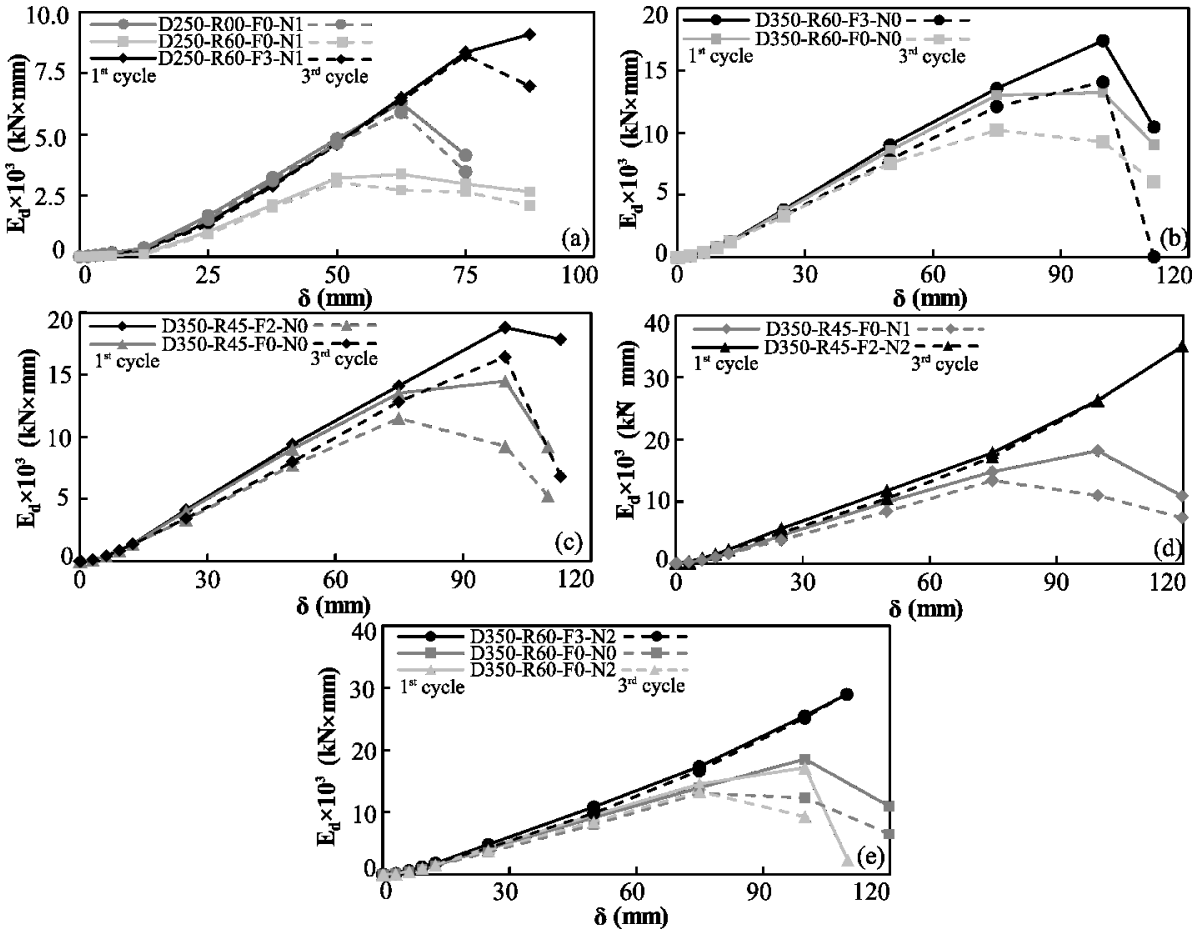


Figure 6.32 Energy dissipation: a) Ø250 members, b) Ø350 R60 members without axial load, c) Ø350 R45 members without axial load, d) Ø350 R45 members with axial load, e) Ø350 R60 members with axial load

The behaviour of Ø350 CRRuC members with v>0 shows significant improvement (up to 145%) in energy dissipation in comparison with members with no axial load (Figure 6.32d,e). As the axial load increases, the confinement is activated thus allowing considerably more energy dissipation. Unlike RRuC members, the energy dissipated through hysteresis in CRRuC increases with the deformation level, which shows a change in slope at 75 mm due to concrete degradation and the onset of spalling. For both types of member, without and with axial load (Figure 6.32b-e), the external confinement had a beneficial effect restricting concrete from dilation and resulting in enhancement in the energy dissipation. The inter-cycle degradation, for specimens from Figures 6.32a-e, represented by the difference between the continuous and corresponding dashed lines, suggests minor reduction in the energy dissipated by the CRRuC members in comparison to RRuC members between the first and third cycle, particularly for cases in which v>0. In contrast, for RC and RRuC, the level of inter-cycle degradation increases with the applied deformation.

6.4 Concluding Remarks

This chapter presented an experimental study into the behaviour of RC beam-column members, incorporating a significant proportion of rubber particles as a replacement for mineral aggregates, and subjected to inelastic lateral cyclic deformations and co-existing axial loads. A detailed account of the results from fourteen large-scale tests on circular reinforced rubberised concrete members, with or without external confinement, was given (pilot test excluded). Based on the test results and observations, a number of performance characteristics were examined, including the axial-bending strength interaction as well as ductility and energy dissipation properties.

The experimental results provided direct information on the influence of the rubber content and axial loading on the behaviour. In comparison with conventional reinforced concrete members, the tests showed that reinforced rubberised concrete specimens exhibit soft crushing behaviour leading to favourable ductility and energy dissipation properties. Highly stable hysteretic response was also obtained for externally confined reinforced rubberised concrete members provided with external AFRP confinement, which offers a viable solution in the presence of significant axial loading to compensate for the reduction in compressive strength when a large rubber content is employed in concrete.

The envelope curves of the tested specimens show that members with higher rubber content develop lower member stiffness as expected, while the axial load may produce a stiffness enhancement up to two folds in the presence of lateral confinement. For cantilever members, the inelastic stiffness is about 45% of the elastic member stiffness. Members subjected to a relatively low axial load have a lower flexural strength and stiffness, whilst members with comparatively high axial loads, with or without external confinement, showed enhancements in terms of both stiffness and strength.

The estimation of the bending-axial strength interaction diagrams based on Eurocode 2 guidelines with modified material characteristic that account for rubber content provided good agreement with the experimental results of RC and RRuC members. Similar procedure can also be applied for externally-confined specimens, except that the stress-strain behaviour under compression accounts for the influence of both external confinement and loading eccentricity. The proposed approach for assessing the strength interaction diagrams of AFRP confined members considering the above listed factors provides reliable estimates compared to the test results reported in this investigation.

The evaluation of ductility related parameters showed that the ultimate rotations are influenced by the type of concrete and level of axial load, with rubberised concrete members typically exhibiting relatively high rotation capacity levels depending on the level of axial load. The tests also

demonstrate the beneficial effects on ductility from the level of confinement, particularly when external wrapping is employed. For externally confined rubberised members with high axial loads, the rotational ductility levels reached were up to 40% higher than in rubberised members without external confinement.

An estimation of the plasticity region along the member length was obtained from the distribution of the longitudinal reinforcement strains. The plasticity region varied in the range of 29% to 39% of the cantilever length for the rubberised members, with lower values obtained for members subjected to axial load. These values were higher than those typically obtained for similar conventional reinforced concrete members.

The beam-column member test results demonstrated in this chapter, combined with the asymmetric shear test results in Chapter 4, are also used in the following Chapter 7 to validate and calibrate numerical models using the finite element analysis programme Abaqus. The validated models are subsequently applied in Chapter 8 to perform detailed sensitivity and parametric assessments about the structural behaviour of rubberised concrete members.

Chapter 7

7 Numerical simulations

Nomenclature

Greek letters

δ - displacement
$\delta_{f,num}$ – numerical fracture displacement
$\delta_{f,test}$ – test fracture displacement
$\delta_{y,num}$ – numerical yield displacement
$\delta_{y,test}$ – test yield displacement
ρ_{vr} - rubber replacement ratio
ε_c^{pl} – compressive plastic strain
ε_c^{pl} – tensile plastic strain
σ_{b0} – biaxial compressive strength
σ_{c0} – uniaxial compressive strength
ψ – dilation angle
ϵ - potential eccentricity

Lowercase latin letters

$d_{c(t)}$ – damage parameter
l_m - mesh size
l_s - shear bandwidth
$\overline{p}$ - effective hydrostatic stress
$\overline{q}$ - Mises equivalent effective stress
$w_{max,r}$ - maximum crack displacement
w_{max0} - base crack displacement

Uppercase latin letters

F – yield function
K_c – factor for the shape of the deviatoric plane
$P_{u,num}$ - numerical ultimate strength
$P_{u,test}$ - test ultimate strength
$V_{max,num}$ – numerical maximum lateral load
$V_{max,test}$ – test maximum lateral load

7.1 General

The experimental results presented in previous chapters provided physical understanding into the material behaviour of rubberised concrete under uniaxial compression and Mode II shear response. Further tests on large scale beam-column members also offered valuable insights into the key behavioural characteristics of reinforced rubberised concrete elements. In order to obtain more detailed information on the material behaviour, and to permit further parametric studies to enrich the experiment data, it is necessary to develop numerical modelling procedures which firstly need to be validated and calibrated against the experimental results.

This chapter describes the numerical assessments carried out in order to simulate the experimental behaviour of FRP-confined and unconfined rubberised concrete specimens using the advanced nonlinear finite element analysis program Abaqus (Simulia, 2010). Calibration of the uniaxial compressive behaviour of rubberised concrete is carried out in conjunction with the cylinder tests described in Chapter 3. This procedure provides reliable material models which are then applied in further validation against the prismatic shear tests as well as the large-scale beam-column member tests described in Chapter 4 and 6, respectively.

7.2 Concrete modelling

7.2.1 Yield and failure criteria

The concrete damage plasticity (CDP) model in Abaqus/Standard was used to simulate the tri-axial constitutive behaviour of concrete (Abaqus, 2010). This model is a continuum plasticity-based damage model for concrete, which assumes both compressive crushing and tensile cracking failure mechanisms of the material. This plastic-damage model for concrete, first proposed by Lubliner et al. (1989) and then modified by Lee and Fenves (1998), is a modification of Druker-Prager yield criteria with the yield function given in Equation (7.1).

$$F = \frac{1}{1-\alpha}(\bar{q} - 3\alpha\bar{p} + \beta(\varepsilon^{pl})(\bar{\sigma}_{\max}) - \gamma(-\bar{\sigma}_{\max})) - \bar{\sigma}_c(\varepsilon_c^{pl}) = 0 \tag{7.1}$$

where $\bar{p}$ and $\bar{q}$ are the effective hydrostatic stress and Mises equivalent effective stress respectively; α and β are the dimensionless constants with the expressions as shown in Equation (7.2) and Equation (7.3)

$$\alpha = \frac{(\sigma_{b0}/\sigma_{c0}) - 1}{2(\sigma_{b0}/\sigma_{c0}) - 1} \tag{7.2}$$

$$\beta = \frac{\bar{\sigma}_c(\varepsilon_c^{pl})}{\bar{\sigma}_t(\varepsilon_t^{pl})}(1-\alpha) - (1+\alpha) \tag{7.3}$$

where σ_{b0} and σ_{c0} refer to the biaxial and uniaxial compressive strength of the material. The ratio σ_{b0}/σ_{c0} was shown to be in the range of 1.10 and 1.16 (Kupfer and Gerstle, 1973), while the default value is set to be 1.16 in Abaqus. $\bar{\sigma}_c(\varepsilon_c^{pl})$ and $\bar{\sigma}_t(\varepsilon_t^{pl})$ represent the effective compressive and tensile stress, where ε_c^{pl} and ε_t^{pl} are referred to as compressive and tensile equivalent plastic strains, which are linked to the failure mechanisms of concrete under compression and tension, respectively.

The parameter γ in Equation (7.1) defines the shape of the yield surface of concrete in the deviatoric plane as shown in Figure 7.1. The parameter γ is expressed in the function as given in Equation (7.4).

$$\gamma = \frac{3(1-K_c)}{2K_c - 1} \tag{7.4}$$

where K_c is the ratio of the second stress invariant on the tensile meridian ($\sqrt{(J_2)_{TM}}$) to that on the compressive meridian ($\sqrt{(J_2)_{CM}}$) at the initial yield under any pressure invariant such that the maximum principle stress ($\sigma_{\max}$) is negative. The value of K_c must satisfy the condition $0.5 \le K_c \le 1.0$. As shown in Figure 7.1, as K_c tends to unity, the deviatoric cross-section of the yield surface approaches a circle.

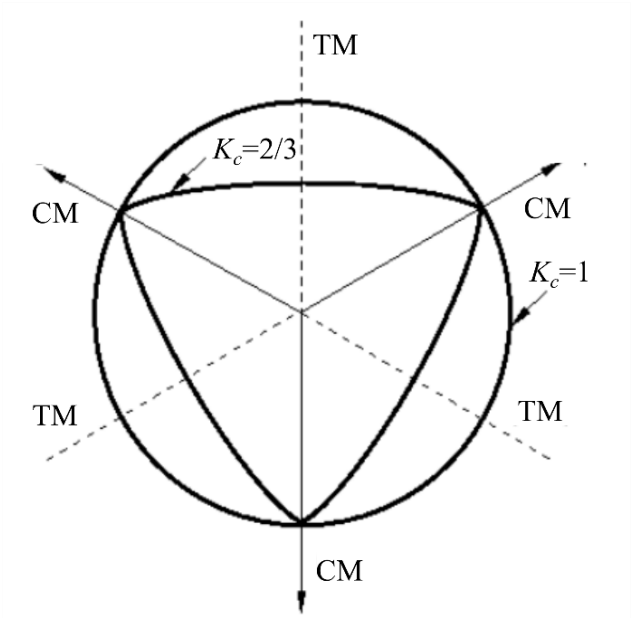


Figure 7.1 Typical yield surface on the deviatoric plane

The concrete damage plasticity (CDP) model considers the non-associated plastic potential flow rule in defining the volumetric plastic strain changes of the material. The plastic potential flow function (*G*), which has different expression from the yield function, takes the form of the Drucker-Prager hyperbolic function as given in Equation (7.5).

$$G = \sqrt{(\varepsilon \sigma_t \tan\psi)^2 + \bar{q}^2} - \bar{p}\tan\psi \tag{7.5}$$

where σ_t is the uniaxial tensile stress at failure, which is identical to the concrete tensile strength f_t. The non-associated flow rule is controlled by the dilation angle ψ, measured at high confining pressure, which determines the direction of the plastic strain increment tensor $d\varepsilon^{pl}$ in the meridian plane ($\bar{p}$ - $\bar{q}$ plane) as shown in Figure 7.2. The eccentricity parameter ϵ is a mathematical parameter that defines the rate at which the function approaches the asymptote as indicated in

Figure 7.2. It can be noted that the hyperbolic function in Equation (7.5) becomes a straight line as ϵ tends to zero.

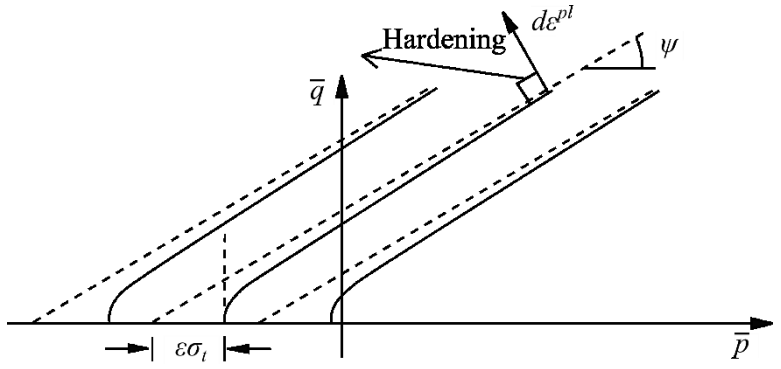


Figure 7.2 Yield criteria of concrete damage plasticity model in the meridian plane

7.2.2 Post-elastic behaviour

The damage plasticity model for concrete defines two main failure mechanisms, namely compressive crushing and tensile cracking of concrete at the same time. Consequently, the uniaxial behaviour under compression and tension are required to define the failure.

The uniaxial compressive and tensile behaviour of concrete is characterised by damage plasticity through the damage variable $d_{c(t)}$ and the corresponding effective plastic strain $\varepsilon_{c(t)}^{pl}$ as indicated in Figure 7.3. In this concept, the damage-based stress-strain relationship of the concrete compressive and tensile behaviour can be written as Equation (7.6).

$$\sigma_{c(t)} = (1-d_{c(t)})E_0(\varepsilon_{c(t)} - \varepsilon_{c(t)}^{pl}) = E_{c(t)}(\varepsilon_{c(t)} - \varepsilon_{c(t)}^{pl}) \tag{7.6}$$

where $\sigma_{c(t)}$, $\varepsilon_{c(t)}$ and E_0 represent the stress, total strain and initial (undamaged) stiffness of uniaxial compressive and tensile behaviour, respectively, as shown in Figure 7.3. The degraded stiffness *E* is defined as $E_{c(t)} = (1-d_{c(t)})E_0$, while $d_{c(t)}$ is a user-defined degradation parameter. According to Lubliner et al. (1989), the plastic degradations are available only in the softening range of the uniaxial compressive and tensile stress-strain curves while also in proportion to the cohesion stresses of the material $C_{c(t)}$ as indicated in Equation (7.7a). It should be noted that the cohesion stresses $C_{c(t)}$ is proportional to the uniaxial stresses of concrete $\sigma_{c(t)}$ as well. Consequently, the relationship between the degradation parameters and concrete strength is proposed as given

Equation (7.7b) where $f_{c(t)}$ and $\varepsilon_{c(t)}$ represent the uniaxial compressive and tensile strengths of concrete and corresponding strains.

$$d_{c(t)} = 1 - \frac{C_{c(t)}}{C_{c(t)\max}} \tag{7.7a}$$

$$d_{c(t)} = \begin{cases} 0, \varepsilon \geq \varepsilon_{c(t)} \\ 1 - \dfrac{\sigma_{c(t)}}{f_{c(t)}}, \varepsilon \geq \varepsilon_{c(t)} \end{cases} \tag{7.7b}$$

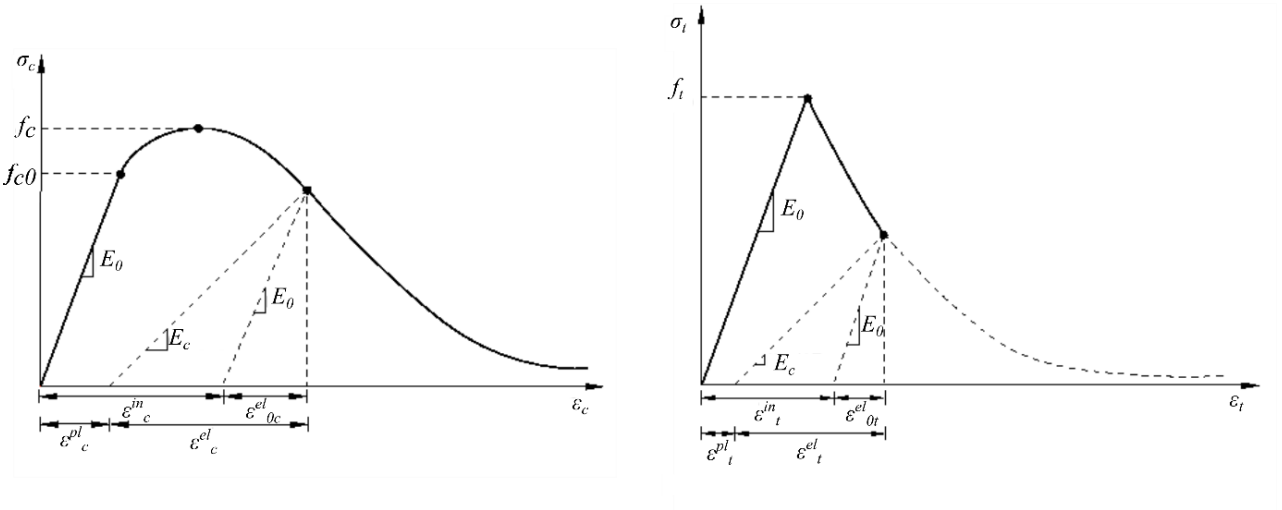


Figure 7.3 Uniaxial loading response of concrete in damage plasticity model

In this study, as introduced in Chapter 3, the uniaxial compressive behaviour of rubberised and reference normal concrete was tested, and the corresponding full stress-strain constitutive models were proposed as given in Equation (3.3) - (3.11). The uniaxial tension stiffening behaviour of rubberised concrete in this study takes the exponential expression proposed by Hordijk (1992) as given in Equation (7.8).

$$\frac{\sigma_t}{f_{ctr}} = [1 + (c_1 \frac{w}{w_{\max,r}})^3] \exp(-c_2 \frac{w}{w_{\max,r}}) - \frac{w}{w_{\max,r}}(1 + c_1^3)\exp(-c_2) \tag{7.8}$$

where σ_t is the tensile stress normal to the crack width w; c_1=3 and c_2=6.93 are fitting parameters; f_{ctr} and $w_{\max,r}$ represent the uniaxial tensile strength and the maximum crack width of rubberised concrete which are given in Equation (3.17), (3.18) in Chapter 3. As described earlier in Chapter 3, the uniaxial behaviour of rubberised concrete materials can be represented in a similar manner as

conventional concrete materials considering the influence of the rubber content on stiffness, strength and softening. Consequently, the fundamentals of CDP from Abaqus may be directly applicable for rubberised concrete (Abaqus, 2010). As for conventional concrete, the CDP constitutive parameters (e.g. dilation angle, viscosity parameter) need to be validated for each different modelling configuration by carrying out sensitivity studies. The above-mentioned analytical uniaxial compression and tension representations may be directly used as input, with mesh-dependent corrections for the softening regime for modelling the characteristic rubberised concrete behaviour.

With the adoption of the above-described nonlinear properties for concrete, simulation of all the test results on rubberised concrete prisms, cylinders and beam-column members (described in Chapter 3-6) are carried out and discussed in the following sections.

7.3 Asymmetric shear tests

As described in Chapter 4, three different types of failure modes were defined based on experimental observations (tensile-governed, shear-governed and mixed-mode responses) from the four-point shear tests. In this section, numerical simulations are undertaken and validated against tests developing shear-governed failures.

7.3.1 Modelling procedures

As shown in Figure 7.4, to simulate the response of the test specimens, the numerical models accounted for the full geometry described in Figure 4.11. The 150×150×600 mm concrete prisms, incorporating the two 5 mm wide notches, were connected through four 50mm loading plates and rollers at the top to a block element replicating the load transfer beam, and at the bottom to the boundary condition reference points. The side supporting plate had frictionless property contact with the roller which allowed the movement of the specimen after its fracture. The displacements of the middle supporting plate were restricted, while the rotations were allowed. A tri-dimensional full-sized geometry consisting of eight-noded solid elements with reduced integration (C3D8R) was adopted in all model elements. Newton-Raphson procedures were adopted, and displacement was used in which a vertical displacement δ was applied at the middle of the transfer beam and distributed onto the concrete member through loading plates.

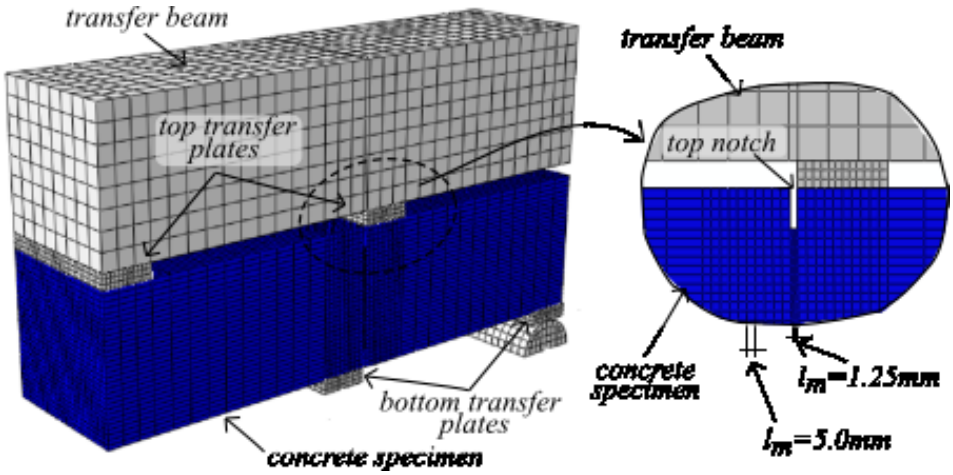


Figure 7.4 Tri-dimensional numerical modelling configuration of asymmetric shear tests

The transfer beam, support plates and rollers were assigned a linear elastic steel material whereas the concrete damage plasticity (CDP) model was used for the concrete specimen. Surface-to-surface interactions, represented through a penalty friction steel-concrete interaction with the coefficient of friction parameter of 0.4, were created between the loading plates and concrete specimen as well as the steel transfer beam. The mesh size l_m of the model was determined from sensitivity studies performed on the test geometry of the Reference Specimen R00N-1. Since the shear-governed failure (SGF) occurs along the notch-to-notch critical section, l_m was varied only along that region. A baseline l_m = 5mm, equal to the notch width, was initially chosen and compared with a finer l_m=1.25mm (Figure 7.4). As shown in Figure 7.5, the fine mesh size shows a closer estimation of the peak load $P_{u,num}$ in comparison to the test $P_{u,test}$ result with a difference of 6.4%, whereas a coarse mesh represented by a single line of elements (l_m=5mm) does not provide correct damage propagation along the critical area. Hence, the finer mesh size (l_m=1.25mm) along the critical section was chosen for all models described in this study.

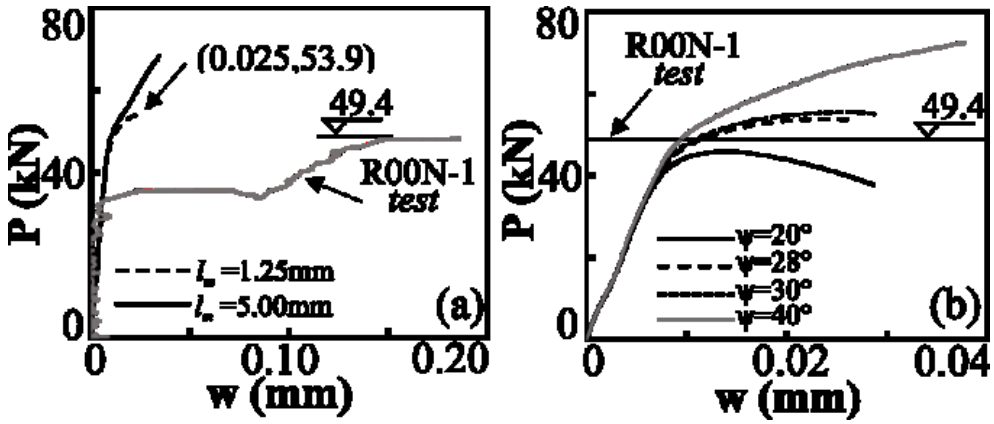


Figure 7.5 Sensitivity studies on R00N-1 configuration: a) Mesh size, b) Dilation angle

7.3.2 Constitutive properties

The concrete damage plasticity (CDP) model, accounting for a non-associated potential plastic flow with a default eccentricity ϵ=0.1, was chosen to simulate the tri-axial behaviour of the concrete material. The tri-dimensional yield surface is controlled by the shape parameter K_c=0.667 and the ratio between the biaxial and uniaxial compressive strength f_b/f_c=1.16. A relatively low viscosity parameter of 4×10^{-6} was chosen for the analysis. The non-associative plastic volumetric deformations of the material are not directly proportional to the changes in stresses and these are represented by a dilation angle ψ with a typical range of 10-50°; e.g. ψ = 10° for RC corbels (Syroka et al. 2011); ψ = 25° for RC and hybrid RC beams (Moharram et al. 2017); ψ=40° for RC flat slabs (Bompa and Onet, 2016); ψ=49° for hybrid RC flat slabs (Bompa and Elghazouli, 2017). A sensitivity study with ψ=20-40°on the R00N-1 specimen showed that the estimated strength increases with the increase in the dilation angle and both ψ=28° and 30° offer good agreement with the test result in terms of strength (Figure 7.5b). The former value (ψ=28°) was finally chosen since it showed consistent agreement for the other specimens considered (i.e. R20, R45, R60).

As described in Equation (7.7), no damage occurs before concrete reaches its compression or tensile strength while d_i has a linear relationship with the strength degradation in the softening range. The uniaxial constitutive model in Equations (3.3) - (3.11) was adopted in this study with due account of the material strength at testing. Additionally, a linear representation of the softening branch was taken into consideration for computational efficiency.

A linear σ-ε relationship up to the tensile strength f_{ct}, and an exponential decay function for the softening behaviour, were considered for the concrete uniaxial tensile behaviour as described in Equation (7.8) with $f_{ct}=0.3\times f_c^{1/2}$ (ACI, 2014). In this formulation, the tensile stress-crack opening width w relationship is a function of both f_{ct} and the maximum crack opening $w_{max,r}$. The latter was determined using Equation (3.18) which considers the influence of ρ_{vr} on the crack opening width

and transformed to strain accounting for the characteristic length l_m (Bompa and Elghazouli 2017). The input material parameters for this investigation is listed in Table 7-1.

Table 7-1 Input parameters used in the analysis for shear-governed specimens

Material parameter	ψ	ϵ	f_b/f_c	K_c	Viscosity parameter	l_m	Uniaxial compression	Uniaxial tension
Input value	28°	0.1	1.16	0.667	4×10^{-6}	1.25	Equation (3.3)-(3.11)	Hordijk (1992)+ Equation (3.18)

7.3.3 Comparative results

Specimens R00N-1, R20-1, R45-2, R60-1 and R60-3 which had shear-governed failures (SGF) were simulated using the material parameters and modelling configuration discussed above. The numerical simulations of the load-crack opening displacement *P*-*w* relationship compared with the corresponding test results as obtained from the DIC data are shown in Figures 7.6 and 7.7, and the results are summarised in Table 7-2. The elastic stiffness, initial crack opening displacement *w*, as well as the predicted ultimate strength are in close agreement with the test results for all cases with an average test-to-simulated ratio of 1.03 and a coefficient of variation of 0.09. Although the capacities are well predicted, due to the intrinsic nature of continuum modelling that does not allow for separation of the model geometry at cracked interfaces, the deformations at peak are underestimated for R00N and R60 models since in the tests the crack widths exhibited jumps resulting from sudden crack propagation (Figure 4.18).

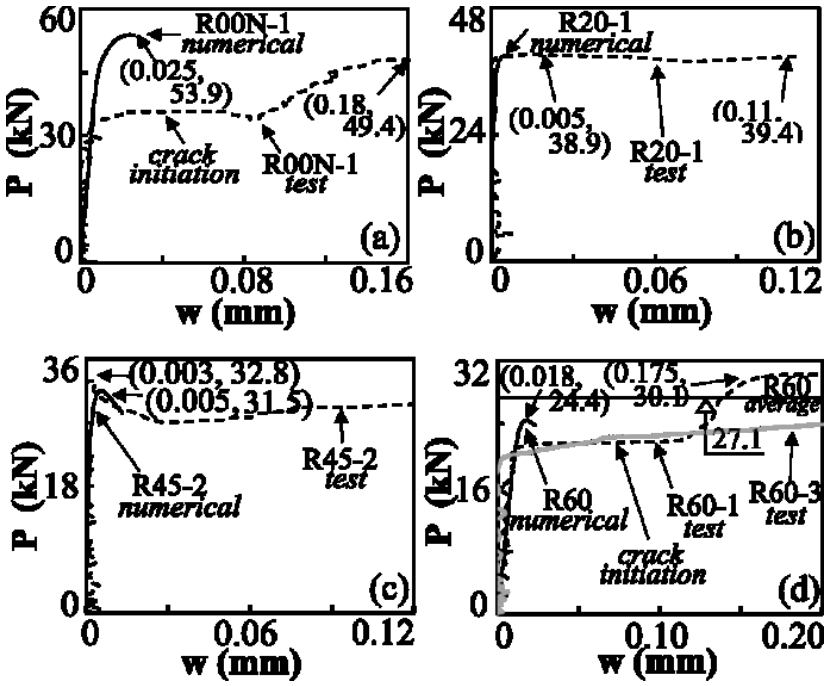


Figure 7.6 Comparison of numerical and test results: a) R00N-1, b) R20-1, c) R45-2, d) R60-1

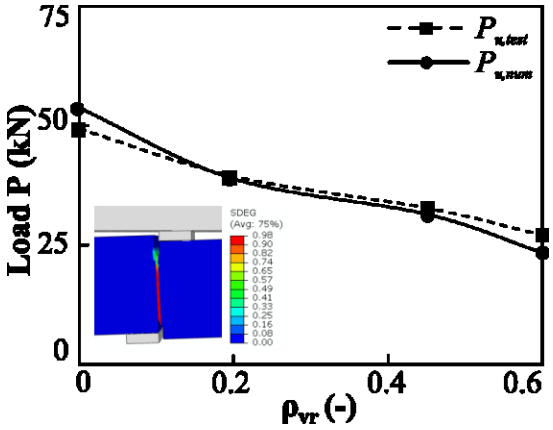


Figure 7.7 Predicted load reduction compared to the corresponding test results

Table 7-2 Test results and numerical simulation of the shear governed failure cases

Specimen	f_c [1)] (MPa)	f_{ct} (MPa)	$P_{u,test}$ (kN)	ρ_{vr}	$P_{u,num}$ (kN)	$P_{u,test}/P_{u,num}$
R00N-1	46.1	2.04	49.4	0	53.8	0.92
R20-1	21.0	1.37	39.4	0.20	38.9	1.01
R45-2	10.3	1.06	32.8	0.45	31.5	1.04
R60-1	7.30	0.81	30.1	0.60	24.4	1.16 [1)]
R60-3	7.30	0.81	24.1			
Average						1.03
COV						0.09

1) In the case of R60-1 and R60-3, $P_{u,test}$ is the average value of the two test results.

7.4 Beam-column member tests

The experimental results of the reinforced rubberised concrete beam-column members described in Chapter 6 were also simulated using the concrete damage plasticity (CDP) model in Abaqus. This section first discusses the members without external confinement, followed by the FRP-confined cylinders and the FRP-confined beam-column members.

7.4.1 Modelling procedures

As for the shear specimens, full geometries were considered in the numerical modelling of the beam-column tests as shown in Figure 7.8 (a)-(d) in order to validate the constitutive properties of concrete and reinforcement materials. Simplified representative models were also created for further parametric studies which are introduced in detail in Chapter 8. The specimen, including the foundation block, member and head, was modelled as in the test-set-up described in Section 5.2. The steel reaction plates and beams on both sides of the footing blocks, as well as the load transfer plates around the column head, were also included in the numerical models to represent faithfully the boundary conditions. Eight-noded solid element with reduced integration (C3D8R) were used for modelling the specimens as well as the steel plates and beams, whereas the two-noded linear truss element (T3D2) was used in modelling the steel reinforcement components.

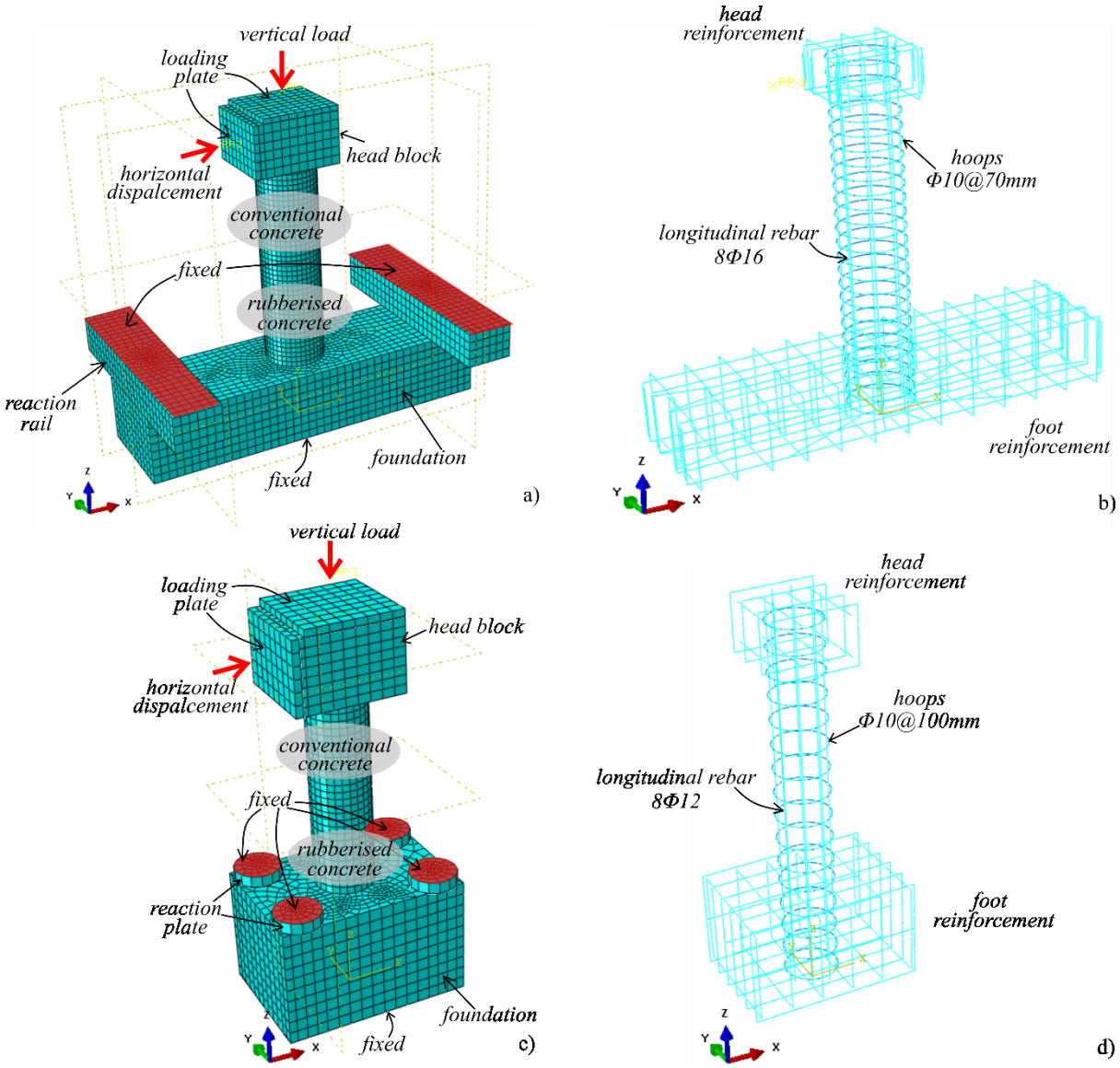


Figure 7.8 Three-dimensional numerical representation for: a) Ø350 specimen, b) Ø350 reinforcement cage, c) Ø250 specimen and d) Ø250 reinforcement cage

The reinforcement was fully embedded in the concrete region and assigned full bond conditions (no slip). Perfect contact was created between the reaction components and concrete specimen while the displacements and rotations of the reaction plates and the bottom surface of the footing block were restricted (see Figure 7.8). The constant vertical load, if present, was applied through a reference point that was linked to the top load transfer plate allowing the relative rotation between the column head and loading direction during the test. A displacement control procedure was adopted after the vertical load was stabilised where a horizontal displacement was applied through a reference point that was linked to the load transfer plate as well (see Figure 7.8 a, c). The Newton-Raphson iterative procedure was employed, with monotonic lateral displacements applied to simulate the load-displacement envelope of the test specimens.

The FRP jacket was modelled as thin layers of shell as shown in Figure 7.9. Considering the uni-directional properties of aramid-fibre sheets, the four-noded quadrilateral membrane element with reduced integration (M3D4R) which only transmits in-plane forces and have no bending stiffness, was adopted in the model. The thickness of the FRP jacket in the numerical model was in accordance with the number of layers applied to the specimen in each case. Perfect bond was assumed between the FRP jacket and the concrete surface in accordance with test observations.

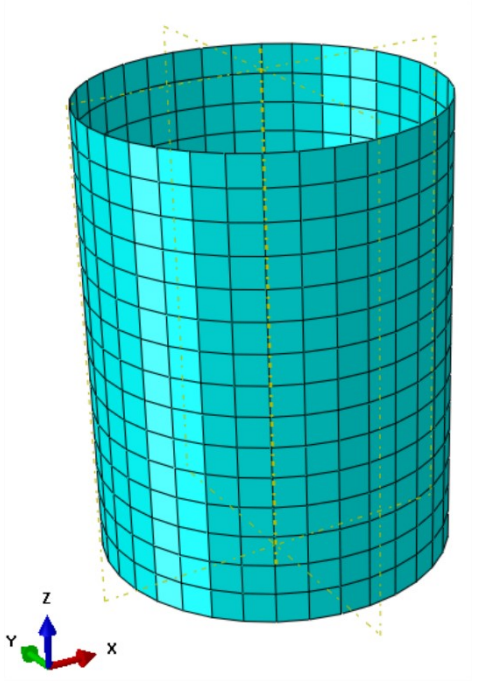


Figure 7.9 Numerical modelling of FRP jackets

7.4.2 Constitutive parameters

Similar to the shear tests, the yield surface of the concrete material and the element size chosen were calibrated first and maintained for all the specimens. Specimen D350-R60-F0-N2 was chosen as the reference specimen for the calibration process since it represented a typical reinforced rubberised concrete member under the highest vertical load. The mesh size l_m for the model was determined first based on the sensitivity study performed on the reference specimen. As shown in Figure 7.10, mesh sizes of $l_m \approx C/35$, $C/25$, $C/20$ were considered for the monotonic analysis where C represents perimeter of the circular column. It is evident in Figure 7.10 that the analysis provides very good correlation with the test results using the selected mesh sizes. The difference in the lateral capacity between the numerical models and the test results was within 3%. It should be noted that the "finest" mesh (l_m=30 $\approx C/35$) was able to predict the loss of capacity due to the fracture of reinforcement, unlike the "coarser" meshes. The loss of lateral capacity was included in the model

to indicate approximately the predicted occurence of reinforcement fracture rather than to represent it in an accurate manner. This aspect of behaviour is described in Section 7.4.3. A mesh size of l_m=30mm was therefore chosen for the analysis of all specimens.

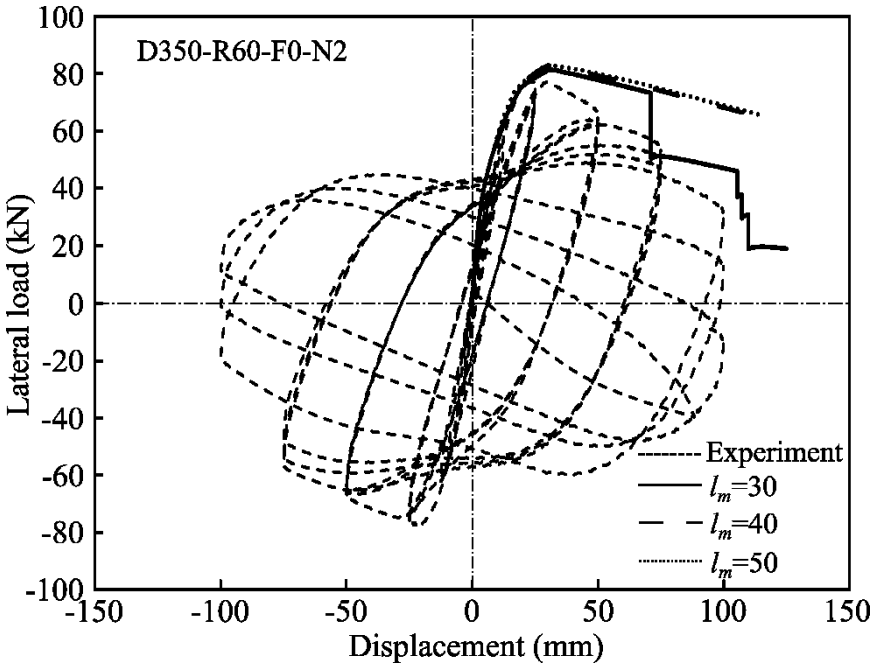


Figure 7.10 Mesh sensitivity analysis of the Reference Specimen D350-R60-F0-N2

To assess the appropriate value of ψ, a sensitivity study was carried out with the dilation angle varying in the range ψ =10°-50 °. It can be noted from Figure 7.11 that with the high value of ψ=50 °, the model showed a stiffer response compared to those with lower dilation angles and the test result. On the other hand, for the low value of dilation angle ψ=10 °, the model showed much lower lateral load capacity compared to the test result while the stiffness was also reduced as the lateral displacement increased. The value of ψ=30 ° for the dilation angle was therefore chosen for the analysis of all the members.

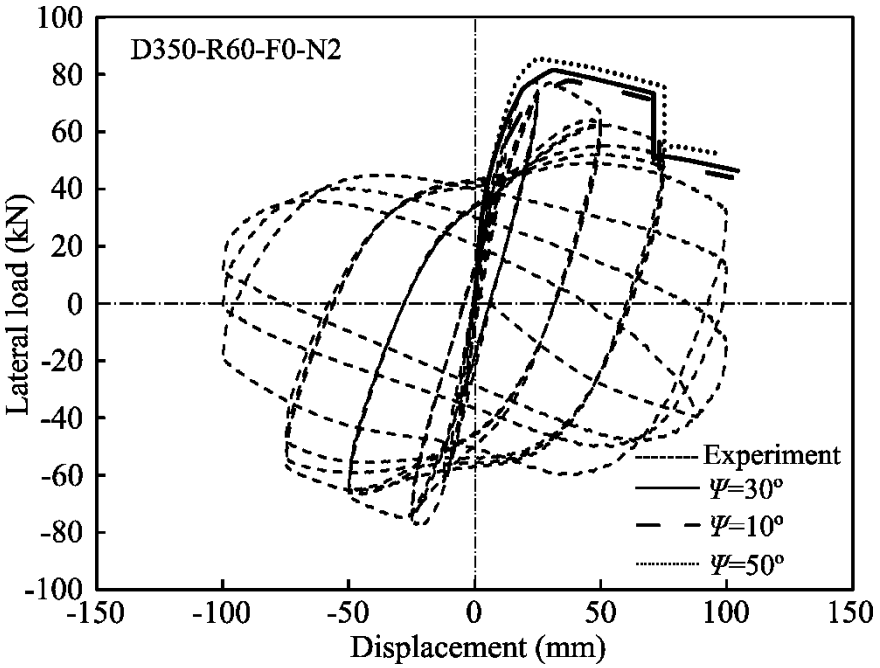


Figure 7.11 Influence of dilation angle on the behaviour of Specimen D350-R60-F0-N2

Similar to the shear test, the values of yield surface shape parameter K_c=0.667, biaxial-uniaxial compressive strength ratio f_b/f_c=1.16 and viscosity parameter of 4×10^{-6} were also used for the member tests. The uniaxial compressive behaviour was defined by Equation (3.3) - (3.11), and the exponential tension stiffening behaviour in Equation (7.8), with the modification of the maximum crack width in Equation (3.18), was applied in this validation process. The input material parameters required for concrete damage plasticity (CDP) model of the beam-column simulations are listed in Table 7-3.

Table 7-3 Input parameters of concrete material used in the analysis of beam-column member tests

Material parameter	ψ	ϵ	f_b/f_c	K_c	Viscosity parameter	l_m	Uniaxial compression	Uniaxial tension
Input value	30°	0.1	1.16	0.667	4×10^{-6}	30	Equation (3.3)-(3.11)	Hordijk (1992)+ Equation (3.18)

Bi-linear elasto-plastic behaviour was adopted for the steel reinforcement with an elastic modulus of 200GPa and a Poisson's ratio of 0.3. The input elasto-plastic properties for longitudinal reinforcement and stirrups were the same as the test results shown in Figure 6.3 and Table 6-3 whereas the fracture of reinforcement was assumed to occur at the ultimate strength point.

7.4.3 RC and RRuC member tests

As discussed previously in Section 6.2.1, failure of all the conventional reinforced concrete (RC) and rubberised concrete (RRuC) beam-column members was flexural. As shown in Figure 6.13, flexural cracks formed initially at relative lower lateral displacement followed by crushing of concrete as the lateral displacement increased. After reaching the maximum lateral strengths, the specimens experienced notable deterioration in their capacities as the flexural cracks and spalling of concrete accumulated. Fractures of the outermost reinforcement occurred in all the unconfined column members at a displacement of around 100mm which defined the ultimate failure of the specimens.

Table 7-4 Summary of monotonic analysis results for the RRuC specimens

Specimen	$V_{max,test}$ (kN)	$V_{max,num}$ (kN)	$V_{max,test}/ V_{max,num}$
D250-R00-F0-N1	57.3	60.0	0.95
D250-R60-F0-N1	38.5	38.4	1.00
D350-R45-F0-N0	80.1	81.9	0.98
D350-R45-F0-N1	84.9	82.4	1.03
D350-R60-F0-N0	74	76.8	0.96
D350-R60-F0-N1	77	78.0	0.99
D350-R60-F0-N2	79.2	81.4	0.97
D350-R60-F0-N2S	73.9	81.4	0.91
Average	-	-	*0.97*
STDEV	-	-	*0.04*
COV	-	-	*0.04*

Simulation of the monotonic response of all the RC and RRuC specimens aimed at representing the stiffness and lateral capacity as well as the failure modes. Figure 7.12 (a)-(h) illustrate the predicted monotonic numerical response for all the RC and RRuC specimens compared to the test result envelopes. It should be pointed out that the contribution of vertical loads in the horizontal directions were taken into account. The numerical simulations showed very good agreement with the test results in terms of the initial stiffness, cracked stiffness and the maximum lateral capacities. However, the numerical simulations overestimated the post-peak degradation compared to the experimental response, which is attributed to modelling idealisations employed particularly with respect to the monotonic nature of the analysis which does not account for cyclic deterioration. The overall average test-to-numerical capacity ratios was 0.97 with a coefficient of variation of 0.04 as indicated in Table 7-4.

Table 7-5 Summary of reinforcement analysis for RRuC specimens

Batch	Specimen	$\delta_{y,test}$ (mm)	$\delta_{y,num}$ (mm)	$\delta_{y,test}$ /$\delta_{y,num}$	$\delta_{f,test}$ (mm)	$\delta_{f,num}$ (mm)	$\delta_{f,test}$ /$\delta_{f,num}$
1	D250-R00-F0-N1	10.8	8.30	0.77	62.5	58.5	1.07
	D250-R60-F0-N1	10.8	9.70	0.90	87.5	87.4	1.00
2	D350-R45-F0-N0	12.4	12.8	1.03	110	83.1	1.32
	D350-R45-F0-N1	14.0	11.6	0.83	100	92.1	1.09
3	D350-R60-F0-N0	12.7	13.2	1.04	112	101	1.11
	D350-R60-F0-N1	15.1	15.5	1.03	100	101	0.99
	D350-R60-F0-N2	15.8	19.1	1.21	100	71.0	1.41
	D350-R60-F0-N2S	14.6	18.0	1.23	100	69.2	1.45
Average	-	-	-	*1.00*	-	-	*1.18*
STDEV	-	-	-	*0.17*	-	-	*0.18*
COV	-	-	-	*0.17*	-	-	*0.16*

In order to assess the ability of the models to simulate the behaviour, further validation of the test results focused on the reinforcement. As shown in Figure 7.13 (a)-(h) and Table 7-5, the strain propagation process of the longitudinal reinforcement at the interface between the circular column and foundation (recorded by strain gauge L1W (E) as shown in Figures 5.10 and 5.11) was well predicted by the numerical models. In addition, the fracture of reinforcement was also captured in several models represented by the sudden loss of lateral load capacity as shown in Figure 7.12 (a)-(h). As described in Chapter 6, three different batches of reinforcement were used, and the properties of the reinforcement in the numerical simulations was based on the average behaviour of each batch, as shown in Figure 6.3.

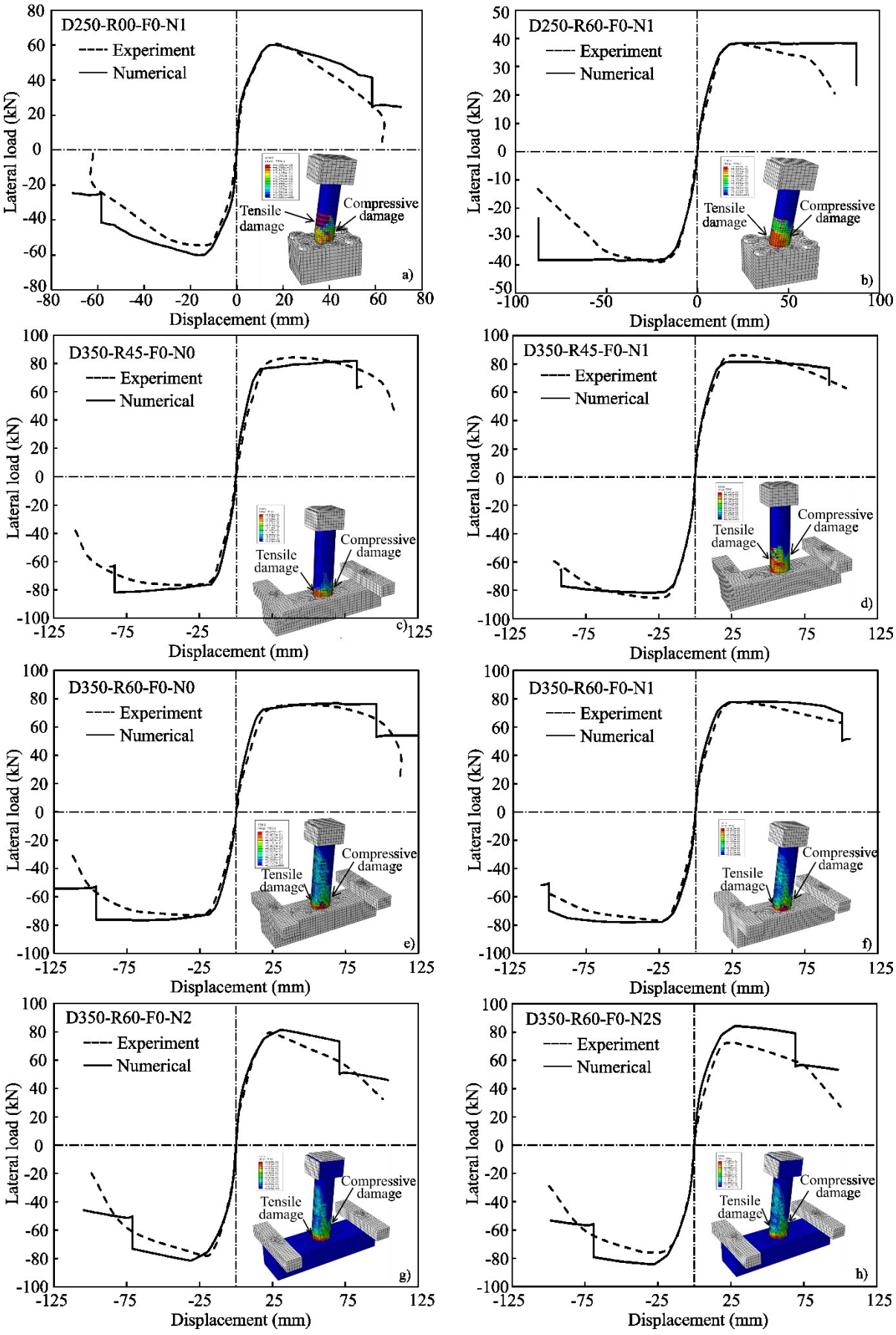


Figure 7.12 Load-displacement response of RRuC beam-column members

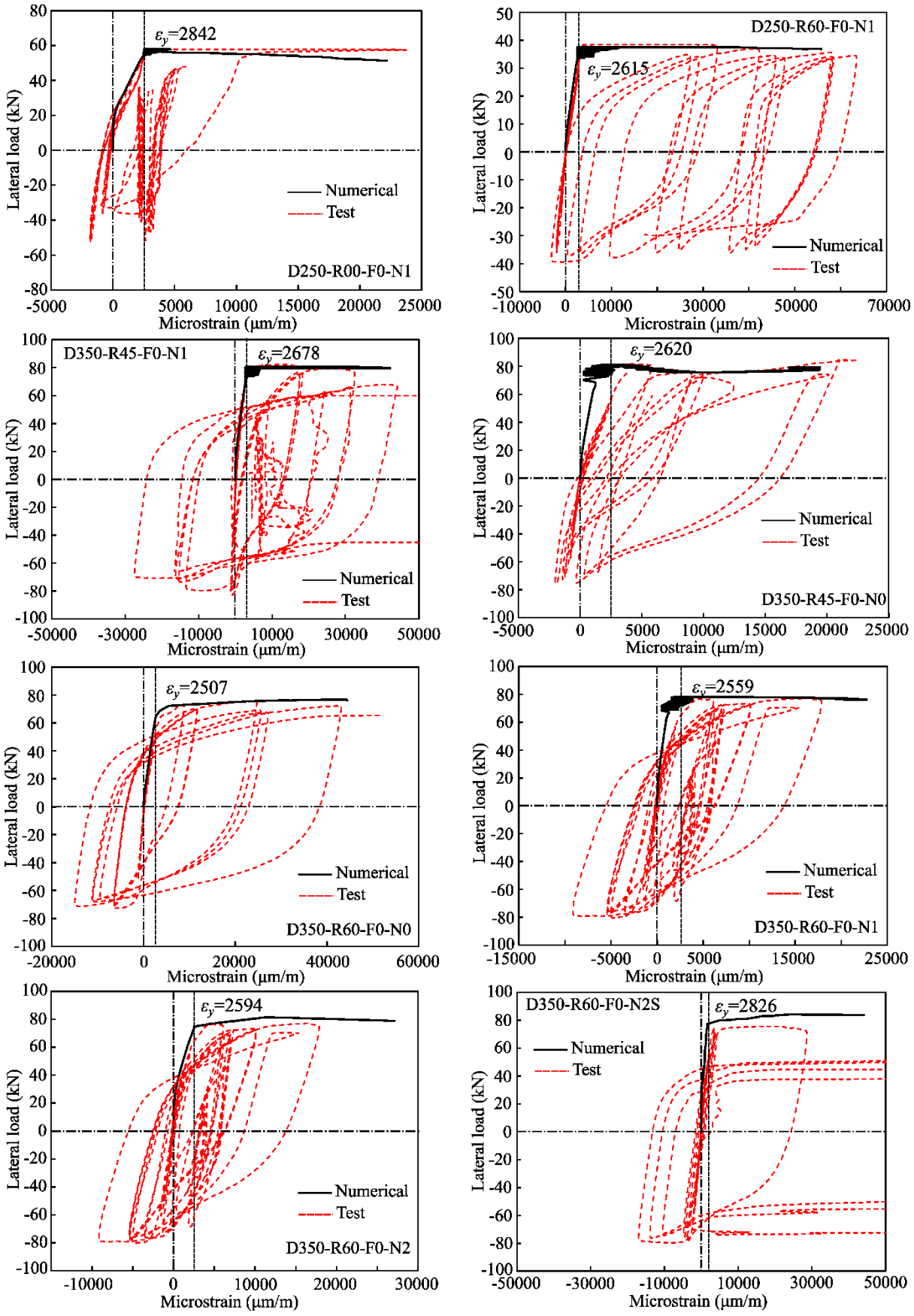


Figure 7.13 Longitudinal strain at the specimen-footing interface of RRuC beam-column members

As listed in Table 7-5, the fracture of longitudinal reinforcement of all test members were well represented in numerical simulations. For Specimen D350-R60-F0-N0 and D350-R60-F0-N1, the predicted fracture displacements were around 100mm which were in accordance with the test results whereas models of Batch 2 specimens (D350-R45-F0-N0 and D350-R45-F0-N1) predicted slightly lower fracture displacement. The predicted fracture in D350-R60-F0-N2 occurred at 75mm which was lower than the observations from the test (100mm). Nevertheless, Figure 7.10 indicates that significant degradation in lateral stiffness took place within the cycles at the displacement level of δ=75 mm during the test, which was followed by the fracture of reinforcement within the next level of lateral displacement. This behaviour was governed by severe concrete degradation as well as the strength loss of reinforcement at this level of displacement.

7.4.4 Externally confined (CRRuC) member tests

As noted above, before considering the externally-confined member tests, numerical simulation is firstly carried out for the confined cylindrical material tests described in Section 3.6. The cylinders had rubber replacement ratios of 45% and 60%, were wrapped with 2-3 layers of AFRP jackets, and were tested under uniaxial compressive loads. Numerical simulation of R45F2, R60F2 and R60F3 specimens were performed to validate the feasibility of the confinement model. Figure 7.14 shows the numerical model of an FRP confined cylinder with the same modelling procedure and constitutive parameters described in Sections 7.4.1 and 7.4.2 above, with a finer mesh size of l_m=5 mm considering the diameter of the material cylinders compared to the beam-column specimens.

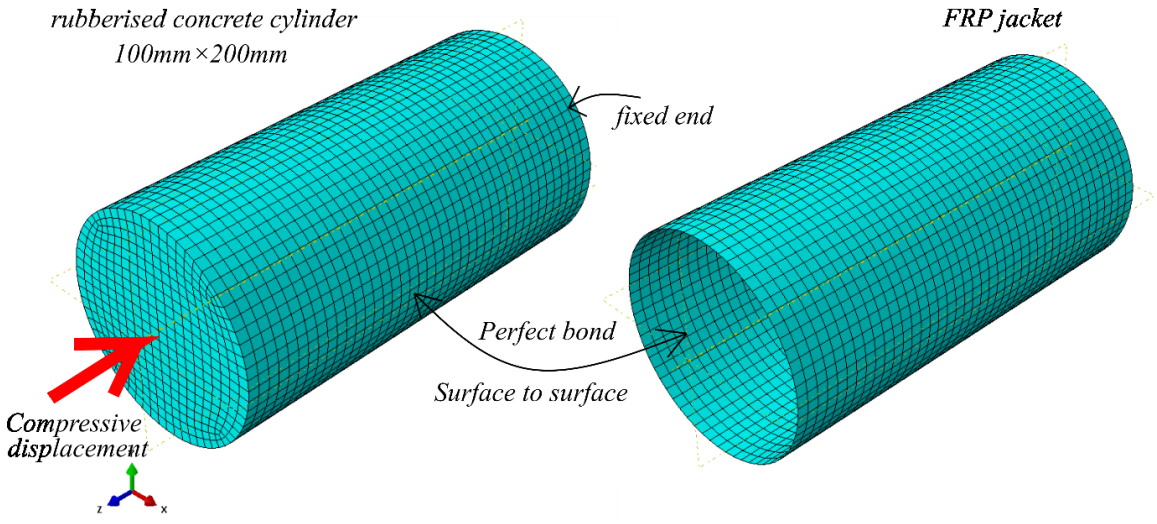


Figure 7.14 Numerical model of rubberised concrete cylinders and FRP jacket

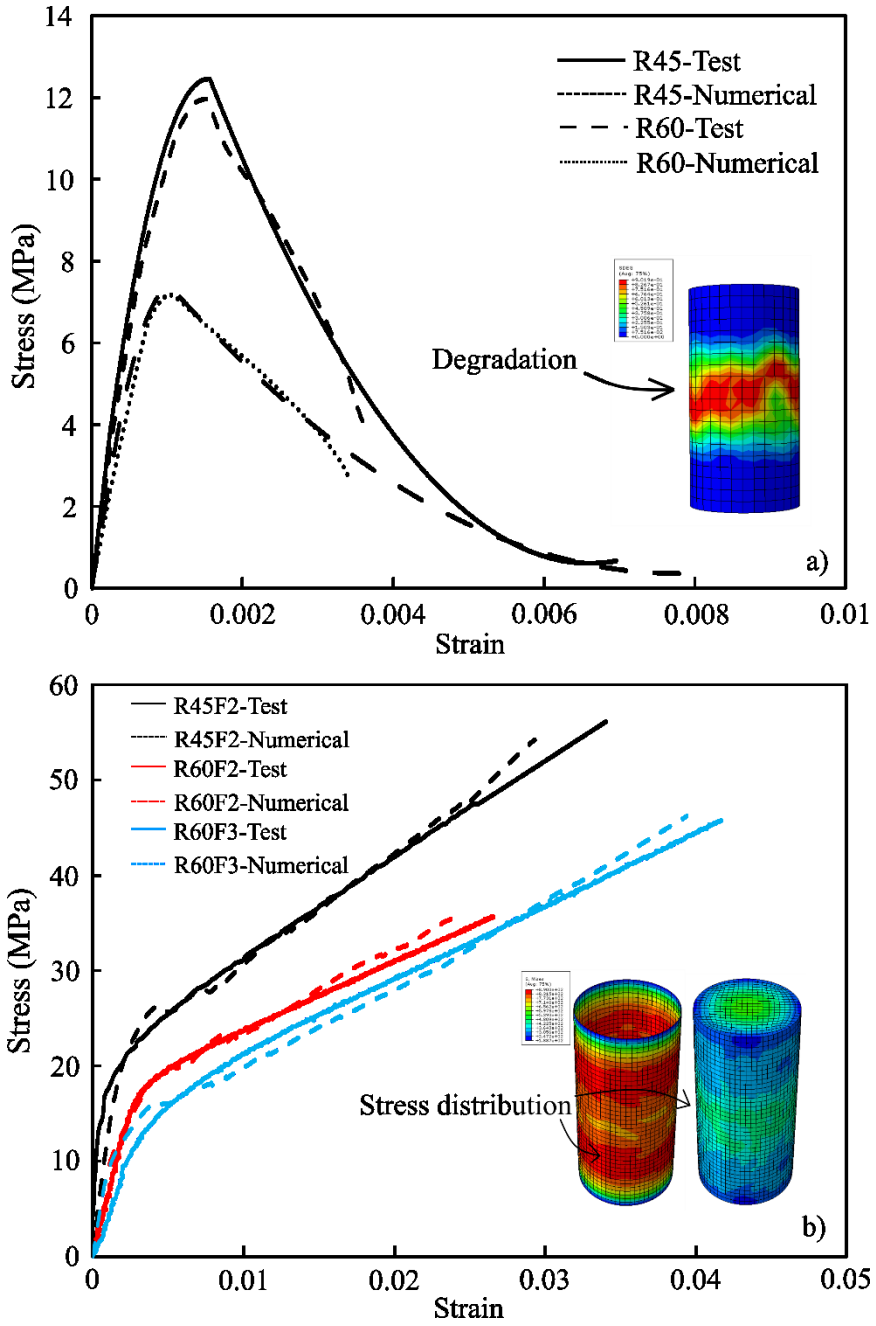


Figure 7.15 Numerical simulation of material cylinders: a) unconfined and b) FRP confined

As shown in Figure 7.15, the numerical models provides a very close prediction of the uniaxial compressive behaviour of unconfined and FRP confined rubberised concrete. For the unconfined rubberised concrete cylinders, the initial stiffness, capacity and post-peak behaviour are all well predicted (see Figure 7.15(a)). The difference in compressive strength with the tests is below 3%. The bilinear stress-strain behaviour of FRP confined rubberised concrete was also closely predicted in terms of the ultimate strength, stiffness of both branches as well as the transition points. Consequently, the same modelling procedure and perfect bond behaviour between the concrete

surface and FRP jacket were applied for the subsequent modelling of the FRP confined reinforced rubberised concrete (CRRuC) member specimens.

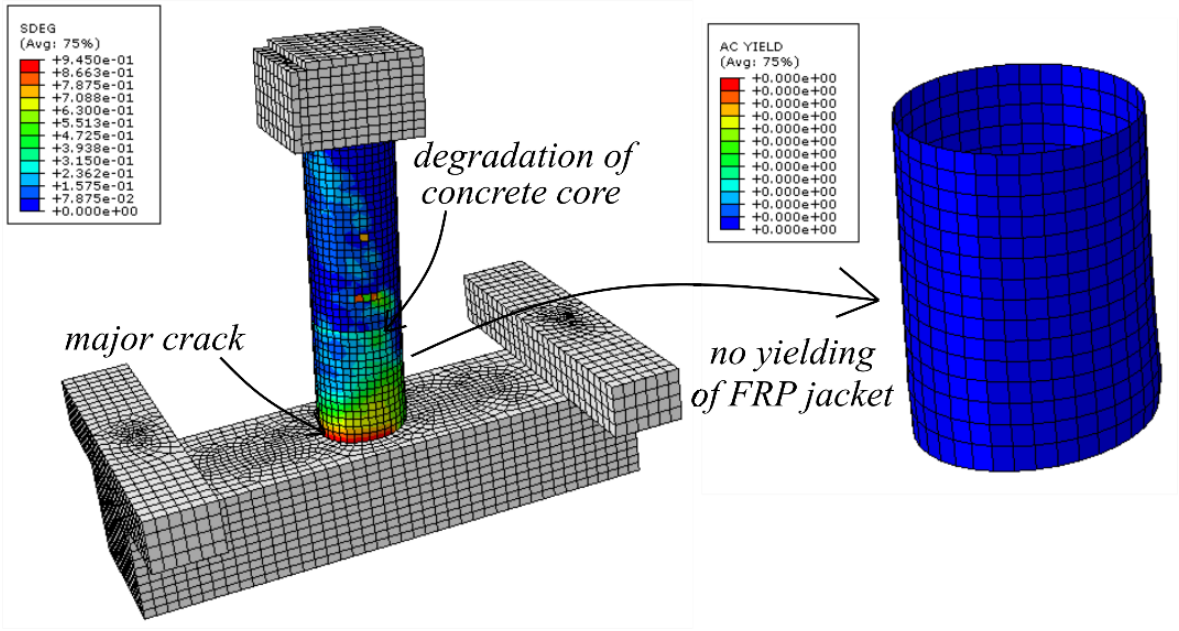


Figure 7.16 Typical ultimate behaviour of the CRRuC member models

As discussed in Section 7.4.1, the three-dimensional model of the FRP confined reinforced rubberised concrete (CRRuC) members considered the specimen as shown in Figure 7.8 (a)-(d) as well as the FRP sheet as in Figure 7.9 around the rubberised concrete part. As indicated in Figure 7.16, the typical failure mode of the CRRuC members obtained in the models was in accordance with test results. Although the rubberised concrete core experienced high damage in both tension and compression around the critical area at significant inelastic deformation levels, the external confinement kept the integrity of the concrete while the FRP jacket remained largely elastic throughout.

Table 7-6 Summary of comparative results for the CRRuC specimens

Specimen	$V_{max,test}$ (kN)	$V_{max,num}$ (kN)	$V_{max,test}/V_{max,num}$
D250-R60-F3-N1	43.4	44.3	0.98
D350-R45-F2-N0	84.4	81.6	1.03
D350-R45-F2-N2	94.4	99.5	0.95
D350-R60-F3-N0	78.1	76.3	1.02
D350-R60-F3-N2	78.1	97.5	0.80
Average	-	-	*0.96*
STDEV	-	-	*0.09*
COV	-	-	*0.10*

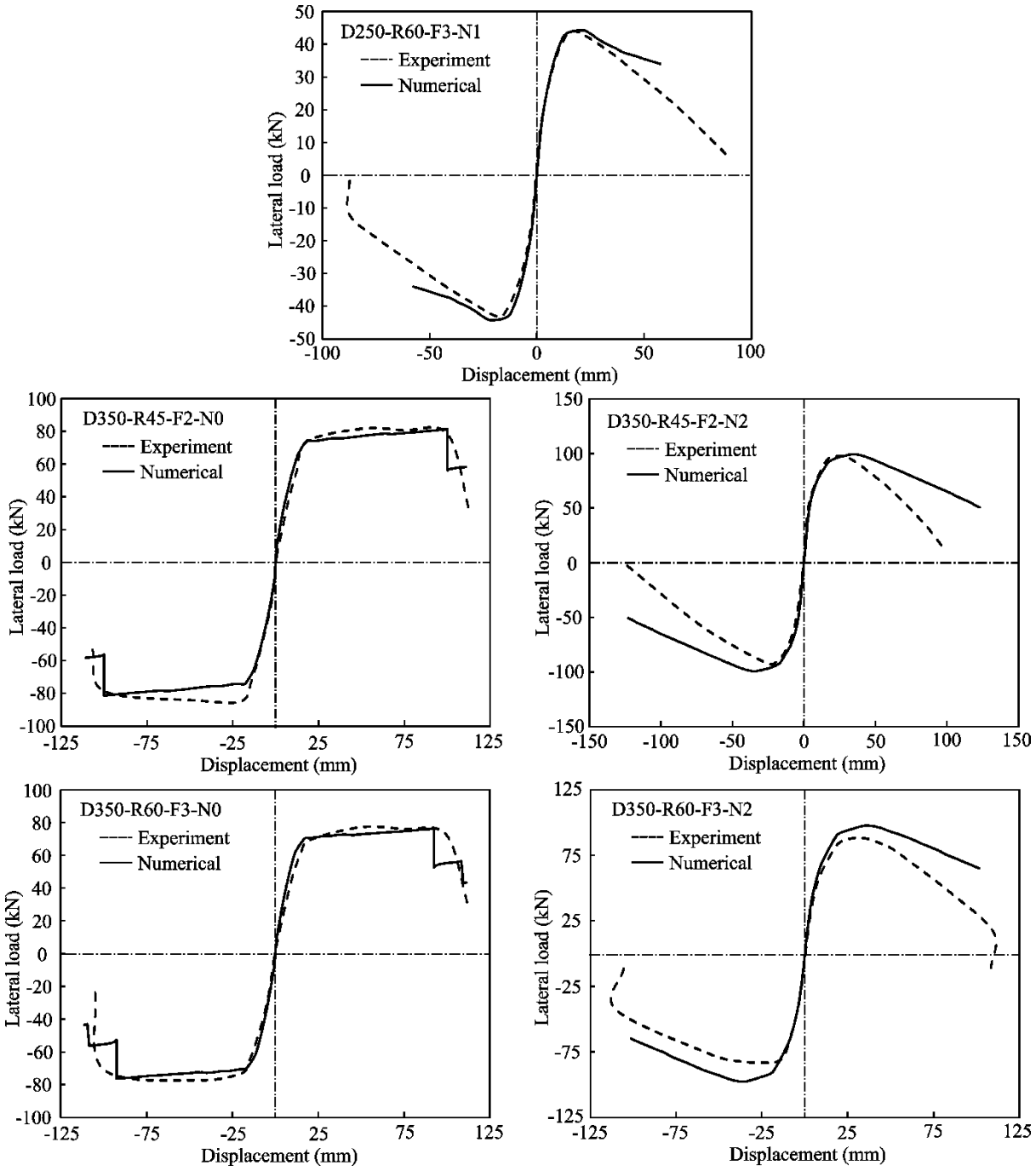


Figure 7.17 Load-displacament response of CRRuC beam-column members

The monotonic lateral load-displacement response of the five CRRuC members are shown in Figure 7.17 (a)-(e). Similar to the RC and RRuC member simulations, the numerical simulations show good agreement with the corresponding test results in terms of stiffness and lateral capacity whereas the degradation of lateral capacities were overestimated. Similar to the test results, the numerical models without axial loads showed less degradation after reaching the ultimate lateral capacity until the fracture of the reinforcement occurred (D350-R45-F2-N0, D350-R60-F3-N0). On the other hand, the models subjected a high level of axial load (D350-R45-F2-N2, D350-R60-F3-N2)

experienced notable deterioration with the increase of lateral post-peak displacement. Table 7-6 summarises the comparative results of the lateral capacities between the numerical and test results, indicating an average test-to-model ratio of 0.96 with a coefficient of variation of 0.10.

Table 7-7 and Figure 7.18 show the comparative analysis and test results with respect to the reinforcement behaviour at the member-footing interface. The numerical models provide reasonably good prediction of the strain propagation in the reinforcement. The test-to-numerical yield displacement ratio is 1.06 with a COV of 0.11. The reinforcement fracture occurs in the CCRuC member tests under low or no axial loads as reported in Chapter 6 (D250-R60-F3-N1, D350-R45-F2-N0, D350-R60-F3-N0), and similar findings are obtained from the numerical models as well. As shown in Table 7-7, the numerical models of Specimens D350-R45-F2-N0 and D350-R60-F3-N0 indicated that reinforcement fracture occurred at a lateral displacement of 100 mm and 92 mm respectively (about 10% difference compared to the tests). On the other hand, the model of D250-R60-F3-N1 predicted higher fracture displacement of 103 mm compared to the test (87.5 mm).

Table 7-7 Summary of reinforcement analysis for the CRRuC specimens

Specimen	$\delta_{y,test}$ *(mm)*	$\delta_{y,num}$ *(mm)*	$\delta_{y,test}/\delta_{y,num}$	$\delta_{f,test}$ *(mm)*	$\delta_{f,num}$ *(mm)*
D250-R60-F2-N1	10.8	11.4	0.95	87.5	103
D350-R45-F2-N2	12.0	14.2	0.85	N/A	N/A
D350-R45-F2-N0	12.4	11.1	1.12	113	100
D350-R60-F3-N2	12.0	11.6	1.03	N/A	N/A
D350-R60-F3-N0	12.2	11.9	1.03	100	92
Average	-	-	*0.99*	-	-
STDEV	-	-	*0.10*	-	-
COV	-	-	*0.10*	-	-

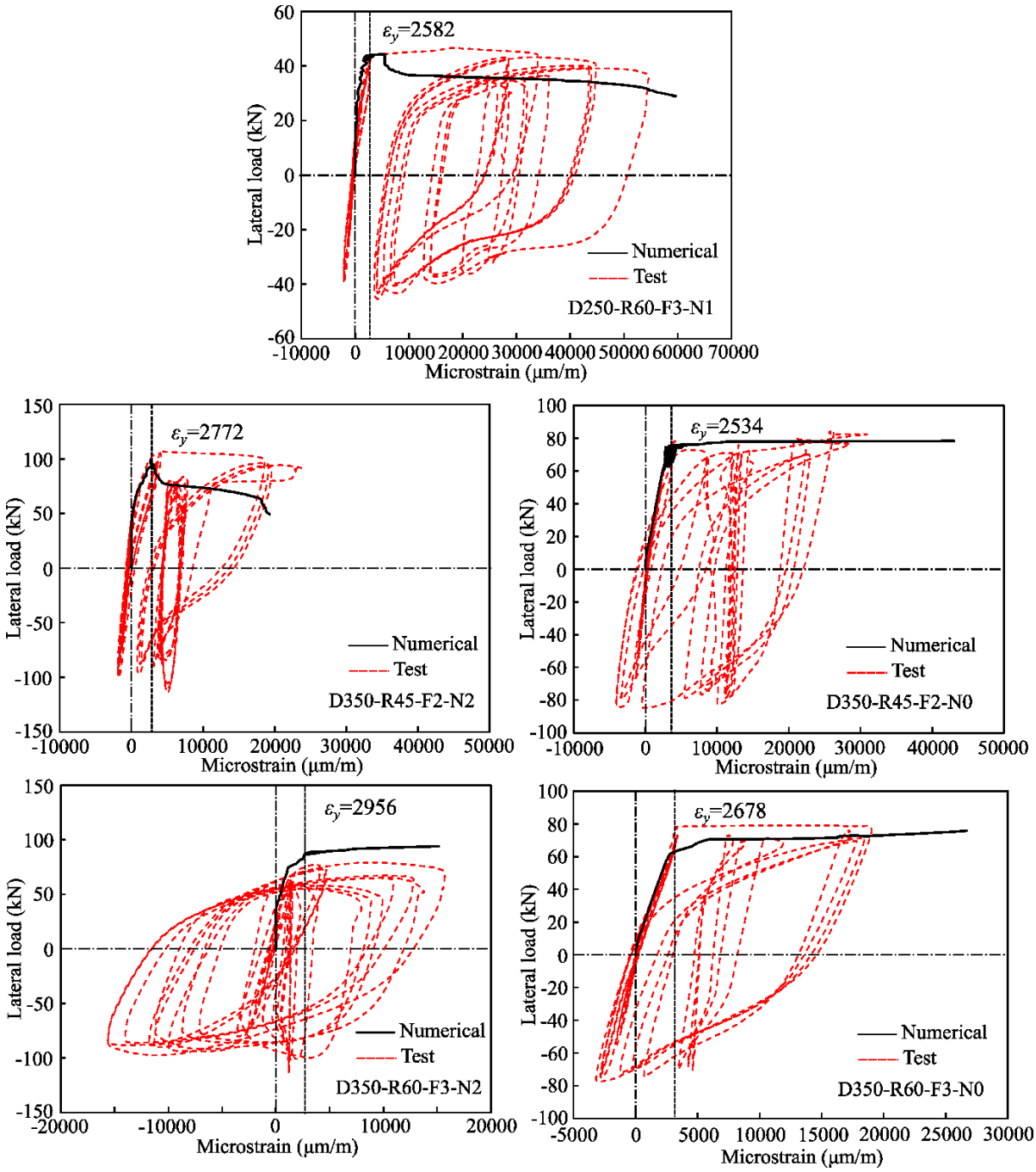


Figure 7.18 Longitudinal strain at the specimen-footing interface of CRRuC beam-column members

7.5 Concluding remarks

This chapter described the numerical modelling procedures used for simulating the test results described previously in Chapter 3 to Chapter 6, including the uniaxial compressive tests on cylinders, asymmetric shear tests on prisms and large-scale beam-column tests. The concrete damage plasticity (CDP) model, incorporated within the nonlinear finite element analysis software Abaqus was adopted in this investigation to simulate all the tests.

Detailed comparisons between the numerical and test results have illustrated the overall accuracy of the numerical models in predicting the behaviour of rubberised concrete specimens under various loading arrangements. The proposed uniaxial constitutive models described through Equations (3.3)-(3.11) and Equation (3.18) in Chapter 3, were shown to offer a reliable characterisation of rubberised concrete through the CDP model, when combined with an appropriate representation of the reinforcement. For externally-confined members, the FRP jacket was assumed as a unidirectional tensile material (membrane element) while the interaction between the FRP and concrete surface could be defined through perfect bond based on experimental observations as well as numerical validations.

The above discussed numerical validation process against the experimental results illustrates the overall reliability of the numerical models in capturing the key response characteristics, and their suitability for use in detailed parametric assessments. Accordingly, Chapter 8 describes a number of numerical parametric studies which focus on examining the influence of salient geometric and material properties on the inelastic behaviour of rubberised concrete structural members.

Chapter 8

8 Parametric assessments and design considerations

Nomenclature

Greek letters

δ – lateral displacement
$\delta_{u,pred}$ – predicted lateral deformation at ultimate load corresponding herein to 20% decrease in capacity
$\delta_{u,test}$ – test lateral deformation at ultimate load corresponding herein to 20% decrease in capacity
Δ_u – ultimate drift ratio
Δ_k – stiffness reduction factor
Δ_a – axial capacity enhancement factor
ε_{cu2} – ultimate compressive strain
$\varepsilon_{cu2,c}$ – confined ultimate compressive strain
$\varepsilon_{cr1,1}$ - crushing strain for rubberised concrete
$\varepsilon_{cru,c}$ – proposed confined ultimate compressive strain of rubberised concrete
λ - factor for the type of aggregate replaced
ρ – longitudinal reinforcement ratio
ρ_{vr} - volumetric rubber ratio
μ_ψ - rotation ductility
μ_ψ' - modified rotation ductility
υ - axial load ratio
υ' - modified axial load ratio
τ_u - shear resistance
$\phi_{s,y}$ – yield curvature
ψ_y - rotation at yielding
ψ_p – plastic rotation
ψ_u - ultimate rotation

Lowercase latin letters

f_{c0} - normal concrete cylinder compressive strength
f_{cr} - rubberised concrete cylinder compressive strength
f_{rct} - rubberised concrete tensile strength
$f_{s,y}$ – yield strength of steel
f_{crc} – confined rubberised concrete strength
f_l – lateral confining pressure
$k_{cr,0}$ – member stiffness of reference concrete member
$k_{cr,r}$ – member stiffness of rubberised concrete member
l_{col} – column length

Uppercase latin letters

A_c – cross-sectional area of concrete
A_s – cross-sectional area of steel
D - diameter
E_{cr} - elastic modulus
F_{calc} – calculated axial compression capacity
F_{num} – numerical axial compression capacity
F_{calc} – stirrup confined axial compression capacity
l_{cr} – critical length where detailing is required
L_{sp} – spread of plasticity
$L_{sp,gradient}$ – spread of plasticity from moment gradient
$L_{sp,gradient}$' – modified spread of plasticity from moment gradient
$L_{sp,local}$ – spread of plasticity from local deformation
$L_{sp,local}$ ' – modified spread of plasticity from local deformation
M_y – bending moment at yield
M_u – bending moment at ultimate
P_u - ultimate strength

8.1 General

The experimental programme described in Chapters 4 to 6 mainly examined the shear and flexural behaviour of rubberised concrete components. The parameters involved in experimental studies were largely related to the rubber content ratios, in addition to a limited assessment of geometry and

loading. The structural behaviour of rubberised concrete members can be influenced by various other parameters that require further assessment. It was shown in Chapter 7 that the adopted finite element analysis procedures can represent the nonlinear behaviour of rubberised concrete members, and can be used in conducting parametric studies.

This chapter describes the details of a number of parametric assessments on prismatic shear elements as well as large-scale beam-column members. The rubberised concrete strength, influenced by the reference concrete strength and rubber content, is the key parameter investigated in the parametric study on Mode II shear behaviour. The main purpose of the study on large-scale beam-column members, on the other hand, is to assess the flexural behaviour of externally unconfined reinforced rubberised concrete members and its sensitivity to a number of important parameters. These include the rubber content ratio, reinforcement ratio and level of applied axial. The choice and range of each parameter are discussed, and the corresponding numerical results are presented, based on an idealised cantilever type representation of the beam-column elements. The numerical results are discussed and the main design implications are highlighted.

8.2 Behaviour of asymmetric shear members

Following the numerical validation of the shear-governed members, as discussed in Chapter 7, a series of parametric assessments accounting for varying reference concrete strengths f_{c0} and different rubber content ρ_{vr} were conducted. An identical tri-dimensional model having the same geometry and mesh as the models used for validation was employed for the parametric studies (as shown in Figure 7.4). Four different reference concrete materials with strengths f_{c0}=20, 40, 60 and 70 MPa, and variations in rubber replacement ratios ρ_{vr}=0, 0.2, 0.4 and 0.6 were modelled analytically using the constitutive models and recommendations from Chapter 3 as described in Equation (3.2)-(3.11).

As shown in Table 8-1 and Figure 8.1, with the increase in rubber content, concrete with different reference strengths f_{c0} exhibit a similar reduction of strength for members developing shear governed response. All predictions show reductions around 40% in the estimated capacities for 20% of rubber replacement. The reduction rate in strength is much smaller when the rubber content is increased further: 60% for ρ_{vr}=0.4 and about 70% for ρ_{vr}=0.6. It can be noted from the parametric study that the rubber content influences the member shear resistance in a comparable way to the compressive strength. Further discussion on the influence of rubber content on the shear resistance of rubberised concrete based on the numerical models and test results is given below.

Table 8-1 Details and results for asymmetric shear members

f_{c0} (MPa)	20				40			
ρ_{vr} (-)	0	0.20	0.40	0.60	0	0.20	0.40	0.60
Name	F20R0	F20R20	F20R40	F20R60	F40R0	F40R20	F40R40	F40R60
f_{rc} (MPa)	20.0	7.58	3.56	2.21	40.0	15.2	7.12	4.21
f_{rct} (MPa)	1.34	0.82	0.57	0.44	1.89	1.17	0.80	0.62
E_{rc} (GPa)	19.0	9.98	6.02	4.27	30.1	15.8	9.56	6.75
P_u (kN)	33.7	19.9	13.0	9.32	48.6	29.0	19.6	14.5
ΔP_{ur} (%) [1)]	0	41.0	61.3	72.3	0	40.4	60.0	70.0
f_{c0} (MPa)	60				70			
ρ_{vr} (-)	0	0.20	0.40	0.60	0	0.20	0.40	0.60
Name	F60R0	F60R20	F60R40	F60R60	F70R0	F70R20	F70R40	F70R60
f_{rc} (MPa)	60.0	22.7	10.7	6.32	70.0	26.5	12.5	7.37
f_{rct} (MPa)	2.32	1.43	0.98	0.75	2.50	1.55	1.06	0.90
E_{rc} (GPa)	39.5	20.8	12.5	8.84	43.8	23.0	13.9	9.79
P_u (kN)	60.7	35.8	24.5	18.3	66.1	36.4	26.6	20.1
ΔP_{ur} (%) [1)]	0	41.1	59.7	69.8	0	44.9	59.7	69.6

1) The reduction in load capacity is based on the rubberised concrete mixes compared to the corresponding reference mix.

The term ‘shear strength’ is used to refer to several concepts in previous studies, ranging from the resistance of a material subjected to pure shear stress to the capacity of a reinforced concrete beam under external shear action. On the other hand, shear resistance τ_u refers to the ultimate shear stress imposed on the plane of fracture A_f in the absence of a normal force (Everling, 1964). In this study, shear strength is defined as the ratio between the ultimate load P_u and the corresponding fracture surfaces, where $A_{f,}$ is used as a metric for comparison. From the tested specimens, members having shear-governed failures (SGF) are considered for detailed assessment with respect to the influence of ρ_{vr} on τ_u.

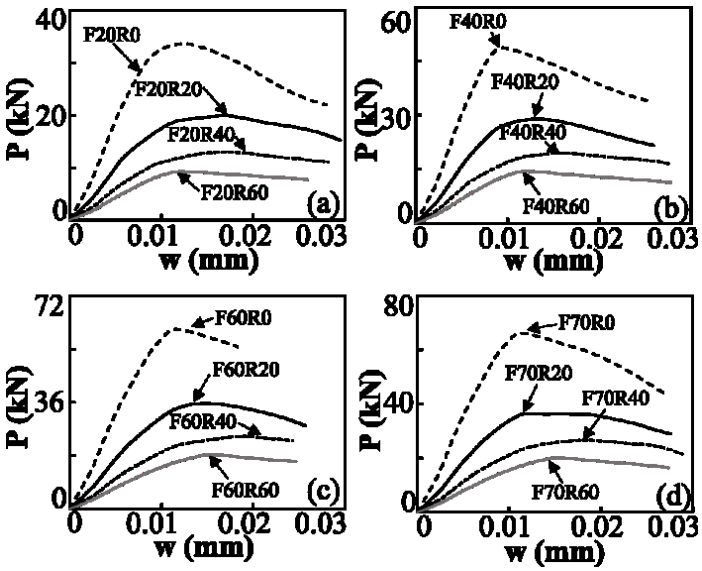


Figure 8.1 Influence of rubber content on the shear governed load capacity of concrete with reference compressive strength of: a) 20MPa, b) 40MPa, c) 60MPa, d) 70 MPa

In addition to the experimental results shown in Chapter 4, a parametric assessment was carried out on 16 simulations in which f_{c0} and ρ_{vr} were varied, and led to similar reductions of τ_u in relationship to ρ_{vr} (Figure 8.2a). These enable the definition of τ_u-ρ_{vr} expressions with material configurations covering wider ranges.

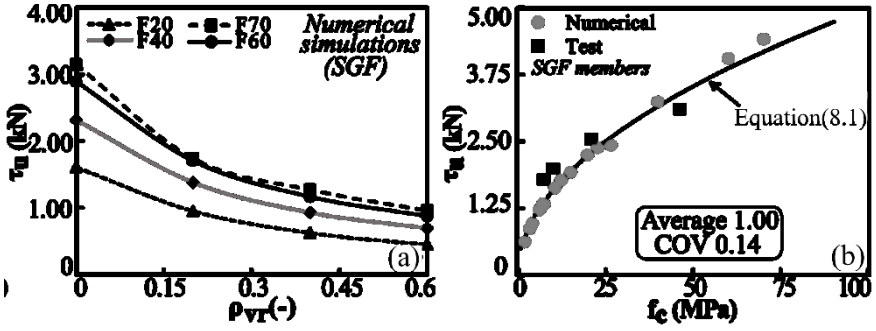


Figure 8.2 Relationships between: a) τ_u and ρ_{vr} from SGF numerical simulations; b) Prediction of the shear resistance τ_u (Equation 8.1)

Based on the results obtained from the tests as well as the numerical parametric assessments described herein, a relationship to assess the shear resistance τ_u as a function of the concrete strength f_c (f_{c0} for normal concrete or f_{rc} for rubberised concrete) is proposed. Equation (8.1a) may be used for assessing τ_u both for normal and rubberised concrete materials. The relationship between τ_u for rubberised concrete materials and ρ_{vr} can be expressed indirectly through the rubberised concrete compressive strength f_{rc} using Equations (8.1b,c), in which f_{c0} is the concrete compressive strength

of the reference normal concrete from which the rubberised concrete material is derived, whilst λ is a function of the type of mineral aggregate replaced (Equation 3.2a,b).

$$\tau_u = \frac{1}{2}\sqrt{f_c} \tag{8.1a}$$

$$f_{rc} = \frac{f_{c0}}{1+2\left(1.5\lambda\rho_{vr}\right)^{3/2}} \tag{8.1b}$$

$$\tau_u = \frac{1}{2}\sqrt{\frac{f_{c0}}{1+2\left(1.5\lambda\rho_{vr}\right)^{3/2}}} \tag{8.1c}$$

Figure 8.2b depicts predictions of Equation (8.1) using the concrete strengths given in Table 4-2 for the SGF test specimens described in Chapter 4 and the numerical models in Table 8-1, as well as the τ_u curve predicted for f_c varying in the range of 5 to 90 MPa. The proposed equation may be used to estimate τ_u since the average test and numerically assessed-to-predicted τ_u is 1.00, whilst the COV is 14.1%.

The expressions proposed above offer reliable representations for the assessment of the shear resistance of rubberised concrete as a function of the rubber content and the compressive strength of the reference non-rubberised concrete. Such relationships have been lacking to date and enable the use of these materials, not only in non-structural applications, but also in structural members.

8.3 Beam-column modelling

8.3.1 Idealised member model

The detailed numerical models of all reinforced concrete (RC) and reinforced rubberised concrete (RRuC) were validated against the corresponding experimental results in Chapter 7. For the sake of computational efficiency in the parametric assessments, whilst retaining accuracy, a simplified numerical model was employed as shown in Figure 8.3(a). The model considered the shear span of the member as a cantilever, with a fixed end boundary condition as well as a free end where axial load and lateral displacement were applied. The element types, sizes as well as the material properties were the same as introduced in Chapter 7. Figure 8.3(b) also illustrates the comparison of lateral load-displacement response of the typical experimental member D350-R60-F0-N2 acquired from both models. It can be noted that response of a simplified model shows good agreement with that from the full-sized model with slightly stiffer behaviour prior to ultimate and earlier fracture of reinforcement due to the absence of the footing.

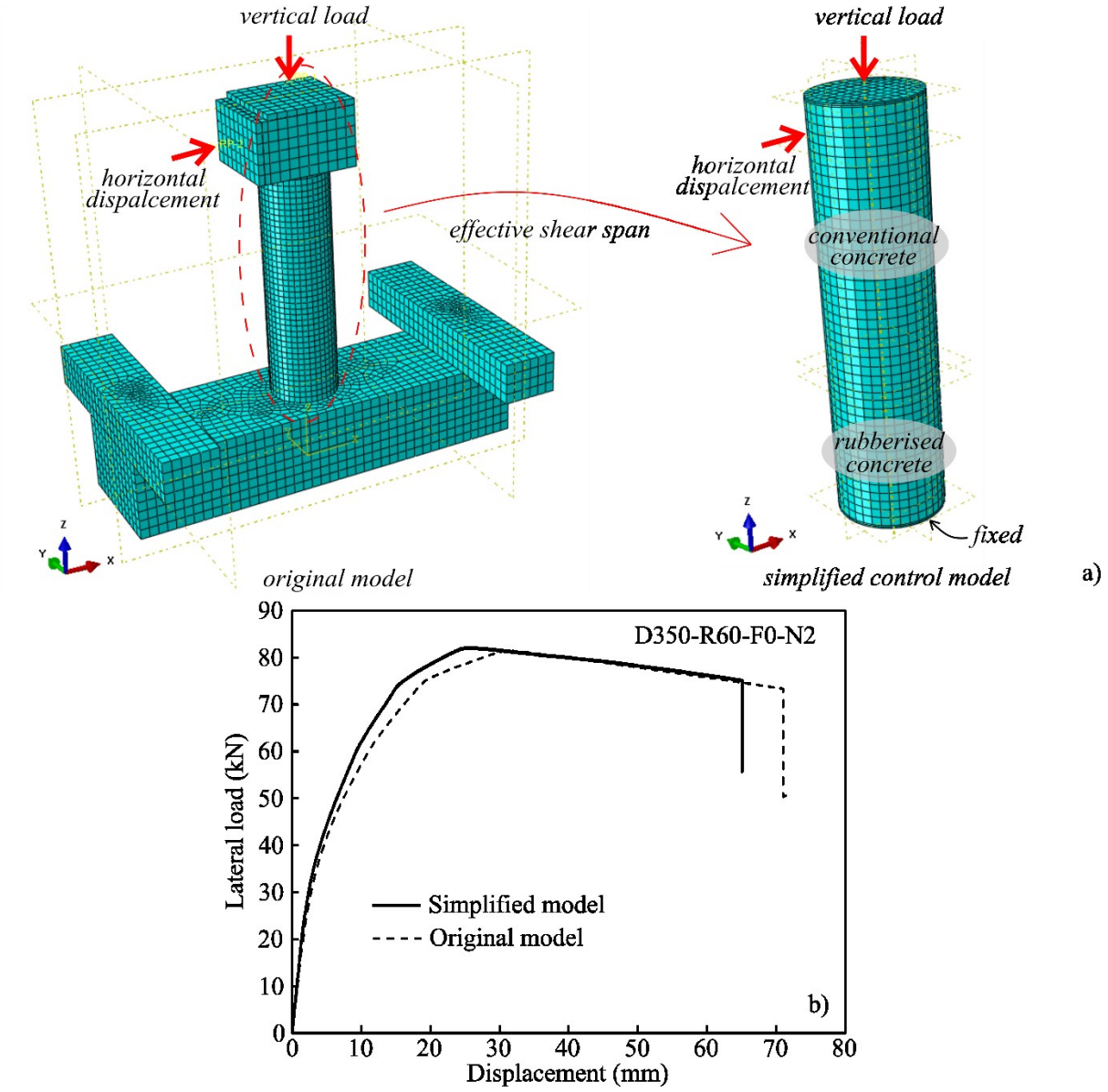


Figure 8.3 Comparison between original and simplified numerical models: (a) modelling geometry, (b) load-displacement response

Since this study focuses on flexural member behaviour, the influence of overall member slenderness was not of direct relevance, and it was decided to retain the dimensions of the test members. In addition, to limit the number of analyses, Class C reinforcement properties (EN 1992-1-1) were chosen to define the steel material in all cases. Details of control (i.e. reference) numerical model, used for the parametric assessment, are listed in Table 8.2.

Table 8-2 Details of the control model

Member length l_{col} (mm)	1350
Length of rubberised concrete l_{rub} (mm)	450
Length of external confinement l_{conf} (mm)	500
Gross cross-section diameter D (mm)	350
Reference concrete compressive strength f_{c0} (Mpa)	70
No. of longitudinal rebars	8
Stirrup layout	Ø10 at 70 mm
Yield stress of steel rebar $f_{s,y}$ (Mpa)	500
Yield strain of steel rebar $\varepsilon_{s,\,y}$ (mm/mm)	0.0025
Ultimate stress of steel rebar $f_{s,u}$ (Mpa)	575
Ultimate strain of steel rebar $\varepsilon_{s,\,u}$ (mm/mm)	0.075
Rubber content ρ_{vr} (%)	Investigated parameter
Reinforcement ratio ρ (%)	Investigated parameter
Applied axial load υ	Investigated parameter

8.3.2 Main parameters

Concrete properties

As one of the key parameters considered in this research, the rubber content was examined in all parametric studies. As in the shear members, the rubber replacement ratios were chosen as ρ_{vr}=0, 0.2, 0.4 and 0.6 of the total aggregate volume, referred to as R00, R20, R40 and R60 respectively. The original conventional concrete strength was set as f_{c0}=70 MPa and unchanged throughout the study which was also similar to that in the experimental programme.

Reinforcement ratio

The reinforcement ratio is one of the key factors affecting the load carrying capacity, stiffness, as well as the failure mode of members. The reinforcement ratio is defined here as $\rho=A_s/A_c$, where A_s and A_c are the cross-sectional area of longitudinal reinforcement and concrete respectively. Three different reinforcement ratios were chosen for the analyses (i.e. ρ_1= 1.0%, ρ_2= 1.7% and ρ_3= 4.0%). The upper bound value ρ_3=4.0% was chosen as the maximum reinforcement ratio suggested by Eurocode 2 (EN 1992-1-1). The reinforcement ratio of ρ_2= 1.7% was the same as that applied in the test programme described in Chapter 6.

Axial load

The axial load applied on the member is one of the important parameters that influence the behaviour. It was shown in the experimental investigation described in Chapter 6 that the member stiffness and ductility are directly affected by the applied axial load. However, due to the experimental constraints, the range investigated in the tests was limited to 20% of the member axial capacity.

In the parametric assessments, representative values of the axial compressive load were chosen as 0, 0.1, 0.2, 0.3, 0.4 and 0.6 of the cross-section axial capacity, represented by the axial load ratio υ, referred to as N0, N10, N20, N30, N40 and N60, respectively. It should be noted that the cross-sectional axial capacities of RC and RRuC members were estimated as:

$$F_{calc} = f_{cr} A_c + f_{s,y} A_s \tag{8.2}$$

where f_{cr} is the (rubberised) concrete strength without considering the effect of stirrup confinement.

Considering the above-listed parameters, a total of more than 70 numerical models were analysed within the parametric assessments. Based on the parameters discussed above, the reference for the numerical models adopts the format of R*xx*-*ρx*-N*z* which indicate the rubber content, longitudinal reinforcement ratio and level of applied compression load. Since the geometry of the model was not varied, the member diameter *D* is not included in the discussion below.

8.3.3 Failure criteria

In the experimental investigation, the ultimate failure of the beam-column specimens typically occurred through fracture of reinforcement, particularly when a relatively low level of axial load was applied. For members subjected to relatively high axial compression, significant degradation in moment capacity occurred (Figure 6.24) prior to fracture of the reinforcement.

Based on the above, the ultimate state is determined by either a flexural dominated failure criterion resulting in reinforcement fracture (FF) or a concrete crushing dominated failure criterion (CF), whichever occurs first. The FF criterion is characterised as the first fracture of longitudinal reinforcement, while the CF criterion is defined as a compressive crushing of the concrete core inside the stirrup confinement. An ultimate compression strain of the concrete core is defined to represent the crushing failure as discussed in detail below in Section 8.4.3.

8.4 Performance of beam-column members

A large amount of data was acquired from the analyses carried out within the parametric assessments. A number of key performance characteristics of flexural members were considered, including the member stiffness, axial bending strength interaction, ductility as well as the spread of plasticity. The results are first presented in the form of charts to illustrate the general trends and to provide a comparative assessment of the results, followed up by discussions of the main findings.

8.4.1 Member stiffness

As discussed in Chapter 6, the member stiffness was evaluated as the tangential stiffness $k_{cr} = \frac{40\%V_{\max}}{\delta_{40\%}}$, determined from the ratio of the lateral load at 40% of the maximum load capacity V_{max} and the corresponding lateral displacement $\delta_{40\%}$. Figure 8.4 highlights the stiffness reduction ratios (Δ_k=1-$k_{cr,r}$/$k_{cr,0}$) between RRuC members with different rubber contents ($k_{cr,r}$) and the corresponding reference RC members ($k_{cr,0}$) under various levels of axial loads. It is shown that the rubber content had the major influence on the member stiffness where members with higher rubber content develop lower stiffness. The experimental observations in Chapter 6 also revealed the same behaviour. In addition, Δ_k increases as the axial load ratio increases from 0 to 0.1 while further increase in axial load does not provide significant influence which is also indicated by the bilinear representative curves in Figure 8.4.

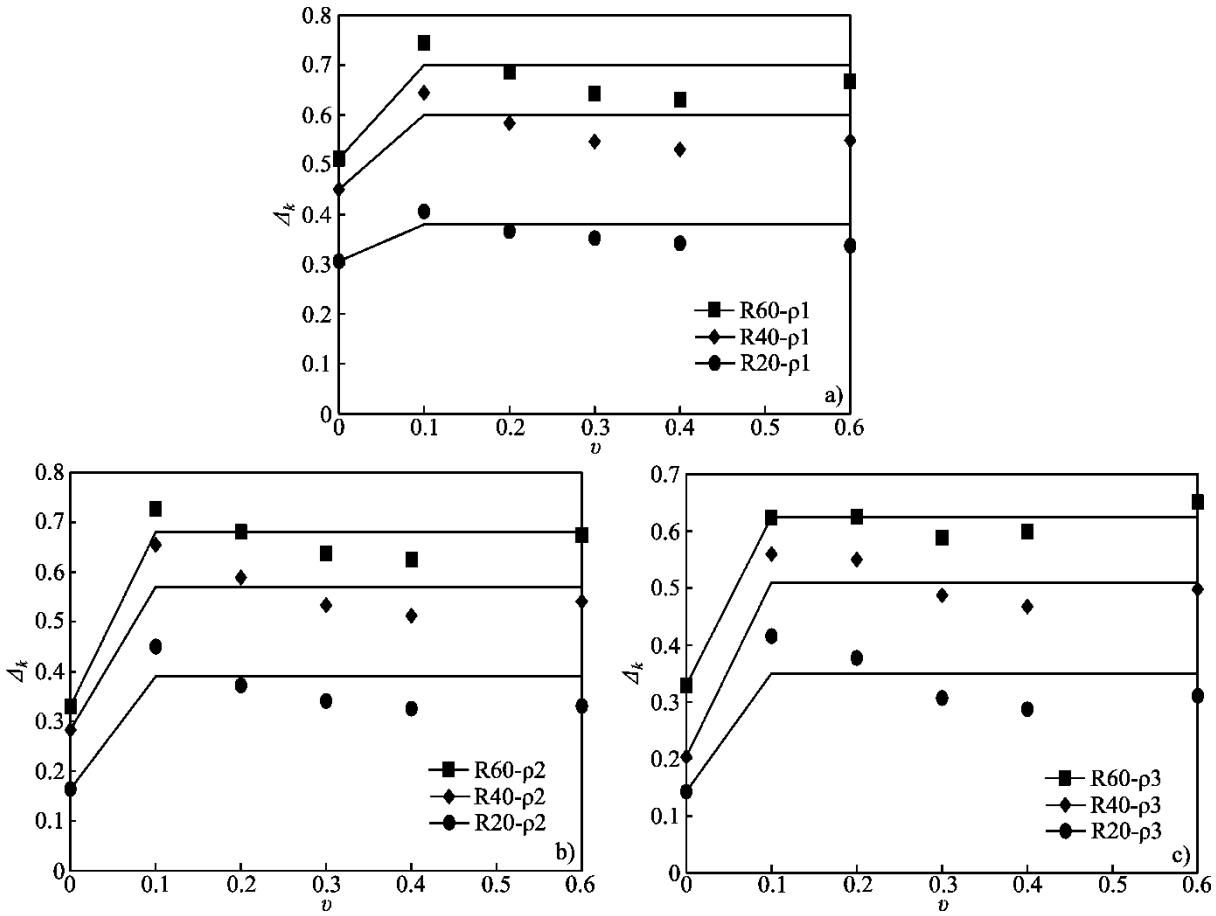


Figure 8.4 Stiffness reduction ratio between RRuC and RC members with reinforcement ratio of ρ_1= *1.0*%, (b) ρ_2= 1.7% and (c) ρ_3= 4.0%

Table 8-3 also lists the values of Δ_k under each axial load level and reinforcement ratio. It can be noted that Δ_k shows a lower value for cantilever case (υ=0) which generally decreases with the

increase in reinforcement ratio. The longitudinal reinforcement plays an important role in determining the stiffness of RRuC and RC members hence the increase in reinforcement ratio compensates for the reduction of stiffness caused by the increase of rubber content. With the presence of axial load, compared to the cantilever case, the member stiffness is governed by the constituent concrete material where RRuC members provide much higher stiffness reduction. In addition, as listed in Table 8-3, the stiffness reduction ratio remains nearly constant regardless of the reinforcement ratio while it only increases with higher rubber content in the presence of axial load. This indicates that the increase of rubber content has the most notable influence on the stiffness reduction of RRuC members under combined axial-bending actions.

Table 8-3 Bilinear representation of stiffness reduction ratios of RRuC members

Rubber content	Reinforcement ratio	Stiffness reduction ratio Δ_k	
		Axial load υ=0	Axial load υ=0.1-0.6
R20	ρ_1= 1.0%	0.31	0.39
	ρ_2= 1.7%	0.16	0.38
	ρ_3= 4.0%	0.14	0.35
R40	ρ_1= 1.0%	0.45	0.60
	ρ_2= 1.7%	0.28	0.57
	ρ_3= 4.0%	0.20	0.51
R60	ρ_1= 1.0%	0.51	0.70
	ρ_2= 1.7%	0.33	0.68
	ρ_3= 4.0%	0.33	0.62

8.4.2 Strength interaction

The cross-sectional capacity of the beam-column member under combined loads is typically identified through a moment-axial (*M*-*N*) diagram. The strength interaction is influenced by both the concrete strength and reinforcement properties. Figures 8.5 (a)-(d) illustrate the contributions of the rubber content and reinforcement ratio on the member capacity. It is evident that the increase in rubber content reduced the capacity of the member cross-section significantly. It is noteworthy that the maximum reinforcement ratio (ρ_3= 4.0%) specified by the code is not practically applicable for the extreme low strength concrete. In addition, due to the low strength of R60 rubberised concrete and high reinforcement ratio, the neutral axis of the cross-section at failure was shifted to the tensile fibre side causing excessive compressive strain on the other side. Combined with the high deformability of rubberised concrete, compressive distortion of concrete and reinforcement element occurred in the numerical model.

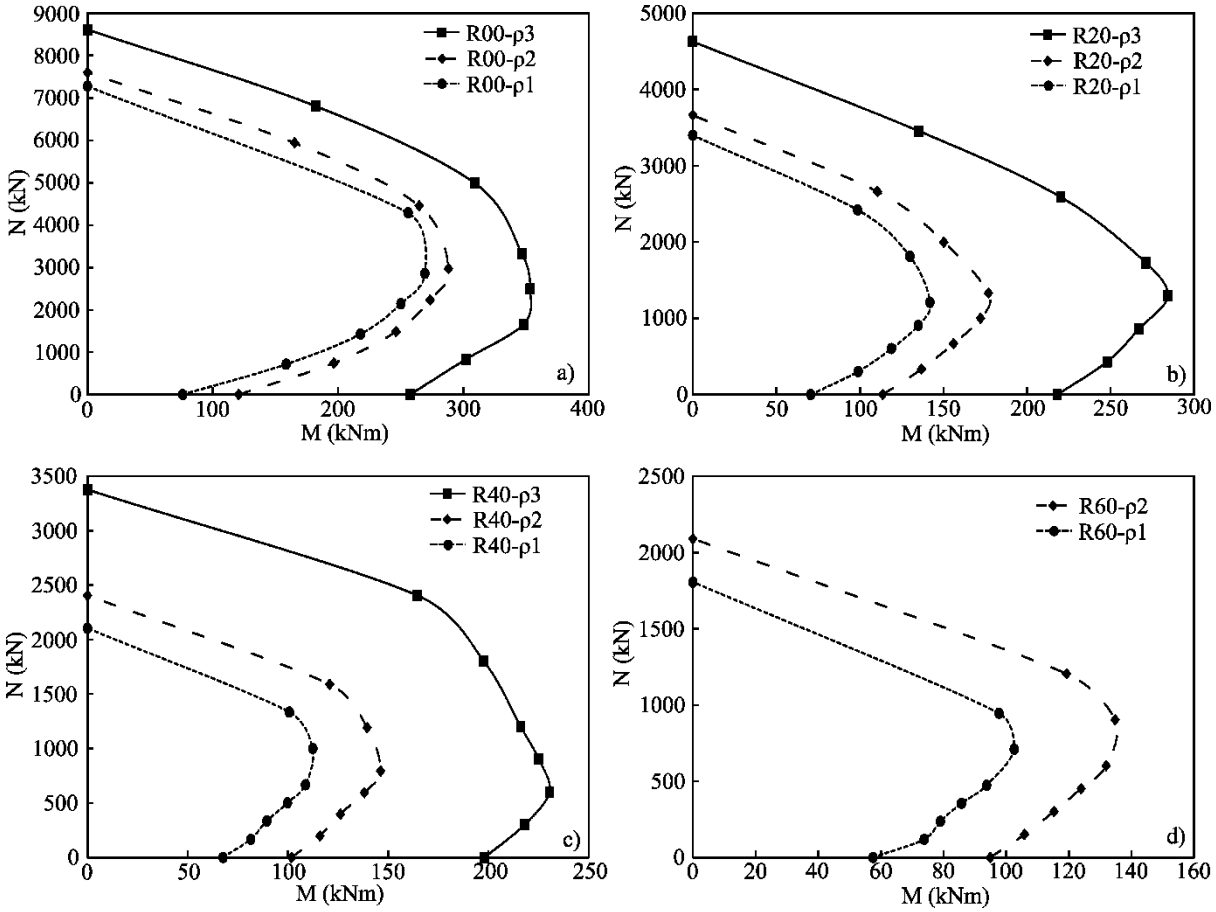


Figure 8.5 Bending-axial interaction diagrams for: a) R00, b) R20, c) R40 and d) R60 models

Table 8-4 compares the member axial compression capacities acquired from the numerical models F_{num} and the calculated counterpart F_{calc} from Equation (8.2). It can be noted that the actual axial capacities obtained from the analysis are generally higher than those from the calculation. In addition, the ratio F_{num}/F_{calc} shows a significant increase with the increase in rubber content while also decreases with the reinforcement ratio, with the underestimation in the ratio of F_{calc} reaching more than 80% for R60 members.

One of the main factors leading to the higher axial capacity is the influence of stirrup confinement on the concrete strength (e.g. Mander et al. 1988). Figure 8.6 indicates the axial capacity enhancement ratio $\Delta_a=F_{sc}/F_{calc}$ between the stirrup-confined concrete (F_{sc}) and unconfined concrete (F_{calc}) at different longitudinal reinforcement ratios, using the hoop confinement ratio applied herein. In this figure, the values of F_{sc} acquired from the analysis ($F_{sc}=F_{num}$), and that determined from the stirrup confined concrete strength model proposed by Mander et al. (1988), are compared. It can be noted that the enhancement ratio decreased significantly with the increase of the original concrete strength from both the numerical and confinement models. On the other hand, the confinement

model predicted almost 20% higher capacity than the numerical models in cases where the unconfined concrete strengths were lower than 30 Mpa. This difference decreased with the increase in unconfined concrete strength.

Table 8-4 Axial compression capacities from numerical analysis and Equation (8.2)

Model reference	F_{num} (kN)	F_{calc} (kN) (Equation 8.2)	F_{num}/F_{calc}	Model reference	F_{num} (kN)	F_{calc} (kN) (Equaion 8.2)	F_{num}/F_{calc}
R00-F0- ρ1	7277	7144	1.02	R40-F0- ρ1	2105	1667	1.26
R00-F0- ρ2	7599	7426	1.02	R40-F0- ρ2	2406	1987	1.21
R00-F0- ρ3	8510	8326	1.02	R40-F0- ρ3	3378	3007	1.12
R20-F0- ρ1	3399	3020	1.13	R60-F0- ρ1	1806	1181	1.53
R20-F0- ρ2	3663	3330	1.10	R60-F0- ρ2	2090	1504	1.39
R20-F0- ρ3	4628	4320	1.07	R60-F0- ρ3	3014	2535	1.19

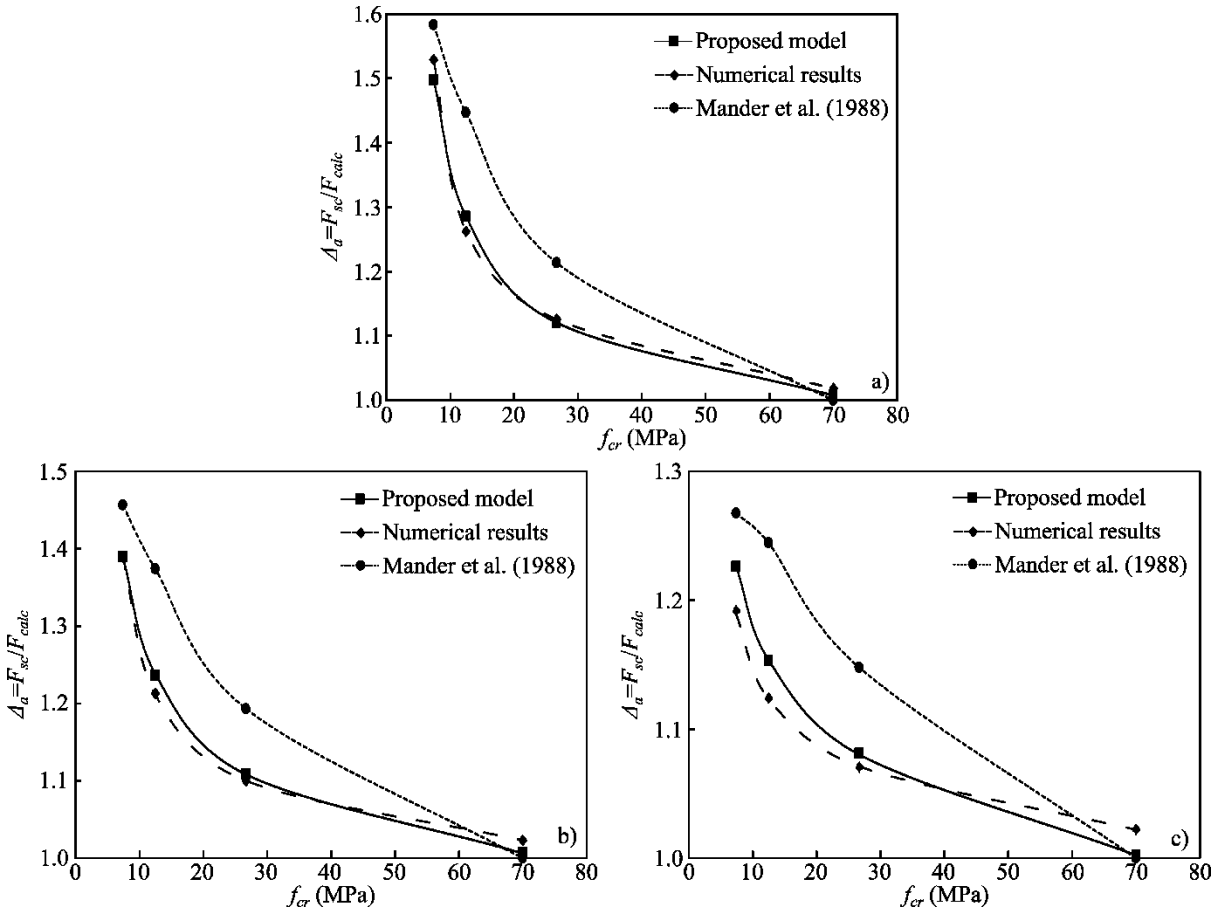


Figure 8.6 Comparison of axial capacity enhancement ratio from analysis compared to existing and proposed models with reinforcement ratio of: (a) ρ_1= *1.0*%, (b) ρ_2= 1.7% and (c) ρ_3= 4.0%

In order to develop a more accurate and conservative model for the compressive strength of stirrup-confined rubberised concrete, a modification of the confined concrete strength model proposed by Mander et al. (1988) is suggested based on the analysis results as follows:

$$\frac{f_{crc}}{f_{cr}} = -1.254 + 2.254 \times (1 + \frac{2.45 f_l}{f_{cr} - 2.75})^{0.6} - 3.75 \times (\frac{f_l}{f_{cr} + 2.7})^{1.7} \quad (8.3a)$$

where f_{crc} is the stirrup-confined rubberised concrete strength, f_{cr} is the unconfined rubberised concrete strength, which can be estimated from Equation 3.2, and f_l is the lateral confining pressure from stirrups using the expression proposed by Mander et al. (1988) and given as:

$$f_l = \frac{(1 - \frac{s}{2d_s})^2}{2(1 - \rho_{cc})} \rho_s f_{yh} \quad (8.3b)$$

where s and d_s are the spacing and diameter of stirrups respectively; ρ_{cc} is the ratio of area of longitudinal reinforcement to area of section; and ρ_s is the ratio of the volume of stirrup-confining steel to the volume of confined concrete core. The new axial capacity enhancement ratio $\Delta_a = F_{sc}/F_{calc}$, where F_{sc} is estimated based on Equation (8.3), is also shown in Figure 8.6 in comparison to the analysis results and the original confined concrete strength model. It is evident that Equation 8.3 provides a much more accurate prediction of the confined concrete strength when compared to the analysis results, for unconfined rubberised concrete strength in the range of f_{cr}=7-70MPa. Table 8-5 gives the detailed values of Δ_a as acquired from the analysis ($\Delta_{a,num}$) and Equation 8.3 ($\Delta_{a,pred}$). The comparison shows an average prediction-to-analysis ratio of 1.00 with a COV of 0.02.

Table 8-5 Axial capacity enhancement ratio based on Equation (8.3) and the numerical analysis

Model reference	$\Delta_{a,pred}$	$\Delta_{a,num}$	$\Delta_{a,pred}$ / $\Delta_{a,num}$
R60-F0- ρ_1	1.50	1.53	0.98
R40-F0- ρ_1	1.29	1.26	1.02
R20-F0- ρ_1	1.12	1.13	1.00
R00-F0- ρ_1	1.01	1.02	0.99
R60-F0- ρ_2	1.39	1.39	1.00
R40-F0- ρ_2	1.24	1.21	1.02
R20-F0- ρ_2	1.11	1.10	1.01
R00-F0- ρ_2	1.01	1.02	0.98
R60-F0- ρ_3	1.23	1.19	1.03
R40-F0- ρ_3	1.15	1.12	1.03
R20-F0- ρ_3	1.08	1.07	1.01
R00-F0- ρ_3	1.00	1.02	0.98
		AVG	1.00
		COV	0.02

8.4.3 Member ductility

The member rotational ductility μ_ψ was examined by considering the rotation at yield ψ_y (corresponding to the first yield of longitudinal reinforcement), and the ultimate rotation ψ_u as represented by Equation (8.4), in which ψ_u is the ultimate rotation related to the failure criteria of the member.

$$\mu_\psi = \frac{\psi_P}{\psi_y} = \frac{\psi_u}{\psi_y} - 1 \tag{8.4}$$

As defined in Section 8.3.3, the ultimate state of the member is defined corresponding to either the first fracture of longitudinal reinforcement (FF) or the crushing of the concrete core in compression (CF). An ultimate compression strain threshold of the stirrup-confined rubberised concrete core was defined in advance for the CF criterion. Figure 8.7 indicates the stress-strain relationships for confined concrete as proposed by Eurocode 2 (EN 1992-1-1). The crushing strain of confined concrete considers the superposition of the ultimate crushing strain of unconfined material and the linear contribution of confinement as shown in Equation (8.5).

$$\varepsilon_{cu2,c} = \varepsilon_{cu2} + 0.2\frac{f_l}{f_{ck}} \tag{8.5}$$

where ε_{cu2} and f_{ck} are the ultimate compressive strain and strength of unconfined concrete as defined in Table 3.1 of Eurocode 2 (EN 1992-1-1), while f_l is the lateral compressive stress.

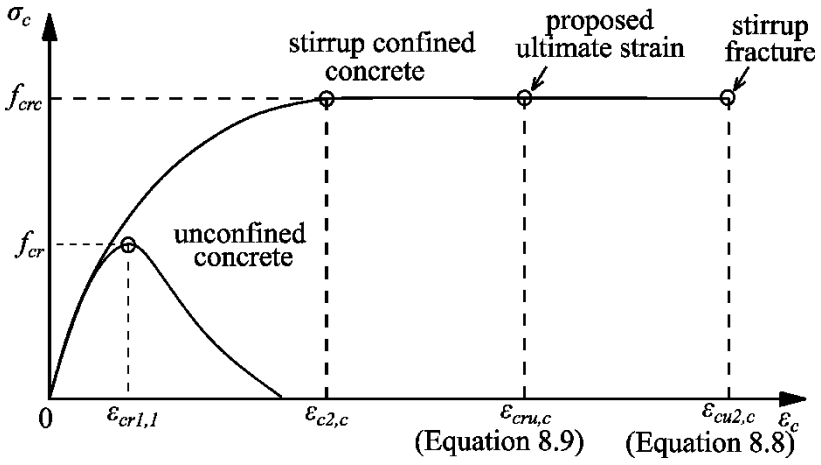


Figure 8.7 Comparison between the ultimate compressive strain from EC2 (Equation 8.8) and the proposed value (Equation 8.9)

A proposed ultimate compression strain threshold $\varepsilon_{cru,c}$ is considered herein to represent the strain state at the extreme compressive fibre of the rubberised concrete core when it reaches its ultimate rotation ψ_u as indicated in Figure 8.8. In addition, as mentioned in Chapter 6, the ultimate rotation ψ_u was defined as the deformation state of the member when its lateral capacity was reduced by 20%. Equation (8.6) is proposed here to represent the value of $\varepsilon_{cru,c}$ which accounts for the rubber content.

$$\varepsilon_{cru,c} = \varepsilon_{cr1,1} + 0.11\frac{f_l}{f_{cr}} \tag{8.6}$$

where $\varepsilon_{cru,c}$ is the compressive strain of unconfined rubberised concrete from Equation (3.5) and (3.9); f_{cr} is unconfined rubberised concrete strength from Equation (3.2); and f_l is the lateral confining pressure from Equation (8.3b). It is worth noting that the proposed compressive strain threshold of $\varepsilon_{cru,c}$ is more conservative compared to the ultimate compressive strain $\varepsilon_{cu2,c}$ from Eurocode 2 which is indicated in Figure 8.7.

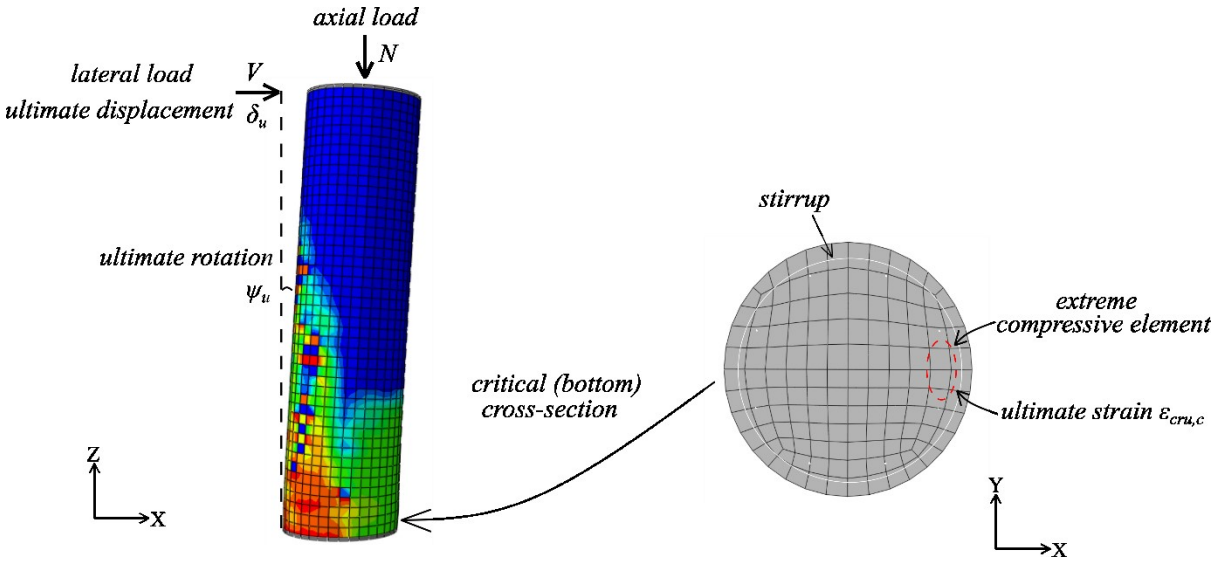


Figure 8.8 Ultimate state of member failed in CF criterion specified in this research

Figure 8.9 shows the increase in stirrup confined compressive strain $\varepsilon_{cr,c}$ of the extreme compressive element with the increase of lateral displacement δ for all RRuC specimens as obtained from the numerical simulations described in Chapter 7. The corresponding ultimate compressive strain $\varepsilon_{cru,c}$ of R00, R45 and R60 members was calculated from Equation (8.6) and listed in Table 8-6. It can be noted that $\varepsilon_{cr,c}$ generally increased with the increase of rubber content as well as the applied axial load. The ultimate strain value and corresponding displacement are marked in the figure, noting that

these increase significantly with the rubber content. Table 8-6 compares the ultimate displacements δ_u obtained from the numerical analysis based on the CF criterion described above and the counterparts measured in experimental programme (as in Table 6-4 in Chapter 6). As expected, the proposed ultimate compressive strain and CF criterion represent well the ultimate state (considered as 20% loss of lateral capacity) of test members, with the average test-to-predicted ultimate displacement (rotation) ratio of 1.11 and COV of 0.22.

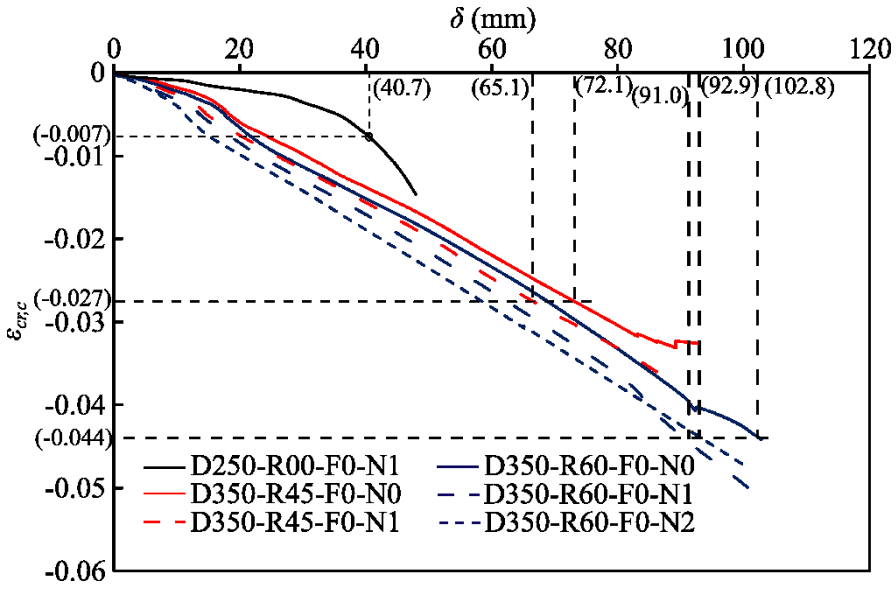


Figure 8.9 Development of $\varepsilon_{cr,c}$ with respect to lateral displacement for the test members

Table 8-6 Comparison of ultimate displacement from the tests and analysis

Member reference	$\varepsilon_{cru,c}$	$\delta_{u,test}$ (mm)	$\delta_{u,pred}$ (mm)	$\delta_{u,test}/\ \delta_{u,pred}$
D250-R00-F0-N1	0.007	41.5	40.7	1.02
D350-R40-F0-N0	0.027	96.6	72.1	1.34
D350-R40-F0-N1	0.027	96.0	65.1	1.47
D350-R60-F0-N0	0.044	96.9	102.8	0.99
D350-R60-F0-N1	0.044	101.9	92.9	1.04
D350-R60-F0-N2	0.044	72.9	91.0	0.87
			AVG	1.11
			COV	0.22

Figure 8.10(a) summarised the member ductility against the axial load level of all RRuC models based on the previously described failure criteria, and it is also found that all the models failed under the CF criterion. As expected, the rotational ductility substantially reduces with the increase in axial load. Very low values were achieved for N40 and N60, and even a negative value of ductility was attained with further increase of axial load based on the proposed failure criteria. In this case, the crushing failure criterion of the member was reached prior to the tensile yielding of

longitudinal reinforcement, i.e. $\psi_u < \psi_y$. The rotational ductility, on the other hand, increased with the increase in rubber content. As shown in Figure 8.20(a), the increase in rubber content is shown to have a positive influence on ductility with a reduced effect for cases with higher reinforcement ratio. Meanwhile, members with higher rubber content maintain a favourable level of ductility under high axial loads, while conventional concrete members in comparison exhibit reduced ductility under much lower axial load level.

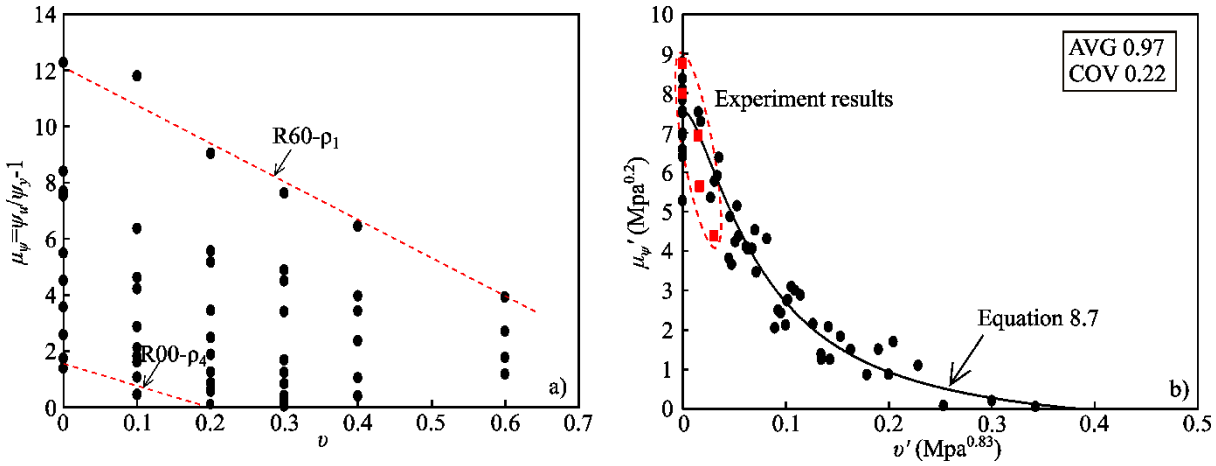


Figure 8.10 Relationship between (a) ductility and axial load μ_ψ -υ, (b) modified ductility and axial load μ_ψ'-υ'

For design purposes, a relationship between rotational ductility and rubber content, reinforcement ratio as well as the axial load level is also proposed based on the analysis results. Figure 8.10(b) indicates the μ_ψ'-υ' relationship, where μ_ψ' and υ' are the modified ductility and axial load parameter, whilst also considering the influence of the rubberised concrete strength and reinforcement ratio.

$$\mu_\psi = \frac{2.24\mu_\psi' f_{cr}^{-0.2}}{(100\rho)^{1.1}} \tag{8.7a}$$

$$\upsilon = \frac{33.9\upsilon' f_{cr}^{-0.83}}{(100\rho)^{0.25}} \tag{8.7b}$$

f_{cr} can be derived from Equation (3.2) considering different types of reference concrete strength f_{c0} and rubber content ρ_{vr}. The proposed equation hence takes the form:

$$\mu_\psi' = \frac{1}{0.12 + 5.5\upsilon'^{1.5}} - 0.7$$

$$\mu_{\psi} = \frac{2.24}{0.12(100\rho)^{1.1} f_{cr}^{0.2} + 0.03[(100\rho)^{0.98} f_{cr}^{0.96} \upsilon]^{1.5}} - 0.7 \quad (8.7c)$$

The experimental results of the RRuC members reported in Chapter 6 are also converted through Equation (8.7) and compared with the proposed model. The relationship compares very well with the results as indicated in Figure 8.10(b).

The semi-empirical relationship of Equation (8.7) was proposed for the estimation of rotational ductility of RRuC member at 20% reduction of lateral capacity according to the pre-established failure criteria. The equation compares well with the results, with an average analysis-to-prediction ratio of 0.97 and a COV of 0.22. Several limitations, on the other hand, need to be clarified for the application of the above equation:

1) The proposed equation is based on the pre-established failure criteria when the concrete core crushing failure occurs corresponding to 20% reduction in member lateral capacity. Consequently, Equation 8.7 may not be valid for the prediction of rotational ductility based on other specified failure criteria.
2) It is suggested that, when applying Equation (8.7), in order to consider positive ductility values, the axial load ratio should be limited to $\nu < 0.3$ for R00 members and $\nu \leq 0.4$ for R20 members. The axial load ratio can be further increased to 0.6 for members with higher rubber content such as R40 and R60.

8.4.4 Spread of plasticity

The spread of plasticity, referred to here as L_{sp}, represents the physical length over which plasticity actually spreads. The prediction of L_{sp} has a strong influence on the ductile seismic design for the assessment of rotation capacity, hence the accuracy of L_{sp} has generated primarily theoretical discussions. For conventional RC members with seismic detailing, an estimate of the spread of plasticity length L_{sp} may be obtained as a sum of the moment-to-shear ratio (for cantilevers $M/V=l_{col}$), a tension shift component and strain penetration (Eurocode 8). Whilst the moment-to-shear ratio influences directly the moment gradient, the latter occurs due to localised deformations in the axially loaded reinforcing bars and accounts for a potential rebar slip from the member or footing (Priestley et al. 2007; Hines et al. 2004). Eurocode 8 Part 3 (EN 1998-3, 2004) also estimated L_{sp} through Equation (8.8) considering the linear superposition of the above-mentioned phenomena. More recent studies, on the other hand, investigated much wider parameters influencing L_{sp} in RC members through numerical modelling. It has been proposed that other factors such as axial load also have a significant influence on the value of L_{sp} (Youssf et al. 2015).

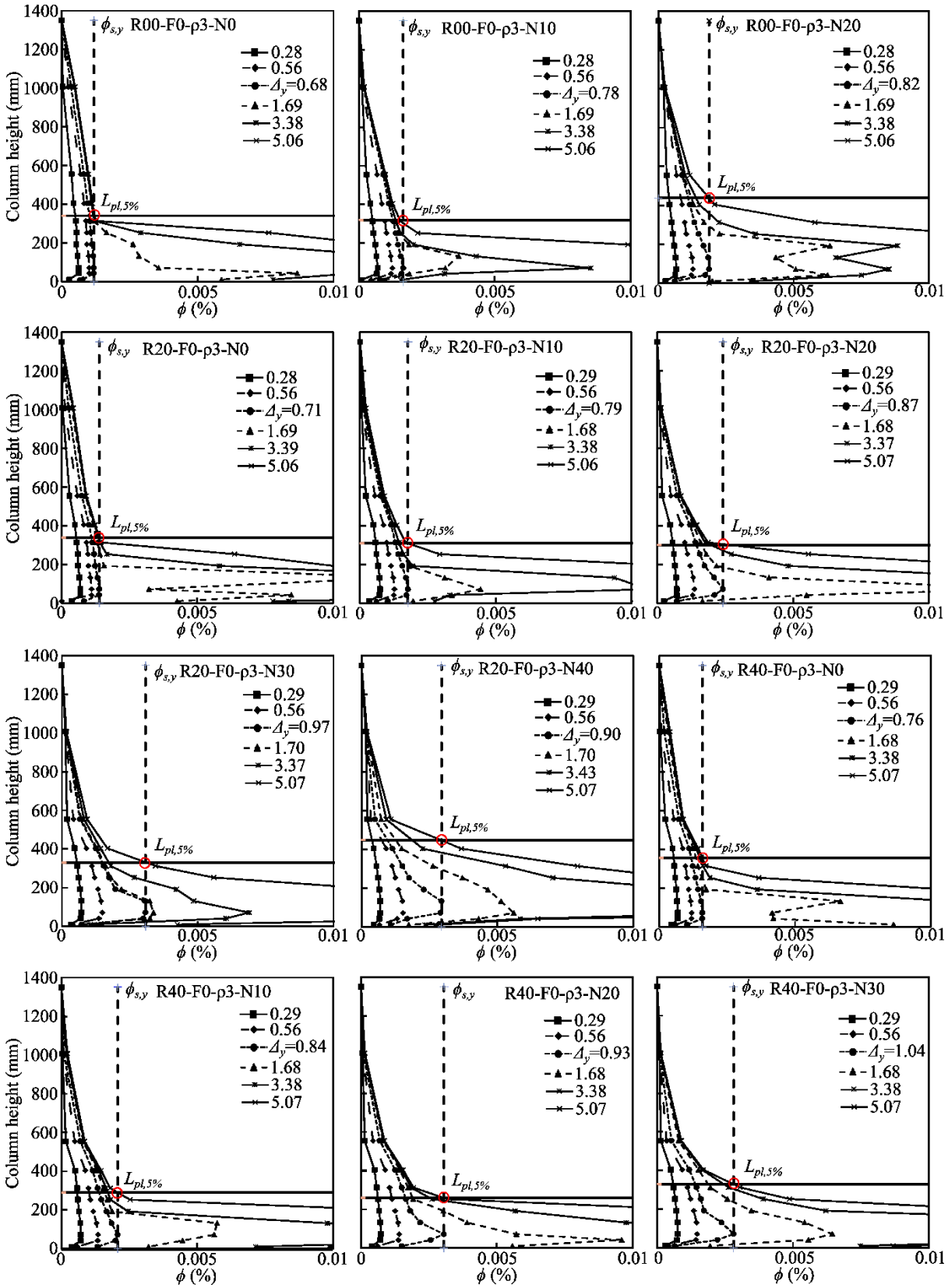
$$L_{sp} = l_{col} / 30 + 0.20D + 0.11 d_b f_y / \sqrt{f_c} \quad (8.8)$$

This section aims at providing a practical prediction method for the spread of plasticity length L_{sp} of RRuC members with a typical reinforcement ratio of ρ_2= 1.7% under a axial load ratio $\upsilon \leq 0.4$ based on the numerical parametric study. The control model described in Section 8.3.1 of this chapter considers a cantilever member as shown in Figure 8.3. Consequently, the proposed equation for L_{sp} takes the form of Equation (8.9), where $L_{sp,gradient}$ represents the plasticity length from the moment gradient, while $L_{sp,local}$ represents the additional length due to local deformations.

$$L_{sp} = L_{sp,gradient} + L_{sp,local} \quad (8.9)$$

Figure 8.11 shows the cross-sectional curvature distributions along the height of the member at various drift ratios for the investigated models. The typical curvature profiles corresponding to various drift ratios show concentrations of curvature near the base of the members. The vertical dashed line shows the "yield curvature" $\phi_{s,y}$ corresponding to the first yield of flexural reinforcement. The intersection between the curvature distribution curves and the $\phi_{s,y}$ line shows the limit between inelastic-to-elastic deformations, and implicitly, the spread of plasticity length L_{sp} at each drift ratio. In this study, a target drift ratio of Δ_u=5% was chosen to represent the average ultimate displacement level (δ_u) of the selected models based on observations from the parametric analysis results. It can also be noted from the figure that the increase of the spread of plasticity is not significant as the member reaches high drift ratios (i.e. Δ>4%). Therefore, the intersection between the $\phi_{s,y}$ line and the curvature distribution line at Δ_u=5% represents the spread of plasticity L_{sp} as marked in Figure 8.11 with the detailed values given in Table 8-7.

It is notable that the presence of rubber reduced the plasticity length in comparison to that of conventional concrete members under various levels of axial load. Since the reinforced rubberised members adopted exhibited a much softer type of cross-section along the bottom area of the member, the rotational (curvature) demand of the rubberised concrete area was higher than that of the upper normal concrete area at a chosen drift ratio (i.e. damage was localised in the rubberised concrete area). Therefore, with the increase of rubber content, curvature of the member tended to localise at the bottom softer cross-section. The axial compression load also has a significant influence on the value of L_{sp}. The plasticity length of rubberised concrete members tends to reduce with the presence of low axial load, but to increase with a higher applied compression load.


Column height (mm)
ϕ (%)
$\phi_{s,y}$ R00-F0-ρ3-N0
0.28
0.56
Δ_y=0.68
1.69
3.38
5.06
$L_{pl,5\%}$
$\phi_{s,y}$ R00-F0-ρ3-N10
0.28
0.56
Δ_y=0.78
1.69
3.38
5.06
$\phi_{s,y}$ R00-F0-ρ3-N20
0.28
0.56
Δ_y=0.82
1.69
3.38
5.06
$\phi_{s,y}$ R20-F0-ρ3-N0
0.28
0.56
Δ_y=0.71
1.69
3.39
5.06
$\phi_{s,y}$ R20-F0-ρ3-N10
0.29
0.56
Δ_y=0.79
1.68
3.38
5.06
$\phi_{s,y}$ R20-F0-ρ3-N20
0.29
0.56
Δ_y=0.87
1.68
3.37
5.07
$\phi_{s,y}$ R20-F0-ρ3-N30
0.29
0.56
Δ_y=0.97
1.70
3.37
5.07
$\phi_{s,y}$ R20-F0-ρ3-N40
0.29
0.56
Δ_y=0.90
1.70
3.43
5.07
$\phi_{s,y}$ R40-F0-ρ3-N0
0.29
0.56
Δ_y=0.76
1.68
3.38
5.07
$\phi_{s,y}$ R40-F0-ρ3-N10
0.29
0.56
Δ_y=0.84
1.68
3.38
5.07
$\phi_{s,y}$ R40-F0-ρ3-N20
0.29
0.56
Δ_y=0.93
1.68
3.38
5.07
$\phi_{s,y}$ R40-F0-ρ3-N30
0.29
0.56
Δ_y=1.04
1.68
3.38
5.07

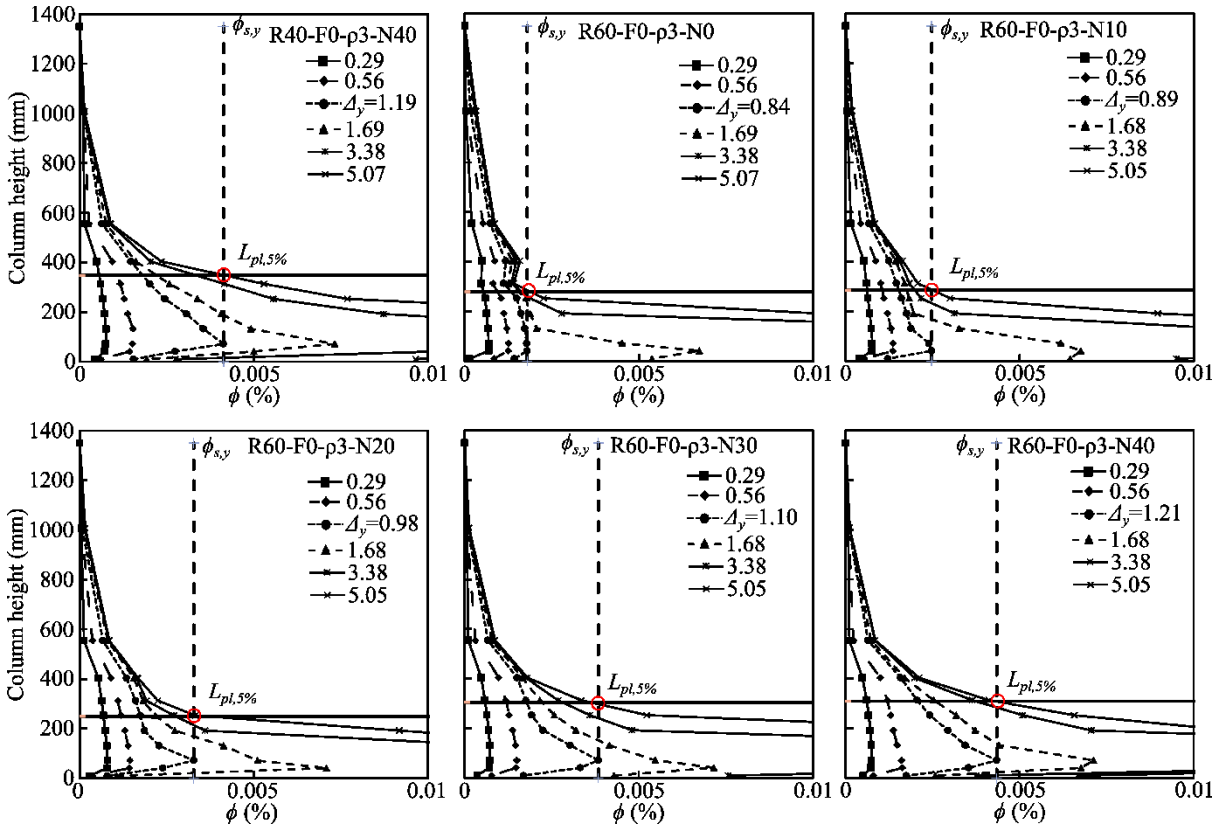


Figure 8.11 Spread of plasticity at various drift ratios for the selected models

Table 8-7 Summary of spread length of plasticity of selected models

L_{sp} (mm)	R00	R20	R40	R60
N0	340	338	355	280
N10	320	310	290	285
N20	438	300	260	250
N30	-	330	330	305
N40	-	448	348	310

The spread of plasticity due to the moment gradient reflects the transition between the yield moment M_y and ultimate moment M_u. This effect can only be accounted for by assuming nonlinear material behaviour and also that plane sections remain plane after bending as indicated in Figures 6.29 (c), (d) and (e). Based on this, the spread of plasticity due to the moment gradient $L_{sp,gradiend}$ is given by Equation 8.10, where l_{col} is the shear span of the member.

$$L_{sp,gradient} = (1 - \frac{M_y}{M_u}) l_{col} \tag{8.10}$$

The expression for $L_{sp,gradient}$-υ of unconfined models with a reinforcement ratio of ρ_2= 1.7% is derived based on the numerical results, with modifications considering the influence of rubber content. It is found that the level of axial load has a significant influence on the plastic hinge length where the increase of axial compressive load generally reduces the level of $L_{sp,gradient}$. Meanwhile, the reduction in concrete strength due to high rubber content, as expected, causes more significant decrease in ultimate moment capacity M_u of the cross-section, which leads to a lower value of $L_{sp,gradient.}$ Figure 8.12 (a) shows the relationship between the modified spread of plasticity by moment gradient $L_{sp,gradient}$' and the axial load parameter υ' considering the influence of the rubberised concrete strength as expressed in Equation (8.11a, b). The proposed equation which determines $L_{sp,gradient}$' for RRuC members with ρ_3= 1.7% takes the form of Equation (8.11c), with a average test-to-prediction ratio of 1.12 and a COV of 0.23.

$$L_{sp,gradient} = 1.63 f_{cr}^{-\frac{1}{3}} L_{sp,gradient}' \tag{8.11a}$$

$$\upsilon = 4.33 f_{cr}^{-1} \upsilon' \tag{8.11b}$$

$$L_{sp,gradient}' = \frac{l_{col}}{4 + 5\upsilon'^{0.6}} \tag{8.11c}$$

The term $L_{sp,local}$, representing the spread of plasticity due to local deformations of the investigated models, can be calculated from Equation (8.9) by subtracting the part of $L_{sp,gradient}$ from L_{sp} shown in Figure 8.11 and Table 8-7. Similar to the modification of $L_{sp,gradient}$ discussed above, Figure 8.12(b) shows the relationship between $L_{sp,local}$'- υ where the modification between $L_{sp,local}$- $L_{sp,local}$' is shown in Equation (8.12a). A linear expression is proposed representing the $L_{sp,local}$'- υ relationship in Equation (8.12b), with an average test-to-prediction ratio of 1.00 and COV of 0.32.

$$L_{sp,local} = \frac{L_{sp,local}'}{8.35 f_{cr}^{-\frac{1}{2}}} \tag{8.12a}$$

$$L_{sp,local}' = 552\upsilon + 0.46D \tag{8.12b}$$

where D is the outside diameter of the member, while f_{cr} can be derived through Equation (3.2) considering different types of reference concrete strength f_{c0} and rubber content ρ_{vr}.

Based on the above-described expressions, the prediction of L_{sp} for RRuC members with a reinforcement ratio ρ_2= 1.7% under an axial load level $\upsilon \le 0.4$ can be obtained from Equation (8.13).

$$L_{sp} = \frac{1.63 f_{cr}^{-\frac{1}{3}}}{4 + 0.42(\upsilon f_{cr})^{0.6}} l_{col} + (66.11\upsilon + 0.056D)\sqrt{f_{cr}} \tag{8.13}$$

Figure 8.12(c) presents the results of L_{sp} obtained from both the numerical analyses (as in Table 8-7) and from Equation (8.13) where the proposed prediction shows conservative consideration of the L_{sp} value, yet also good agreement with the numerical analysis results, with an average test-to-prediction ratio of 1.11 and a COV of 0.15.

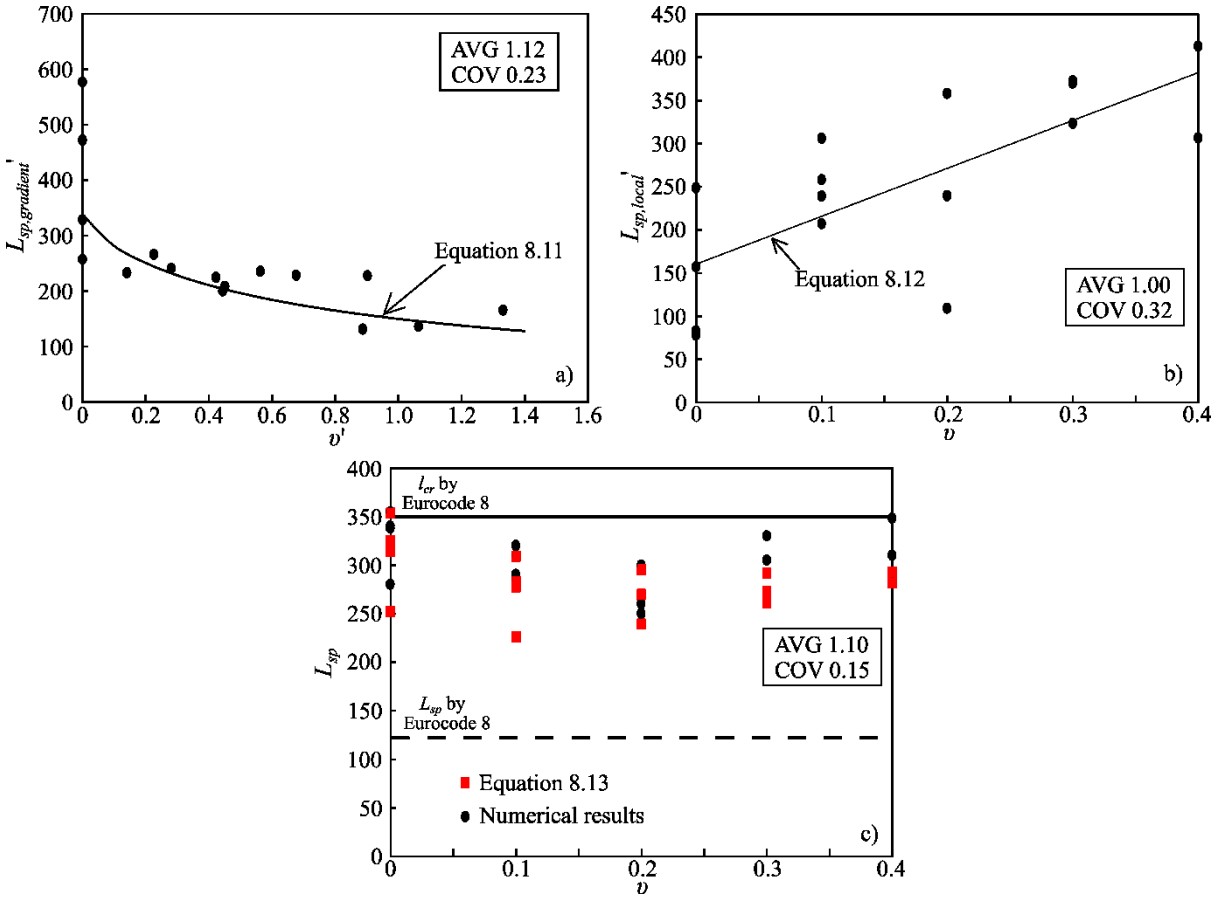


Figure 8.12 Prediction of: (a) $L_{sp,gradient}$ of Equation (8.11), (b) $L_{sp,local}$ of Equation (8.12), (c) L_{sp} of Equation (8.13)

It is also indicated in Figure 8.12(c) that the estimated plastic hinge length L_{sp} by Eurocode 8 Part 3 (EN 1998-3, 2004), considering the effect of moment gradient and local deformation, gives a largely conservative evaluation of the spread of plasticity. Meanwhile, the spread of plasticity area also indicates the critical length l_{cr} of structural members where sufficient detailing is required. According to Eurocode 8 Part 1 (EN 1998-1, 2004), the critical region of the column model in this investigation is the gross diameter of the member $l_{cr}=D$=350mm, as indicated in Figure 8.12(c). It is notable that the spread of plasticity lengths acquired from the selected numerical models and Equation 8.13 are generally lower than the critical region suggested by the code. Consequently,

Eurocode 8 provides largely conservative and applicable estimates of the critical region l_{cr} for RRuC members where sufficient detailing is required.

8.5 Concluding remarks

This chapter presented the results of a number of parametric assessments on the behaviour of rubberised concrete members. The aim of this study was to provide more detailed insights into the performance of rubberised concrete members by considering a wider scope of key parameters compared to those examined in the experimental studies. The numerical models, which were validated in Chapter 7, were used in this chapter to conduct parametric studies focusing on shear behaviour as well as the performance of beam-column members.

The parametric investigation on asymmetric shear members accounted for a wide range of material constitutive parameters with focus on the rubber content and concrete compressive strength. Based on the numerical and experimental results, a representative expression for predicting the shear resistance as a function of the rubber content and the concrete compressive strength was proposed. The suggested expression can be employed for rubberised concrete materials used in non-structural and structural members which are governed by shear behaviour.

A large number of models were also considered in order to obtain detailed insights into the physical behaviour of reinforced rubberised beam-column members. The parametric assessments focussed on four key factors, namely the rubber content, reinforcement ratio, axial load ratio and external confinement ratio. On the other hand, the performance of beam-column members was assessed through four main response parameters, namely the member strength, stiffness, ductility and spread of plasticity.

The numerical investigations described in this chapter, in conjunction with the experimental results, showed that although the presence of rubber particles leads to a reduction in the strength and stiffness of a member, it has a significant positive influence on the ductility of a flexural member. The findings from the parametric studies also provided information which enables the use of rubberised concrete materials in practical design. In particular, equations to assess the key performance characteristics of members, considering the rubber content and other key factors, were proposed. The proposed expressions were validated against the numerical and experimental results, and are given in a form that is suitable for implementation in design guidelines.

Chapter 9

9 Closure

9.1 Summary and conclusions

In this thesis, the behaviour of concrete materials and reinforced concrete members incorporating recycles rubber particles, as partial replacement of mineral aggregates, was examined. The research involved several experimental investigations on materials and members, coupled with detailed numerical simulations and parametric assessments. Specific conclusions and observations corresponding to each aspect of the research were included within the main body of the thesis. An overall summary of the main conclusions of this research is as follows:

- An overview of previous research on the behaviour of rubberised concrete materials was carried out. The soft behaviour of rubber particles leads to a reduction in concrete material strength while rubberised concrete specimens exhibit much softer post-peak strength degradation under uniaxial compression or flexural loads. This is due to the presence of soft rubber particles which slow the crack propagation in the rubber/cement–matrix interface and lead to a high deformability of the material before final failure.
- Previous studies on rubberised concrete material behaviour did not provide information on the full constitutive response. Assessment of the shear behaviour of rubberised concrete was also lacking. Moreover, previous investigations were limited to a relatively low level of rubber content, in terms of replacement of mineral aggregate, of up to 20%. These research needs were addressed in the work described in this thesis through the experimental assessments and associated numerical studies.
- Experimental results, described in this thesis, of over 100 rubberised concrete samples under uniaxial compression tests showed that both the volumetric replacement ratio and the type of mineral aggregate replaced significantly affected the mechanical properties of rubberised concrete. The increase in rubber content reduced the compressive strength, elastic modulus, but increased the lateral strain at crushing as well as the energy released during crushing of rubberised concrete cylinders.
- The low elastic stiffness of rubberised concrete is mainly due to the flexibility and light weight of rubber aggregates. The rubber particles possess inherently low bond capacity with the concrete mix which leads to premature crushing as a function of the rubber content. The accumulation of tensile cracks within the material caused by early crushing eventually leads to a sliding macrocrack which produces large lateral expansion and volume increase. On the other

hand, the experimental response of rubberised concrete cylinders under uniaxial compression loading typically exhibited softer post-crushing behaviour and similar or higher energy dissipated in the post-peak regime.

- The proposed expressions for estimating the mechanical properties of rubberised concrete materials based on the experimental results and an extensive database of 198 rubberised concrete mixes collected from available literature, offer significant improvements for design purposes in comparison with existing analytical models. Compared with other existing models, which have only been validated for a limited amount of rubber replacement ratio and number of concrete mixes, the proposed expressions cover a much wider rubber replacement ratio and larger size of data base. The novel uniaxial constitutive analytical model for rubberized concrete proposed in this study also provides a reliable representation, which has been lacking to date, for assessing the complete axial and lateral stress-strain response for rubberized concrete.
- The external AFRP confinement provided notable enhancement to the compressive strength and deformation capacity of rubberised concrete materials. Bilinear stress-strain response was observed through the compressive tests of AFRP confined rubberised concrete cylinders.
- Based on an assessment of different testing methods for loading in shear, the proposed asymmetric four-point tests can be used to obtain the shear-governed failures of rubberised concrete prismatic specimens. However, the specimen response is sensitive to the testing arrangement where a slight asymmetry can lead to tensile-governed or mixed-mode failures rather than the desired shear governed ultimate behaviour.
- Typical load-deformation curves obtained from 18 shear test specimens showed that the interlock of mineral aggregates and clamping of rubber particles provided enhancement in the shear strength. The results also indicated that the decreasing member strength-rubber content relationship was similar to that for compressive strength-rubber content acquired from the material compression tests carried out in this research.
- In the shear tests, detailed measurements of the crack kinematics through a DIC system showed that rubber particles provided additional rubber clamping effect between the two crack interfaces after the fracture of the specimen. This contributes to a smaller crack width and also a softer post-peak response of specimens with higher rubber content. However, the toughness parameters showed similar crack resistance for all tested rubberised members.
- The AFRP confinement restrained the dilation of rubberised concrete specimens under shear loads, which restricted potential tensile cracks and enhanced the shear behaviour of the material. Consequently, external AFRP confinement can be a suitable method to ensure shear failures which can assess actual shear strength of the material.

- In total 14 large-scale beam-column member specimens were tested to investigate the cyclic behaviour of reinforced rubberised concrete (RRuC) beam-column members. Compared to previous studies, a significant proportion of recycled rubber particles were used as a replacement of mineral aggregates, reaching up to 60% replacement. Two test rig arrangements were used for specimens with different geometries.
- The beam-column tests were carried out on members of circular cross-section with different proportions of rubber content and axial loads. Five RRuC specimens were externally confined with AFRP sheets, in order to examine the effect of external confinement on member behaviour. Detailed instrumentations, including DIC measurements, LVDTs, inclinometers and strain gauges on reinforcement, were utilised to monitor the member behaviour during each test.
- The beam-column member test results showed that the presence of rubber and external AFRP confinement combined with axial load had a clear influence on the behaviour. In comparison with RC members, it was shown that RRuC members exhibit soft crushing behaviour leading to favourable ductility and energy dissipation properties. The CRRuC members also provided highly stable hysteretic response, which indicates that additional external confinement may be a solution for members with large rubber content under significant axial loading to compensate for the reduction in compressive strength.
- The envelope curves of the tested beam-column specimens showed that members with higher rubber content develop lower member stiffness as expected, while the axial load may produce at most twice the stiffness enhancement in the presence of external lateral confinement. It was observed that members with comparatively high axial loads, with or without external confinement, exhibited enhancements in terms of both stiffness and strength compared to those under relatively low axial load.
- Further evaluation of ductility related parameters showed that both the rubber content and axial load had a clear influence on the ultimate rotation of members. As expected, RRuC members typically exhibited higher rotation capacity depending on the level of axial load. The AFRP confinement also enhanced the member ductility, with the rotational ductility levels of CRRuC members being up to 40% higher than those of RRuC members.
- The plasticity distribution along the beam-column test members was defined as the distribution of the longitudinal reinforcement plastic strains. The plasticity distribution length varied in the range of 29 to 39% of the cantilever length for the rubberised concrete members, with lower values obtained for members subjected to axial load. These values were higher than those typically obtained for similar conventional reinforced concrete members.

- The nonlinear finite element analysis software Abaqus was adopted to simulate the behaviour of all specimens from the three types of experiments carried out in this study, including the uniaxial compressive tests on cylinders, asymmetric shear tests on prisms and large-scale beam-column tests with or without external confinement. 3D models were constructed for each test case, while the specimen geometry, material properties and boundary conditions applied in numerical models were the same as those used in the tests in order to provide a faithful representation. The concrete damage plasticity (CDP) model was used to represent the constitutive behaviour of rubberised concrete. Linear elasto-plastic behaviour was applied for the reinforcement material, while the unidirectional linear elastic behaviour was chosen for AFRP sheets.
- The comparisons between the results of the numerical simulations and the corresponding test results showed very good correlations for all types of experiments. The proposed uniaxial constitutive models in Chapter 3 offered a reliable characterisation of rubberised concrete through the CDP model. The perfect bond assumption between concrete material and reinforcement as well as external confinement provided a good representation of the behaviour. Although the monotonic simulations of the beam-column member behaviour overestimated the degradation of the members compared to the experimental response, all the simulations showed very good agreement with the test results in terms of the initial stiffness, cracked stiffness and the maximum lateral capacities.
- The parametric study on rubberised concrete members carried out based on the validated numerical models aimed at investigating the effects of key influencing factors on the behaviour. The parametric assessment first focused on the rubberised concrete shear strength-compressive strength relations. This was followed by an assessment of the effects of rubber content, reinforcement ratio, and axial load on the key performance characteristics of beam-column members.
- In total, 16 simulations on models subjected to asymmetric shear were considered, in which the reference concrete strength and rubber content were varied. Based on the findings from the tests and numerical parametric assessments, an expression was proposed in this study, for the first time, in order to relate directly the rubberised concrete shear resistance and concrete strength.
- More than 70 models were established to examine the performance characteristics of flexural rubberised concrete members. These parametric studies focused on quantifying the member axial-bending strength interaction, stiffness, ductility as well as the spread of plasticity.
- The sensitivity assessments indicated that members with higher rubber content provided lower stiffness. Meanwhile, with the presence of axial load, the member stiffness was governed by the

constituent concrete material compared to the cantilever case hence rubberised concrete members showed much higher stiffness reduction under axial loads. In addition, it was shown that further increase of axial load and reinforcement ratio had minor influence on stiffness reduction ratios which indicated that the increase of rubber content has the most notable influence on the stiffness reduction of RRuC members under combined axial-bending actions.

- The study of the compressive strength of stirrup confined rubberised concrete suggested that the effect of stirrup confinement on concrete strength increased significantly with rubber content. A new stirrup confined concrete strength model was proposed based on the analysis, which provided more accurate prediction of confined rubberised concrete strength compared to existing models.
- The rotational ductility of members is substantially reduced with the increase of axial load, but increases with the increase of rubber content. For practical application, a relationship between the rotational ductility and rubber content, reinforcement ratio as well as the axial load level was proposed, and showed good agreement with the experimental and numerical results.
- The spread of plasticity within the beam-column member was examined based on the sum of the "moment gradient" portion and the "local deformation" portion, which are influenced by the rubber content simultaneously. As before, prediction equations were proposed based on the experimental and numerical findings, for use in practical applications.

In general, although the presence rubber particles leads to a reduction in the strength and stiffness of concrete members under various types of loading, it provides considerable enhancement in the deformation capacity compared to conventional reinforced concrete members. Combined with longitudinal and lateral reinforcement as well as possible external confinement, rubberised concrete has significant potential for use in practice within structural members. With careful design in detailing, reinforced rubberised concrete members can offer an ideal combination of structural performance characteristics and an environmentally-friendly design solution.

9.2 Suggestions for future research

This thesis described detailed investigations into the behaviour of concrete incorporating rubber particles, starting from the fundamental mechanical properties of the materials to the performance of reinforced rubberised concrete members under various loading conditions. However, a number of issues were not examined and require further future research. Several suggestions are given as follows:

- Additional work is required to establish a constitutive model for externally confined rubberised concrete. The effectiveness of external confinement is influenced by the geometry of the

element and the constituent material properties. Also, the type of applied loading plays a significant role in the level of activation of the confinement. Further tests on confined rubberised concrete cylinders under various loading conditions can be performed together with complementary numerical simulations to examine and quantify this behaviour.

- Further work is required to simulate the cyclic behaviour of RRuC and CRRuC members within detailed numerical models. This would enable further assessment of the energy dissipation capabilities under various loading histories.
- Previous research indicated that the presence of rubber particles effectively increases the damping levels exhibited by members. This needs to be quantified in future studies.
- In addition to the mechanical properties investigated in this research, other properties of the rubberised concrete mixes, such as thermal and electric conductivity are also worth examining as they may be of importance in various applications.
- Unlike mineral aggregates, the physical behaviour of rubber materials can be influenced by heat, moisture and ultraviolet rays through time, which may alter the structural behaviour of rubberised concrete. Consequently, further experimental and analytical studies on the aging and corrosion behaviour of rubberised concrete materials are also necessary for future applications.
- The mechanical properties of concrete mixes can be altered by incorporating various types of additives and aggregates, such as recycled rubber in this research. Such new mixes can possess the merits of constituent materials, which allows wider application. Based on the research methodology and findings from this research, further studies on various types of concrete mixes can provide other innovative materials, such as energy storage concrete and insulation concrete.

References

Abendeh R., Ahmad H.S. and Hunaiti Y.M. (2016) Experimental studies on the behavior of concrete-filled steel tubes incorporating crumb rubber. *Journal of Constructional Steel Research*. 122, 251–260.

ACI Committee, (2014) *ACI 318-14: Building code requirements for structural concrete and commentary*. Farmington Hills: American Concrete Institute.

AD.RI.A Abruzzo SRL, Adriatica Riciclaggio e Ambiente, Granulato di Gomma, http://www.adria-abruzzo.it/ADRIA/index.html.

Aiello M.A. and Leuzzi F. (2010) Waste tyre rubberised concrete: properties at fresh and hardened state. *Waste Management*. 30 (8–9), 1696–1704.

Aliabdo A.A., Elmoaty A.E. and AbdElbaset M.M. (2015) Utilization of waste rubber in non-structural applications. *Construction and Building Materials*. 30 (91), 195–207.

Anagennisi Project, ' Innovative Use of all Tyre Components in Concrete ' : http://www.anagennisi.org/.

Arrea M. and Ingraffea A. (1982) Mixed Mode Crack Propagation in Mortar and Concrete Dpt. of Structural Engineering, Cornell University, Report 81–13.

ASTM International (2010) *C1609/C1609M – 12, Standard Test Method for Flexural Performance of Fiber-Reinforced Concrete (Using Beam with Third-Point Loading)*, West Conshohocken (USA).

ASTM International (2015) *C39/C39M _ 15. Standard Test Method for Compressive Strength of Cylindrical Concrete Specimens*, West Conshohocken (USA).

ASTM International (2011) *C496/C496M _ 11. Standard Test Method for Splitting Tensile Strength of Cylindrical Concrete Specimens*. West Conshohocken (USA).

Atahan A.O. and Sevim U.K. (2008) Testing and comparison of concrete barriers containing shredded waste tire chips. *Materials Letters.* 62 (21–22), 3754–3757.

Atahan A.O. and Yücel A.Ö. (2012) Crumb rubber in concrete: static and dynamic evaluation. *Construction and Building Materials.* 36, 617–622.

Azevedo F., Pacheco-Torgal F., Jesus C., Barroso de Aguiar J.L. and Camões A.F. (2012) Properties and durability of HPC with tyre rubber wastes. *Construction and Building Materials.* 34, 186–191.

Azmi N.J., Mohammed B.S. and Al-Mattarneh H.M.A. (2008) Engineering properties of concrete containing recycled tire rubber. in: *International Conference on Construction and Building Technology*. 373, 382.

BAG column formers: http://www.euroacc.co.uk/products/

Banks-Sills L. and Arcan M. (1983) An edge-cracked mode II fracture specimen. *Experimental Mechanics*. 23(3), 257-261.

Barragan B., Gettu R., Agullo L. and Zerbino R. (2006) Shear failure of steel fiber-reinforced concrete based on push-off tests. *ACI materials journal*. *103*(4), 251.

Batayneh M.K., Marie I. and Asi I. (2007) Promoting the use of crumb rubber concrete in developing countries. *Waste Management*. 28, 2171-2176.

Bažant Z.P. (1985) *Fracture in concrete and reinforced concrete*. John Wiley & Sons.

Bažant, Z. P., and Pfeiffer P.A. (1986) Shear fracture tests of concrete. *Materials and Structures*. 19(2), 111.

Benazzouk A., Douzane O., Langlet T., Mezreb K., Roucoult J. M. and Quéneudec M. (2007) Physico-mechanical properties and water absorption of cement composite containing shredded rubber wastes. *Cement and Concrete Composites*. 29(10), 732-740.

Bewick B.T., Salim H.A., Saucierm A., and Jackson C.J. (2010) *Crumb rubber-concrete panels under blast loads*. Air Force Research Lab Tyndall AFB FL, Material and Manufacturing Directorate, Report ADA523338, Florida FL, USA.

Bignozzi M.C. and Sandrolini F. (2006) Tyre rubber waste recycling in self-compacting concrete. *Cement and Concrete Research.* 36 (4), 735–739.

Bing C., and Ning L., (2014) Experimental research on properties of fresh and hardened rubberised concrete. *ASCE Journal of Materials in Civil Engineering*. 26 (8).

Binici B. (2005) An analytical model for stress–strain behavior of confined concrete. *Engineering Structures*. 27(7), 1040-1051.

Bompa D.V. and Elghazouli A.Y. (2015) Ultimate shear behaviour of hybrid reinforced concrete beam-to-steel column assemblages. *Engineering Structures*. 101, 318-336.

Bompa D.V. and Elghazouli A.Y. (2017) Bond-slip response of deformed bars in rubberised concrete. *Construction and Building Materials*. 154 884–898.

Bompa D.V. and Elghazouli A.Y. (2017) Numerical modelling and parametric assessment of hybrid flat slabs with steel shear heads. *Engineering Structures*. *142*, 67-83.

Bompa D.V., Elghazouli A.Y., Xu B. Stafford P.J. and Ruiz-Teran A.M. (2017) Experimental assessment and constitutive modelling of rubberised concrete materials. *Construction and Building Materials.* 137, 246–260.

Bompa D.V. and Oneţ T. (2016) Punching shear strength of RC flat slabs at interior connections to columns. *Magazine of Concrete Research*. 68 (1), 24–42.

Boulifa R., Samai M.L. and Benhassine, M.T. (2013) A new technique for studying the behaviour of concrete in shear. *Journal of King Saud University-Engineering Sciences*. 25(2), 149-159.

BSI (British Standards Institute) (2004) *BS EN 1504-4:2004. Products and systems for the protection and repair of concrete structures. Definitions, requirements, quality control and evaluation of conformity. Structural bonding*. London (UK), BSI.

Campana S., Fernández Ruiz M., Anastasi A. and Muttoni A. (2013) Analysis of shear transfer actions on one-way RC members based on measured cracking pattern and failure kinematics. *Magazine of Concrete Research*. 56 (6), 386–404

Cairns R.A., Kew H.Y. and Kenny M.J.(Eds) (2004) The Use of Recycled Rubber Tyres in Concrete Construction. *Sustainable Waste Management and Recycling.* Thomas Telford Ltd, London, UK, 135–142.

CEB-fib (2012) fib Model Code 2010. fib Bulletins 65 and 66. Lausanne (Switzerland), fib.

CEN (European Committee for Standardization) (2009) *EN 12390-2:2009, Testing Hardened Concrete: Making and Curing Specimens for Strength Tests*, Brussels (Belgium), CEN.

CEN (European Committee for Standardization) (2004) *EN 1992-1-1, Eurocode 2: Design of Concrete Structures, Part 1–1: General Rules for Buildings*. Brussels (Belgium), CEN.

CEN (European Committee for Standardization) (2004) *EN 1998-3, Eurocode 8: Design of structures for earthquake resistance - Part 3: assessment and retrofitting of buildings*. Brussels (Belgium), CEN.

CEN (European Committee for Standardization) (2000) *EN 206-1:2000. Concrete —Part 1: specification, performance, production and conformity*. Brussels (Belgium), CEN.

CEN (European Committee for Standardization) (2000) *EN 450-1:2012. Fly ash for concrete – Part 1: definition, specifications and conformity criteria*. Brussels (Belgium), CEN.

CEN (European Committee for Standardization) (2005) *EN 933-1:2012. Tests for geometrical properties of aggregates – Part 1: determination of particle size distribution – Sieving method*. Brussels (Belgium), CEN.

CONICA, Recycled Rubber from Used Tyres, http://www.conica.com/en/commodities/black-granules/rubber-granules/recycled-tyre-rubber/.

Dai J. G., Bai Y. L. and Teng J. G. (2011) Behavior and modeling of concrete confined with FRP composites of large deformability. *Journal of composites for construction*. 15(6), 963-973.

Douglah S. and Everett J.W. (1998) Scrap tire disposal: I. Survey of state programs. *Journal of Solid Waste Technology and Management*. 25(1), 40–50.

DSS (Dassault Systèmes Simulia Corp.) (2010) *Abaqus Analysis Users' Manual, Version 6.10*. DSS, Providence, RI, USA.

Duarte A.P.C., Silva B.A., Silvestre N., De Brito J., Júlio E. and Castro J.M. (2016) Tests and design of short steel tubes filled with rubberised concrete. *Engineering Structures*. 112, 274-286.

Eldin N.N. and Senouci A.B. (1993) Rubber-tyre particles as concrete aggregate. *ASCE Journal of Materials in Civil Engineering*. 5 (4), 478–496.

Elghazouli A.Y. and Treadway J. (2008) Inelastic behaviour of composite members under combined bending and axial loading. *Journal of Constructional Steel Research*. 64(9), 1008-1019.

Elghazouli, A. Y., Bompa, D. V., Xu, B., Stafford, P. J., and Ruiz-Teran, A. M. (2017) Inelastic behaviour of RC members incorporating high deformability concrete. *fib Symposium Maastricht, Netherlands.* 2399-2406.

Elghazouli, A. Y., Bompa, D. V., Xu, B., Stafford, P. J., and Ruiz-Teran, A. M. (2018) Performance of rubberised reinforced concrete members under cyclic loading. *Engineering Structures*. 166, 526-545.

ELKEM, Elkem Microsilica Grade 940 for Concrete, https://www.elkem.com/silicon-materials/high-performance-concrete/microsilica-concrete-grades/microsilica-grade-940-construction/.

Epps J.A. (1994) Uses of recycled rubber tires in highways. *Synthesis of Highway Practice 198*. Transportation Research Board, National Research Council, Washington, D.C.

Everling G. (1964) Comments Upon the Definition of Shear Strength. *International Journal of Rock Mechanics and Mining Sciences & Geomechanics Abstracts*. 1(2), 145–154.

Fam A., Flisak B. and Rizkalla S. (2003) Experimental and analytical modeling of concrete-filled FRP tubes subjected to combined bending and axial loads. *ACI Structural Journal*. 100(4), 499-509.

Fardis M.N. and Khalili H.H. (1982) FRP-encased concrete as a structural material. *Magazine of Concrete Research*. *34*(121), 191-202.

Fattuhi N.I. and Clark L.A. (1996) Cement-based materials containing shredded scrap truck tyre rubber. *Construction and Building Materials*. 10 (4), 229–236.

Ganesan N., Raj B. and Shashikala A.P. (2013) Behavior of self-consolidating rubberized concrete beam-column joints, *ACI Materials Journal*, 110 (6) 697.

Ganjian E., Khorami M., and Maghsoudi A.A. (2009) Scrap-tyre-rubber replacement for aggregate and filler in concrete. *Construction and Building Materials.* 23 (5), 1828–1836.

Ghaly A.M. and Cahill IV J.D. (2005) Correlation of strength, rubber content, and water to cement ratio in rubberised concrete. *Canadian Journal of Civil Engineering*. 32 (6), 1075–1081.

Ghizdaˇveţ Z., Ştefan B.M., Nastac D., Vasile O. and Bratu M. (2016) Sound absorbing materials made by embedding crumb rubber waste in a concrete matrix. *Construction and Building Materials.* 15 (124), 755–763.

Gopalaratnam V. S. and Gettu R. (1995) On the characterization of flexural toughness in fiber reinforced concretes. *Cement and concrete composites*. *17*(3), 239-254.

Guneyisi E., Gesoglu M. and Ozturan T. (2004) Properties of rubberised concretes containing silica fume. *Cement and Concrete Research*. 34 (12), 2309–2317.

Hall M.R. and Najim K.B. (2014) Structural behaviour and durability of steel-reinforced structural Plain/Self-Compacting Rubberised Concrete (PRC/SCRC). *Construction and Building Materials.* 30 (73), 490–497.

Han Q., Wang Y., Xu J. and Xing Y. (2015) Static behavior of stud shear connectors in elastic concrete–steel composite beams. *Journal of Constructional Steel Research*. 113, 115–126.

He L., Ma Y., Liu Q. and Mu Y. (2016) Surface modification of crumb rubber and its influence on the mechanical properties of rubber-cement concrete. *Construction and Building Materials*. 120, 403-407.

Hernandez-Olivares F., Barluenga G., Bollatib M. and Witoszekc B. (2002) Static and dynamic behaviour of recycled tyre rubber-filled concrete. *Cement and Concrete Research*. 32 (10), 1587–1596.

Hesami S., Hikouei I.S. and Emadi S.A.A. (2016) Mechanical behavior of self-compacting concrete pavements incorporating recycled tire rubber crumb and reinforced with polypropylene fiber. *Journal of Cleaner Production*. 133, 228-234.

Himsworth F.R. (1954) The variability of concrete and its effect on mix design, *Proceedings of the institution of Civil Engineers.* 3 (2) 163–200.

Hines E.M., Seible, F. and Priestley M.N. (2002) *Experimental spread of plasticity in reinforced concrete bridge piers*. Department of Structural Engineering, University of California, San Diego.

Hognestad E. (1951) *Study of combined bending and axial load in reinforced concrete members*. University of Illinois at Urbana Champaign, College of Engineering. Engineering Experiment Station.

HOPE Construction Materials, High Strength 52.5N Cement, http://hopecement.com/product/high-strength-52-5n-cement/.

Hordijk, P. A. (1991). Local approach to fatigue of concrete. *Doctoral Thesis, Delft University*.

Hordijk D.A. (1992) Tensile and Tensile Fatigue Behaviour of Concrete; Experiments, Modelling and Analyses. *Heron.* 37 (1).

Hsu T.T.C, Slate F.O., Sturman G.M. and Winter G. (1963) Microcracking of plain concrete and the shape of the stress-strain curve. *ACI Journal*. 60 (14), 209-224.

Ingraffea A. R. (1985). Analysis of shear fracture tests of concrete beams. In*: US-Japan Seminar on Finite Element Analysis of Reinforced Concrete Structures*, Tokyo, 71-91.

Iosipescu N., Negoita A. (1969) A new method for determining the pure shearing strength of concrete. *Concrete*. 3(1), 63.

Ismail M.K. and Hassan A.A. (2016) Ductility and cracking behavior of reinforced self-consolidating rubberized concrete beams. *Journal of Materials in Civil Engineering.* 29 (1), 04016174.

Ismail, M. K., and Hassan, A. A. (2016). Impact Resistance and Acoustic Absorption Capacity of Self-Consolidating Rubberized Concrete. *ACI Materials Journal*, 113(6).

Ismail M.K. and Hassan A.A. (2016) Performance of full-scale self-consolidating rubberized concrete beams in flexure. *ACI Materials Journal*. 113 (2), 207.

Jenq Y. S. and Shah S. P. (1988) Mixed-mode fracture of concrete. *International Journal of Fracture. 38*(2), 123-142.

JSCE-SF6 (1990). Method of Test for Shear Strength of Steel Fiber Reinforced Concrete (SFRC). *Japan Society of Civil Engineers*, Tokyo, 67–69.

Kardos A.J. and Durham S.A. (2015) Strength, durability, and environmental properties of concrete utilizing recycled tire particles for pavement applications. *Construction and Building Materials*. 98, 832-845.

Khaloo A.R., Dehestani M. and Rahmatabadi P. (2008). Mechanical properties of concrete containing a high volume of tyre-rubber particles. *Waste Management*. 28(12), 2472–2482.

Khatib Z.K. and Bayomy F.M. (1999) Rubberised Portland cement concrete. *ASCE Journal of Materials in Civil Engineering*. 11 (3), 206–213.

Kupfer H. B. and Gerstle K. H. (1973) Behavior of concrete under biaxial stresses. *Journal of the Engineering Mechanics Division*. 99(4), 853-866.

Lam L. and Teng J.G. (2003) Design-oriented stress–strain model for FRP-confined concrete. *Construction and Building Materials*. 17(6-7), 471-489.

LaVision - DaVis digital image correlation software http://www.lavision.de/en/products/davis-software/index.php

Lee J. and Fenves G. L. (1998) Plastic-damage model for cyclic loading of concrete structures. *Journal of engineering mechanics*. 124(8), 892-900.

Li G., Pang S.S. and Ibekwe S.I. (2011) FRP tube encased rubberized concrete cylinders. *Materials and Structures*. 44(1), 233-243.

Li L.J., Chen Z.Z., Xie W.F. and Liu F. (2009) Experimental study of recycled rubber-filled high-strength concrete. *Magazine of Concrete Research*. 61 (7) 549–556.

Liu F., Zheng W., Li L., Feng W. and Ning F. (2013) Mechanical and fatigue performance of rubber concrete. *Construction and Building Materials*. 47, 711–719.

Lubliner J., Oliver J., Oller, S. and Onate, E. (1989) A plastic-damage model for concrete. *International Journal of solids and structures*. *25*(3), 299-326.

Luong, M. P. (1990) Tensile and shear strengths of concrete and rock. *Engineering fracture mechanics*. 35(1-3), 127-135.

Luong, M. P. (1992) Fracture testing of concrete and rock materials. *Nuclear engineering and design*. 133(1), 83-95.

Mansur M. and Islam M. (2002) Interpretation of concrete strength for nonstandard specimens. *ASCE Journal of Materials in Civil Engineering*. 14 (2), 151–155.

Mattock A. H. and Hawkins N. M. (1972) Shear transfer in reinforced concrete-recent research. *Precast/Prestressed Concrete Institute Journal,* 17(2).

Medina N.F., Flores-Medina D., and Hernández-Olivares F. (2016) Influence of fibers partially coated with rubber from tire recycling as aggregate on the acoustical properties of rubberized concrete. *Construction and Building Materials*. 30 (129), 25–36.

Moharram M.I., Bompa D.V. and Elghazouli A.Y. (2017) Experimental and numerical assessment of mixed RC beam and steel column systems. *Journal of Constructional Steel Research*. *131*, 51-67.

Moustafa A., and ElGawady M.A. (2015) Mechanical properties of high strength concrete with scrap tire rubber. *Construction and Building Materials*. 15 (93), 249-256.

Naito C., States J., Jackson C. and Bewick B.T. (2013) Crumb rubber concrete performance under near-field blast and ballistic demands. *Journal of Materials in Civil Engineering.* 26 (9), 04014062.

Naito C., States J., Jackson C., and Bewick B. (2014) Assessment of crumb rubber concrete for flexural structural members. *ASCE Journal of Materials in Civil Engineering*. 26 (10).

Najim K.B. and Hall M.R. (2013) Crumb rubber aggregate coatings/pre-treatments and their effects on interfacial bonding, air entrapment and fracture toughness in self-compacting rubberised concrete (SCRC). *Materials and Structures*. 46 (12), 2029–2043.

Najim K.B. and Hall M.R. (2012) Workability and mechanical properties of crumb-rubber concrete. *Proceedings of the Institution of Civil Engineers-Construction Materials*. 166(1), 7-17.

Neville A.M. (1959) The relation between standard deviation and mean strength of concrete test cubes. *Magazine of Concrete Research*. 11 (32), 75–84.

Neville A.M. (1993) *Properties of Concrete, fourth ed.* London, Longman.

Nielsen M.P. and Hoang L.C. (2010) *Limit Analysis and Concrete Plasticity, third ed*. Boca Raton (FL, USA), CRC Press, Taylor and Francis Group.

Old Tyres Around the World: Illegally dumped tyres in US town of Shreveport, Louisiana (2017) *Green Distillation Technologies Corporation LTD*, viewed August 2018, <https://www.gdtc6.com/old-tyres-around-world-illegally-dumped-tyres-us-town-shreveport/>

Ozbakkaloglu T., Lim J.C. and Vincent T. (2013) FRP-confined concrete in circular sections: Review and assessment of stress–strain models. *Engineering Structures*. 49, 1068-1088.

Pilakoutas K., Raffoul S., Papastergiou P., Garcia R., Guadagnini M. and Hajirasouliha I. (2015) A study of the reuse of all tyre components in concrete. in: *The Anagennisi Project. Int. Conference on Sustainable sStructural Concrete. 15–18 Sept 2015, La Plata, Argentina*, 221.

Popovics S. (1987) A hypothesis concerning the effects of macro-porosity on mechanical properties of concrete. In: *Fracture of Concrete and Rock: SEM-RILEM International Conference*, Houston, Tex., June 1987. Edited by S.P. Shah and S.E. Swartz. Society for Experimental Mechanics Inc., Bethel, Conn., 220–225.

Priestley M.J.N., Calvi G.M. and Kowalsky M.J. (2007). Direct displacement-based seismic design. In *2005 NZSEE Conference*. 33-43.

Priestley M.N. Seible F. Calvi G.M. and Calvi G.M. (1996) *Seismic design and retrofit of bridges*. New York, John Wiley & Sons.

Raffoul S., Garcia R., Pilakoutas K., Guadagnini M. and Hajirasouliha I. (2015) Fresh properties and stress-strain behaviour of crumb rubberised concrete in axial compression. in: *The Anagennisi Project. Int. Conference on Sustainable Structural Concrete, 15–18 Sept 2015, La Plata, Argentina*, 222.

Raffoul S., Garcia R., Pilakoutas K., Guadagnini M. and Flores Medina N. (2016) Optimisation of rubberised concrete with high rubber content: an experimental investigation. *Construction and Building Materials.* 124, 391–404.

Raffoul S., Garcia R., Escolano-Margarit D., Guadagnini M., Hajirasouliha I. and Pilakoutas K. (2017) Behaviour of unconfined and FRP-confined rubberised concrete in axial compression. *Construction and Building Materials*. 147, 388-397.

Reinhardt H., Cornelissen H. and Hordijk D. (1986) Tensile tests and failure analysis of concrete. *Journal of Structural Engineering*. 112 (11), 2462-2477.

Reinhardt H.W., Ošbolt J., Shilang X. and Dinku, A. (1997). Shear of structural concrete members and pure mode II testing. *Advanced cement based materials*, 5(3-4), 75-85.

Rezaifar O., Hasanzadeh M., and Gholhaki M. (2016) Concrete made with hybrid blends of crumb rubber and metakaolin: optimization using response surface method. *Construction and Building Materials.* 1 (123), 59–68.

Richard H.A. (1981) A new compact shear specimen. *International Journal of Fracture*. 17(5), R105-R107.

RILEM Technical Committees (2000) RILEM TC 148-SSC: strain softening of concrete test methods for compressive softening. *Materials and Structures*. 33 (6), 347–351.

Rocca S., Galati N. and Nanni A. (2009) Interaction diagram methodology for design of FRP-confined reinforced concrete columns. *Construction and Building Materials*. 23(4), 1508-1520.

Saafi M., Toutanji H.A. and Li Z. (1999) Behavior of concrete columns confined with fiber-reinforced polymer tubes. *ACI Materials Journal*. 96 (4), 500-509.

Sadek D.M. and El-Attar M.M. (2015) Structural behavior of rubberized masonry walls. *Journal of Cleaner Production*. 15 (89), 174–186.

Samaan M., Mirmiran A. and Shahawy M. (1998) Model of concrete confined by fiber composites. *Journal of structural engineering*. *124*(9), 1025-1031.

Schlangen H.E.J.G. (1993) Experimental and numerical analysis of fracture processes in concrete, *Heron*, 38 (2).

Seible F., Priestley M.N. Hegemier G.A. and Innamorato D. (1997) Seismic retrofit of RC columns with continuous carbon fiber jackets. *Journal of composites for construction*. 1(2), 52-62.

Sgobba S., Borsa M., Molfetta M. and Marano G.C. (2015) Mechanical performance and medium-term degradation of rubberised concrete. *Construction and Building Materials.* 15 (98), 820–831.

Siddique R. and Naik T.R. (2004) Properties of concrete containing scrap-tire rubber–an overview. *Waste Management*. 24 (6), 563–569.

Sika ViscoFlow 1000 (2015) High Range Water Reducing/Superplasticing Concrete Admixture with Enhanced Workability Retention, Product Data Sheet, Edition 21/5/2015, Sika Limited, UK.

Sika ViscoFlow (2000) High Range Water Reducing/Superplasticing Concrete Admixture with Enhanced Workability Retention, Product Data Sheet, Edition 17/2/2016, Sika Limited, UK.

Silva A., Jiang Y., Castro J.M., Silvestre N. and Monteiro R. (2016) Experimental assessment of the flexural behaviour of circular rubberized concrete-filled steel tubes. *Journal of Constructional Steel Research*. 122, 557-570.

Son K.S., Hajirasouliha I. and Pilakoutas K. (2011) Strength and deformability of waste tyre rubber-filled reinforced concrete columns. *Construction and Building Materials*. 25(1), 218-226.

Su H., Yang J., Ling T.C., Ghataora G.S. and Dirar S. (2015) Properties of concrete prepared with waste tyre rubber particles of uniform and varying sizes. *Journal of Cleaner Production.* 91, 288–296.

Syroka E., Bobiński J. and Tejchman J. (2011) FE analysis of reinforced concrete corbels with enhanced continuum models. *Finite Elements in Analysis and Design*. *47*(9), 1066-1078.

Taha M.M.R., El-Dieb A.S., Ab El-Wahab M.A., and Abdel-Hameed M.E. (2008) Mechanical, fracture, and microstructural investigations of rubber concrete. *ASCE Journal of Materials in Civil Engineering.* 20 (10), 640–649.

TARMAC, Tarmac Trupak building aggregates, http://www.tarmac.com/building-aggregates/.

Teng J.G., Chen J.F., Smith S.T. and Lam L. (2002) FRP: strengthened RC structures. *Frontiers in Physics*. 266.

Topçu L.B. (1995) The properties of rubberised concretes. *Cement and Concrete Research*. 25 (2), 304–310.

Toutanji H.A. (1996) The use of rubber tyre particles in concrete to replace mineral aggregates. *Cement and Concrete Composites*. 18 (2), 135–139.

Tuan H.N., Otsuka H., Ishikawa Y., Takeshita E. (2006) A study on shear strength under direct shear of concrete test. *Japanese Concrete Institute*. 28 (1), 1529–1534

Turatsinze A. and Garros M. (2008) On the modulus of elasticity and strain capacity of self-compacting concrete incorporating rubber aggregates. *Resources, Conservation and Recycling*. 52 (10), 1209–1215.

Tyre Pyrolysis Plant (2016), viewed August 2018, <http://www.tyrepyrolysisplant.com/tyre-recycling-solution/>

Van Mier, J. G. M. (1984). *Strain-softening of concrete under multiaxial loading conditions*. Eindhoven: Technische Hogeschool Eindhoven.

Van Mier J.G.M. Shah S.P., Arnaud M. et al. (1997) Strain-softening of concrete in uniaxial compression. *Materials and Structures*. 30 (4), 195–209.

Vonk R.A. (1992). *Softening of concrete loaded in compression*. Dissertation, Eindhoven University of Technology, Eindhoven.

Walraven J.C. and Reinhard H.W. (1981) Theory and experiments on the mechanical behaviour of cracks in plain and reinforced concrete subjected to shear loading. *Heron.* 26 (1a) 5–68.

Watkins J. (1983) Fracture toughness test for soll-cement samples in mode II. *International Journal of Fracture*. *23*(4), R135-R138.

Weber.tec force aramid sheet - enforce aramid A120 sheet:http://www.epmssupplies.co.uk/admin/products/documents/Weber%20(SBD)/Data/10025%20weber.tec%20force%20aramid%20sheet.pdf

Xiao Y. and Wu H. (2003) Compressive behavior of concrete confined by various types of FRP composite jackets. *Journal of Reinforced Plastics and Composites*. 22(13), 1187-1201.

Xu B., Bompa D.V., Elghazouli A.Y., Ruiz-Teran A.M. and Stafford P.J. (2018) Behaviour of rubberised concrete members in asymmetric shear tests. *Construction and Building Materials*. 159, 361-375.

Xue J. and Shinozuka M. (2013) Rubberised concrete: a green structural material with enhanced energy-dissipation capability. *Construction and Building Materials.* 42, 196–204.

Yi S.T., Yang I.K. and Choi J.C. (2006) Effect of specimen sizes, specimen shapes, and placement directions on compressive strength of concrete. *Nuclear Engineering and Design.* 23 (2), 115–127.

Youssf O., ElGawady M.A., Mills J.E. and Ma X. (2014) An experimental investigation of crumb rubber concrete confined by fibre reinforced polymer tubes. *Construction and Building Materials*. 53, 522-532.

Youssf O., ElGawady M.A. and Mills J.E. (2015) Experimental investigation of crumb rubber concrete columns under seismic loading. *Structures*. 3 13–27.

Youssf O., Mills J.E., and Hassanli R. (2016) Assessment of the mechanical performance of crumb rubber concrete. *Construction and Building Materials.* 30 (125), 175–183.

Zheng L., Huo X.S. and Yuan Y. (2008) Strength, modulus of elasticity, and brittleness index of rubberised concrete. *ASCE Journal of Materials in Civil Engineering*. 20 (11), 692–699.